Influence of radiation induced defect clusters on silicon particle detectors

Dissertation

zur Erlangung des Doktorgrades

des Fachbereichs Physik

der Universität Hamburg

vorgelegt von

Alexandra Junkes

aus Hamburg

Hamburg
2011

Gutachter der Dissertation:	Prof. Dr. Robert Klanner
	Dr. Erika Garutti
Gutachter der Disputation:	Prof. Dr. Robert Klanner
	Prof. Dr. Lutz Feld
Datum der Disputation:	14.07.2011
Vorsitzender des Prüfungsausschusses:	Dr. Georg Steinbrück
Vorsitzender des Promotionsausschusses:	Prof. Dr. Peter Hausschlid
Dekan der MIN Fakultät:	Prof. Dr. Heinrich Graener
Leiter des Department Physik:	Prof. Dr. Daniela Pfannkuche

Für Robert

Abstract

The *Large Hadron Collider* (LHC) at the *European Organization for Nuclear Research* (CERN) addresses some of today's most fundamental questions of particle physics, like the existence of the Higgs boson and supersymmetry. Two large general-purpose experiments (ATLAS, CMS) are installed to detect the products of high energy proton-proton and nucleon-nucleon collisions. Silicon detectors are largely employed in the innermost region, the tracking area of the experiments. The proven technology and large scale availability make them the favorite choice. Within the framework of the LHC upgrade to the high-luminosity LHC, the luminosity will be increased to $L = 10^{35}$ cm^{-2} s^{-1}. In particular the pixel sensors in the innermost layers of the silicon trackers will be exposed to an extremely intense radiation field of mainly hadronic particles with fluences of up to $\Phi_{eq} = 10^{16}$ cm^{-2}.

The radiation induced bulk damage in silicon sensors will lead to a severe degradation of the performance during their operational time. This work focusses on the improvement of the radiation tolerance of silicon materials (Float Zone, Magnetic Czochralski, epitaxial silicon) based on the evaluation of radiation induced defects in the silicon lattice using the *Deep Level Transient Spectroscopy* and the *Thermally Stimulated Current* methods. It reveals the outstanding role of extended defects *(clusters)* on the degradation of sensor properties after hadron irradiation in contrast to previous works that treated effects as caused by point defects.

It has been found that two cluster related defects are responsible for the main generation of leakage current, the $E5$ defects with a level in the band gap at E_C-0.460 eV and $E205a$ at E_C-0.395 eV where E_C is the energy of the edge of the conduction band. The $E5$ defect can be assigned to the tri-vacancy (V_3) defect. Furthermore, isochronal annealing experiments have shown that the V_3 defect exhibits a bistability, as does the leakage current. In oxygen rich material the defect transforms (V_3 activation energy for migration $E_a = 1.77 \pm 0.08$ eV) to the L defect, which can be assigned to the V_3O defect.

In the second part of this work, it is demonstrated that the radiation induced effective doping concentration can be attributed to the generation of three deep acceptors ($H(116K)$, $H(140K)$, $H(151K)$), two donors (BD defect and $E(30K)$) and the vacancy-phosphorus defect VP. The reverse annealing of the effective doping concentration is presented for samples irradiated with neutrons for fluences up to $\Phi = 10^{15}$ cm^{-2}. From defect concentrations it is possible to reproduce the effective doping concentration as extracted from capacitance-voltage characteristics.

The last part of this work deals with the characterisation of Float Zone pad sensors in the frame of the CMS tracker upgrade programme. Due to a new production process, several material defects were introduced in the sensors. They explain unexpected electrical properties in thin sensors.

Kurzfassung

Der *Large Hadron Collider* (LHC) am *European Organization for Nuclear Research* (CERN) versucht elementare Fragen der Teilchenphysik zu klären, wie die Existenz des Higgs-Bosons oder der Super-Symmetrie. Dafür untersuchen zwei Experimente (ATLAS, CMS) die Produkte von hochenergetischen Proton-Proton und Nukleon-Nukleon Kollisionen. Aufgrund ihrer gut ausgereiften Technologie und Verbreitung sind Siliziumsensoren die erste Wahl für Spurdetektoren, besonders im innersten Bereich der Experimente. Durch den Ausbau zum *high luminosity* LHC wird die Luminosität auf $L = 10^{35}$ cm^{-2} s^{-1} erhöht und die zumeist hadronische Strahlenbelastung der innersten Siliziumsensoren auf $\Phi_{eq} = 10^{16}$ cm^{-2} gesteigert.
Während der Betriebszeit führen strahleninduzierte Kristalldefekte zu einer Verschlechterung der Sensoreigenschaften. Aus diesem Grund wird in dieser Arbeit die Verbesserung der Strahlenhärte unterschiedlicher Materialien (Float Zone, Magnetic Czochralski, epitaktisches Silizium) anhand einer Auswertung von strahleninduzierten Defekten im Silizium-Gitter untersucht. Die Defekte werden mittels *Deep Level Transient Spectroscopy* und *Thermally Stimulated Current* charakterisiert. Anders als in früheren Studien, in denen hauptsächlich Auswirkungen von Punktdefekte analysierten wurden, steht in dieser Arbeit die aussergewöhnliche Rolle von Regionen mit hohen Defektdichten, den sogenannten *cluster* im Fokus der Untersuchungen.
Hauptsächliche Verantwortung für die Generation von Dunkelstrom tragen zwei Defekte, zum einen der $E5$-Defekt mit einem Niveau in der Bandlücke bei E_C-0,460 eV zum anderen der $E205a$ bei E_C-0.395 eV, wobei E_C die Energie der Kante des Leitungsbandes darstellt. Die chemische Struktur des $E5$-Defektes kann der *tri-vacancy* (drei Leerstellen V_3) zugeordnet werden. Isochronale Ausheilstudien haben eine Bistabilität des V_3-Defektes aufgezeigt, die ebenso für den Dunkelstrom beobachtet werden kann. V_3 wandelt sich in sauerstoffreichem Material (Migrations-Aktivierungsenergie $E_a = 1,77 \pm 0,08$ eV) in den V_3O-Defekt (L-Defekt) um.
Im zweiten Teil dieser Arbeit wird die Änderung der effektiven Dotierungskonzentration auf drei tiefe Akzeptorniveaus ($H(116K)$, $H(140K)$, $H(151K)$), zwei Donatorniveaus (BD and $E(30K)$) und den Leerstelle-Phosphor-Komplex VP zurückgefürt. Die Änderung der Dotierungs-konzentration während des sogenannte *reverse annealing* wird für Neutronenbestrahlungen bis zu Fluenzen von $\Phi = 10^{15}$ cm^{-2} präsentiert. Die gemessenen Defektkonzentrationen reproduzieren die Werte der effektive Dotierungskonzentration aus Kapazitäts-Charakteristika während der Ausheilstudie.
Im letzten Teil dieser Arbeit wird Float Zone Material für den Ausbau des CMS-Spurdetektors untersucht. Aufgrund eines neuartigen Produktionsprozesses wurden Materialdefekte gebildet, deren Analyse die unerwartete elektrische Eigenschaften in abgedünnten Sensoren erklären.

Contents

List of Abbreviations, Physical Constants and Symbols

Abbreviations

CERN	*European Organization for Nuclear Research*
C-V	*Capacitance-Voltage characteristics*
DLTS	*Deep Level Transient Spectroscopy*
Epi	Epitaxially grown silicon
et al.	lat.: *et allii*
FZ	Float Zone silicon
GR	Guard Ring
HL LHC	*high luminosity LHC*
I-V	*Current-Voltage characteristics*
MCz	Magnetic Czochralski
MIP	*Minimum Ionising Particle*
PAD	Pad area
PKA	*Primary Knock on Atom*
RT	Room temperature
SCR	*Space Charge Region*
sLHC	*super Large Hadron Collider*
TSC	*Thermally Stimulated Current*

Physical Constants		**Value**
Å	Angström unit	1 Å$=10^{-4}$ µm $=10^{-10}$ m
k_B	Boltzmann constant	$1.380\,658 \times 10^{-23}\,\mathrm{J\,K^{-1}}$ $=8.617\,385 \times 10^{-5}\,\mathrm{eV\,K^{-1}}$

m_0	Electron rest mass	$9.109\,389\,7 \times 10^{-31}\,\mathrm{kg}$
q_0	Elementary charge	$1.602\,177\,33 \times 10^{-19}\,\mathrm{C}$
eV	Electron volt	1 eV=1.6o21810^{-19} J
ϵ_0	Permittivity in vacuum	$8.854\,187 \times 10^{-14}\,\mathrm{F\,cm^{-1}}$
Physical Constants		**Value**
h	PLANCK constant	$6.626\,17 \times 10^{-34}\,\mathrm{J\,s}$
$\hbar$	Reduced PLANCK constant	$h/2\pi$

Values taken from [2]

Symbols		**Unit**
A	Area	$\left[\mathrm{cm^2}\right]$
C	Capacitance	$\left[\mathrm{F}\right]$
C_{end}	Capacitance at full depletion	$\left[\mathrm{F}\right]$
D	Diffusivity	$\left[\mathrm{cm^2\,s^{-1}}\right]$
D_0	Diffusion constant	$\left[\mathrm{cm^2\,s^{-1}}\right]$
E_a	Activation energy	$\left[\mathrm{cm^{-2}}\right]$
E_C	Bottom of conduction band	$\left[\mathrm{eV}\right]$
E_F	FERMI energy level	$\left[\mathrm{eV}\right]$
E_G	Energy bandgap	$\left[\mathrm{eV}\right]$
E_I	Intrinsic FERMI level	$\left[\mathrm{eV}\right]$
E_V	Top of valence band	$\left[\mathrm{eV}\right]$
I	Current	$\left[\mathrm{A}\right]$
I_{dep}	Current at full depletion	$\left[\mathrm{A}\right]$
I_{fw}	Forward current	$\left[\mathrm{A}\right]$
I_{leak}	leakage current	$\left[\mathrm{A}\right]$
J	Current density	$\left[\mathrm{A\,cm^{-2}}\right]$
k	Wave vektor	$\left[\mathrm{m^{-1}}\right]$

k_0	Frequency factor	$\left[\mathrm{s}^{-1}\right]$
$N_{eff,0}$	Original doping concentration	$\left[\mathrm{cm}^{-3}\right]$
N_{eff}	Effective doping concentration	$\left[\mathrm{cm}^{-3}\right]$
N_D	Concentration of donors	$\left[\mathrm{cm}^{-3}\right]$
Symbols		**Unit**
N_A	Concentration of acceptors	$\left[\mathrm{cm}^{-3}\right]$
N_P	Phosphorus doping concentration	$\left[\mathrm{cm}^{-3}\right]$
N_t	Trap concentration	$\left[\mathrm{cm}^{-3}\right]$
t	Time	$\left[\mathrm{s}\right]$
T	Temperature	$\left[\mathrm{K}\right]$
t_{fill}	Filling pulse length (TSC)	$\left[\mathrm{s}\right]$
t_w	Time window	$\left[\mathrm{s}\right]$
V	Volume	$\left[\mathrm{m}^3\right]$
V_{bi}	Built-in voltage	$\left[\mathrm{V}\right]$
V_{bias}	Bias voltage	$\left[\mathrm{V}\right]$
V_{dep}	Voltage at full depletion	$\left[\mathrm{V}\right]$
V_{fill}	Filling pulse voltage (TSC)	$\left[\mathrm{V}\right]$
V_R	Reverse bias voltage (DLTS)	$\left[\mathrm{V}\right]$
V_P	Pulse voltage (DLTS)	$\left[\mathrm{V}\right]$
Vol	Volume	$\left[\mathrm{cm}^3\right]$
W	Width of depletion region	$\left[\mu\mathrm{m}\right]$
α	Current related damage rate	$\left[\mathrm{A\,cm}^{-1}\right]$
κ	Hardness factor	
ρ	Resistivity	$\left[\Omega\,\mathrm{cm}\right]$
σ	Capture cross section	$\left[\mathrm{cm}^2\right]$
$\sigma_{n,p}$	Capture cross section for electrons or holes	$\left[\mathrm{cm}^2\right]$

τ_n	Time constant	$\left[\mathrm{s}\right]$
Φ	Fluence	$\left[\mathrm{cm}^{-2}\right]$
Φ_{eq}	Φ normalised to 1 MeV neutron damage	$\left[\mathrm{cm}^{-2}\right]$
Φ_{nom}	Nominal fluence	$\left[\mathrm{cm}^{-2}\right]$

Some silicon properties	**Value**
Atom density	$5.02 \times 10^{22}\,\mathrm{cm}^{-3}$
Density	$2.329\,\mathrm{g\,cm}^{-3}$
Dielectric constant	11.9
Energy gap	1.12 eV (indirect)
Intrinsic carrier concentration	$9.65 \times 10^{9}\,\Omega\,\mathrm{cm}$
Intrinsic DEBYE *length*	24 µm
Intrinsic resistivity	$1.45 \times 10^{10}\,\mathrm{cm}^{-3}$
Lattice constant	5.431 02 Å
Optical-phonon energy	0.063 eV
Thermal conductivity at 300 K	$1.56\,\mathrm{W\,cm}^{-1}\,\mathrm{K}$

Note: all properties at room temperature and taken from [2].

1. Introduction

The world's largest particle physics accelerator, the *Large Hadron Collider* (LHC) at CERN[1] in Geneva, started operations in 2009 after two decades of planning and construction. Some of today's most fundamental open questions about the structure of matter are addressed by the four LHC-Experiments (CMS[2], ATLAS[3], LHC-B[4], ALICE[5]). So far, the *standard model* of particle physics describes all measurements well. However, it is known that something is missing. The *standard model* cannot be combined with the description of gravity and an explanation for the origin of masses in the *standard model* could not be experimentally proven, yet. From the products of high centre of mass energy proton-proton collisions, it is possible to investigate conditions as seconds after the big bang. At such high energies the discovery of the theoretically predicted *Higgs* boson is anticipated. Furthermore it is aimed to convey results from elementary particle physics to cosmology, for example the search for dark matter and dark energy, the matter-antimatter asymmetry and black holes. Supersymmetry and extra dimensions are candidates for physics beyond the *standard model*.
These rare events can result in spectacular signatures in the detector, which makes it possible to distinguish them from those of the *standard model* back ground. As an example, a signature of a possible heavy *Higgs* boson can be observed via the decay into two Z bosons, which subsequently decay into muon or electron pairs. A centre of mass energy of 14 TeV and a luminosity for proton-proton collision of $L \approx 10^{34}\ \mathrm{cm}^{-2}\ \mathrm{s}^{-1}$ is anticipated. The proton bunches of 1.5×10^{11} particles per bunch collide 40 million times per second in the interaction points in the experiments (25 ns bunch-crossing time).
The collection of data produced by these collisions put a big challenge on the construction of the detector systems. They are usually created in layers of different sensor types. In the two general-purpose experiments, CMS and ATLAS, silicon sensors are installed inside a magnetic field close to the interaction points. They are followed by electromagnetic and hadronic calorimeters. Muon systems are installed in the outermost region of the detector. The demand for the silicon sensors in the innermost part of the detector is the tracking of traversing charged particles and their vertices with high accuracy. From these information it is possible to obtain momenta and charge and sometimes the particle ID.

[1] *European Laboratory for Particle Physics*
[2] *Compact Muon Solenoid*
[3] *A Toroidal Lhc ApparatuS*
[4] *Large Hadron Collider Beauty*
[5] *A Large Ion Collider Experiment*

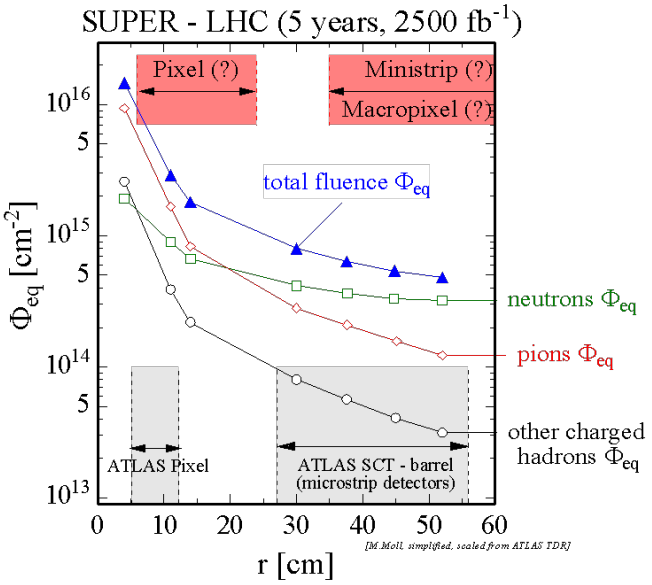

Figure 1.0.1.: Fluence (Φ_{eq}) environment calculated for sLHC detectors (now HL LHC) depending on the distance to the interaction point. Fig. taken from [3].

The silicon sensors installed in the current experiments meet all requirements for tracking systems. They comprise a good spacial resolution due to the very fine granularity, a signal response of 10 ns adequate for the LHC's bunch crossing time and a low ionisation energy leading to a high signal to noise ratio for sensors with typical thicknesses between 300 and 500 µm. The large scale availability and proven technology of the sensors are further reasons to make them first choice for the application in high energy experiments. In CMS, at a radius of 4-11 cm, layers of pixel sensors are installed around the beam pipe with a spacial resolution of 10 µm followed by silicon strip sensors with a resolution better than 30 µm in a distance of up to 55 cm. Overall, this results in 205 m^2 of silicon incorporated in the CMS tracker. The high particle rate, on the other hand, creates a harsh radiation environment. Especially the innermost parts of the detector will be exposed to high radiation levels.
There are already plans for an upgrade of the LHC in 2020 towards the *high luminosity* (HL) LHC. Plans foresee the increase of the instantaneous luminosity to $L \approx 10^{35}$ cm^{-2} s^{-1}. In five years of operation at a radius of 4 cm this would lead to an expected particle fluence of 2×10^{16} cm^{-2}. Fig. 1.0.1 demonstrates the expected particle fluence as function of the distance to the interaction point. It can be observed, that the total fluence decreases towards larger radii. Furthermore, the total fluence has contributions from different particles, mostly dominated by pions up to 15 cm radius, followed by a nearly constant background of backscattered neutrons.
These particles are able to kick out silicon atoms from their lattice site and form defects in the crystal lattice. The radiation damage in the sensors leads to a severe

deterioration of the silicon sensor properties during the operational time of the LHC. Today's LHC sensors will not stand more than the expected radiation exposure for 10 years of LHC operation. Thus, new sensors need to be developed in order to guarantee a satisfying performance of the experiments during the HL LHC era.
There are several approaches for the development of such radiation hard sensors [4]. One possibility focuses on newly developed materials for the sensor fabrication, which are less susceptible to radiation damage. This option is often termed *material engineering*. Furthermore, the development of an optimal sensor design (geometry, polarity) may lead to higher radiation tolerance, or to a reduction of the impact of radiation induced damage effects. This option is often referred to as *device engineering*. A further possibility is the change of detector operation conditions, both during operation and maintenance times. Under the name of CERN-RD50, an international research collaboration was founded with the aim of the *Development of Radiation Hard Semiconductor Devices for Very High Luminosity Colliders* [5]. This work was carried out in the framework of the CERN-RD50 collaboration, focusing on *material engineering*.
The main changes in detector properties after irradiation can be found in the increase of dark current, an increase of trapping and a change of the depletion voltage of the sensor. They lead to a decrease of the signal-to-noise ratio and a degradation of spatial resolution. A *cure* for the radiation induced damage has not been found, yet. However, previous investigations stated a beneficial influence of oxygen in silicon on radiation hardness [4].
The reason for changes of the sensor properties can be found in the formation of lattice defects. A particle kicks out a silicon atom *(primary knock on atom, PKA)*, creating *Frenkel-pairs*. Defect compounds are a consequence of the coupling of impurities with radiation induced *Frenkel-pairs*. If the PKA has a recoil energy of less than 25 eV only point defects can be created. Electrically active defects can introduce levels in the band gap which alter the sensor properties dramatically. Even unirradiated sensors may exhibit process induced defects that are able to deteriorate the properties. Special emphasis has to be put on large conglomerations of defects, the so called *clusters*. They are created if the recoil energy of the PKA is larger than 5 keV. These conglomerations of defects play the key-role for understanding radiation induced sensor degradation after hadron irradiation. Unfortunately there is, up to now, not much information available about their composition. This work focuses on defects which are related to clusters. The aim of this work is the fundamental understanding of the impact of cluster defects on electrical sensor properties and the possible assignment of defect levels to their chemical structure. This knowledge contributes to the development of new radiation tolerant materials as well as to the selection of the best option. The final result of all efforts is supposed to be a sensor that endures 5 years of operation in the hostile HL LHC radiation environment.
In this work silicon materials with different impurity content are investigated. Samples with high oxygen content used in this work are Magnetic Czochralski (MCz) and oxygen enriched epitaxial (Epi-Do), low oxygen concentration is present in standard epitaxial (Epi-St) and standard float zone (FZ) silicon. The samples were irradiated

with 1 MeV neutrons and 24 GeV/c protons and subsequently studied for changes of the depletion voltage and the increase of dark current by the *capacitance-voltage/current-voltage* C-V/I-V method. A comparison of these macroscopic properties with results of defect analysis by *Deep Level Transient Spectroscopy* (DLTS) and *Thermally Stimulated Current* (TSC) technique was performed in order to link specific defects to the macroscopic results. During this work also *annealing* studies were performed. Material and irradiation were selected depending on the demand of the defect study.
In chapter 2 the main materials and material properties of the investigated sensors are introduced, followed by a discussion of the basic properties of silicon in chapter 3, and the impact of radiation damage and change of the sensor properties in chapters 4 and 5. A brief introduction to the measurement methods is given in chapter 6, followed by an overview of the most important impurities and defects in silicon in chapter 7. The main research results are divided in three parts, beginning with the results concerning the dark current in chapter 8, followed by the analyses of the change of the depletion voltage of highly neutron irradiated epitaxial material in chapter 9.
Chapter 10 is reserved for the analyses of non-irradiated new silicon materials for future CMS detectors. This chapter's content differs from the very fundamental research topic of *cluster* defects in silicon. However, it illustrates impressively the prospects offered by of defect analysis regarding the understanding of material properties. Thus the result of this chapter can be considered as an *application* of defect investigation with direct impact on newly developed detector grade silicon.
In the end a summary will conclude the main outcome of this work.

2. Semiconductor Detectors

Position sensitive silicon detectors are largely employed in the tracking systems of high energy physics (HEP) experiments due to their outstanding performance. They meet all requirements for the observation of particle tracks, delivering information about particle momenta and charge in a very hostile environment in the innermost part of the detectors. The operation of silicon sensors principally is possible at room temperature, it is not necessary to operate them at cryogenic temperatures like germanium detectors for example. This is very convenient, nevertheless, in the experiments the sensors will be later kept at temperatures around -10 °C to reduce noise created by leakage current. They offer a short signal response (10 ns) adequate for the bunch crossing of the LHC (25 ns). The production of very finely segmented structures (pixels, strips) is necessary for very precise track reconstruction. A low mean ionisation energy of about 3.6 eV to produce an e/h pair (gas ionisation chambers: 30 eV) and the large density of silicon guarantees good signal quality due to a number of 80 electron/hole-pairs (e/h-pairs) created by a traversing *minimum ionising particle* (MIP) per µm. Those properties enable the use of thin sensors (typically 300-500 µm), offering multi-layer structures without too much demand of the material budget. Furthermore, the large scale availability and mass market production offers high quality monolithic active sensors at low cost.
However, silicon sensors as used in the present LHC experiments have some disadvantages. They need a high quantity of support materials, for structural integrity, biasing, cooling etc. Although the sensors themselves are thin, the whole sensor system results in a rather large material budget (Up to X/X0=0.2 radiation length for CMS Pixel barrel).
The radiation tolerance of silicon sensors is high, e.g. compared to *Gas Electron Multipliers* (GEM). Nevertheless, the silicon sensors installed in existing LHC experiments cannot cope with the radiation environment expected in the future HL LHC. New structures and materials, offering the same advantages as explained above have to be developed for applications in future HL LHC experiments. In contrast to the requirements of the experiments, the basic research dealing with radiation tolerance of silicon investigates much simpler structures and materials. Therefore, the samples used in this work are designed as simple as possible with material properties that will never be suggested for real applications. However, such materials offer indispensable insight into the basic generation of radiation damage and their impact on the sensor properties. This chapter introduces the used sensors design and main materials.

2.1. Modus operandi

The principle of a semiconductor used as particle detector is very similar to a solid state ionisation chambers. As depicted in Fig. 2.1.1, a sensor is operated under reverse bias, being totally depleted of charge carriers. When a particle traverses the depleted sensor, the silicon atoms get ionised and e/h-pairs are created. The electrical field forces the charge carriers to travel through the sensor volume towards the electrodes and thus a current is induced. The current can be measured and the integrated current is proportional to the number of e/h-pairs created in the bulk. The number of e/h-pairs on the other hand is proportional to the absorbed energy divided by the ionisation energy.

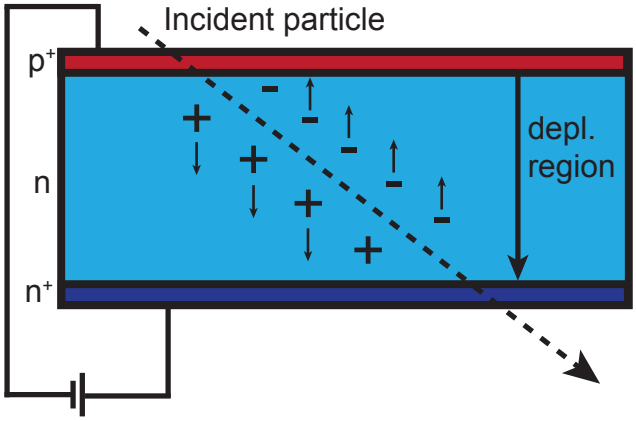

Figure 2.1.1.: Schematic principle of a semiconductor particle detector used in HEP experiments.

2.2. Materials and devices

The formation of radiation induced defects in the silicon crystal is strongly influenced by the impurity content of the material. Therefore, it is vital to chose the appropriate material for the systematic study of the defect generation, annealing and the defect's impact on electrical properties. In fact, the impurity content of the silicon material is the key issue for the investigations described in this work.
The impurity content of the different materials is mainly determined by the growth technique. The materials are of high purity, but there are always some impurities remaining. The dominating impurities that can be found in high-purity silicon are oxygen and carbon and of course the doping atoms.
The silicon investigated in this work cover the most commonly used detector grade materials. They are grown by three different methods which result in different oxygen, carbon and doping concentrations and profiles. Their main parameters are listed in

Tab. 2.2.1. One can distinguish between three different crystal-growth methods, which are Float Zone (FZ), Magnetic Czochralski (MCz) and epitaxial growth (Epi) processes. A brief description of the growth principles can be found in [6].

Float Zone

The FZ method is based on the zone-melting principle and was develeoped by THEUERER in 1962 [7]. The resulting silicon is characterised by an exceptional high purity, with low levels of oxygen and carbon concentration. The growth of large FZ single crystal rods is possible up to diameters of 150 mm. Oxygen enrichment can be done as a first step of the device fabrication at the wafer level. Because of the a non-uniform preheating during the zone melting process, FZ materials may exhibit a radial inhomogeneity in the impurity and resistivity distribution.

In this work *n*-type FZ material produced by SILTRONIC [8] with a crystal orientation of <100> was used. The processed wafers were thinned to a nominal thickness of $d = 100 \pm 10$ µm. The sensors were delivered with a doping of 1.4×10^{13} cm^{-3} and a nominal resistivity of ρ =300 Ω cm. The sensors made of this material exhibit a low oxygen concentration at an average of [O]= 10^{16} cm^{-3}. Impurity depth profiles after full processing obtained from *secondary ion mass spectrometry* (SIMS) [9] performed by A. Barcz at the Institute of Electron Technology (ITE) [10] are presented in Fig. 2.2.1 (a) for oxygen and Fig. 2.2.1 (b) for carbon. FZ is denoted by green squares in both figures. While the carbon concentration is decreasing towards the rear-side, an out-diffusion of oxygen into the bulk can be observed starting from the SiO_2 layer at the front side.

Magnetic Czochralski

The production of crucible grown Cz material is based on the work of J. CZOCHRALSKI in 1918 [11]. He observed that the growth of a crystal is possible by slowly pulling a seed-crystal out of a melt held in a crucible. With this technique, it is possible to influence the impurity concentration in the silicon by controlling the ingredients of the melt. The resulting material is called standard Czochralski silicon (Cz). With today's technologies it is possible to further influence the impurity concentrations by applying a magnetic field (MCz material). Thus controlling the impurity flow inside the melt it is possible to reduce the concentration of oxygen in the silicon crystal and provide a much better homogeneity of the impurity content.

The MCz silicon used in this work was produced by OKMETIC [12] with a crystal orientation of <100>. The thickness of the wafers was chosen to be d =300 µm with a doping of 4.9×10^{12} cm^{-3}. This material has a high resistivity of ρ =1 kΩ cm.

The oxygen concentration for MCz is in general high and homogeneously distributed, here with an average value of about [O]= 6×10^{17} cm^{-3}. Impurity depth profiles after full processing obtained from SIMS are presented in Fig. 2.2.1 (a) for oxygen and Fig. 2.2.1 (b) for carbon. The MCz sample is denoted with the black diamond in both figures and present the expected result of a very homogenous oxygen distribution. At the front side a small layer with lower oxygen concentration was observed as a result of out-diffusion. The carbon concentration observed for MCz is at the edge or even below the detection limit of the SIMS method [13].

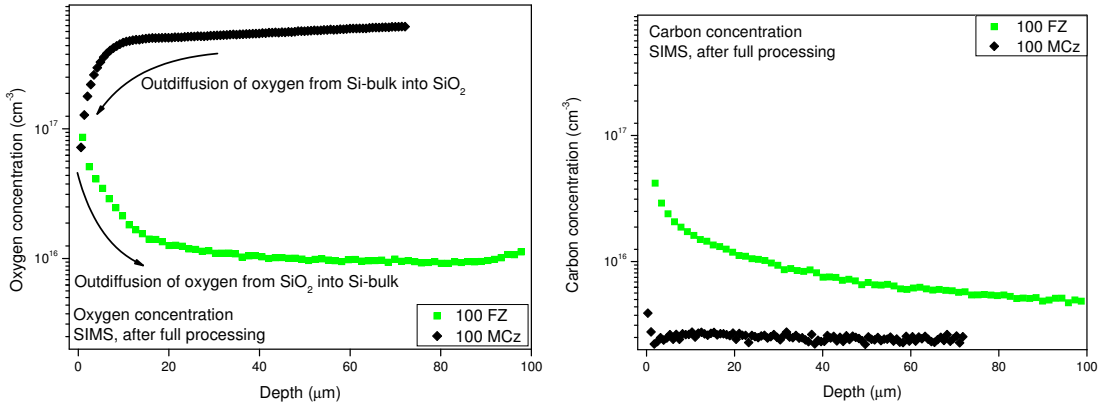

Figure 2.2.1.: SIMS [9] measurements performed by ITE Warsaw [10] revealing the oxygen (a) and carbon concentration (b) of different materials used in this work. The carbon concentration of the MCz material is supposed to be below the detection limit of the SIMS method [13].

Material	Labelling	Thickn. µm No.	Orient.	$N_{eff,0}$ 10^{12} cm^{-3}	ρ Ω cm	[O] 10^{16} cm^{-3}
Epi-Do	75 DO	73	<111>	26	177	60
Epi-St	75 ST	75	<111>	26	174	10
Epi-Do	100 DO	100	<100>	15	290	27
Epi-St	100 ST	101	<100>	15	286	5
Epi-Do	150 DO	152	<100>	8	548	14
Epi-St	150 ST	149	<100>	8	512	5
Float Zone	100 FZ	98	<100>	14	309	1
Magnetic Czochralski	300 MCz	276	<100>	5	885	52

Table 2.2.1.: Properties of silicon materials used in this work. $N_{eff,0}$ denotes the original doping and ρ the resistivity.

Epitaxially grown silicon

Epitaxy means the deposition of mono-crystalline layers on a substrate that acts as seed crystal. The material itself is of high purity, but depending on the substrate, the oxygen concentration in the Epi-layer may be highly inhomogeneous due to the out-diffusion from the substrate with a high oxygen concentration.

The epitaxial material used in this work was produced by ITME by means of *chemical vapor deposition* (CVD) on a Cz substrate. The substrate was heavily doped with antimony (Sb) with a resistivity of ρ =0.02 Ω cm in order to prevent the substrate from acting as active sensor volume and to guarantee a good ohmic contact. In this

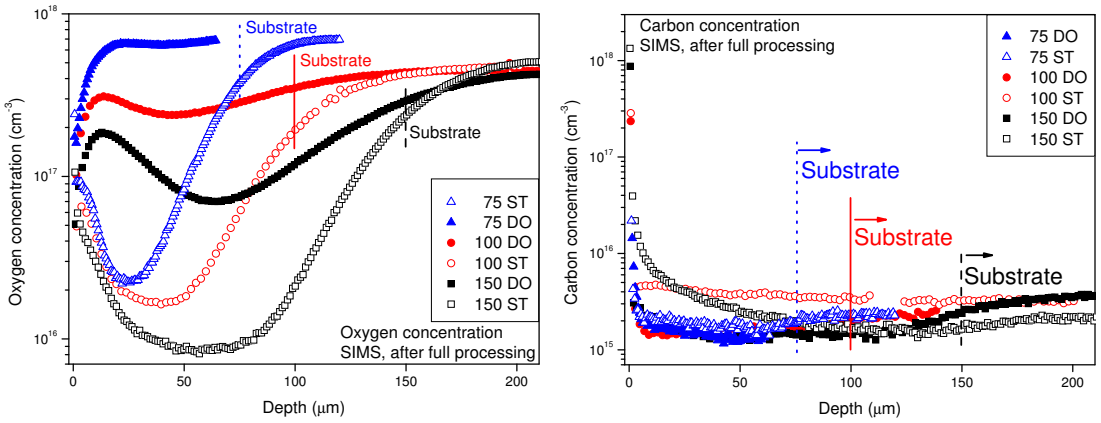

Figure 2.2.2.: Oxygen (a) and carbon (b) concentration depth profiles measured by SIMS [9] for 75, 100 and 150 µm *n*-type for standard Epi and oxygen enriched Epi diodes (see text). Measurements were performed by A. Barcz at ITE Warsaw [10]. The observed concentrations of carbon are below the detection limit of the SIMS method [13].

work three different layer-thicknesses were investigated. The thinnest layer had a nominal thickness of d =75 µm and was grown in <111> crystal orientation. The two other thicknesses were chosen to be d = 100 µm and d = 150 µm both with a crystal orientations of <100>. The initial doping concentrations ($N_{eff,0}$) of the three thicknesses were chosen in order to result in an similar depletion voltage of about 100 V, for all materials. Therefore, thin diodes were doped higher than the thick diodes. Starting from 2.5×10^{13} cm^{-3} for d =75 µm, 1.5×10^{13} cm^{-3} for a layer thickness of d =100 µm and finally $8 - 9 \times 10^{12}$ cm^{-3} for the d =150 µm thick sensors.
In order to investigate the influence of [O] on the defect formation in the same material, a part of the Epi-material was oxygen enriched (Epi-Do). Therefore, the wafers were heated for 24 hours at 1100 °C. Oxygen diffuses at such high temperatures from the Cz-substrate with high [O] into the epitaxial-layer, increasing the oxygen concentration and the homogeneity. The depth profiles of the oxygen concentration is displayed in Fig. 2.2.2 (a) for the three different layer thicknesses with and without oxygen enrichment.
The level and homogeneity of oxygen in the material is highest for the 75 DO sample. Only at the front-side a small layer of lower oxygen concentration is observed. The mean concentration was measured with [O]= 6×10^{17} cm^{-3}. Compared to that, the non-enriched sample 75 ST is very inhomogeneous with a minimum concentration at d =30 µm. The samples become more inhomogeneous for thicker Epi-layers for the ST and for the DO materials, respectively. The concentration of carbon is at the detection limit of the SIMS method [13], and expected to be very low. This is presented in Fig. 2.2.2 (b).

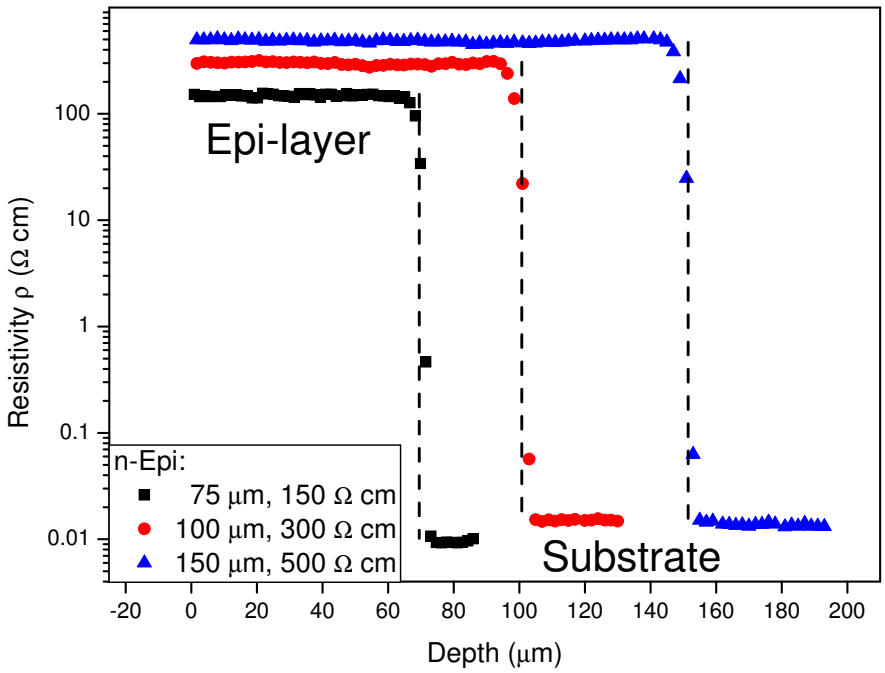

Figure 2.2.3.: Resistivity depth profiles as measured by *spreading resistance measurements* measured at ITE [10] (symbols) for 75, 100 and 150 µm *n*-type Epi-diodes.

Spreading resistance measurements were performed by A. Barcz at ITE [10] on the different epitaxial materials in order to determine the active layer thickness, the absolute value of the resistivity (ρ) and the homogeneity of the doping concentration ($N_{eff,0}$), deduced from ρ. For that reason one wafer out of ten was used to measure *spreading resistance measurements* and only 9 wafers were delivered. The results are illustrated in Fig. 2.2.3. It is well visible that the interface between the Epi-layer and the substrate is very abrupt for all three materials, hence no problem due to the interface is expected for the operation and examination of the Epi-sensors used in this work.

Devices

The analysis of defects in silicon requires a simple geometry for a well-defined sensor volume, a high electrical strength and a simple electrical field distribution. *Pad diodes* are simple planar diodes without segmentation that correspond to these requirements. A schematic cross section of the FZ and MCz samples is given in Fig. 2.2.4 (a) the epitaxial grown samples are grown on a 400 to 500 µm thick substrate, which is not included in the figure. The top-view is illustrated in Fig. 2.2.4 (b). All devices used in this work were fabricated by CIS [14], except for samples discussed in chapter 10. Their sensor designs and properties are discussed ibidem.

The diodes are all manufactured in the same way: at the front-side of the sensor a *pn*-junction is created by a one µm thin p^+ layer, that was implanted (boron, doping

concentration: $N_{boron} = 10^{19}$ cm^{-3}, implantation energy $E_B = 70$ keV through 200 nm oxyde) into the *n*-type materials. The 0.5×0.5 cm^2 wide active sensor area (PAD) is centred in the middle of the sample, surrounded by a *guard ring* (GR). This structure is located 10 µm next to the PAD and 100 µm wide. The GR can either be kept floating (GR flt) or at the same potential as the PAD (GR grd). When kept at the same potential, the GR acts as boundary of the electrical field and thus keeps the active sensor volume well-defined. Furthermore it prevents surface or edge leakage currents collected by the PAD but neglecting part of the surface between PAD and GR. Surrounding the GR, a few thin potential rings are arranged in order to keep the potential drop between GR and the outside region of the diode smooth. These rings are always kept floating. The samples used in this work were operated with GR grd if possible, otherwise it is stated in the corresponding description.
The front-contact is metallised with a 1.2 µm thick aluminium layer. In the centre a circular hole of 2 mm diameter was spared, there illumination with light is possible that enables the optical filling with charge carriers (e.g. by laser light) for *Deep Level Transient Spectroscopy, Thermally Stimulated Current* and *Transient Current Technique* [15]. At the rear-side an Al grid was deposited for optical filling with charge carriers. The sensor is coated with a SiO_2 layer in regions without metallisation in order to act as passivation as well as protection layer.
The thickness of the rear-side doping layer depends on the diodes type. MCz and FZ sensors are kept with a very thin layer of n^+ only to act as good ohmic contact, while the Epi samples have a 400 to 500 µm thick low resistivity substrate at the rear side.

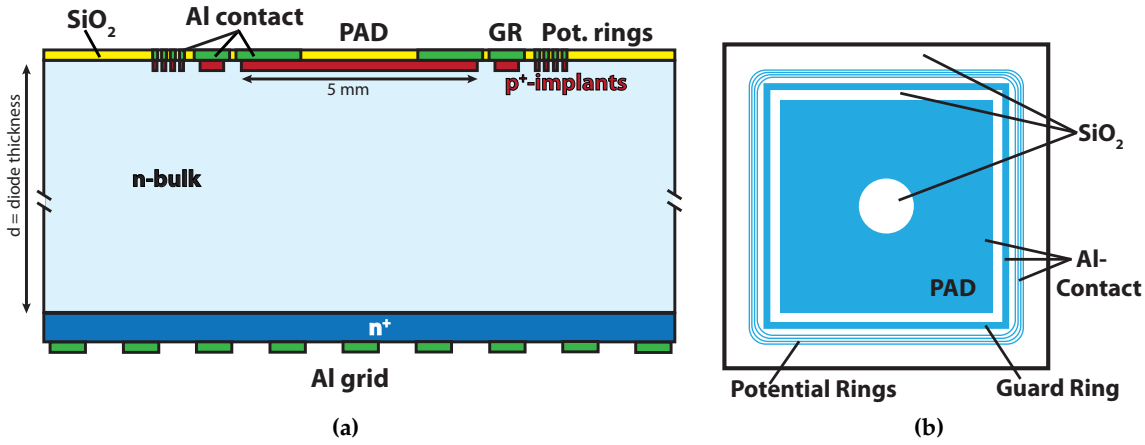

Figure 2.2.4.: Schematic cross section of FZ and MCz samples (a) and top view (b) of the diode geometry used in this work. Epitaxial grown samples have a 400 - 500 µm thick n^{++} substrate instead of the n^+ layer. The samples were manufactured on the basis of University of Hamburg design that was later adopted by the RD50 [5] community.

2.2.1. Future test-materials for defect analysis

The study of the defect generation in silicon requires specific test-materials, different from the detector grade silicon used in the final applications. A good option for future defect investigations appears to be highly doped material (advantage: delayed type inversion) with an exactly known impurity content. Besides the incorporation of oxygen it is useful to have samples with different concentrations of carbon and hydrogen. Some elements useful as markers for measurement techniques like *electron paramagnetic resonance* (EPR) [16] implanted into the material could also help to assign some of the defects.
Some of the materials investigated in this work are candidates for a possible application in HEP particle detector experiments. Nevertheless, this work does not intend to suggest one of the investigated materials for applications in future HEP experiments. The aim of this work is the identification of irradiation induced cluster related defects and their impact on sensor properties. This knowledge combined with information collected from macroscopic investigations will help to determine the advantages of the available materials and to chose the best option.

2.3. Alternatives to Planar Silicon Sensors

Of course, there are alternatives to the silicon materials investigated in this work. The range of candidates is large and depends strongly on the application in HL LHC experiments. Depending on the distance to the interaction point and on the environmental conditions in which the sensors are supposed to work, several approaches may lead to alternatives.
There are three different general scientific strategies for finding the best material:

- Material engineering
- Device engineering
- Change of detector operational conditions

The first topic is mainly focused on the sensor material. This approach aims at finding the best material for the needed application. Yet, it covers a large range of materials, including the generally well understood silicon, but also new materials like diamond. The understanding of radiation damage in silicon is well advanced and has already influenced the choice for the currently used LHC silicon sensors. On the other hand, diamond as a new candidate scores with good radiation tolerance and a low dark current generation due to the large band gap. Because of its radiation hardness diamond is already used in the beam condition monitoring system in ATLAS [17] and is considered as detector material for pixel sensors. Whether the signal-to-noise rate and the position resolution for diamond are still acceptable after high irradiations is part of the ongoing work.

The second topic covers new detector designs, like 3-D detectors [18, 19], thin planar sensors and the polarity of materials. Here 3-D detectors have matured in the last years, as they offer some advantages in the drift time of the charges and low capacitances. However, there are some problems concerning the production process and the quality of the sensors, which limit the applicability of these new devices. Thin sensors have a similar approach, the reduction of the active sensor volume reduced depletion voltage and drift time of the charge carriers. Here, further charge multiplication effects due to high electric fields are under extensive investigation [20–23]. Finally, the polarity of the sensor material may improve the radiation hardness, e.g. by using *n*-in-*p* or *n*-in-*n* technologies.
In a third approach the environmental conditions of the experiments are investigated. Cooling of silicon sensors for example reduces dark currents, while new *cryogenic tracking detectors* (CIDs) operating at temperatures between 100 K and 200 K offer a range of new possibilities. Unfortunately, the cooling of more than 200 m^2 of silicon sensors again raises problems in the power consumption of the full system. In the end, all alternatives exhibit problems, and the studies performed in the next few years will influence strongly which materials are used in future beam colliding experiments.

3. Properties of Silicon Sensors

Silicon is an intrinsic semiconductor. One of its main properties is the resistivity (about $10^2 - 10^4\,\Omega\,\mathrm{cm}$) which ranges between those two of isolators (>$10^8\,\Omega\,\mathrm{cm}$ at 300 K) and a conductors (<$10^{-4}\,\Omega\,\mathrm{cm}$). The resistivity in intrinsic semiconductors ($2.3 \times 10^5\,\Omega\,\mathrm{cm}$ at 300 K [24]) is a result of the crystal structure of the material and atomic orbitals in the periodic potential of the crystal. The electrons of one single atom occupy atomic orbitals, forming a discrete set of possible energy levels. The quantum state of each electron can be described by a wave function. If several atoms are brought together, the individual wave functions influence each other and the discrete energy levels become therefore deformed. Multiple energy levels build up, only separated by small energy gaps. In case of solids a great number of atoms is involved in the interaction, and the energy levels effectively form continuous bands.

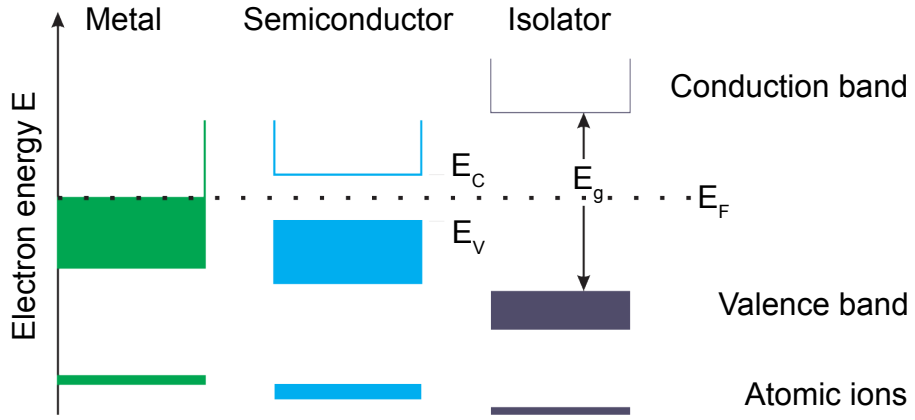

Figure 3.0.1.: Term diagram of metal, semi-conductor and isolator; coloured: occupied states. E_F: Fermi level, E_G: band gap, E_L: edge of valance band, E_C: edge of conduction band. Figure reproduced from [25].

The highest energy band which is occupied by electrons at zero Kelvin, is called valence band (E_V). Valence electrons are typically involved in the bonding process of atoms. The next higher electron energy band is called conduction band (E_C). Electrons from the conduction band contribute to the conductivity of the the material. The energy gap (E_g) between valence and conduction band plays an important role for the electrical properties of the solids. It is sometimes also referred to as forbidden band or forbidden gap.

Fig. 3.0.1 shows the term diagram of the energy bands for three different types: metal, semi-conductor and insulator. If valence and conduction band overlap, like in the case of metals, the conduction band may be partially occupied by electrons even in the limit of zero Kelvin. Then electrons can move freely and conduction is possible.
If the distance between valence and conduction band is about several eV (insulators), it is very improbable to excite an electron into the conduction band via thermal excitation even at temperatures above 100 °C. Due to the small number of free charge carriers, only little conductivity can be observed.
If the size of the band gap allows excitation of electrons into the conduction band at room temperatures, conductivity is possible and the material is called semi-conductor. Due to the fact that only (partially) filled electronic bands contribute to the conductance, also semi-conductors are insulators at zero Kelvin. The energy at which a state has a 50 % probability of being occupied by an electron is called FERMI level (E_F). This probability is described by the FERMI-DIRAC-distribution [26, 27], which depends on the temperature.
In the periodic table of elements elementary semiconductors can be found in the IV main group: Si (silicon, E_G: 1.10 eV), Ge (germanium, E_G: 0.67 eV), α Sn (tin, E_G: 0.08 eV), note that with increasing atomic number the band gap usually decreases. Compound semi-conductors like GaAs and high temperature semiconductors like SiC are possible as well.
The following chapter describes some of the main parameters and fundamentals that are necessary to understand and interpret the measurements performed in this work.

3.1. Silicon crystal structure

Silicon (like carbon or germanium) can be found in the IV main group of the periodic table. Four valence electrons in the outermost shell can contribute to the bonding processes. The arrangement in a periodic lattice leads to the formation of a solid crystal with four covalent bonds per atom. Neighbouring atoms share the available four electrons by forming energetically preferred states.
A very common two-dimensional illustration of the spatial structure of the covalent binding is shown in Fig. 3.1.1. It will be used later to explain the artificial doping of the silicon. The covalent bonding can be described by a linear combination of interacting wave functions of the single states, allowing the arrangement in a periodical three dimensional lattice (BRAVAIS lattice). The established mixed atomic orbitals are called hybrid orbitals. Silicon and diamond form perfect tetrahedrons with an angle between the bonds of 109.5 °(see Fig. 3.1.2 a), also called sp^3-hybridisation. The resulting lattice is a variation of the face centred cubic (fcc), also called diamond structure (see Fig. 3.1.2 b). The crystal structure of silicon will become important in a later part of this work, where different configurations of lattice disorders will be discussed.
The quantum mechanical description of the occupancy of atomic orbitals for silicon leads to the binding scheme presented in Fig. 3.1.3. s- and p-orbitals split up at

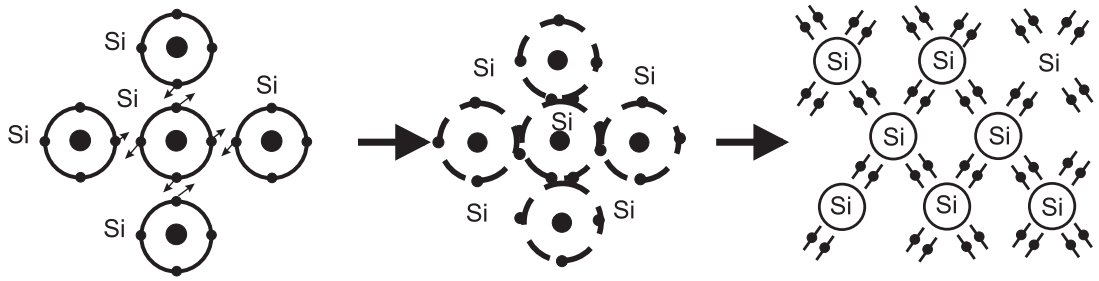

Figure 3.1.1.: Schematic, two-dimensional illustration of the covalent bond structure of silicon. Figure taken from [28].

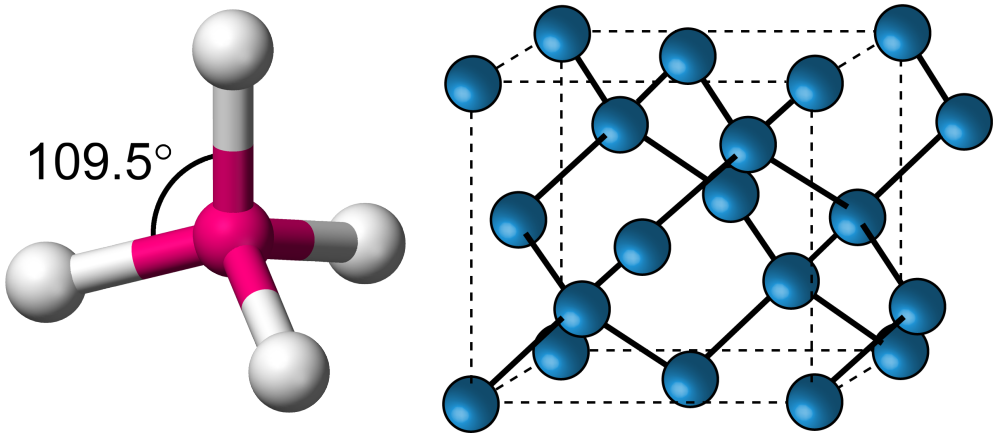

Figure 3.1.2.: Tedrahedral structure of silicon atoms with four neighbors sharing covalent bonds (a) and the diamond structure of silicon in face centred cubic *(fcc)* orientation. Figure (a) taken from [29].

low interatomic distances. Moreover with decreasing distance between the atoms, a forbidden zone builds up between binding and anti-binding sp^3-bands.

3.2. Silicon band structure

The wave function of an electron in a crystal can be described as a particle in a given periodic potential (BLOCH wave). The periodicity of the potential influences the probability density $|\Psi|^2$ of the particle within the potential. For a solid crystal the periodicity is determined by the lattice. In crystallography, the lattice is usually described in the reciprocal momentum space (also called $k-space$). The respective reciprocal lattice is a periodic set of points that build the Fourier transform of the periodic spatial lattice.

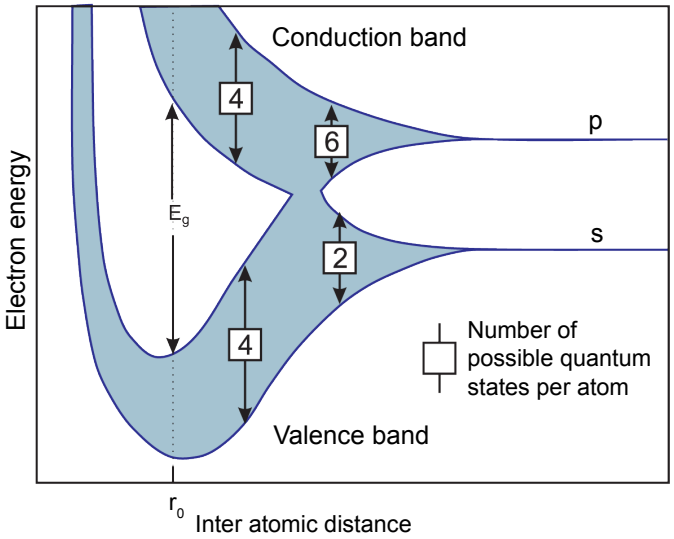

Figure 3.1.3.: Band diagram after [30].

The motion of electrons in the crystal is depending on the wave vector $\vec{k}$, which also gives, multiplied with $\hbar$, the electron's crystal momentum. This also illustrates one major advantage of the momentum-space, it is possible to directly express the electron energy as function of the electron momentum, this is known as the dispersion relation or energy-momentum (E-$\vec{k}$) relationship.
The WIGNER-SEITZ cell is the most elementary cell unit which is necessary to construct the whole periodical crystal. In the reciprocal space the corresponding cell unit is called BRILLOIUN zone. The solution for the BLOCH wave can be extracted from a single BRILLOIUN zone. Also the crystal momentum has to be calculated only for the first BRILLOIUN zone. The reflection of wave vectors $\vec{k}$ at BRAGG planes in the BRILLOIUN zone is maximal. The BRILLOIUN zone of the fcc structure is shown in Fig. 3.2.1. Important points of high symmetry are of special interest and labelled. The Γ point can be found at the centre of the BRILLOIUN zone at $\vec{k} = (0,0,0)$ and the X point ($\vec{k} = (0,1,0)$) is the centre of a square face, looking into the k_y-direction.
In order to obtain a more complete view of the allowed electronic states in a crystal (more complete than Figure 3.1.3), it is useful to illustrate the possible electron energies in the momentum space (or $k-space$). Cuts along high symmetry $\vec{k}$-planes of the BRILLOIUN zone allow to understand the complete energy band structure of silicon. This collection of all possible momenta and energies depending on the crystal orientation is shown in Figure 3.2.2.
The maximum of the valence band can be found at Γ, which is per definition at $E = 0$. The lowermost edge of the conduction band appears at X (looking along the ΓX=[100] plane). The band gap (E_G) is therefore 1.12 eV at room temperature. The transition of an electron from the valence band into the conduction band is not possible without

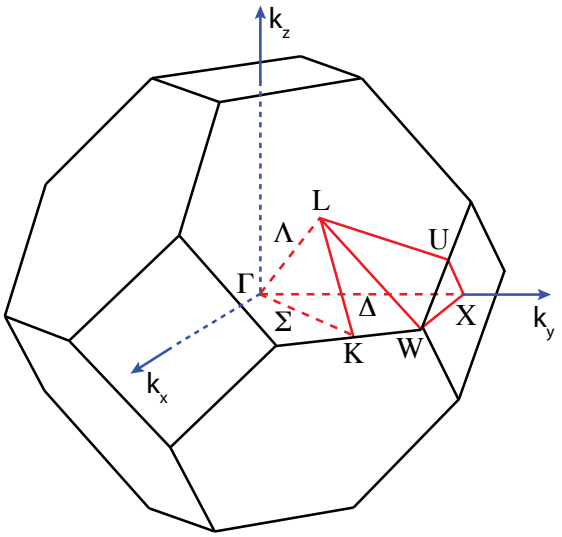

Figure 3.2.1.: BRILLOIUN zone of fcc lattice. Fig. taken from [25].

changing the momentum $\vec{k}$, this means silicon is an indirect semi-conductor. The importance of the E-$\vec{k}$ relationship is now obvious. To satisfy energy and momentum conservation, phonons are required to excite an electron from the maximum of the valence band to the minimum of the conduction band.

3.3. Carrier concentration at thermal equilibrium

There are only few charge carriers available for conduction in pure silicon as the band gap is about $E_g = 1.12$ eV in comparison to $k_B T = 0.025$ eV at $T = 300$ K. One option for increasing the conductivity of silicon is the intentional introduction of dopants (foreign atoms) with energy levels in the forbidden band close ($\propto 0.05$ eV) to the valence or conductance band into the silicon lattice and therefore increasing the amount of free charge carriers. This can be done by adding impurities during the silicon crystal growth process or by implantation.
Elements of the group XII or XV of the periodic system incorporated into the silicon lattice either provide a weakly bound additional hole or electron. The commonly used doping elements are the pentavalent phosphorus and antimony or the trivalent boron. Figure 3.3.1 illustrates the principle of the doping with a donor type impurity. In this case phosphorus is introduced into the lattice to replace silicon atoms. Only four out of five available electrons (black dots) in the outer shell ligate covalently to the silicon atoms, one of the electrons remains loosely bound such that the P-atom can easily be ionized, e.g. by thermal excitation. At room temperature all the phosphorus atoms are ionized (ionisation energy for phosphorus: 45 meV below the conduction band,

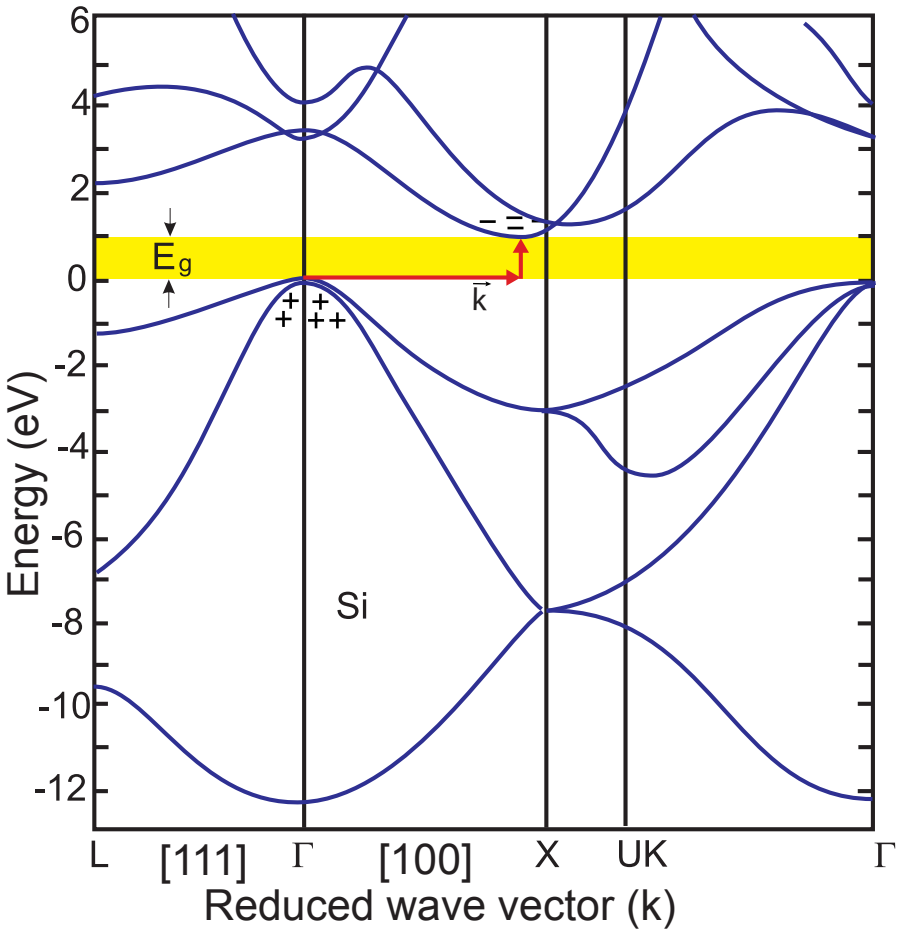

Figure 3.2.2.: Band structure of silicon. Size of indirect band gap E_G (yellow), valence band occupied with holes (+) and conduction band with electrons (-) are shown. Figure reproduced from [25] and modified.

value taken from [25]). The current conduction process works in this case via electron conduction. Silicon material doped with donor type impurities is called *n*-type silicon. In order to increase the amount of free holes, the material is doped with acceptor type elements. Figure 3.3.2 illustrates the introduction of the trivalent boron (ionisation energy for boron: 45 meV above the valence band, value taken from [25]). The three electrons in the outer shell ligate covalently to the neighbouring silicon atoms. But there is still one electron missing to achieve the optimal inert gas electron configuration. At the position of this missing negative charge instead a positive hole (open dot) appears. This hole can be filled by electrons from the conduction band and give rise to another hole, which can again be replaced by another electron and so on and so forth. The current conduction process in this case works via the conduction of holes. Silicon material doped with acceptor type impurities is called *p*-type silicon.

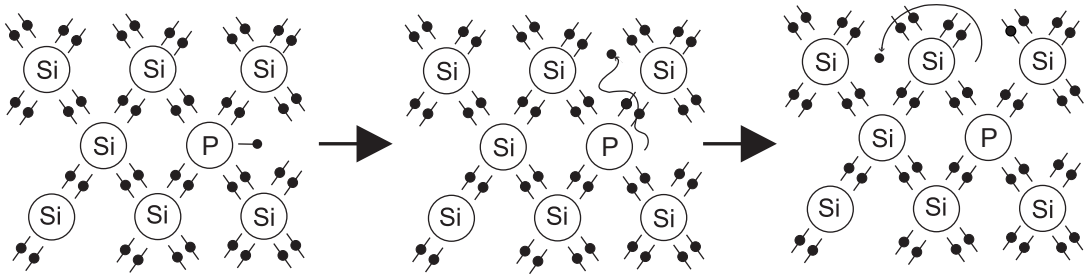

Figure 3.3.1.: Principle of electron conduction in *n*-type silicon. Black dots represent electrons. Neutral phosphorus has five electrons, one of them is only loosely bound and acts as a free charge carrier.

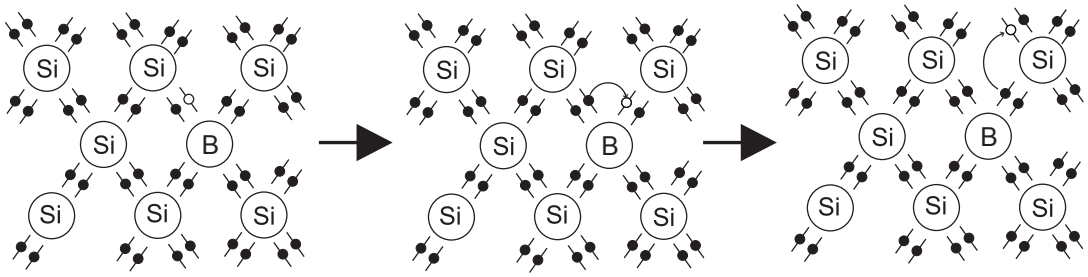

Figure 3.3.2.: Principle of hole conduction in *p*-type silicon. Black dots represent electrons, while open white dots represent holes. Neutral boron has only three electrons, therefore one missing electron is a *quasi* hole that can migrate through the lattice when electrons take its place.

3.3.1. Free carrier concentration

A very important value is the concentration of free charge carriers available for conduction. The calculation can be done firstly without impurities added to the silicon material; this is called the intrinsic case. The density of free electrons (n) in the conduction band can be calculated from the density of states $N(E)$ multiplied with the occupancy probability $F(E)$, integrated over the conduction band :

$$n = \int_{E_C}^{\infty} N(E)F(E)\,\mathrm{d}E. \tag{3.3.1}$$

The occupancy probability for an electronic state with the energy E is given by the FERMI-DIRAC distribution function [2]:

$$F(E) = \frac{1}{1 + \exp\left(\frac{E - E_F}{k_B T}\right)}, \tag{3.3.2}$$

with k_B is the BOLTZMANN constant, T the absolute temperature and E_F the FERMI level as explained in the beginning of the chapter.
The effective density of states in the conduction band is given by

$$\frac{dN_C(E)}{dE} = \frac{\sqrt{2}}{\pi^2} \frac{m_{dC}^{3/2} \, (E - E_C)^{1/2}}{\hbar^3}, \tag{3.3.3}$$

with m_{dC} is the density-of-state effective mass for electrons given in appendix A.1 by Eq. A.1.2.
In case of $|E_C - E_F| > 3k_B T$ the density of states in the conduction band can be approximated by

$$N_C = 2 \left(\frac{2\pi m_{dC} k_B T}{h^2}\right)^{3/2} \tag{3.3.4}$$

and the integral of Eq. 3.3.1 can be evaluated to

$$n = N_C \exp\left(-\frac{E_C - E_F}{k_B T}\right) \quad \text{or} \quad E_C - E_F = k_B T \ln\left(\frac{N_C}{n}\right). \tag{3.3.5}$$

This calculation can be similarly obtained for the hole density in the valence band

$$p = N_V \exp\left(-\frac{E_F - E_V}{k_B T}\right) \quad \text{or} \quad E_F - E_V = k_B T \ln\left(\frac{N_V}{p}\right), \tag{3.3.6}$$

where N_V denotes the effective density of states in the valence band, which is given by

$$N_V = 2 \left(\frac{2\pi m_{dV} k_B T}{h^2}\right)^{3/2}. \tag{3.3.7}$$

Here the density-of-state effective mass of the valence band is given by Eq. A.1.1. An illustration of the band diagram, density of states, FERMI-DIRAC distribution and carrier concentration is shown in Fig. 3.3.3 (a).

3.3.2. Calculation of the Fermi level

For intrinsic semiconductors electrons are thermally excited from the valence band into the conduction band, leaving an equal number of holes in the valence band. In steady state (equal rate of generation and recombination) further recombination of

electrons with holes from the valence band leads to a net result $n = p = n_i$, where n_i denotes the intrinsic carrier density. The FERMI level is the energy at which the occupancy probability equals 1/2.

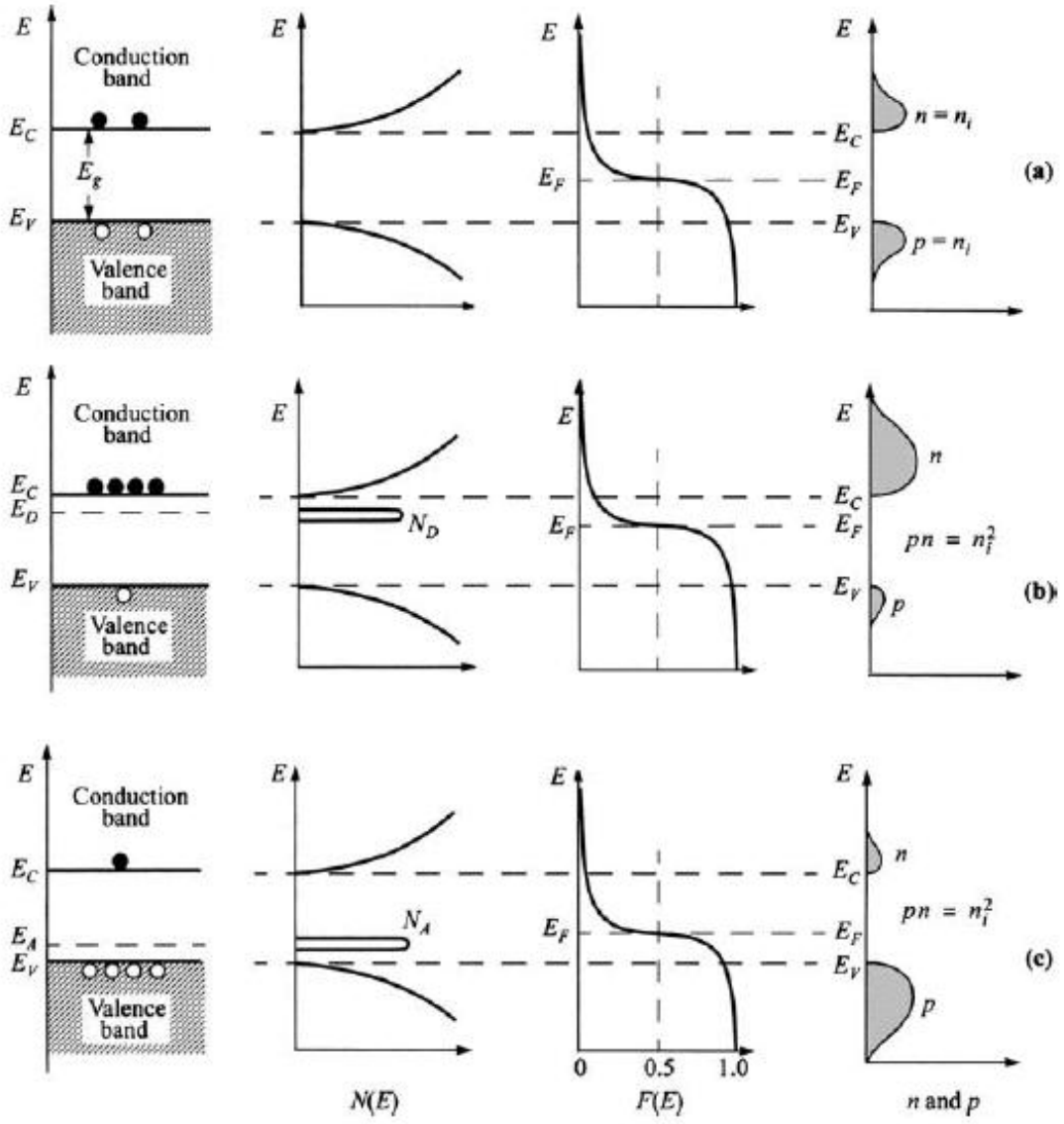

Figure 3.3.3.: Schematic band diagram, density of states, FERMI-DIRAC distribution and carrier concentrations for (a) intrinsic, (b) n-type and (c) p-type semiconductors at thermal equilibrium. Figure taken from [2].

For intrinsic semiconductors where the concentration of electrons and holes are equal,

it is often called *intrinsic* FERMI *level* E_i[1]. It can be calculated from Eqs. 3.3.5 and 3.3.6:

$$E_i = E_F = \frac{E_C + E_V}{2} + \frac{k_B T}{2} \ln \frac{N_V}{N_C} = \frac{E_C + E_V}{2} + \frac{3}{4} k_B T \ln \left(\frac{m_{dC}}{m_{dV}} \right). \tag{3.3.8}$$

Te corresponding carrier concentration n_i follows

$$n_i = \sqrt{N_C N_V} \exp \left(-\frac{E_g}{2 k_B T} \right) \tag{3.3.9}$$

and the *mass-action-law* $pn = n_i^2$ is veryfied. Here $E_g = E_C - E_V$ denotes the band gap energy. Taking E_i as reference energy and using Eq. 3.3.9, the free carrier concentration for electrons can be simplified to

$$n = n_i \exp \left(\frac{E_F - E_i}{k_B T} \right) \quad \text{or} \quad E_F - E_i = k_B T \ln \left(\frac{n}{n_i} \right) \tag{3.3.10}$$

and for holes

$$p = n_i \exp \left(\frac{E_i - E_F}{k_B T} \right) \quad \text{or} \quad E_i - E_F = k_B T \ln \left(\frac{p}{n_i} \right). \tag{3.3.11}$$

3.3.3. Donors and acceptors

When a semiconductor is doped with impurities, new levels in the band gap can be introduced. A donor is defined as being neutral if filled by an electron, and positive if empty. An acceptor on the other hand is neutral if empty and negative if filled by an electron. For the results shown in the later part of this work, it is very important to know, which fraction of the dopants is ionised or electrically active.
If the FERMI level is known, in thermal equilibrium the density of donors (acceptors) filled with electrons n_t (holes p_t) can be calculated from

$$\begin{aligned} n_t &= N_t \frac{1}{1 + \exp\left(+ \frac{E_t - E_F}{k_B T} \right)} = N_t \, F(E_t) \\ p_t &= N_t \frac{1}{1 + \exp\left(- \frac{E_t - E_F}{k_B T} \right)} = N_t \, (1 - F(E_t)), \end{aligned} \tag{3.3.12}$$

where N_t is the concentration of the acceptor or donor level with an energy level at E_t with $n_t + p_t = N_t$. This is pretty obvious, due to the fact, that if a defect is not occupied by an electron, by definition it is occupied by a hole and if a defect is not occupied by a hole, it is occupied by an electron. The band diagram, density of states,

[1] E_i generally lies close but not exactly in the middle of the band gap, due to the difference in electron and hole effective masses.

FERMI-DIRAC distribution and carrier concentration for donor and acceptor doped semiconductors is shown in Fig. 3.3.3 (b) and (c).
For the calculation of the effective doping concentration, it is necessary to know the electrically active acceptor and donor concentration, which results in

$$N_{eff} = \sum_{donors} p_t - \sum_{acceptors} n_t. \tag{3.3.13}$$

In case of extrinsic semiconductors the FERMI level can be calculated for any temperature and defect concentration from Eq. 3.3.4, 3.3.5, 3.3.6 and 3.3.7, 3.3.12 and 3.3.13. As an example the temperature dependence of the FERMI level is shown in Fig. 3.3.4 for various defect levels and concentrations.

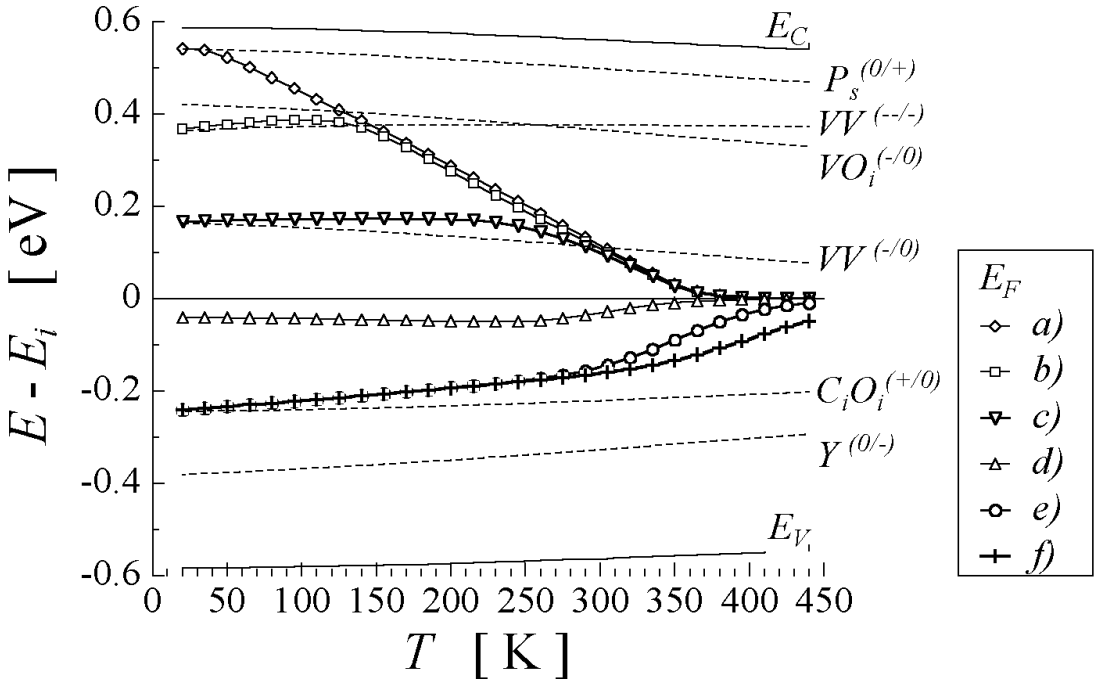

Figure 3.3.4.: FERMI level as function of energy and defect concentrations taken from [31]. Calculations were performed using a phosphorus concentration $[P_S]$ =1×10^{12} cm^{-3} and various concentrations of defects in silicon V_2, VO_i, C_iO_i and an acceptor level Y placed at $E_V + 0.2$ eV. The concentrations have been: $[V_2] = [VO_i] = [C_iO_i]$ = a) 10^{11} b) 5×10^{11} c) 10^{12} d) 10^{13} e) 10^{14} f) 10^{15} cm^{-3} and in all cases $[Y] = 0.1\times$ [e.g. V_2].

3.4. Basic features of the *pn*-juction

3.4.1. Principle of the *pn*-junction

The basic principle of a *pn*-junction is shown in figure 3.4.1. The upper part shows the *p*- and *n*-type semiconductor before and after physical contact. The lower part illustrates the schematic energy band diagram. On the left hand side the unconnected *p*- and *n*-materials are electrically neutral. On the *p*-side there is an excess of holes (empty circles), while on the *n*-side electrons dominate (filled circles). In the energy band diagram the location of the conduction band (E_C), the valence band (E_V), the FERMI level (E_F) and the FERMI level for intrinsic semiconductor (E_i) which is located in the middle of the band gap are shown.

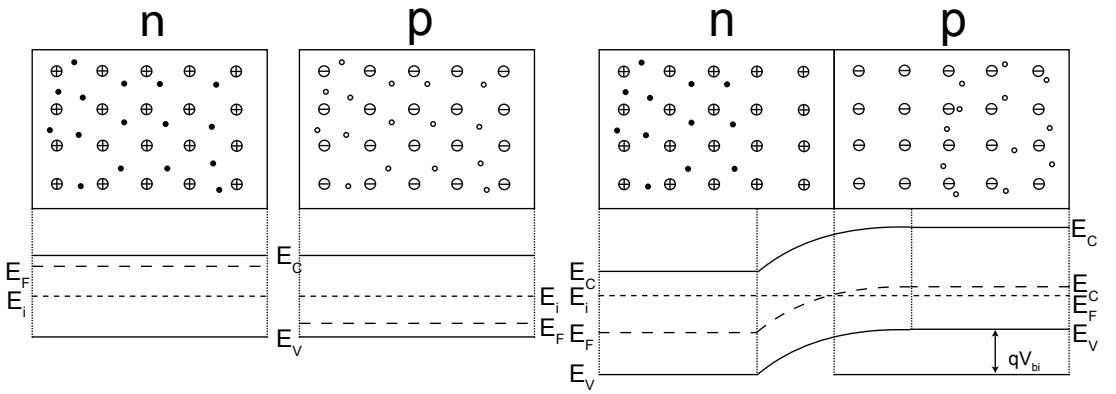

Figure 3.4.1.: Principle of a *pn*-junction before and after contact. For discription see text.

After the contact holes from the *p*-side diffuse to the *n*-side and electrons from the *n*-side diffuse to the *p*-side. The diffusion of holes leaves negative ions on the *p*-side and the diffusion of electrons leaves positive ions on the *n*-side; an electrical field builds up which acts against the diffusion. This stabilises a small region depleted of free charge carriers called the *space charge region* (SCR).
In the energy band diagram the FERMI level is shown in thermal equilibrium. It is constant inside the crystal including the junction area. The potential difference is called *built-in voltage* V_{bi} and depends on the doping concentrations. Since charge neutrality is valid, the number of positive charges equals the number of negative charges. Therefore the width of the SCR multiplied with the charge density must be equal for both sides: $N_A d_p = N_D d_n$ with $N_{A,D}$ the ionised acceptors or donors and $d_{n,p}$ is the thickness of the *n*- or *p*-region as labelled in Fig. 3.4.1.
In case of an abrupt *pn*-junction, for which one side is heavily doped and the other low, the depleted region of a thickness W extends much further into the low doped side of the material. Figure 3.4.2 1. shows the charge density of a reversely biased p^+n diode with thickness d and a reverse bias voltage V. The description of this diode is

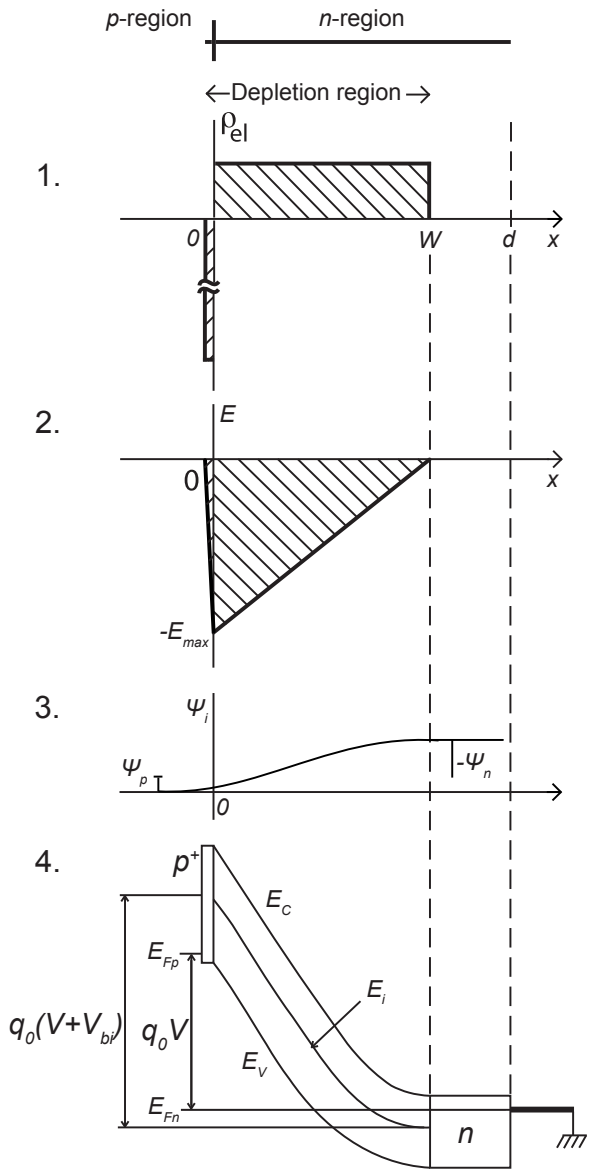

Schematic figure of an abrupt p^+n-junction:
1. space charge distribution,
2. electric field distribution,
3. potental distribution,
4. electron potential energy.
Figure reproduced from [32] and [2].

Figure 3.4.2.: Schematic figure of an abrupt p^+n junction.

possible in the *depletion assumption* which demands that n and p are zero in the SCR, and thus the space charge is defined by $N_D - N_A$. If the dopant atoms are distributed homogeneously, the depleted region has a box profile. For a pad diode the electrical field distribution can be calculated by solving the 1-d *Poisson equation*

$$-\frac{d^2\Psi}{dx^2} = \frac{d\mathscr{E}}{dx} = \frac{\rho_{el}}{\epsilon\epsilon_0} = \frac{q_0}{\epsilon\epsilon_0}(N_D - N_A), \tag{3.4.1}$$

here, N_A and N_D denotes the concentration of ionised donors and acceptors in the lowly doped region which results in the effective doping concentration N_{eff}. The first integration of Eq. 3.4.1 leads to the electric field distribution ($\mathscr{E}(x)$) as shown in fig. 3.4.2 2. The electric field strength depends linearly on x and the maximum ($\mathscr{E}_{max}$) at $x = 0$

$$|\mathscr{E}_{max}| = \frac{q_0 N_{eff,n} W_n}{\epsilon\epsilon_0} = \frac{q_0 N_{eff,p} W_p}{\epsilon\epsilon_0}, \tag{3.4.2}$$

and $W_{n,p}$ the depletion depth either in the n-type or in the p-type region.
Further integration of Eq. 3.4.2 results in the parabolic potential distribution Ψ (Fig. 3.4.2 3.), neglecting the depletion region in the highly doped region

$$\Psi(x) = -\frac{1}{2}\frac{q_0 N_{eff}}{\epsilon\epsilon_0}(x - W)^2 \quad \text{for} \quad 0 \leq x \leq W \quad \text{and} \quad W \leq d. \tag{3.4.3}$$

The electron band diagram with reverse bias V applied is shown in Fig. 3.4.2 4. An expression for the depletion depth can be extracted under the condition $\Psi(x = 0) = -V_{bi} - V$:

$$W(V) = \sqrt{\frac{2\epsilon\epsilon_0}{q_0|N_{eff}|}(V + V_{bi})} \quad \text{for} \quad W \leq d, \tag{3.4.4}$$

with further increase of the reverse bias the depletion region extends to the back contact. The voltage needed to fully deplete the diode is called *depletion voltage* V_{dep}. For the effective doping concentration N_{eff} it follows:

$$V_{dep} + V_{bi} = \frac{q_0}{2\epsilon\epsilon_0}|N_{eff}|\, d^2. \tag{3.4.5}$$

The *built-in voltage* V_{bi} is ofthen neglected because it is more than one order of magnitude smaller than the depletion voltage V_{dep}.
The *depletion approximation* uses box profiles for the depletion region. A more accurate result for the depletion-layer properties can be acquired by replacing V_{bi} by $V_{bi} + k_B T/q_0$ in the equations above [2].

3.4.2. Capacitance of the *pn*-junction

The depletion region of a *pn*-junction can be considered as an insulator. The capacitance of a *pn*-junction can be calculated by:

$$C(V) = \frac{\mathrm{d}Q}{\mathrm{d}V} = \frac{\mathrm{d}Q}{\mathrm{d}W}\frac{\mathrm{d}W}{\mathrm{d}V} \tag{3.4.6}$$

Where Q is the space charge and $\mathrm{d}Q$ is given by $\mathrm{d}Q = q_0 N_{eff} A \mathrm{d}W$ and A denotes the area of the diode. Using the first derivative of Eq. 3.4.4 one gets the expression

$$C(V) = \epsilon\epsilon_0 \frac{A}{W(V)} = A\sqrt{\frac{\epsilon\epsilon_0 q_0 |N_{eff}|}{2(V + V_{bi})}} \quad \text{for} \quad W \leq d, \tag{3.4.7}$$

which corresponds to a plate capacitor with the thickness $W(V)$. When the depletion region reaches the backplane the capacitance at full depletion is reached ($V = V_{dep}$, where $W = d$):

$$C_{end} = \frac{\epsilon\epsilon_0 A}{d}. \tag{3.4.8}$$

Due to the fact that this capacitance only depends on the geometrical size of the diode it is called *geometrical end capacitance*. Despite a further increase of the bias voltage, the depletion depth cannot increase any more and the capacitance stays constant. V_{dep} and C_{end} are illustrated in Fig. 3.4.3 (a) which shows an ideal *capacitance-voltage* (C-V) characteristics for a diode in log-log-scale. If the depleted volume does not stay

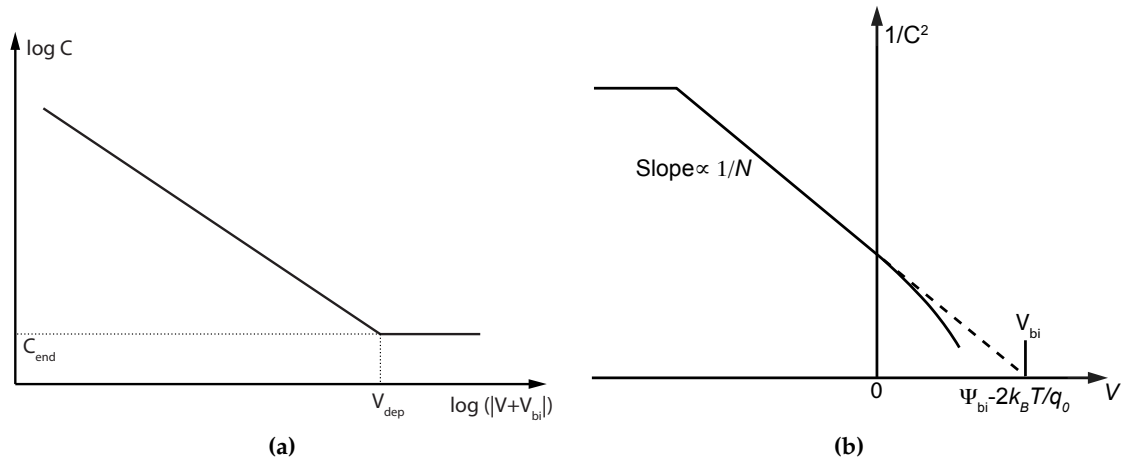

Figure 3.4.3.: Ideal C-V characteristics (a). $1/C^2$ vs. V plot (b), a $1/C^2$ vs. V plot gives the information about *built-in voltage* and doping concentration N. Figure (b) taken from [2].

constant, the capacitance may decrease even more, due to a lateral extension of the

depletion zone. Technically this may happen if the guard ring of a diode is left floating. From formula 3.4.7 it is clear, that the effective doping concentration can be calculated. By plotting $1/C^2$ versus V a straight line should result as shown in Fig. 3.4.3 (b). The slope gives the doping concentration of the substrate. From the derivative of $1/C^2$ versus depth $W(V)$ from Eq. 3.4.7 it is possible to extract the doping profile of the silicon by

$$\frac{\mathrm{d}(1/C^2)}{\mathrm{d}V} = -\frac{2}{A^2 \epsilon \epsilon_0 q_0 |N_{eff}|}. \tag{3.4.9}$$

For an oxygen enriched epitaxial sensor the C-V measurement was performed and is presented in 3.4.4 (a). The resulting N_{eff}-depth profile calculated by Eq.3.4.9 is illustrated in Fig. 3.4.4 (b). The distribution of the effective doping N_{eff} concentration is very homogeneous, as expected. This approximation does not hold for highly irradiated sensors (see Sec. 6.2.2).

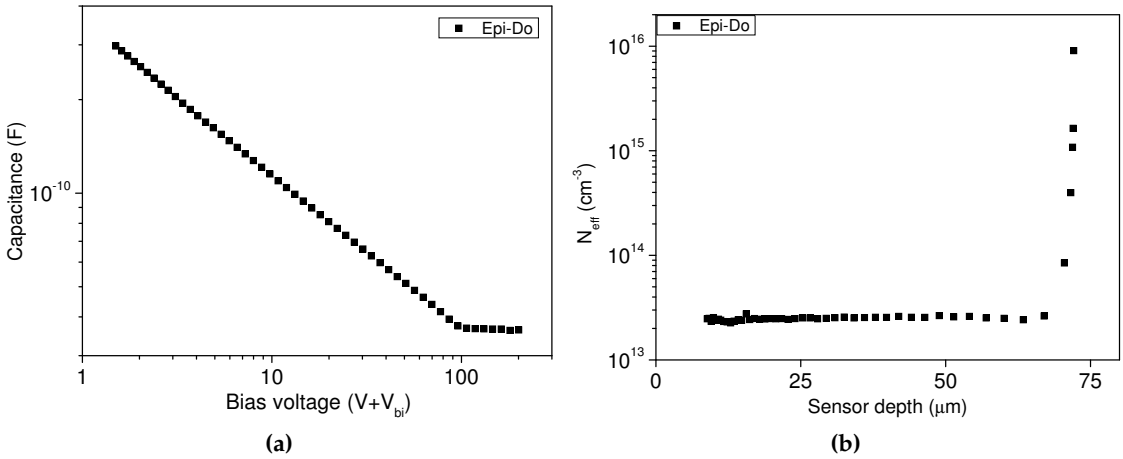

Figure 3.4.4.: C-V plot of an Epi-Do diode (a) and resulting N_{eff} depth profile with thickness of 75 µm (b). Note the semilogarithmic scale in (b).

3.4.3. Current flow through a diode

Ideal diode

The current flow through an ideal diode is given by the diffusion current density of holes J_p and electrons J_n

$$J_p = \frac{q_0 D_p p_{n0}}{L_p} \left[\exp\left(\frac{q_0 V}{k_B T}\right) - 1 \right] \tag{3.4.10}$$

$$J_n = \frac{q_0 D_n n_{p0}}{L_n} \left[\exp\left(\frac{q_0 V}{k_B T}\right) - 1 \right] \tag{3.4.11}$$

with p_{n0} is the equilibrium hole density on the n-side, n_{p0} is the equilibrium electron density on the p-side. The diffusion length for electrons and holes is $L_{n,p} = \sqrt{D_{n,p}\tau_{n,p}}$, with the diffusivity $D_{n,p}$ and the carrier lifetime $\tau_{n,p}$.
The ideal *current-voltage* (I-V) characteristics as shown in Fig. 3.4.5 can be described by the sum of Eq. 3.4.10 and Eq. 3.4.11. This equation is also known as SHOCKLEY equation [2]

$$J_d = J_p + J_n = J_0 \left[\exp\left(\frac{q_o V}{k_B T}\right) \right], \tag{3.4.12}$$

where J_0, the saturation current density, is given by

$$J_0 = \frac{q_0 D_p n_i^2}{L_p N_D} + \frac{q_0 D_n n_i^2}{L_n N_A}. \tag{3.4.13}$$

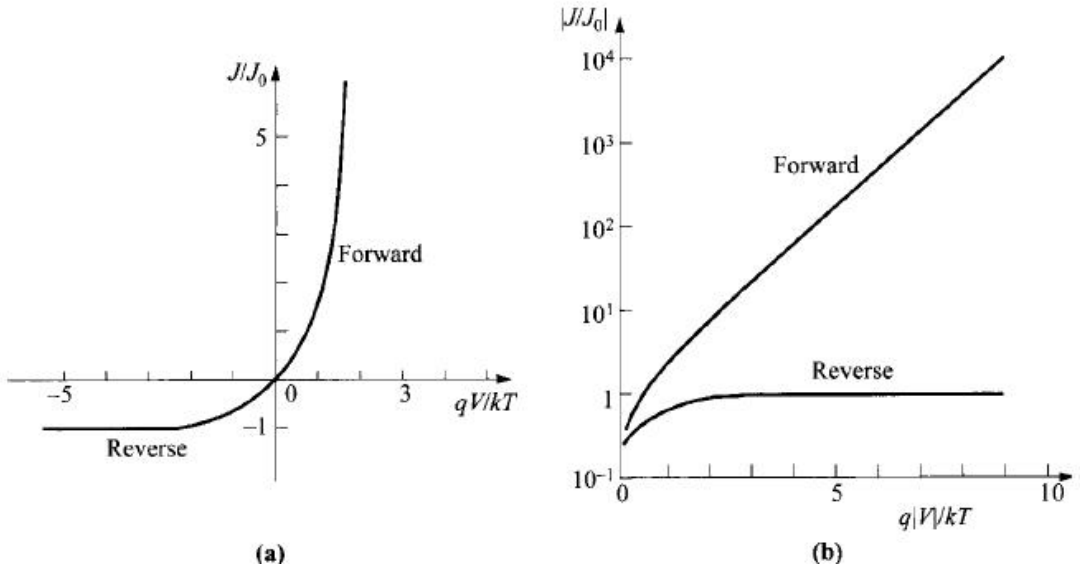

Figure 3.4.5.: Ideal *current-voltage* characteristics for (a) linear plot and (b) semilog plot. Figures taken from [2].

The temperature dependence of the saturation current density J_0 of an abrupt p^+n-junction can be approximated by

$$J_0 \approx q_0 \sqrt{\frac{D_p}{\tau_p}} \frac{n_i^2}{N_D} \propto T^{\gamma/2} \left[T^3 \exp\left(-\frac{E_g}{k_B T}\right) \right] \propto T^{(3+\gamma/2)} \exp\left(-\frac{E_g}{k_B T}\right), \tag{3.4.14}$$

where γ is a constant [2].

Real case
The SHOCKLEY equation describes the I-V characteristics perfectly for *pn*-junctions without defects. For real Si *pn*-junctions there are several further effects in addition to the diffusion current to be considered. Surface effects, the generation and recombination of charge carriers in the depletion layer, the high injection condition under forward bias and parasitic $IR - circuit$ drops due to series resistance. Further effects like tunnelling of carriers and the junction breakdown will not be discussed here, but can be found in [2].
The surface generation current arises from defect states at the $Si - SiO_2$ interface. It is usually very small compared to other components of the current and is neglected in most of the cases. Furthermore the measurements are usually done with GR at the same potential as the PAD in order to prevent edge effects and to define the volume.

Reverse current
The current flow through a reverse biased diode can be described by the reverse current density or leakage current density. It consists of two main components, the diffusion current and the generation current

$$J_{leak} = J_d + J_{gen}. \tag{3.4.15}$$

The diffusion current density J_d is given by Eq. 3.4.12, while the generation current density arises from e/h-pair generation. These charge carriers are thermally stimulated and generated by defects (radiation or process induced) located near the middle of the band gap. Only defects in the *space charge region* contribute to the bulk generation current. Therefore J_{gen} depends on voltage or the width W of the depleted area.

$$J_{gen} \propto W \propto \sqrt{V + V_{bi}} \quad \text{for } V \leqslant V_{dep}. \tag{3.4.16}$$

J_{gen} will saturate when the voltage reaches the depletion voltage. The bulk generation current density is often described by the generation life time τ_{g}

$$J_{gen} = \frac{q_0 n_i W(V)}{\tau_g}, \tag{3.4.17}$$

n_i is the intrinsic charge carrier concentration and $\frac{1}{\tau_g}$ describes the probability per unit time of emitting e/h-pairs from the generation centres in the conduction band.
The total reverse current density for an abrupt p^+n-junction can be described by the sum of diffusion current (3.4.12) and generation current density (3.4.17):

$$J_{leak} = q_0 \sqrt{\frac{D_p}{\tau_p}} \frac{n_i^2}{N_D} + \frac{q_0 n_i W(V)}{\tau_g}. \tag{3.4.18}$$

At moderate temperatures J_{gen} will dominate in Si, although at high temperatures J_d dominates.

Normalisation to room temperature
All measurements performed during this work were either done on a cold chuck and a temperature stabilised at 20 °C, or measured at room temperature and afterwards scaled to T_{RT} =20 °C with the dependance of current with temperature, given by $\exp(-E_g/2k_BT)$ [24]

$$I(T_{RT}) = I(T) \cdot R(T) \quad \text{mit} \quad R(T) = \left(\frac{T_{RT}}{T}\right)^2 \exp\left(-\frac{E_g}{2k_B}\left[\frac{1}{T_{RT}} - \frac{1}{T}\right]\right). \tag{3.4.19}$$

Forward current
The current under forward bias provides information e.g. about the series resistance of the diode and is very important to understand some of the measurement methods used in this work. The first part is well described in [2] and was investigated previously by [33]. The forward current characteristic of a p^+n-junction for $V \geq 3k_BT/q_0$ can be described by the sum of the ideal Shockley equation (3.4.12) and the recombination current I_{rec} given by [2]

$$I_{fw} = I_d + I_{rec} = q_0 A \sqrt{\frac{D_p}{\tau_p}} \frac{n_i^2}{N_D} \exp\left(\frac{q_0 V}{k_B T}\right) + \sqrt{\frac{\pi}{2}} \frac{k_B T n_i}{\tau \mathscr{E}} \exp\left(\frac{q_0 V}{2k_B T}\right), \tag{3.4.20}$$

where $\mathscr{E}$ is the electric field at maximum recombination (see [2]). A common representation of the experimental results is given by

$$I_{fw}(V) \propto \exp\left(\frac{q_0 V}{\eta k_B T}\right), \tag{3.4.21}$$

were the *ideality factor* η equals 2 when the recombination current dominates and η equals 1 when the diffusion current dominates (see [32]). In case the contribution of both currents are comparable, η ranges between 1 and 2.
For high current flow, the series bulk resistance R_S has to be taken into account by replacing V with $V - IR_S$

$$I_{fw}(V) \propto \exp\left(\frac{q_0 V - I R_S}{\eta k_B T}\right). \tag{3.4.22}$$

4. Radiation Damage

The harsh radiation environment in the HL LHC will lead to severe lattice damage in the silicon sensors of tracking detectors. The thus created defects change the properties of those sensors dramatically. In order to understand the changes, the next chapter will provide the necessary information.
In general there are two kinds of damages: The surface damage and the bulk damage. For the HL LHC environment the main damage will be created in the bulk of the sensors, while for photon science the main damage will be surface damage.
A comparison of radiation induced damage created by different particles is possible with help of the *Non Ionising Energy Loss* (NIEL) hypothesis. The electrical properties of defects can be described by the Shokeley-Read-Hall (SRH) statistics. Since the defects are not stable with time and temperature, the process of annealing is described in this chapter.

4.1. Creation of defects in the silicon lattice

When a particle interacts with an atom of the semiconductor lattice a displaced silicon atom is produced, this primary displacement is called *primary knock on atom* (PKA). Figure 4.1.1 shows the situation of a dislocated silicon atom, which migrates through

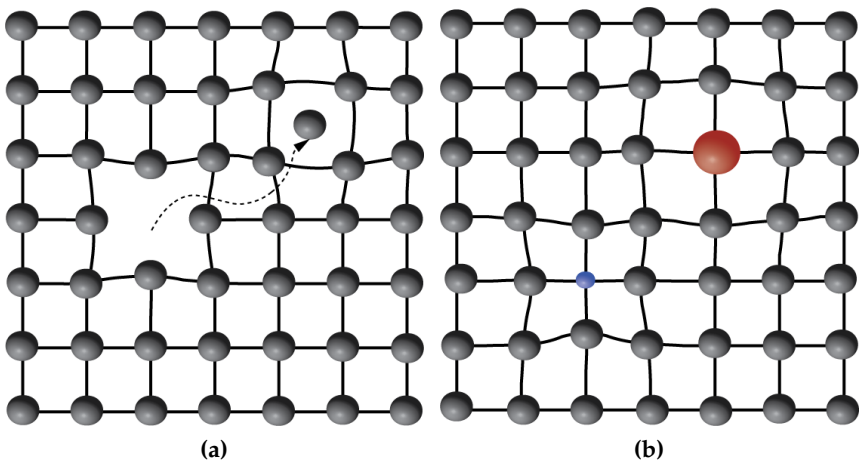

Figure 4.1.1.: Illustration of concepts for defects in silicon: *Frenkel-pair* (a) and additional impurities (b).

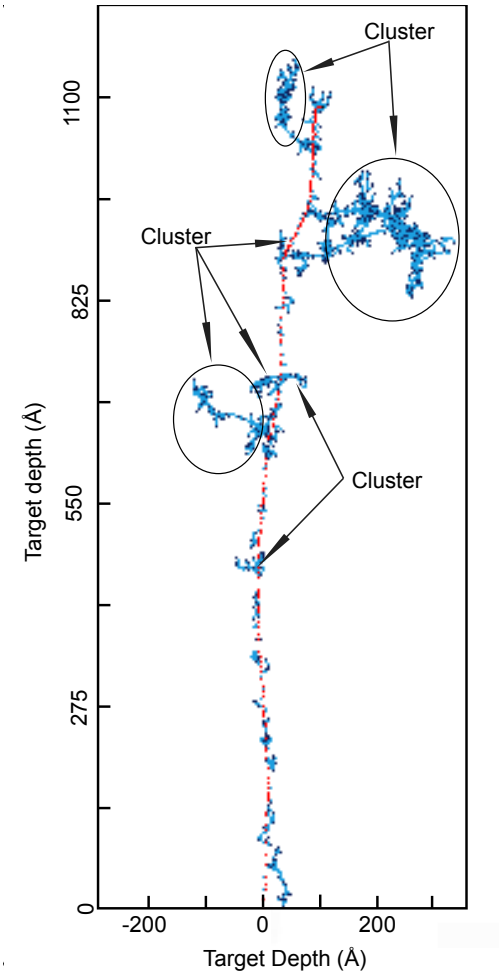

Figure 4.1.2: TRIM simulation of a damage cascade with PKA of E_R = 50 keV. E_R =50 keV is approximately the average kinetic energy a 1 MeV neutron transfers to the PKA. The track of the PKA is shown in red, while the additionally displaced Si atoms (vacancies) are displayed in blue.

the lattice and e.g. forms an interstitial. This defect is called *Frenkel-pair*. The creation of vacancies depends on the energy of the impinging particle. The primary recoil atom can only be displaced when the imparted energy is higher then the displacement threshold energy E_d of about 25 eV [34].
The recoil energy of an atom produced in a nuclear reaction may be much higher. Along its path through the lattice the dislocated PKA may loose its recoil energy E_R through ionisation or further displacements creating single or point defects until it stops and becomes an interstitial. At the end of such a track, the non-ionising interactions are dominating and form dense agglomerations of defects. Those disordered regions are called defect *clusters*. Figure 4.1.2 shows the TRIM simulation[1] of a recoil-atom track induced by a PKA with a recoil energy of E_R=50 keV. The fraction of energy that goes to ionisation effects is shown in Fig. 4.1.3 in red. The main energy loss due

[1]TRIM by James F. Ziegler: TRansport of Ions in Matter, software and manual can be downloaded at [35].

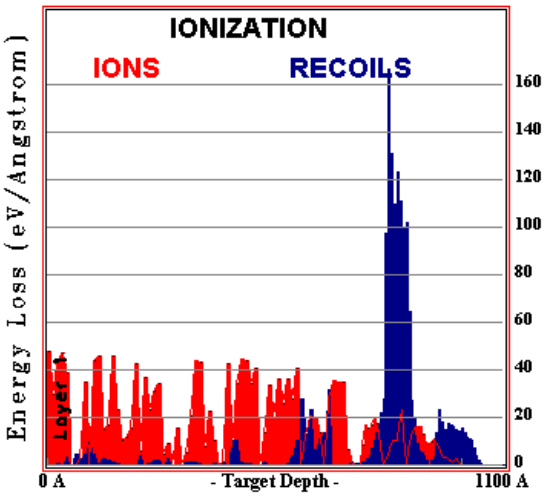

Figure 4.1.3.: TRIM simulation of the fraction of recoil energy transferred to ionisation (red) and further displacements (blue). In total 823 displacements were created in a damage cascade of a 50 keV PKA.

to ionisation is seen in the first 700 Å, while the main recoils are created at the end of the track at about 800 to 1000 Å, here illustrated in blue. Those defects cause most of the relevant damage effects in the silicon bulk that lead to the deterioration of the silicon sensor properties (for details see chapter 5).
The composition of the particles that represent the total fluence on HL LHC experiments depends on the distance from the beam, as illustrated in Fig. Fig. 1.0.1. In the first 10 cm mostly pions and at larger distances to the beam neutrons dominate the total fluence. Pions and other charged hadrons interact mainly via *Coulomb interactions* with the atoms of the silicon lattice. They can create point defects and clusters. Neutrons can only interact with the nucleus by nuclear scattering or reactions, thus the full recoil energy is nearly fully transferred to the PKA, in this case mostly defect cluster are created. A simulation of the defect creation for 10 MeV protons, 24 GeV/c protons and 1 MeV neutrons is shown in Fig. 4.1.4. A scaling model is needed for normalisation, making it possible to compare the radiation induced damage of different particles and different energies. Such a model is given by the *Non Ionising Energy Loss* (NIEL) scaling hypothesis which will be explained in the following.

4.2. The NIEL-scaling hypothesis

The ***N**on **I**onising **E**nergy **L**oss* (NIEL) is a quantity that describes the rate of energy loss due to atomic displacements as a particle traverses a material. The thus created damage effects in the bulk of any material are assumed to scale linearly with the

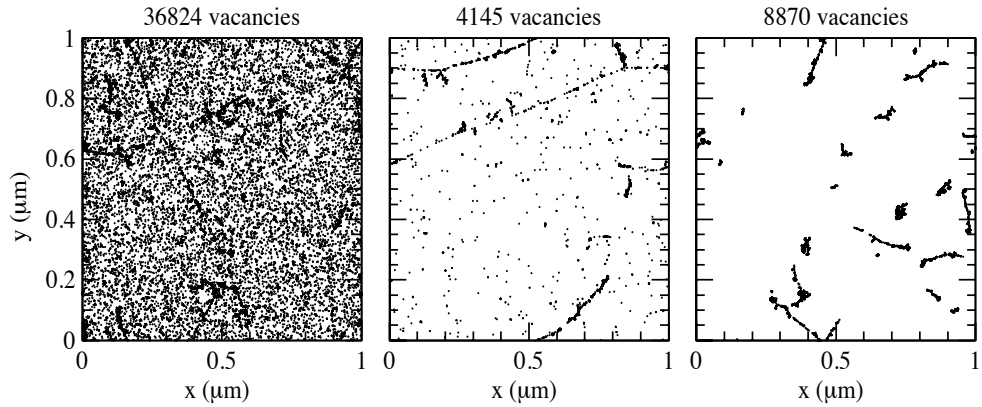

Figure 4.1.4.: Distribution of vacancies after irradiation with 10 MeV protons (left), 24 GeV/c protons (middle) and 1 MeV neutrons (right). The simulation is a projection of over 1 µm of depth (z) and correspond to a fluence of $\Phi = 10^{14}\,\mathrm{cm}^{-2}$. Taken from [36].

amount of this energy that was deposited into displacements. This combination of energy deposition and damage induced changes of the material is referred to as the NIEL-scaling hypothesis [37]. This section describes this hypothesis very briefly on the basis of the PhD thesis of M. Moll [32], where this topic is discussed in detail. The creation of displacement damage is a result of a PKA, with a specific recoil energy E_R, independent of particle type and interaction process of the imparting particle. The fraction of the recoil energy deposited as displacements (in contrast to ionisation) can analytically be calculated by the *Lindhard partition function* $P(E_R)$ [37]. The NIEL can then be expressed by the *displacement damage cross section* or *damage function*

$$D(E) := \sum_{\nu} \sigma_\nu(E) \int_{E_d}^{E_R^{max}} f_\nu(E, E_R) P(E_R) \mathrm{d}E_R, \tag{4.2.1}$$

where σ_ν describes the cross section of a possible reaction ν. $f_\nu(E, E_R)$ is the probability for the generation of a PKA due to the reaction ν. $f_\nu(E, E_R)$ depends on the recoil energy E_R of a particle with energy E. Integration limits are the threshold energy for displacements E_d (25 eV for Si) and the maximal recoil energy E_R^{max}. For further information see [32].

4.2.1. Hardness factors

According to the NIEL-hypotheses the damage of any kind of particle with the energy spectrum of ϕ(E) can be related to the damage of 1 MeV neutrons by the hardness factor:

$$\kappa = \frac{\int D(E)\phi(E)\mathrm{d}E}{D(E_n = 1MeV) \int \phi(E)\mathrm{d}E}. \tag{4.2.2}$$

The *displacement damage function* for 1 MeV neutrons is given by $D_n(1\,\mathrm{MeV}) = 95\,\mathrm{MeV\,mb}$ [38]. With this factor it is possible to compare the damage efficiency of different radiation types to that of 1 MeV neutrons. The 1 MeV neutron equivalent fluence is given by:

$$\Phi_{eq} = \kappa \cdot \Phi = \kappa \int \phi(E)\mathrm{d}E. \tag{4.2.3}$$

It should be noted that the NIEL-hypothesis is not valid for all types of particles and energies. Figure 4.2.1 illustrates the damage created by different types of particles normalised by NIEL to 1 MeV neutrons. The hardness factors used in this work are

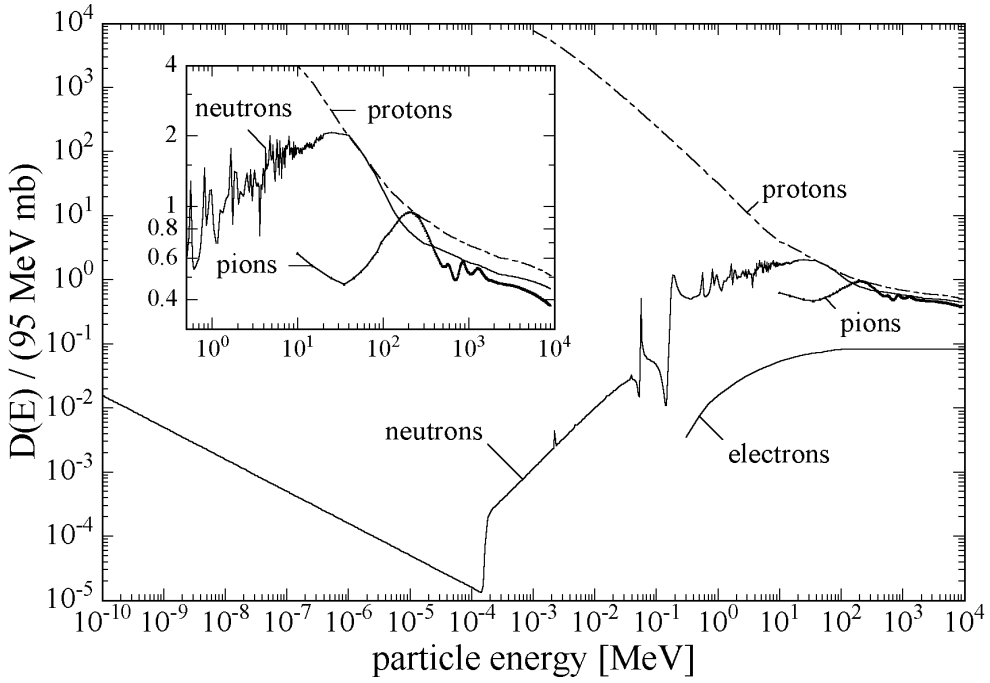

Figure 4.2.1.: Displacement damage functions $D(E)$ normalised to 95 MeVmb for neutrons (10^{-10} to 20 MeV [39], 20 to 400 MeV [40], 805 MeV to 9 GeV [41], protons [41–43], pions [41] and electrons [42]. Due to the normalisation to 95 MeV mb the ordinate represents the damage equivalent to 1 MeV neutrons. The insert displays a zoom of the proton, pion and neutron overlap. Figure taken from [32].

given in Tab. 4.2.1.

Particle	energy [MeV]	hardness factor κ	reference
electrons	1.5	2.01×10^{-2}	[42]
electrons	6	4.20×10^{-2}	[42]
electrons	15	5.80×10^{-2}	[42]

Continued next page ...

Particle	energy [MeV]	hardness factor κ	reference
electrons	900	8.25×10^{-2}	[42][2]
protons	23 000	0.62	[44]
reactor neutrons	average 1	0.91	[39,45]

Table 4.2.1.: Hardness factors of damage created in silicon calculated with the NIEL-approach and used in this work.

4.3. Classification of defects

As explained in Sec. 4.1, the type of defect created in silicon is strongly dependent on type and energy of the irradiating particle. Of course, for HL LHC applications only defects with impact on the electrical properties of sensors are important. We are mainly interested in electrically active defects.
From the previous sections we learn that defects can be classified into two groups, firstly the rather homogeneously distributed *point defects* and secondly the defect *clusters* along the PKA path, that form small regions (about 15 nm diameter [46]) containing high numbers of defects.

4.3.1. Point defects

A clear definition of the terms *point defects* and *clusters* does not exist. In this work, defects which are composed of single vacancies or interstitials, di-vacancies or di-interstitials combined with impurities are usually attributed to *point defects*. *Point defects* may be both impurities from the sensor fabrication process but also the phosphorus or boron doping atoms for example. For that reason it is very important to know the properties and influences of defects in the material under investigation. The classification of point defects according to their electrical properties is described briefly in the following (see also [32]):

- **Acceptors, donors and amphoteric defects**
  Electrically active defects in the band gap are able to capture and emit electrons and holes and thus can be charged or neutral. Fig. 4.3.1 illustrates the position of several defect levels in the band gap and the possible charge states. The defect levels are represented by solid short lines, with either a circle, which denotes the zero charge state, or minus and plus, which denote the positively and negatively charged states[3]. The ionisation energy ΔE_t which is needed to e.g. emit an electron to the conduction band is defined in this notation as the

[2] extrapolated from
[3] Note that the notation used in this work follows the occupation state: (o/+) and (o/-) denote the singly positive or negative charged state of a defect while (-/=) and (+/++) denote the doubly charged states.

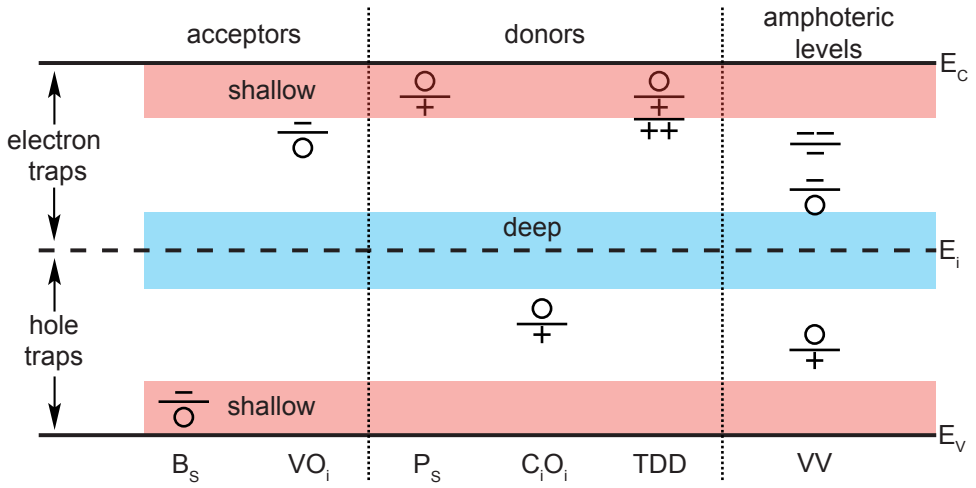

Figure 4.3.1.: Illustration of possible charge states of defects in the band gap. Figure reproduced from [32]. The labelling of charge states of defects follows this graphical representation. Information about the defects see chapter 7.

distance between the conduction band and the trap level ($\Delta E_t = E_C - E_t$). A donor is defined as being neutral if filled by an electron, and positive if empty. An acceptor on the other hand is neutral if empty and negative if filled by an electron. However, the charge state of a defect level (at least in thermal equilibrium) is depends on the relative position to the FERMI level (see Sec. 3.3.2). If located above the FERMI level, acceptors are neutral and donors are positively charged, if the *Fermi* level is located above the defect level, acceptors are negatively charged and donors are neutral (compare [32]).
Defects may have several levels in the band gap. This can be seen for example in the *amphoteric* di-vacancy (VV or V_2). An *amphoteric* defect has both donor and acceptor states in the band gap.

- **Contribution to the space charge**
  Defects are able to change the effective doping concentration (N_{eff}) if they are shallow enough to be ionised and charged at room temperature. Usually levels in the upper part of the band gap are not occupied with electrons, while defects in the lower part are occupied by electrons (depending on the FERMI level). Therefore, being an acceptor in the upper half of the band gap, like the VO_i defect, means that this defect is neutral when not occupied by an electron. The defect is ionised at room temperature and therefore does not change the doping concentration. The same is found for the C_iO_i, which is a donor in the lower part of the band gap. This defect is neutral as well, when ionised.
  In contrast to that, doping atoms like phosphorus (P_S), which is a donor in the upper half of the band gap and boron (B_S), an acceptor in the lower half of the

band gap are charged when ionised. Therefore, they contribute to the space charge at room temperature.

- **Shallow and deep levels**
  A clear definition for the terms *shallow* and *deep* levels is not given in literature. Commonly the term shallow is used for defects which are near to the band edges, while the term deep is used for defects which are in the middle of the band gap. Sometimes levels are called shallow when they are ionised at room temperature, but since the occupation is dependent on the FERMI level and is thus depending on the conduction type and material, the same defect may be called shallow in one material and deep in the other.

- **Electron and hole traps**
  Of course, defects can be occupied by both electrons or holes. Therefore the termini *electron* and *hole traps* are not straightforward. For an *n*-type material, the traps in the upper half of the band gap below the FERMI level are occupied by electrons in thermal equilibrium, regardless of whether the defect is an acceptor or donor. The same is true for *hole traps* in *p*-type silicon sensors.

4.3.2. Cluster defects

As mentioned in this chapters' section 4.1 *clusters* are large agglomerations of defects, mainly vacancies or interstitials in a volume of about (15-20 nm)^3 with 10^5 - 10^6 atoms [46]. In general our knowledge about clusters is very limited. The initial model was proposed in 1959 by GOSSICK [46] in order to explain the high minority carrier recombination after irradiation with heavy particles compared to the one after gamma or electron irradiation (compare [32]). Still we do not know much about the structure of a cluster except for the composition (vacancies and interstitials). Computational simulations of the electrical properties of cluster with density functional theory are still in the beginning, due to the cell-size of such a cluster, and the required CPU time. A report on the structure of vacancy clusters was done by SIECK [47] and a more recent work can be found in [48].
Inside the highly damaged region the so-called *cluster related defects* are introduced. These defects appear to be very similar to that of point defects. They can act as donors, acceptors or amphoteric defects, they can trap electrons or holes, and they can be deep or shallow. On the other hand their defect properties seem to differ from those of point defects [49, 50]. Hence, the models used for the description of cluster related defects are based on measurements of *disturbed* point defects. It is necessary to distinguish between the cluster related defects and the cluster itself. However, the cluster related defects are used in this work as marker to track the condition of the damaged region, since it is not possible to measure the whole cluster.
We can observe some strange effects correlated to the damaged region. An effects that can be observed is the suppression of DLTS and TSC signals of some point defects after proton and neutron irradiation. Unfortunately it is not known if the suppressed

point defects are located inside, outside or close to the cluster region. The high leakage current after fast hadron irradiation as well as the introduction of negative space charge are further effects of the creation of clusters.
The suppression of the DLTS and TSC signals were attributed by SVENSSON ET. AL. to strain fields arising from the agglomeration of defects inside the cluster [51]. The effect is discussed in this works' Sec. 8.1 as well and can be found in [50]. However, chapter 8 deals mainly with the immense increase of the leakage current after fast hadron irradiation. It was interpreted by WATTS [52] and GILL [53] as interaction between divacancies, located close together inside the cluster. This process is known as *inter-center charge transfer* [54]. The impact of cluster defects on the space charge was recently revealed by PINTILIE [55] and is also discussed in chapter 9.

4.4. Shockley-Read-Hall statistics

The degradation of the sensors used in HEP experiments is due to the trapping and detrapping of charges in defects and the resulting effects. Thus it is necessary to understand the process of the interaction of charge carriers with defects in the band gap and during the capture and emission of charge into the valence and conduction band.
According to SHOCKLEY, READ and HALL this can be described as a statistical processes. Figure 4.4.1 shows the possible reactions and gives the reaction rates that take place. The rate r_1 (r_4) of electrons (holes) emitted to the conduction (valence)

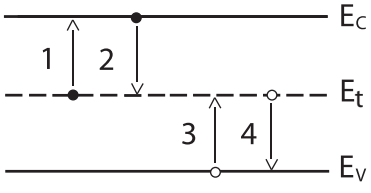

1. Rate for the emission of electrons into the conduction band $r_1 = e_n\ n_t$
2. Rate for the capture of electrons into non occupied trap level $r_2 = c_n\ n\ p_t$
3. Rate for the capture of holes into states occupied by electrons (equivalent to emission of electrons into valence band) $r_3 = c_p\ p\ n_t$
4. Rate for emission of holes into the valence band (equivalent to capture of electrons from the valence band) $r_4 = e_p\ p_t$

Figure 4.4.1.: Emission and capture rates of an energy level E_t. Figure taken from [32] and modified.

band E_C (E_V) is proportional to the fraction of defect states occupied by electrons n_t (holes p_t). The capture rate r_2 (r_3) of electrons (holes) from the conduction (va-

lence) band E_C (E_V) is proportional to the fraction of defect states occupied by holes p_t (electrons n_t) and the concentration of free electrons n (holes p) in the conduction (valence) band E_C (E_V) (see also [32]).
The constants of proportionally are given by the *emission rate* e_n (e_p) and *capture coefficient* c_n (c_p). Leading to the differential equation for states occupied by electrons n_t

$$\frac{dn_t}{dt} = -r_1 + r_2 - r_3 + r_4 \tag{4.4.1}$$
$$= -e_n\, n_t + c_n\, n\, p_t - c_p\, p\, n_t + e_p\, p_t. \tag{4.4.2}$$

In thermal equilibrium the concentrations of free charge carriers in the valence and the conduction band are constant. Thus the transition rates with the conduction or the valence band have to take place at the same rate. Using the electron and hole density in the valence band (Eq. 3.3.5, Eq. 3.3.6) and the *mass-action-law* (Eq. 3.3.9) this leads to an expression for the emission rates

$$e_{n,p} = c_{n,p} n_i \exp\left(\pm\frac{E_t - E_i}{k_B T}\right) \tag{4.4.3}$$
$$= c_{n,p} N_{C,V} \exp\left(\pm\frac{E_t - E_{C,V}}{k_B T}\right) \tag{4.4.4}$$

E_t denotes the trap level (see page 40). By using the enthalpy $\Delta H_{n,p}$ and introducing the entropy factors $X_{n,p}$ for electron and hole emissions

$$E_C - E_t = \Delta H_n - k_B T \ln(X_n) \tag{4.4.5}$$
$$E_t - E_V = \Delta H_p - k_X T \ln(X_p). \tag{4.4.6}$$

Equation 4.4.4 can be expressed as

$$e_{n,p} = c_{n,p} N_{C,V} X_{n,p} \exp\left(-\frac{\Delta H_{n,p}}{k_B T}\right). \tag{4.4.7}$$

Due to the fact that $X_{n,p}$ and $c_{n,p}$ are often not known, it is useful (see e.g. [2]) to define a cross section $\sigma_{n,p}$ by setting

$$X_{n,p} c_{n,p} = \sigma_{n,p} v_{th,n,p}. \tag{4.4.8}$$

The *thermal velocity* $v_{th,n,p}$ near the edges of valence and conduction band is given by (see also [1])

$$v_{th,n,p} = \sqrt{\frac{3 k_B T}{m^*_{n,p}}}. \tag{4.4.9}$$

Under the assumption that the capture cross section is independent of temperature, which means that the change in entropy is neglected, it is possible to obtain an

expression for the emission rates:

$$e_{n,p} = \sigma_{n,p} v_{th,n,p} N_{C,V} \exp\left(-\frac{\Delta E_a}{k_B T}\right). \tag{4.4.10}$$

The value ΔE_a is called *activation energy* for the emission of charge carriers in this work.

4.5. Current generation due to defects under reverse bias

The leakage current generated by defects under reverse bias is given by:

$$I(T) = Vol \cdot q_0 \left(\sum_{acceptors} e_n(T) \cdot n_t(T) + \sum_{donors} e_p(T) \cdot p_t(T) \right), \tag{4.5.1}$$

where *Vol* denotes the volume of the depletion region. For the calculation of the current due to one acceptor-like defect, we obtain

$$I(T) = Vol \cdot q_0 \cdot e_n(T) \cdot n_t(T), \tag{4.5.2}$$

for a donor-like defect

$$I(T) = Vol \cdot q_0 \cdot e_p(T) \cdot p_t(T) \tag{4.5.3}$$

with the occupation of states n_t and p_t. Assuming free carriers in the space charge, like in highly irradiated sensors, the occupation of defect levels by electrons can be calculated by solving the Shokeley-Read-Hall differential equation (Eq. 4.4.2):

$$n_t = N_t \frac{c_n \cdot n + e_p}{e_n + e_p + c_n \cdot n + c_p \cdot p} \tag{4.5.4}$$

and for the occupation of holes

$$p_t = N_t \frac{c_p \cdot p + e_n}{e_p + e_n + c_p \cdot p + c_n \cdot n}. \tag{4.5.5}$$

For low irradiated samples we can neglect the free carriers in the space charge ($n \approx p \approx 0$) and the occupation reduces to:

$$n_t = N_t \frac{e_p}{e_n + e_p} \quad \text{and} \quad p_t = N_t \frac{e_n}{e_n + e_p}. \tag{4.5.6}$$

Combining 4.5.2 respectively 4.5.3 with 4.5.6 leads to an expression for the contribution of a deep defect level to the generation current

$$I(T) = q_0 \cdot Vol \cdot N_t \frac{e_n \cdot e_p}{e_n + e_p}. \tag{4.5.7}$$

4.6. Occupation of traps under forward bias

It is very important to understand the filling conditions of defects under forward bias, because this is the main possibility for majority and minority carrier injection in the DLTS and TSC measurements. By injecting a high number of carriers into the silicon bulk the emission rates become small compared to the capture rates ($e_n << c_n n$ and $e_p << c_p p$). In this case the capture rates determine the occupation of the defect states (compare [32]). They are given by Eq. 4.4.2:

$$n_t = N_t \frac{1}{1 + \frac{c_p p}{c_n n}} \quad \text{and} \quad p_t = N_t \frac{1}{1 + \frac{c_n n}{c_p p}} \tag{4.6.1}$$

4.7. Defect annealing

The description and right assignment of defects is a complicated task. Electrical defect properties, as measured by methods like *Deep Level Transient Spectroscopy* (DLTS, see chapter 6) and *Thermally Stimulated Current* (TSC, see chapter 6), give no information about the chemical structure of defects. It is necessary to find ways in order to identify those defects which are responsible for the degradation of sensor properties and successively reveal the structure of the defects. One possibility is to follow the defect migration at room temperature and correlate changes in the detector properties to changes in the defects concentrations. Defect migration at room temperature may take months or years, in order to accelerate this process a heat treatment of the sensor is possible. The thermal energy accelerates defect migration and dissociation in the silicon material. This technique is called *annealing*.
Further information about the assignment of defects can be found via cross correlation of the annealing of defects in silicon observed with DLTS and TSC with other techniques like *infrared-spectroscopy* (information about IR-spectroscopy see [56]) and *electron paramagnetic resonance* (more information about EPR see [16]), two techniques that allow a direct assignment of the chemical structure of a defect. There are two possible ways of annealing studies:

- isochronal annealing
- isothermal annealing

As the name indicates, ***isochronal*** annealing will be done with constant time intervals at different temperatures with constant temperature steps. On the other hand ***isothermal*** will be performed at a constant temperature for an increase of the annealing time. Isochronal annealing takes less time and gives an overview of the defect evolution. Isothermal annealing takes a longer time and gives a complete picture of the defect evolution at that temperature. With respect to the activation energy for defect migration and dissociation of the defects the temperature range for isochronal annealing

has to be considered carefully.
Three processes may happen during annealing (see fig. 4.7.1):

Migration Defects become mobile at distinct temperatures and migrate through the silicon lattice. There they can get trapped in so-called sinks (e.g. surface, dislocations) or impurities.

Complex formation Migrating defects are able to react with other defects or impurities and build new defects or recombine (e.g. $V + O_i \rightarrow VO_i$, $V + (Si)_i \rightarrow (Si)_s$).

Dissociation A defect complex dissociates into its components due to a high energy phonon. Parts of the complex migrate through the lattice until they are trapped by other defects or a sink (e.g. $C_iC_s \overset{T\gtrsim 250C}{\rightarrow} C_i + C_s$).

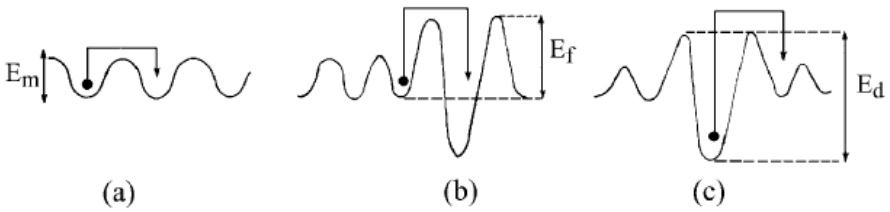

Figure 4.7.1.: Schematic process of (a) defect migration, (b) complex formation and (c) complex dissociation. Energies are indicated as well. Taken from [32].

4.8. Defect kinetics

The annealing of defects due to migration and dissociation can be described by first order processes as explained by Waite in 1957 [57] or more explicitly in Svensson & Lindström [58]. In a first order process each individual defect complex anneals out without being influenced by the remaining defects. Dissociation or formation of more complex defects is given by

$$A + B \rightarrow AB, \tag{4.8.1}$$

where A is a defect and B is a defect or impurity which combines with A into a more complex structure. When the concentration of B is more than one order of magnitude higher than of defect A, B can be treated as constant for the reaction. The rate equation for a first order process is then given by

$$-\frac{d[A]}{dt} = k_1\,[A] \tag{4.8.2}$$

where $[A]$ is the defect concentration and k_1 is the *rate constant*. The k_1 depends on the temperature and can be expressed by the *Arrhenius relation*

$$k_1 = k_0 \cdot \exp\left(-\frac{E_a}{k_B T}\right) \tag{4.8.3}$$

where k_0 is the *frequency factor* and E_a is the activation energy for dissociation or migration.
The rate constant for *diffusion limited reactions* [57] between two different kinds of homogeneously distributed defects can be described by the rate equation

$$-\frac{d[A]}{dt} = 4\pi R D [B]_{t=0}[A] \tag{4.8.4}$$

with R being the *capture radius*[4] of the reaction, $[B]_{t=0}$ is the concentration of the defect B at the beginning of the reaction and D is the sum of the *diffusion coefficients* (sometimes called *diffusivity*). In many cases the diffusion coefficient is dominated by the defect which diffuses fastest. From equation (4.8.2) and (4.8.4) it can be seen, that the rate constant k_1 equals $4\pi R D [B]_{t=0}$. It is well-established to describe the temperature dependence of the diffusivity by an *Arrhenius relation*

$$D = D_0 \cdot \exp\left(-\frac{E_a}{k_B T}\right) \tag{4.8.5}$$

with the *diffusion constant* D_0, that can be approximated by $D_0 = \alpha a^2 \nu$ (α describes the number of possible jump places, a the lattice constant and ν the phonon frequency)(compare [32]).
An integration of equation (4.8.4) leads to the result of an exponential decreasing defect concentration

$$[A] = [A]_{t=0} \exp(-k_1 t). \tag{4.8.6}$$

If a new defect is building up during the annealing of the defect A through the reaction (4.8.1), the new defect can be labeled as $C = AB$. Solving the rate equation for the new defect

$$\frac{d[C]}{dt} = -k_1[A] \tag{4.8.7}$$

leads to the time dependence of the new defect

$$[C] = [A]_{t=0} \exp(1 - \exp(k_1 t)). \tag{4.8.8}$$

If a defect is destroyed by two first order processes it can form higher order complexes or it may dissociate. For example:

$$V_2 + O_i \rightarrow V_2 O_i \quad (k_2) \tag{4.8.9}$$

[4] An approximation for R is given in Moll [32]

or

$$V_2 \rightarrow V + V \quad \text{(via dissociation } k_1\text{)} \tag{4.8.10}$$

If the two processes have comparable rate constants, the rate equation becomes

$$\frac{d[A]}{dt} = -k_2[A] - 4\pi RD[A][B]_{t=0} = -[A](k_1 + k_2). \tag{4.8.11}$$

This differential equation is solved by

$$[A] = [A]_{t=0} \exp(-(k_1 + k_2)t), \tag{4.8.12}$$

the concentration of the resulting defect is given by

$$[C] = [A]_{t=0} \frac{(1 - \exp(-k_1 + k_2)t)}{1 + k_1/k_2}. \tag{4.8.13}$$

For second order processes see SVENSSON ET. AL. [58], further information about the annealing procedure and defect annealing can be found in [32].

5. Macroscopic changes of detector properties

The radiation induced defects are able to change the properties of a detector. The most important changes are shown in Fig. 5.0.1 and explained in this chapter.

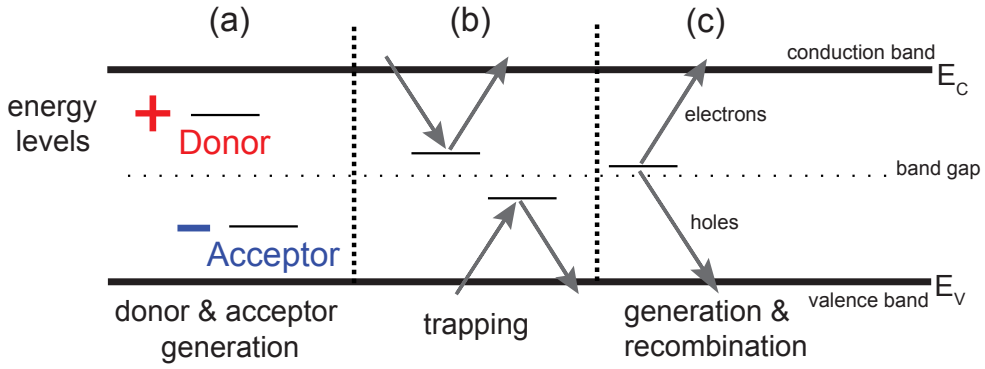

Figure 5.0.1.: Effects on detector properties due to radiation induced defect levels in the band gap. Change of the effective doping concentration (a), trapping of charge carriers (b) and increase of current due to generation and recombination of charge carriers (c). Figure reproduced from M. Moll.

5.1. Donor and acceptor generation

As illustrated in Fig. 5.0.1 (a), the radiation induced defects may act as acceptors or donors with impact on the effective doping concentration ($|N_{eff}|$). Like the dopant atoms phosphorus and boron, impurities build up defect complexes that are able to contribute to the space charge. An overview of the known defects and their impact is given in Sec. 7.3 while the results concerning the effective space charge achieved in this work are presented in chapter 9.
As most of the defects with impact on detector properties are impurity related point defects, naturally the starting material is very important for the operation of the sensors. Assuming for the following considerations that the starting material is very pure and made of high resistivity n-type FZ material, the initial phosphorus doping concentration is given by 1×10^{12} cm^{-3}. If acceptors are created during the irradiation, the positive space charge of the initial doping will be reduced by the negative space

charge of the acceptors. If donors are created, the positive space charge will increase. Usually both acceptors and donors are created during the irradiation. The particle type and the starting material are crucial for the behaviour of the diode.
The change of $|N_{eff}|$ for high resistivity FZ material irradiated with 1 MeV neutrons is displayed in Fig. 5.1.1. Values are measured directly after irradiation. As $|N_{eff}|$ is connected to the voltage at full depletion (V_{dep}) via Eq. 3.4.5, also V_{dep} (here labelled U_{dep}) changes. The initial V_{dep} started below 40 V and decreases rapidly with the irradiation. The neutrons mostly create acceptors in this very pure high resistivity FZ material. The negative space charge reduces the available free carriers and thus the depletion voltage decreases. At a certain point, where the minimum of the curve is seen, the creation of acceptors compensates the initial phosphorus doping and the material undergoes type inversion from *n*-type to *p*-type. Initial phosphorus is deactivated by the formation of vacancy-phosphorus-complexes ($V + P$) creating the *E*-centre or VP (this process is sometimes called *donor removal*).

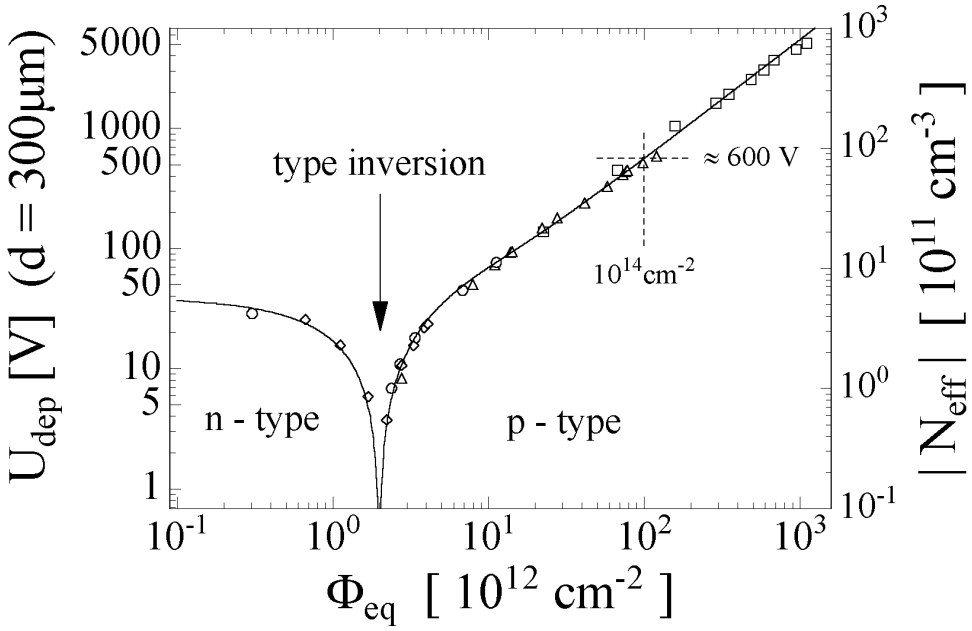

Figure 5.1.1.: Change in the depletion voltage, effective doping concentration as function of the fluence. Figure taken from [59].

As more acceptors are created with increasing fluence, the negative space charge density increases. At $\Phi = 10^{14}$ cm^{-2} the depletion voltage reaches about 600 Volts, resulting in further problems for the actual HEP experiments as illustrated in Fig. 5.1.2. In an undamaged sensor (a), the created electrons and holes are collected at the read out strip of the sensor. Additional donors and acceptors are created during the irradiation, as a result the applied voltage is not sufficiently high to deplete the sensor. The signal will decrease due to the charge loss in the undepleted bulk (b). The case of

the type inverted sensor, which is undepleted at the read out side is the worst, because the only signal that can be collected at the read out strip (c) is due to diffusion.

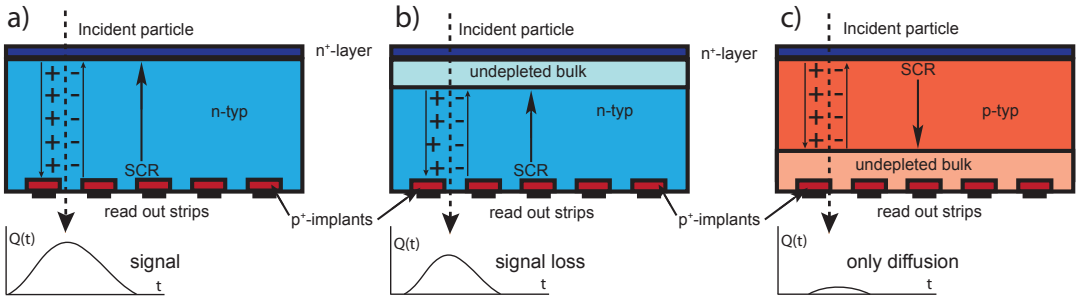

Figure 5.1.2.: Impact of the change of N_{eff} on the signal generation in an undamaged sensor (a), sensor with higher V_{dep} than applied voltage (b) and type inverted sensor (c).

Annealing behaviour

While the sensors are planned to be kept at -10 °C during the operation, during maintenance periods the Si-trackers are heated up to room temperature. The impact of the heating results in the annealing of defects. Therefore it is also interesting to look at the changes due to annealing. A typical result is shown in Fig. 5.1.3. The diode was annealed at 60 °C, then C-V was measured and N_{eff} calculated via Eq. 3.4.5. The change can be described by $\Delta N_{eff} = N_{eff,0} - N_{eff}$, where $N_{eff,0}$ is the initial doping concentration and fitted as shown in Fig. 5.1.3 with the expression [32]

$$\Delta N_{eff}(\Phi_{eq}, T_a, t) = N_A(\Phi_{eq}, T_a, t) + N_C(\Phi_{eq}) + N_Y(\Phi_{eq}, T_a, t). \tag{5.1.1}$$

Up to 80 minutes at 60 °C ΔN_{eff} decreases. The behaviour is called *short term annealing*. It can be explained by the annealing of several defects with different time constants. Therefore it is possible to describe the behaviour by a sum of exponential terms

$$N_A(\Phi_{eq}, T_a, t) = \Phi_{eq} \sum_i g_{a,i} \exp\left(-\frac{t}{\tau_{a,i}(T_a)}\right). \tag{5.1.2}$$

Here, τ_a denotes the time constants for annealing of defects and the other expressions as explained in Fig. 5.1.3. The very short time constants, like minutes and hours are not important for the HEP experiments, thus it is common to reduce Eq. 5.1.2 to a single time constant τ_a and an amplitude $N_A(\Phi_{eq}, T_a, t = 0) = g_a \Phi_{eq}$. Further details can be found in [32, 59]. Moll [32] describes the time constants for the *short term annealing* in detail and presents acceleration factors for different temperatures. The acceleration factor eg. for *short term annealing* at 60 °C compared to 20 °C is 174 and for 80 °C 1490 [32].

At about 80 minutes at 60 °C a minimum is seen. For longer annealing times ΔN_{eff} increases, thus the behaviour is called *long term* or *reverse annealing*. According to

Moll [32] it can be represented by

$$N_Y(\Phi_{eq}, T_a, t) = N_{Y,\infty}\left(1 - \frac{1}{1 + t/\tau_Y(T_a)}\right), \tag{5.1.3}$$

with τ_Y is the time constant of the annealing process and the other expressions as

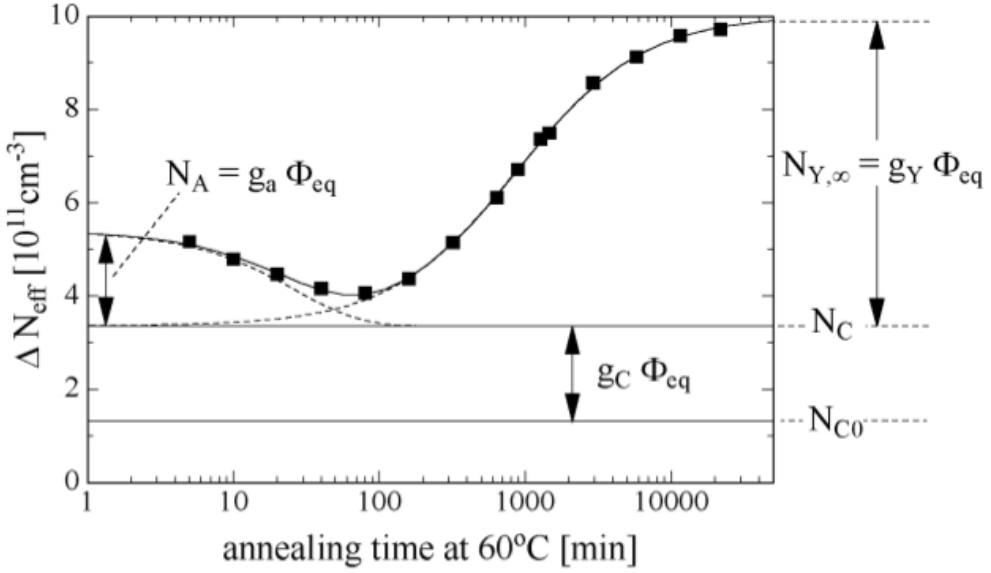

Figure 5.1.3.: Annealing behaviour of $|N_{eff}|$ with description of the main fitting parameters. Figure taken from [32].

illustrated in Fig. 5.1.3. The most important damage component is the *stable damage* (N_C). This parameter can not be changed by environmental conditions, while the *long term annealing* can be prevented by cooling. As well as the *short term annealing* also the *long term annealing* exhibits acceleration factors for the annealing at different temperatures. They can be found in [32].

5.2. Generation current

As illustrated in Fig. 5.0.1, defects near the middle of the band gap are able to generate e/hole-pairs. The generation inside the depletion layer always implies the motion of charge carriers resulting in an increase of the leakage current. The total leakage current due to irradiation (ΔI) is calculated by taking the current at full depletion (I_{dep}) and subtract the initial leakage current before irradiation (I_0). For test structures used in this work typical values for I_0 are about a few 10 - 100 pA (for a 75 µm thick sensor with an area of 0.25 cm^2), while already at doses of $\Phi_{eq} = 1 \times 10^{13}\,\mathrm{cm}^{-2}$ the leakage current reaches some hundred nA.

Fig. 5.2.1 from MOLL [32] shows the increase of the radiation induced leakage current per volume as function of fluence for several materials. In order to be able to compare the generation current for sensors with different thicknesses, the ΔI was normalised to the volume (*Vol*). Each point is an individual sensor irradiated with fast neutrons in a single exposure to the given fluence and stored in liquid nitrogen afterwards to suppress further annealing. Then the sensors were annealed for 80 minutes at 60 °C[1] and I-V characteristics measured at room temperature and normalised to 20 °C according to Eq. 3.4.19 (compare [32]).

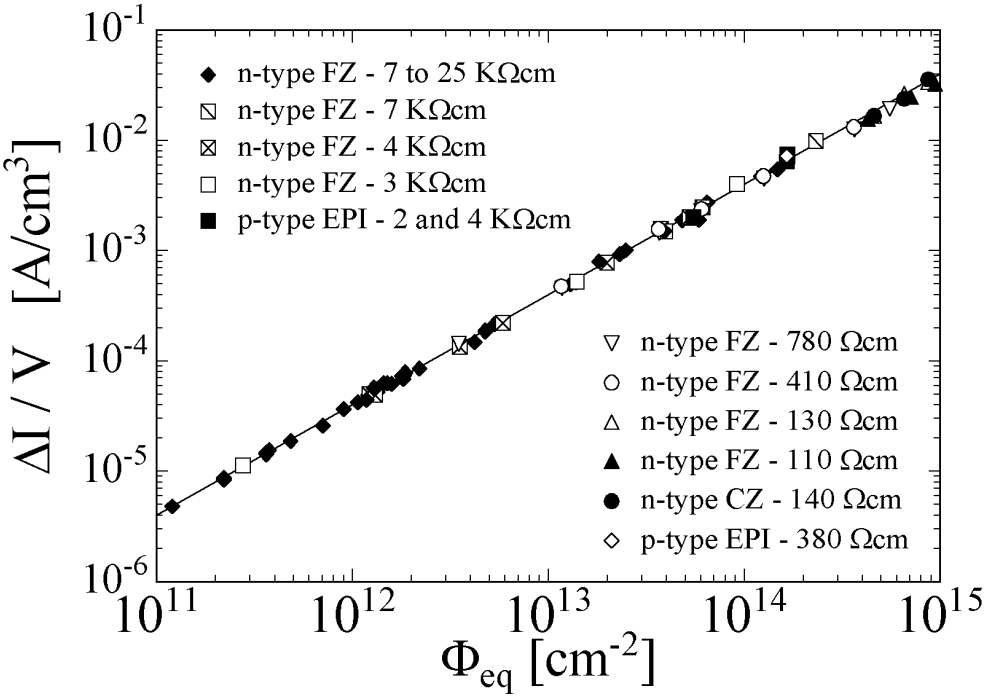

Figure 5.2.1.: Dependance of volume generation current on neutron fluence. Figure taken from [32].

MOLL found that the increase of the leakage current is found to be proportional to the fluence. This can be described by the expression

$$\Delta I = \alpha \Phi_{eq} Vol, \tag{5.2.1}$$

where α is called the *current related damage rate*. As the fluence range in the figure spreads from $\Phi = 1 \times 10^{11}\,\mathrm{cm}^{-2}$ to $\Phi = 1 \times 10^{15}\,\mathrm{cm}^{-2}$, some of the sensors are already type inverted [32] (see sec. 5.1). As seen in Fig. 5.2.1, this has no impact on the leakage current. This is true, as long as the volume is defined by e.g. contacting a guard ring. If not connected the *pn*-junction will grow from the rear-side between the former n-n^+

[1] This annealing state correspond to the minimum of the change of $|N_{eff}|$ after irradiation.

respectively p-p^+ junction and additional current can be collected at the front. Note that type inversion in n-in-p material was seen for MCz or Epi material after 23 GeV proton irradiation.
The effect of subsequent isothermal annealing of the sensors at different temperatures is displayed in to Fig. 5.2.2. Here, α is shown as function of annealing time for different annealing temperatures (for further information see [32]). The curves follow a sum of exponential terms for the short term annealing and a logarithmic function for the long term annealing. The data points were fitted after [32] by (solid lines):

$$\alpha(t) = \alpha_I \cdot \exp\left(-\frac{t}{\tau_I}\right) + \alpha_0 - \beta \cdot \ln(t/t_0). \tag{5.2.2}$$

τ_I denotes the time constant for the annealing out of defects that are responsible for the leakage current. The fit parameters can be found in Appendix A.2.1. Moll

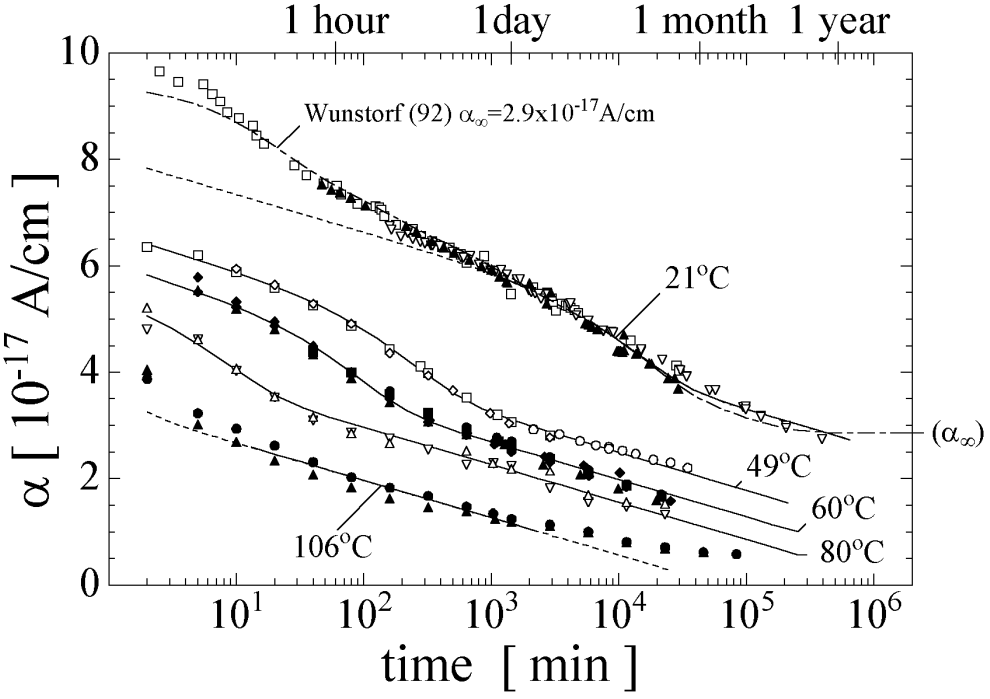

Figure 5.2.2.: Damage parameter α as function of annealing at different temperatures. Measurements were performed at room temperature (normalised to 20 °C). Figure taken from [32].

observed a correlation between the leakage current and two defect levels denoted by $E170/E212$ [32] from the annealing behaviour. Further analyses of this defect can be found in chapter 8, here labelled as $E4/E5$. Note that due to the linearity of the current vs. fluence relation (Eq. 5.2.1), fluence values can be calculated via measured leakage currents at certain annealing times with corresponding α values. For normalisation

purposes it is possible to use the α-value at 80 minutes annealing at 60 °C which equals 8 minutes annealing at 80 °C for which is $\alpha = 3.99 \times 10^{-17}$ A cm^{-1}.

5.3. Trapping

The most important parameter for sensors in HL LHC experiment is the *Charge Collection Efficiency* (CCE). This parameter describes the fraction of a sensor's collected charge compared to an unirradiated sensor which is set to unity. The CCE decreases with irradiation, since charges get trapped in defects. Charge carriers trapped in shallow defects near the edges of the band gap recombine very fast, while charge carriers trapped in deep mid-gap traps keep the charges for µs. Although a lot of effort was put into the identification of defects with impact on the trapping of charge carriers after irradiation, no defect has been identified, yet. Possible candidates for the defects responsible for trapping of electrons and holes were found during the progress of this work. The defect which is assumed to be responsible for the electron trapping is labelled $E205a$ defect, for holes we assume the $H(151K)$ defect to be responsible. The similar annealing behaviour of the trapping times and the defect concentrations led to this assignment, but an unambiguous correlation could be achieved so far.
In the recent time, a newly found *charge multiplication effect* improves the CCE of irradiated thin sensors. The *charge multiplication* increases for increasing fluences and even overcompensates the trapping of defects. Information about this topic can be found in [20–23].

6. Techniques and Equipment

This chapter will introduce the main irradiation facilities used for the reactor neutron and 23 GeV protons irradiations and the measurement techniques used in this work. The electrical properties of the sensors are characterised by *capacitance-voltage* characteristics (C-V) and *current-voltage* characteristics (I-V), often called *macroscopic* measurements. The C-V and I-V measurements are well-established and widely used methods for obtaining electrical properties of semi-conductor materials and diode characteristics.
The crystal defects, on the other hand, are investigated by means of *Deep Level Transient Spectroscopy* (DLTS) and *Thermally Stimulated Current* technique (TSC). Those *microscopic* measurement techniques are off-the-shelf technologies for defect characterisation, borrowed from solid-state physics. Both measurement techniques allow us to obtain valuable information about the radiation induced defects in semiconductor materials. They permit direct access to quantitative concentrations of defects in the bulk material. Furthermore DLTS allows direct measurements of the capture cross sections for electrons and holes ($\sigma_{e,h}$) of the defect and the activation energy for the emission of charge carriers (ΔE_a).

6.1. Irradiation facilities

6.1.1. Neutrons

The neutron irradiation was performed at the TRIGA Mark II reactor [60] operated by the Jožef Stefan Institute, Ljubljana in Slovenia [61]. This pool-type reactor is a 250 kW (max. power) light water reactor with solid fuel elements. The water acts as moderator as well as shielding and can be easily accessed for irradiation purposes. The reactor power can be altered in order to reach different orders of magnitude of fluence. With the TRIGA reactor, it is possible to cover fluxes of about 2×10^9 n cm^{-2} s^{-1} to 2×10^{12} n cm^{-2} s^{-1}.
The neutron energy spectrum extends up to 10 MeV and a hardness factor for normalisation was obtained by ŽONTAR [62]. The fluence accuracy is assured to be within 10 % [63].

6.1.2. Protons

Protons are extracted from the *Proton Synchrotron* PS at CERN with a momentum of 24 GeV/c. The PS delivers one to three spills per cycle depending on the beam sharing

with other experiments. The facility *IRRAD-1* is located at the PS-*T7* beam line in an irradiation zone at the CERN PS *East hall* where samples can be exposed to a 24 GeV/c proton beam scanning over an area of about 2×2 cm^2 [64]. Depending on the beam focussing, a minimum fluence of 1.5×10^{11} protons per spill can be delivered by the PS, resulting in an average proton flux with one spill per cycle of $3 - 9 \times 10^9$ cm^{-2} s^{-1}. The beam profile alignment is monitored by *Gofchromic Dosimetric Films XR* [65, 66] and by a recently installed online monitoring system, recording the X and Y profile perpendicular to the beam (available online at [67]).
The fluence is provided by measurement of the activity of ^{22}Na and ^{24}Na in 5×5 cm^{-2} aluminium (Al) foils. The isotopes are created by the nuclear reactions ^{27}Al(p,3pn)^{24}Na and ^{27}Al(p,3p3n)^{22}Na. A germanium spectrometer allows the measurement of the ^{24}Na gamma emission at $E_\gamma = 1368.53$ keV with a half-life of $\tau_{1/2}$=14.96 h and the ^{22}Na gamma emission at $E_\gamma = 1274.54$ keV with a half-life of $\tau_{1/2}$=2.6 y. The accuracy for this method lies within 7 % [68].
The detectors are packed into stacks of 5×5 cm^2 cardboards and then transported by a shuttle into the beam. The temperature at the point where the irradiation takes place is about 27 °C. As the proton fluence is about $1 - 3 \times 10^{13}$ p cm^{-2} h^{-1}, a fluence of $\Phi = 1 \times 10^{15}$ is reached within 4 days, for $\Phi = 1 \times 10^{16}$ more than 40 days are necessary if the beam is operated properly throughout the whole time. Hence annealing effects during irradiation are possible. Directly after irradiation, the activity of the sensor needs to decay for about 30 minutes to one hour, until it is decreased to a level where the material can be handled safely. Then the irradiated sensor is put into a freezer at the facility and kept at -20 °C until the activity is below the limit allowed for packing and shipping.

6.2. Measurement Techniques

The two measurement techniques for obtaining electrical properties of diodes *(macroscopic)* are *capacitance-voltage* characteristics (C-V) and *current-voltage* characteristics (I-V). The I-V characteristics gives information about the radiation induced increase of leakage current, the homogeneity of current-generating defects inside the sensor and information about the surface current from cut edges.
C-V characteristics give information about the depletion voltage V_{dep} and the capacitance at full depletion C_{end}, allowing us to calculate the thickness of the sensor and the effective doping concentration. From the shape of the C-V curve it is possible to calculate the effective doping profile as function of the sensor depth.
Deep Level Transient Spectroscopy (DLTS) and *Thermally Stimulated Current* (TSC) offer the possibility to gather information about defect concentrations and defect properties (microscopic). DLTS is used on samples with irradiations lower than $\Phi_{eq} < 10^{12}$ cm^{-2}, while TSC offers the possibility to have insight in defect concentrations of medium and highly irradiated samples.
The combination of microscopic and macroscopic measurements offers a good possibil-

ity to detect defects with impact on the diode properties and their annealing behaviour. Thus a combination of both measurement types was performed.
Here, only a short compilation of the measurement techniques and the experimental setups is given. They are described in detail in the PhD thesis of M. Moll [32].

6.2.1. Measurement of diode properties

***Current-voltage* characteristics**
For measuring the current-voltage characteristics, a DC voltage is applied to the back plane of the diode by a voltage source and the p^+-contact is connected to a pA meter. The guard ring (GR) can either be connected to the same potential as the p^+-PAD or left floating. In this work measurements are performed with the GR connected if not stated otherwise. The GR current is hereby measured separately with a picoamperemeter. If the GR is not connected, the volume of the sensor is not well defined, that leads, in particular for type inverted sensors, to a much higher leakage current and larger capacitance values.

***Capacitance-voltage* characteristics**
With a LCR meter the impedance Z or the admittance $Y = Z^{-1}$ of a device is measured. If the device is assumed to be best described by a serial circuit of a capacitor C_s and a resistor R_s (see Fig. 6.2.1) both quantities can be measured from the imaginary part of (C_s) and the real part (R_s) of the impedance. For a serial circuit the impedance results in:

$$Z = R + jX \quad \text{with} \quad X = -\frac{1}{\omega C,} \quad R = R_s \tag{6.2.1}$$

here j denotes the imaginary unit and $\omega/2\pi$ is the frequency of the applied AC-signal. From the imaginary part of the impedance, which is called reactance (Im $Z = X$), the capacitance can be calculated. From the inverse of the electrical impedance we obtain

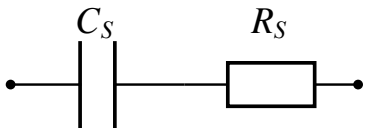

Figure 6.2.1.: Serial equivalent circuit of capacitor (C_S) and resistor (R_S).

the admittance:

$$Z^{-1} = Y = G + jB, \tag{6.2.2}$$

with G denotes the electrical conductance and B the electrical susceptance. Now assuming that the device can be described by a parallel equivalent circuit (see Fig. 6.2.2) the admittance becomes:

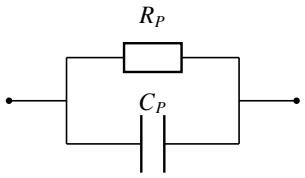

Figure 6.2.2.: Parallel equivalent circuit of capacitor (C_P) and resistor (R_P).

$$Y = \frac{1}{R_P} + j\omega C_P. \tag{6.2.3}$$

It is clear, that the capacitance can be calculated from the imaginary part of the admittance (Im $Y = B$). However, both equivalent circuits describe the same measured data and can be transformed into each other via $Z^{-1} = Y$.
For real sensors, the more realistic description is a capacitor (C) in parallel with a

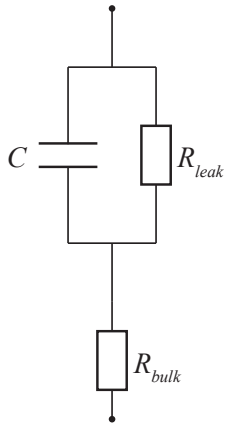

Figure 6.2.3.: Equivalent circuit of a real diode, the parallel resistor R_{leak} represents the leakage current of the sensor and the serial resistor (R_{bulk}) regards the resistivity of the bulk.

resistor describing the leakage current (R_{leak}) and an additional serial resistor regarding the bulk resistance (R_{bulk}) as illustrated in Fig. 6.2.3. In the case of an un-irradiated sensor the bulk resistance can be neglected because it is very low.

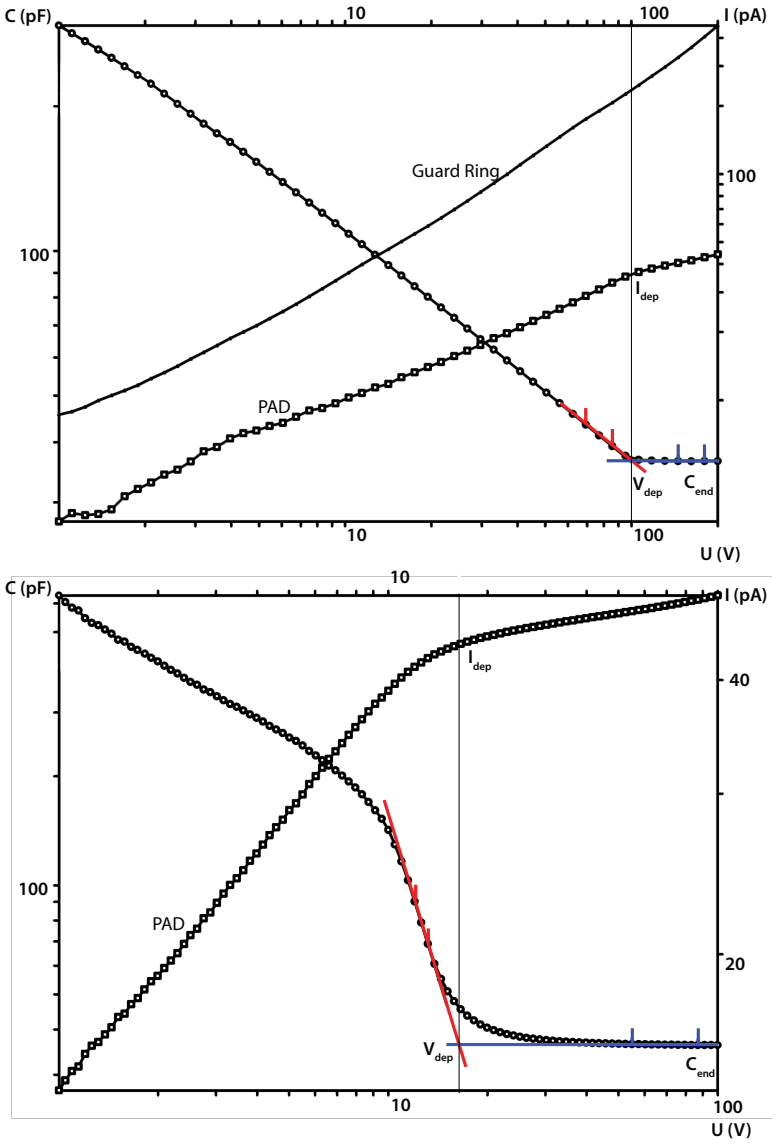

Figure 6.2.4.: *Capacitance-voltage* and *current-voltage* characteristics for an unirradiated (top) and irradiated (bottom) standard Epi detector evaluated with DetWndIV. The irradiation was chosen with $\Phi_{eq} = 6 \times 10^{14}$ cm^{-2} neutrons. The depletion voltage and current at full depletion is obtained from the intersection of two straight lines fittet to the measurement data.

Also the leakage current is very low, hence the admittance describes nearly completely the capacitance of the sensor. In this case, the parallel equivalent circuit describes the situation very well.
For an irradiated sensor the equivalent circuit can be approximated by the parallel circuit of the capacitor and a resistor describing the leakage current (R_{leak}). Further-

more the bulk resistance is not negligible any more, this requires the serial bulk resistor (R_{bulk}). In the case of highly irradiated sensors, the presence of high defect concentrations introduce a strong frequency dependence of the measured AC-signal and non-uniform space charge distributions, demonstrating the assumptions made for the electric circuit are not correct. In this work, only lowly irradiated sensors were used, where the assumption of the described equivalent circuit still represents the measurement quite well.
The measurements are typically performed with an AC voltage of 0.5 V and frequencies of 10 and 100 kHz. The unirradiated samples show no frequency dependence, while for irradiated sensors the lower frequency (usually 10 kHz) was used. The instruments are listed in App. Tab. A.2.2. More information about the measurement setup can be found in [32].

6.2.2. Evaluation of diode properties

As explained above, the analysis of the measured C-V curves is based on the assumption of an equivalent circuit. The depletion voltage can be obtained from the intersection of two straight lines fitted to the log-log presentation of the parallel capacitance as function of the voltage in the region near the depletion voltage, see Fig. 6.2.4. Two cases are illustrated: an unirradiated sensor, with a capacitance curve which looks nearly ideal (top), and an irradiated sample (bottom). The measurement of the irradiated samples reveals changes in the C-V shape and the depletion voltage. For very highly irradiated samples these curves are not well understood and the evaluation of the depletion voltage not well defined. From the evaluated depletion voltage it is possible to calculate the effective doping concentration N_{eff} by using Eq. 3.4.5 which results in:

$$|N_{eff}| = \frac{2\epsilon\epsilon_0}{q_0}\frac{V_{dep}}{d^2}. \tag{6.2.4}$$

For highly irradiated diodes, this procedure is not correct and can only be regarded as a very rough estimation.
The effective doping concentration of sensors with depletion voltages higher than the output of the voltage source can be studied from the slope of the an $1/C^2$-plot as function of the voltage (see Eq. 3.4.9). Since DLTS measurements are usually performed in a small region of the total sensor volume, the $1/C^2$-method is widely used to determine the effective doping concentration in the measurement volume.

Setup
The setup for C-V and I-V measurements is installed in a dark box in order to avoid additional photo currents. The setup consists of a SUESS probe station that allows to mount samples on a vacuum chuck. The high voltage is applied to the back plane of the sample, the front contacts are connected via probe needles to the instrument being at low potential. The diode current depends on the temperature, therefore the temperature at the sensor is measured by a *PT100*.

A second option offers the setting of the temperature by a *cold chuck* with *Peltier* cooling. This *cold chuck* is commercially available by ATT SYSTEMS [69] and offers a temperature stability of 0.5 K and a range of -40 to 60 °C. For low temperature measurements, the volume of the dark box is flooded with nitrogen or dry air. A list of instruments used for measurements can be found in App. Tab. A.2.2.

6.3. *Deep Level Transient Spectroscopy*

The *Deep Level Transient Spectroscopy* (DLTS) is the most powerful, sensitive and widely used spectroscopic technique for studying electrically active defects in semiconductors. DLTS allows the direct measurement of fundamental defect parameters i.e. the capture cross section, activation energy and, most important, the concentration. The sensitivity can be as good as 10^{-3} times the doping concentration. Unfortunately, it can only be applied for sensors with $N_t \ll N_{eff,0}$ (N_t = trap concentration, $N_{eff,0}$ = concentration of shallow dopants).
The DLTS method was originally proposed by D. V. LANG [70] and basically measures capacitance transients resulting from the emission of charge carriers after a defect filling pulse. Thus, the technique is called *Capacitance*-DLTS (C-DLTS). Other DLTS techniques make use of current or voltage transients, these options are called *Current*-DLTS (I-DLTS) and *Constant-Capacitance*-DLTS (CC-DLTS).
In this section the main principle of operation and an introduction to the evaluation of measurement data will be given. This will be done very briefly, for further reading please see the PhD theses of S. WEISS [71], M. MOLL [32] and J. STAHL [72].

6.3.1. Principle

If the crystal structure of the semiconductor is damaged or impurities are introduced, defects in the lattice are created. They can either be electrically inactive or electrically active. Electrically active defects may introduce energy levels in the forbidden band gap, which can be either occupied by charge carriers, or which can be empty. Newly created levels in the band gap alter the electrical properties of the semiconductor.
It is possible to take advantage of the de- and recharging behaviour of electrically active defects. The filling and emission of charge carriers of defect levels in the band gap leads to a change of the capacitance. This change of the capacitance due to the emission of charge carriers can be observed as capacitance transients giving information about defect properties, like activation energy for emission, cross sections for capture and emission of electrons or holes and defect concentrations.
D. V. LANG [70] proposes to keep a semiconductor sample under reverse bias, consequently creating a *space charge region* (SCR) free of charges carriers. Then a filling pulse has to be applied in order to introduce charge carriers into the defects. Finally the emission of charge carriers is recorded. As an example Fig. 6.3.1 displays the filling due to the variation of the bias voltage for a level in the upper half (left) or lower half

(right) of the band gap. The procedure can be divided in three recurring parts, carried out during a temperature scan.

Step 1: Initial state

At the beginning the junction is kept under reverse bias (V_R) and the volume is partially depleted. In the constantly depleted region (SCR), the trap is not occupied by electrons. This prepares the sensor in a way that enables the filling process of defects with charge carriers in the following step. The upper left hand side of Fig. 6.3.1 illustrates an electron trap (E_t) in the upper half of the band gap, black circles denote electrons.

Step 2: Filling

In the second step, the defects are filled with charge carriers either electrically by reducing the depletion layer and introducing majority charge carriers or optically by illumination with light from the front- or rear-side. The ionisation of the silicon generates e/h-pairs which are trapped in the defects. The second figure on the left hand side demonstrates the filling with a majority carrier [1] pulse. The pulse is applied by reducing the bias voltage (V_P) for a short time (about 100 ms). Consequently the depleted region is reduced and majority carriers (electrons) are introduced in the previously charge carrier free zone. Because the defect level is now below the FERMI level, the defect is occupied by electrons. The filling time of defect levels depends on the capture rate (see SHOCKLEY-READ-HALL statistics in Sec. 4.4).

Step 3: Transient recording

In a last step, the initial reverse bias V_R is applied. Only charges kept in the defects remain in the volume. They are emitted successively depending on the emission rate of carriers. The capacitance change due to the emission can be recorded as function of time. As presented in Fig. 3 this immediately re-establishes the space charge region. Compared to the initial state, the capacitance is now smaller, due to the compensating negative charges that are trapped in the defect. The depletion region width is now larger than before, due to the compensation. In the following process the trapped charges are emitted into the conduction band. After the emission of all charges the SCR is constant and equal to the initial depth.

Besides the applied bias pulse, that is given as function of measurement time in the lower part of the figure, also the resulting capacitance transient is presented. Here, the capacitance is illustrated during the whole measurement procedure, indicating the three steps. During step 1 the reverse capacitance C_R is constant. In step 2 the reduction of the SCR leads to a strong increase of the capacitance, followed by step 3 which is the capacitance transient. The transient follows the emission rate of the defect level, with a time constant given by the reciprocal emission rate $\tau_n = (e_n)^{-1}$.

The right hand side of Fig. 6.3.1 depicts the analogue measurement process for a hole trap by injection of minority and majority carriers due to a forward current pulse. Since the trap level is located in the lower part of the band gap, only minority carriers (holes) are captured and emitted. The steps are performed analogous to the

[1] Majority carriers for n-type: electrons, for p-type: holes

case described earlier. It should be noted, that due to the capture of holes (positive charge), the capacitance is larger than the initial reverse capacitance C_R. This leads to a transient with a positive polarity, in contrast to the majority carrier filling pulse.

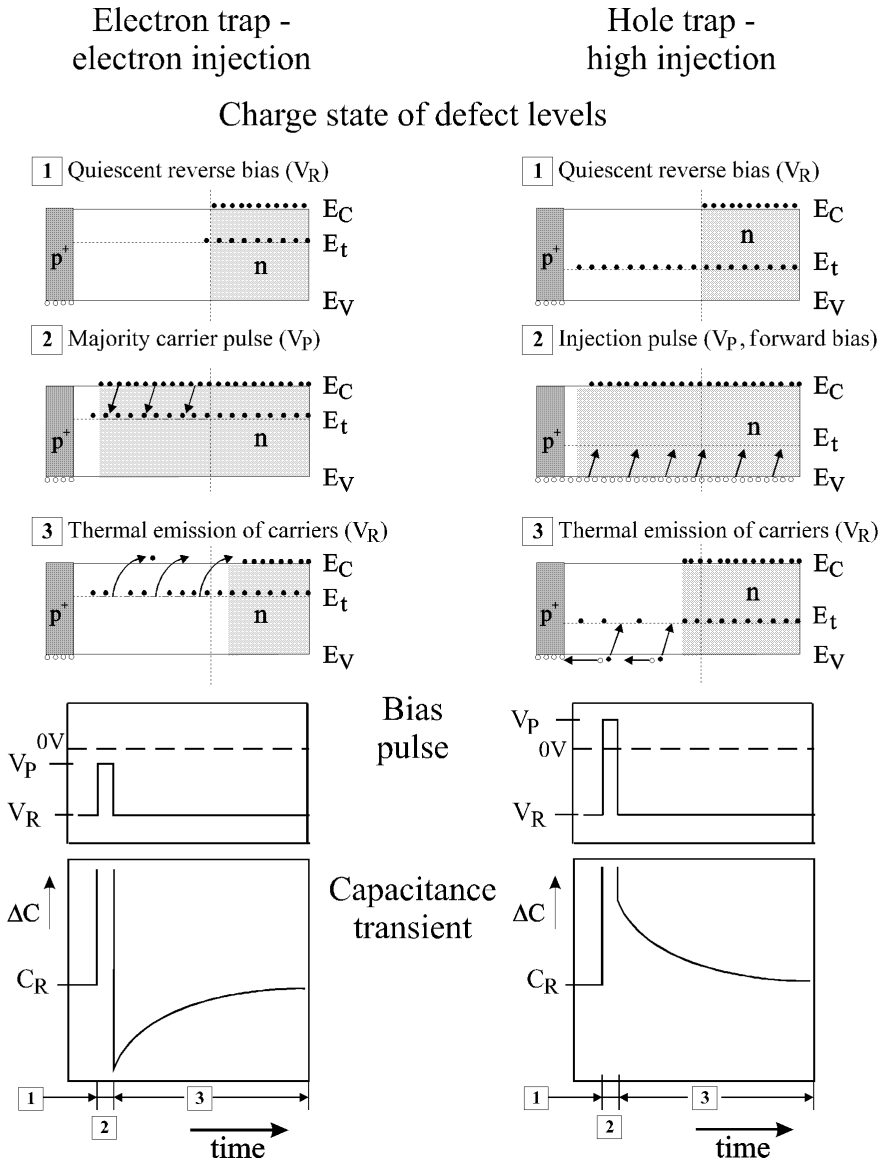

Figure 6.3.1.: Principle of DLTS measurements for *n*-type silicon. The majority carrier injection (left hand side) is obtained by reducing a the reverse bias. Hole injection (right hand side) with a forward bias pulse and the case of high injection (high current density during forward bias). Charge states of defect level, bias pulse and the time dependance of the capacitance are shown. Figure taken from [32].

In theory, this makes a discrimination between electron and hole traps very easy due to the different polarity of the transients. Unfortunately, there are usually both hole and electron traps located in the sensor, therefore the filling with majority and minority carriers leads to a transient with a shape that is composed of both polarities. The filling with charge carriers generated by illumination with light from front and rear side is possible as well.

6.3.2. Determination of defect parameters

Trap concentration
From the capacitance transient of the DLTS measurement it is possible to obtain defect concentrations. The complicated dependence of the space charge distribution as a function of band bending during the DLTS measurement is well described in the PhD thesis of Moll [32]. He describes the space charge region (SCR) as a composition of two parts, on the one hand there is the central part of the SCR, nearly free of charge carriers, on the other hand there is a transition region between the SCR and the neutral bulk with a width λ (see Fig. 6.3.2). From the *Poisson equation* Moll deduces that the amplitude of the capacitance transient is proportional to the defect concentration N_t. Together with a formalism for λ from *Poisson's equation* Moll derives a description of the defect concentration depending on the capacitance measurement:

$$N_t = -2N_{eff,0}\frac{\Delta C_0}{C_R}\left[1-\left(\frac{C_R}{C_P}\right)^2-\frac{2\lambda C_R}{\epsilon\epsilon_0 A}\left(1-\frac{C_R}{C_P}\right)\right]^{-1}, \tag{6.3.1}$$

here $N_{eff,0}$ equals N_{eff}, since the sensors are not irradiated to high fluences and only a small number of defects with impact on the effective doping concentration were created. The trap concentration N_t can be then obtained by the measurement of the reverse capacitance C_R, the capacitance during the filling pulse C_P and the amplitude of the capacitance signal $\Delta C_0 = C(t=0) - C_R$, if $(E_F - E_t)$ is known [32].
The transition region is often neglected and a much simpler equation is used for the determination of the defect concentration:

$$N_t \approx 2N_{eff,0}\frac{\Delta C_0}{C_R}. \tag{6.3.2}$$

Activation energy ΔE_a and cross section $\sigma_{n,p}$
Further defect properties are the activation energy ΔE_a and the capture cross section $\sigma_{n,p}$. Moll describes the extraction of these parameters very elaborately. He notes [32]:

> In the case of $N_t \ll N_{eff,0}$ the capacitance transient follows the emission for electrons
>
> $$\Delta C(t) \propto n_t(t) = N_t \exp(-e_n t). \tag{6.3.3}$$

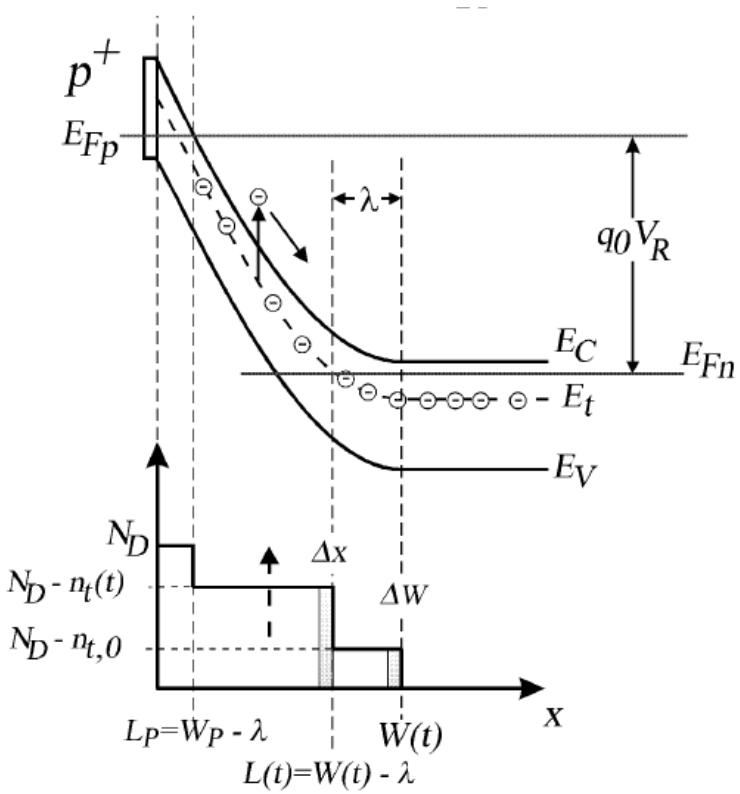

Figure 6.3.2.: Space charge distribution corresponding to the band bending for a p^+n-junction during step 3 of the DLTS measurement procedure. Figure taken from [32].

Thus the characteristic time constant of the transient τ_n is the reciprocal emission coefficient ($\tau_n^{-1} = e_n$). With the help of Eq. 3.2.4 the measured temperature dependence of τ_n can be used to establish an *Arrhenius-plot*

$$\ln(\tau_n c_n N_C X_n) = \frac{\Delta E_a}{k_B T}. \tag{6.3.4}$$

However, the entropy factor X_n and the temperature dependence of the capture coefficient $c_n(T)$ are often not known. In such cases X_n is set to 1 and the capture coefficient to $c_n = \sigma_n v_{th,n}$ with a temperature independent cross section σ_n. The *Arrhenius-plot* is then given by (see Fig. 6.3.4)

$$\ln(\tau_n v_{th,n} N_C) = -\ln(\sigma_n + \frac{\Delta E_a}{k_B T}). \tag{6.3.5}$$

The cross section σ_n can be deduced from the intercept with the ordinate and the activation energy ΔE_a from the slope.

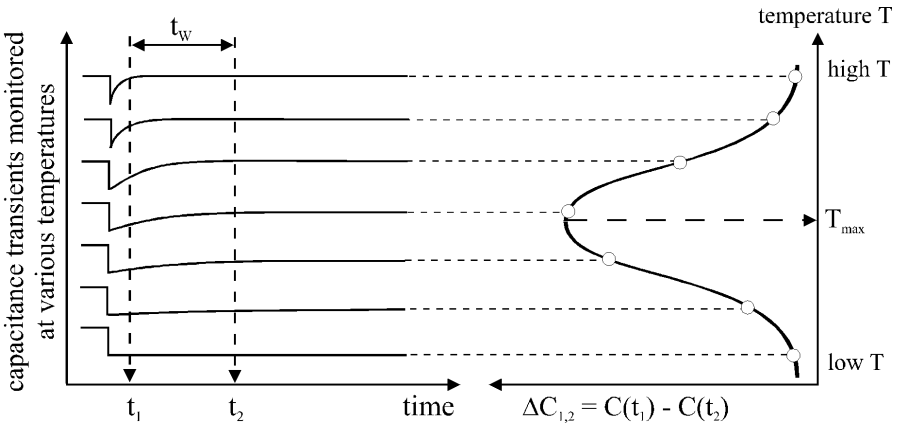

Figure 6.3.3.: *Double box-car* method after LANG [70]. The left hand side illustrates capacitance transients as function of various temperatures, the corresponding DLTS signal resulting from a difference of two capacitance values in a given time window t_w is depicted in the right hand side (description see text). Figure taken from [70].

For holes the corresponding parameters have to be introduced.

Transient analysis
The capacitance transients follow an exponential behaviour given by:

$$C(t) = \Delta C_0 \times \exp\left(-\frac{t+t_0}{\tau_e}\right) + C_R. \tag{6.3.6}$$

Here, t_0 denotes an additional delay time that is set in order to compensate for the pulse overload recovery of the bridge. In practice, this value depends on the capacitance meter and the time window (t_w), in which the transient was recorded. In this work, the smallest time window in use is $t_w = 20$ ms, and the bridge recovery time is set to $t_0 = 0.5$ ms.
The simplest method to analyse capacitance transients is given by the *double box-car* method, which originates from LANG [70]. The principle of this method is illustrated in Fig. 6.3.3. In a certain time window $t_w = \{t_1 < t < t_2\}$ a capacitance difference is taken between $C(t_1)$ and $C(t_2)$ resulting in $\Delta C_{1,2} = C(t_1) - C(t_2)$.
Since the capacitance transients were measured during a temperature scan, the transients depend on the temperature during the measurement. A plot of $\Delta C_{1,2}$ as a function of the measurement temperature reveals a distribution as depicted in the right hand side of Fig. 6.3.3.
At low temperatures the emission from a defect is too slow to be measured and results in $\Delta C_{1,2} \approx 0$, while at high temperatures the emission is too fast to observe a capacitance difference. At the temperature where the emission time constant τ_n fits to the time window a maximum can be observed giving $\tau_n(T_{max})$. The capacitance obtained

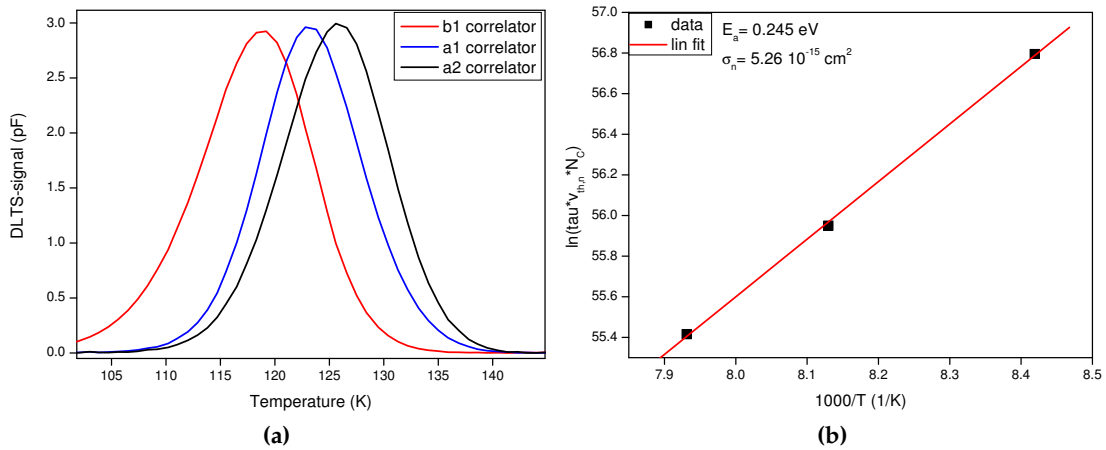

Figure 6.3.4.: DLTS spectra for different time constants τ_n illustrating the temperature dependence (a). Corresponding *Arrhenius-plot* (b). Measurement condition: $V_R = -10$ V, $V_P = -0.1$ V, $t_w = 200$ ms.

at that temperature can be evaluated via Eq. 6.3.2 and gives the defect concentration. Repeating the measurement with different time windows will lead to a temperature dependent shift of the emission time constant at the maximum temperature $\tau_n(T_{max})$. The time constants $\tau_{n,i}(T_{max,i})$ can be used to create *Arrhenius-plot*. Unfortunately, this principle is very prone to disturbances during the measurement cycle as it depends only on the two measurement points $C(t_1)$ and $C(t_2)$. More sophisticated solutions use the full transient to obtain more precise results (further information can be found in [32,73]).
In this work the transient is folded with *correlator* functions, e.g. a sine. The resulting signal of the folded transient depends on the temperature, as it was observed for the *double box-car* method. In total 18 correlator functions[2] are used in the DLTS program for three different time windows (typically: $t_{w1} = 20$ ms, $t_{w2} = 200$ ms, $t_{w3} = 2$ s) resulting in 54 different *correlator* signals that can be used for evaluations of the defect concentrations and *Arrhenius-plot* (see Fig. 6.3.4). The evaluation of the maxima of the correlator signals is called *maxima evaluation* in this work. With this technique, $\tau_n(T_{max})$ can only be calculated numerically, as explained in [71]. A common way of illustrating the DLTS spectra is given by the b_1-*correlator* signal for the time window $t_{w2} = 200$ ms. This procedure of measuring and analysing is offered by the DLTS software, a commercially available system from PhysTech [74]. The DLTS software [75] was developed by S. Weiss during his PhD-work [71] where also the main principle of operation is extensively explained. Further brief information about the correlator functions can be found in the PhD thesis of Moll [32], a complete description of the DLTS software and the extend of operations can be found in the program manual [76].

[2] A description of the different *correlator functions* can be found in [32,71]

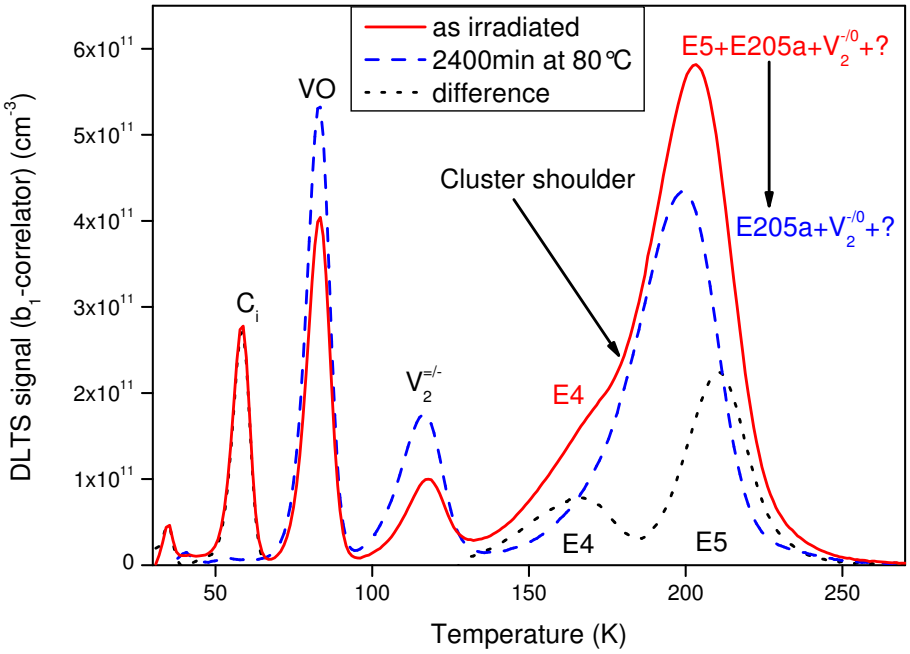

Figure 6.3.5.: Evaluation of the concentration of the $E4$ and $E5$ defects as result of the difference between the DLTS spectra directly after irradiation and after annealing of 2400 minutes at 80 °C. Measurement condition: $V_R = -10$ V, $V_P = -0.1$ V, $t_w = 200$ ms.

Evaluation of DLTS spectra

The analysis of DLTS measurements is usually done by the *maxima evaluation* method. In some cases the application of this procedure is not possible, for example in the case of overlapping signals from nearby defect levels. In this work the *maxima evaluation* method was only applied for nicely separated defect peaks. In particular the cluster related defects $E4/E5$ and $E205a$ overlap with the V_2-peak in the so-called *cluster shoulder* as illustrated in Fig. 6.3.5 (red line). Moreover, transitions between two neighboring peaks can be reliably simulated. In order to be able to evaluate those defects, other techniques are used. The extraction of the defect concentrations is possible by a simulation of the DLTS signal of the overlapping peaks by a manual fit. However, for this procedure it is vital to know the defect properties (capture cross section $\sigma_{n,p}$ and activation Energy ΔE_a). The fitting procedure is explained in [49].

Another possibility to separate overlapping DLTS peaks make use of the difference of two spectra recorded after annealing stages of the same sample and measurement conditions. In this work the technique is called *difference spectra analysis*. Fig. 6.3.5 illustrates the principle of obtaining single defect peaks ($E4$ and $E5$) from a difference of two DLTS spectra. The annealing of the defect levels occurs between the steps directly after irradiation (straight red line) and 2400 minutes at 80 °C (blue dashed line). The difference spectra is presented by the black dotted line. Naturally, this technique can

only be applied if the overlapping defects anneal out at different temperatures. The analyses of the concentration of the resulting difference spectrum has to be analysed by the *maxima evaluation* method or by simulations.

6.3.3. DLTS setup

The DLTS measurements are usually performed in a temperature range between 300 K and 25 K corresponding to the equivalent range of ionisation energies of defects in the band gap of silicon. In order to reach 25 K, the sample has to be cooled by a close-cycle helium refrigerator from CTI-Cryogenics (Model 22C, 50 Hz) in an evacuated cryostat chamber. Evacuation is performed by a two-staged Pfeiffer Vacuum Pump (Model HiP Pace 80, PM P03 942). Inside the cryostat chamber a cooling pipe is connected to the cold stage, as illustrated in Fig. 6.3.6. This cold stage is connected via sapphire rods to the hot stage made from copper in order to grant good thermal contact. The original reason for this construction was to allow higher temperatures at the hot stage than the limit for the cold stage. Inside the hot stage, a 30 Ω resistor is used as heater with a maximum power of 30 Watts. This construction allows heating rates of 1 K/s.
An upright sample holder is mounted on the hot stage. Silicon samples have to be glued on ceramic boards that can be fixed on the sample holder. A guiding bar with clamps fixes the samples to the back plate. Three pins (possibility to expand up to five) contact the pads of the ceramic board. One temperature sensor is mounted on the rear side of the holder, a second one on the cold stage. Measurement cables for the sample contacts and for the temperature measurement are wrapped around the cooling rod to prevent from heating of the ceramic board at low temperatures. A radiation shield is installed in order to prevent thermal radiation. An illumination with red lasers mounted on the outside of the cryostat chamber is provided by holes in the sample holder and in the radiation shield to allow the illumination from front and rear side. The temperature of the sample holder is measured and controlled via a LakeShore 340 temperature controller.
The FT 1030 *Deep-Level Transient Spectroscopy* system used for this work is a commercially available system from PhysTech [74]. The measurement of C-V and I-V is possible with this setup at cryogenic temperatures. Details about the hardware of the system can be found in [76].

6.4. *Thermally Stimulated Current* technique

The *Thermally Stimulated Current* technique (TSC) is a microscopic measurement technique, which provides information about the concentration of defects in the semiconductor material. In contrast to the DLTS method, it is applicable for highly irradiated sensors because it is not limited to small defect concentrations by the requirement of $N_t \ll N_{eff,0}$. The principle of operation is very simple (for details see [31,32,77,78])

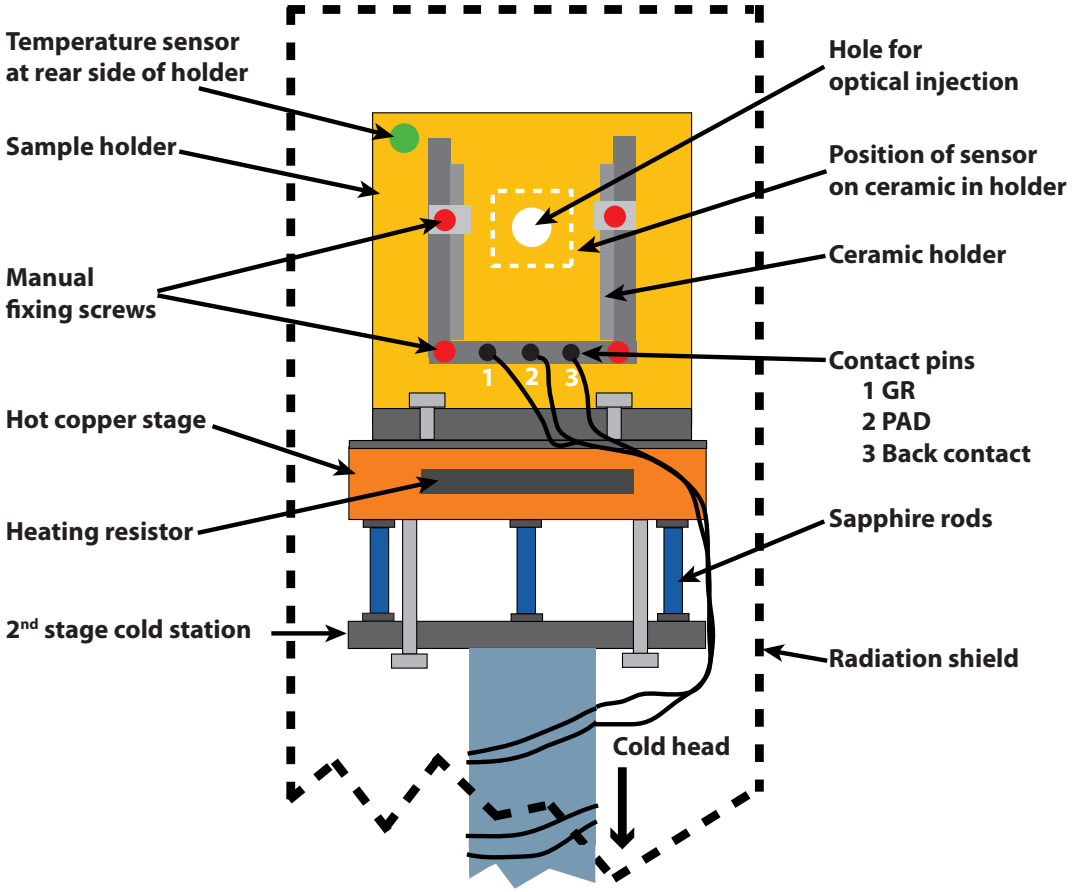

Figure 6.3.6.: Schematic presentation of hot stage and sample holder of the DLTS setup. The presented part of the setup is mounted inside a cryostat chamber. For description see text.

and will be explained in the following. However, the evaluation of the measured data is not as straightforward and requires some effort.

6.4.1. TSC principle

The principle of operation consists of three steps, which are performed during each measurement. The individual implementation of each step may vary for different measurement types.

Step 1: Cooling
As presented in Fig. 6.4.1 (a) a diode is cooled down to low temperatures, either

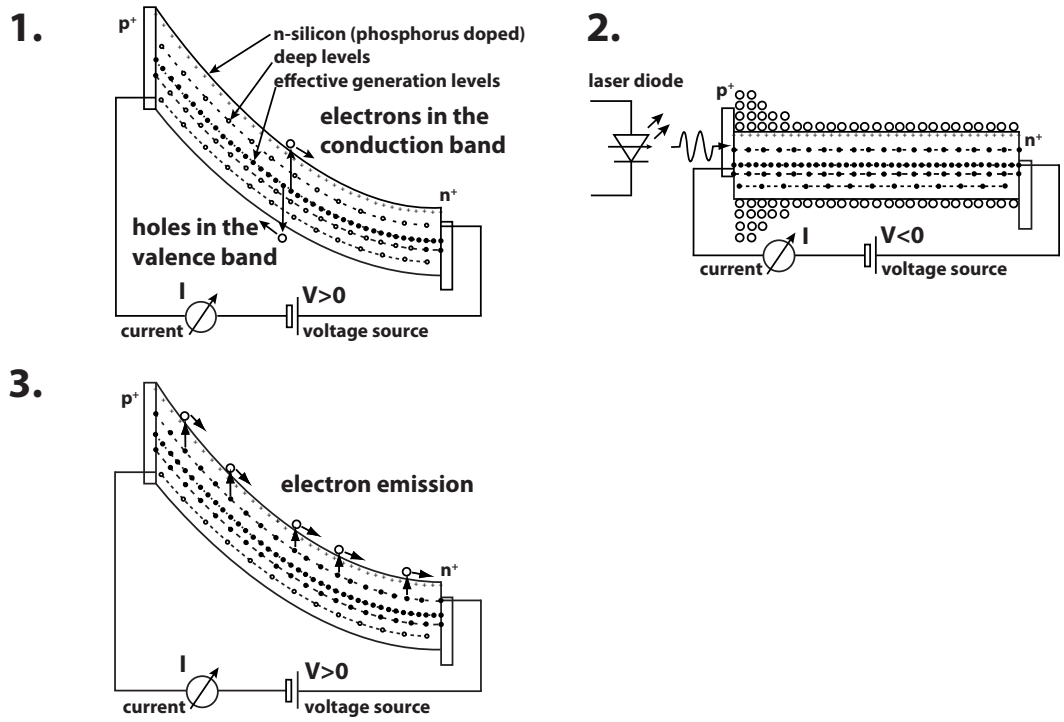

Figure 6.4.1.: Principle of TSC operation based on band structure, taken from [31] and modified.
1. Cooling
Cooling down under reverse bias ($V_{bias} > 0$). Due to the applied bias voltage the sensor is depleted.

2. Filling
Filling of charge carriers either by applied forward bias voltage ($V_{bias} < 0$) or illumination by light ($V_{bias} > 0$).

3. Heating and recording
Recording of TSC spectra with applied bias voltage ($V_{bias} > 0$) during the heating with constant heating rate. Charge carriers are emitted into the conduction band at a temperature corresponding to the levels energy in the band gap.

under reverse bias or at zero bias. Cooling under reverse bias (sufficiently high for full depletion) keeps the traps empty of charge carriers, whereas for cooling at zero bias, majority carriers are trapped in the defects.

Step 2: Filling

At a temperature according to the planned measurement, the defects are filled with charge carriers, see Fig 6.4.1 (b). Depending on the measurement type it is possible to fill the defects either electrically with majority carriers (zero bias), with majority and minority carriers by injection of a forward current, or with majority or minority carriers created by injection of light. According to the type of charge carriers and the filling procedure step 1 has to be adapted.

The extraction of defect concentrations is usually the main goal of these measurements. Therefore, it is vital to fill all defects inside the volume. For that reason it is necessary to note that the electrical filling with majority carriers by applying 0 V or filling during cooling only works properly for low fluences, essentially as long as enough majority carriers are present to fill the traps. On the contrary, the filling with forward current can always be applied. Using this filling technique requires a sufficient high current and filling time to fill all defects.

Filling with light is performed when absolute defect concentrations are not required, but the defect type should be detemined. Illumination of either front or rear side with light with a short absorption length (eg. green laser with a wavelength of 530 nm) ionises the silicon and creates e/h-pairs directly underneath one of the electrodes. Under the influence of an applied electrical field only one type of charge carriers moves through the sensor volume and can be trapped by defects, thus the type of charge carrier is defined.

Unfortunately, the filling with light is usually performed at temperatures below 30 K, where the absorption length of the light source is not known anymore. The penetration depth increases at low temperatures. As a result, the filling of either electrons or holes is superimposed with the other type of charge carriers.

The filling with light cannot serve for a determination of defect concentrations, because the light-cone used in this setup does not illuminate the hole sensor homogeneously. Therefore the measured volume is not well-defined. As long as those measurements are used only qualitatively, they may reveal the location of the defect level in the lower or in the upper part of the band gap.

Step 3: Heating and recording

After the filling process, a bias voltage and constant heating rate is applied to the sensor, providing the thermal energy to stimulate the emission of trapped charges from defect potentials, illustrated in Fig. 6.4.1 (c). A characteristic TSC-current peak from the emission of charge carriers can be observed as function of the temperature.

6.4.2. Evaluation of defect concentrations

The evaluation of defect concentrations and parameters is nicely described in the PhD thesis of M. Moll [32]. This compilation of the most important equations for the evaluation is written on the basis of his excerpt about the evaluation of TSC parameters.
The defect concentration inside a volume with the depletion depth of $W(t)$ depending on the heating time, if the volume is not fully depleted, is given by the total current during the TSC measurement [79].

$$I_{TSC}(t) = q_0 A \int_0^{W(t)} \sum_{all\ defects} \frac{e_n(t)n_t(t) + e_p(t)p_t(t)}{2} \mathrm{d}t \tag{6.4.1}$$

For a temperature scan with a heating rate $\beta(t) = \mathrm{d}T/\mathrm{d}t$ also the emission rates e_n and e_p are time dependent. Considering only an electron trap in a fully depleted volume ($W(t)$) filled by electrons (at T_0), the TSC current is given by:

$$I_{TSC}(t) = \frac{q_0 A d}{2} e_n(t) n_t(t) \tag{6.4.2}$$

and $n_t(t)$ given by:

$$n_t(t) = n_{t,0} \exp\left(-\int_0^t e_n(t')\mathrm{d}t'\right), \tag{6.4.3}$$

where $n_{t,0}$ is the fraction of defects occupied by charge carriers during the filling process. With the substitution of t by $T = T_0 + \beta(t)t$ it follows:

$$I_{TSC}(T) = \frac{q_0 A d}{2} e_n(T) n_{t,0} \exp\left(-\int_{T_0}^T \frac{1}{\beta(T')} e_n(T')\mathrm{d}T'\right), \tag{6.4.4}$$

where T_0 is the starting temperature, $\beta(t)$ is in this work a constant heating rate of β =0.183 K/s and $n_{t,0} = N_t$ if fully occupied. The concentration of the filled defects can then be calculated by the integration over the TSC peak $Q_t = \int \mathrm{d}t\ I_{TSC}(t)$

$$n_{t,0} = 2\frac{Q_t}{q_0 A W}. \tag{6.4.5}$$

However, this method leads to an inaccurate evaluation of defect concentrations for defects with field-enhanced emission characteristic. Such defects are charged at room temperature and contribute to the effective doping concentration of the sensor.
Pintilie et al. [55] describe a method for extracting defect concentrations and properties also for such *Coulombic* centres. The dependence of the emission rates on the electric field and the depth inside the diode volume can be observed by TSC measurements by the three dimensional *Poole-Frenkel* effect (3D-PF), exhibiting a broadening, asymmetry and temperature shift of the peak depending on the applied

bias voltage.
Assuming a linear field dependence of the electric field inside the diode then the local electric field for an n-type diode can be described by the expression

$$F(x) = q_0 \frac{N_{eff}(d-x)}{\epsilon_0 \epsilon} + \frac{V_{bias} - V_{dep}}{d} \tag{6.4.6}$$

if the applied voltage is high enough to totally deplete the diode. Here, x is the distance from the p^+ side, d is the thickness of the diode, V_{bias} the applied reverse bias during the measurement and V_{dep} the depletion voltage. V_{dep} is therefore also the minimum applied bias during the measurement, which depletes the sensor at room temperature. Nevertheless, at deep temperatures and for highly irradiated samples the N_{eff} may change due to the change of the occupation at low temperatures. Thus, using V_{dep} as applied reverse bias may not deplete the whole sensor.
With the help of Eq. 6.4.6 the emission rate of a *Coulombic* donor centre in an electric field is given by

$$e_n^{PF} = e_n^0 \left(\frac{1}{\gamma^2} \right) [e^\gamma (\gamma - 1) - 1] + \frac{1}{2}, \tag{6.4.7}$$

with e_n^{PF}/e_n^0 are the emission rates in the presence/absence of an electric field and γ is given by

$$\gamma = \left(\frac{q_0 F}{\pi \epsilon_0 \epsilon_r} \right)^{1/2} \frac{q_0}{k_B T}. \tag{6.4.8}$$

Using Eq. 6.4.7 and Eq. 6.4.8 the formula for the total current during the TSC measurement (Eq. 6.4.4) can be modified to evaluate defect levels with field enhanced emission rates

$$I_{TSC}^{PF}(T) = \frac{q_0 A N_t}{2} \int_0^w \left\{ e_n^{PF}(x,T) \times \exp \left[\frac{1}{\beta} \int_{T_0}^T e_n^{PF}(x,T) \mathrm{d}T \right] \right\} \mathrm{d}x. \tag{6.4.9}$$

For *Coulombic* acceptor centres the calculation can be performed in an analogous way.

6.4.3. Setup

The TSC measurements are usually performed in a temperature range between 300 K and 5 K. Although temperatures around 5 K are used, very shallow defect levels (as phosphorus or boron) are not observed. In order to reach 5 K, the sample has to be cooled by a close-cycle helium refrigerator from Sumito heavy industries Ltd. (CKW-21) in an evacuated cryostat chamber with a cold head also provided by Sumito heavy industries Ltd. (model RDK-205D). Evacuation is performed by a two-staged Pfeiffer Vacuum Pump (model TMH 071P). Inside the cryostat chamber the cold head is connected to a sample holder via a hot stage. Instead of Sapphire rods, as seen in Fig. 6.3.6 illustration the basic principle of the DLTS setup, the connection in the TSC setup is done via stainless steel rods. Inside the hot stage, a

resistor with 30 Ω is used as heater with a maximum power of 30 Watts.
The sample holder is similar to the one of the DLTS cryostat. In the TSC setup three temperature sensors are installed instead of two in the DLTS cryostat. One temperature sensor is mounted on the rear side of the holder, a second sensor below the hot stage and a third sensor at the cold stage. Measurement cables for the sample contacts and for the temperature measurement are wrapped around the cooling rod to prevent for heating of the ceramic at low temperatures. The temperature is operated via a LakeShore 340 temperature controller. Voltage supply and current measurement is provided by a Keithley 487 Picoamperemeter/Voltage source.

6.5. Error estimation

The statistical error for measurements performed in this work was discussed in detail in the PhD thesis of H. Feick [31]. Measurement errors of the effective doping concentration $N_{eff,0}$ as extracted from the $1/C^2$ representation, the concentration of traps N_t, the activation energy of defects in the band gap ΔE_a and the capture cross sections for electrons and holes $\sigma_{n,p}$ were discussed in detail in the PhD theses of H. Feick, M. Moll and M. Kuhnke [31,32,80].
The main contribution to the error of $N_{eff,0}$ in DLTS measurements results from the lateral extension of the depletion zone. $N_{eff,0}$ is estimated by a linear regression with two points to the slope of the $1/C^2$ plot of Eq. 3.4.4. $1/C^2$ can be calculated via Eq. 3.4.9 from the measurement of the C-V characteristic in a defined volume. The lateral extension of the depletion zone leads to an uncertainty in the volume definition and thus to a reduction of the accuracy of the defect concentration. The error was estimated to be around 20 % [80] in DLTS. However, for a linear regression with a higher number of data points, the error will decrease.
The sensors used in this work were irradiated with low doses compared to sensors used for example in TCT measurement. Hence, at room temperature no frequency dependency due to the capture and emission of defects is observed. However, at cryogenic temperatures some of the irradiation induced defects become charged and change the effective doping concentration and thus the capacitance. A reliable use of the DLTS technique is therefore only possible for sensors damaged by a concentration of defects that is small compared to the original doping concentration ($N_t \ll N_{eff,0}$ (N_t = trap concentration, $N_{eff,0}$ = concentration of shallow dopants). This effect sets the upper limit for the reliable applicability of this method.
The error in the trap concentration N_t in DLTS measurements obtained from Eq. 6.3.1 or the simpler approximation of Eq. 6.3.2

$$N_t \approx 2N_{eff,0}\frac{\Delta C_0}{C_R}$$

consists of the error of $N_{eff,0}$, the accuracy of the capacitance measurements in ΔC_0 and C_R, the lateral extension of the depletion zone and the evaluation of the capacitance

transients. The accuracy of the capacitance meter is about 0.1 % [81] but a high accuracy of ΔC_0 and C_R in different measurement ranges is obtained by the calibration in the range with a *compensation* capacitance. That leads to an overall error for C_R of 1-5 % resulting from the *compensation* capacitance. The error of ΔC_0 is dominated by the evaluation of the transient with the *correlator functions* and the *maxima analysis* and is estimated to be around 10 % [32].
Errors for ΔE_a and $\sigma_{n,p}$ from *Arrhenius-plots* are dominated by the accuracy of the temperature measurement as well as the evaluation by linear regression. The error for the activation energy ΔE_a is calculated to 3-4 % and 10-100 times larger for the capture cross sections for electrons and holes $\sigma_{n,p}$ [80]. This error decreases the more points in the linear regression for the *Arrhenius-plots* are used. The direct measurement of the activation energy ΔE_a and the capture cross sections for electrons and holes $\sigma_{n,p}$ is dominated by the same error as for the capacitance that was already discussed above.
The error of the concentration of defect levels N_t as measured by TSC consists of the error in the current measurement, the temperature measurement and the evaluation. The error of the current measurement and temperature measurements is very small compared to the error due to the evaluation. Here an uncertainty in the change of the N_{eff} as function of temperature in addition to the error of the fit results in an error that is estimated to be around 20 %.
The absolute error for values obtained by DLTS and TSC measurements seems to be very high, however, the relative error is much smaller, since a high contribution is due to systematic uncertainties.

7. Important Defects in Silicon

Due to the growth techniques, a small concentration of impurities is always present in silicon, even if it is material of high purity. The irradiation mainly creates *Frenkel-pairs* as illustrated in Fig. 4.1.1 (a). They either recombine instantly or separate into vacancies (V) and interstitials (I) which are mobile and migrate through the lattice. These irradiation induced defects can form complexes with the present impurities. The newly formed defects are responsible for the degradation of sensor properties after irradiation.
One approach in order to obtain radiation hard silicon as explained in Sec. 2.3 is material or defect engineering. Impurities which are supposed to have positive impact on properties and radiation hardness are intentionally introduced in the material. In the case of doping, e.g. phosphorus or boron are added in order to reduce the resistivity of the material.
Today's knowledge about radiation induced defects considers oxygen as beneficial for the radiation hardness [4]. Oxygen can be introduced rather easily during the growth process and additional oxygen enrichment treatments. Also hydrogen seems to be a good candidate for the reduction of sensor degradation, but the introduction of this impurity is not as easy as for oxygen. Here some progress was achieved in recent years, due to implantation. However, today's methods do not provide sufficient quality (homogeneity, introduction of further dislocations and stacking faults), which requires further investigation.

7.1. Material Defects

All materials studied in this work are considered to be highly pure. However, depending on the type of growth process a small concentration of defects can be found in the silicon materials. A description of the most important growth techniques and the introduction of impurities is given in this works' Sec. 2.2. The most prominent impurities in highly pure silicon are oxygen, carbon and doping atoms, like phosphorus or boron. A brief review of these impurities is given in the following Section. A detailed compilation of material defects and irradiation induced defects can be found in the PhD thesis of Stahl [72].

7.1.1. Oxygen

Oxygen is the main impurity incorporated in the investigated materials (Epi, MCz and FZ). It exists as oxygen interstitial (O_i)[1] creating a pseudo molecule (Si_i-O-Si_i) in the lattice. Oxygen locally increases the lattice spacing, leading to lattice stress [6]. On the other hand, the highest oxygen concentration in the used materials is found in oxygen enriched Epi (Epi-Do) with [O]$= 6 \times 10^{17}$ cm^{-3}. In comparison to Epi-St material, no influence of the increased oxygen concentration on the diode properties could be observed so far.
The combination of two oxygen interstitials creates oxygen dimers (O_{2i}). They are electrically inactive and their concentration can therefore not be detected by DLTS or TSC measurements. Though, the oxygen dimer can be observed by IR-*spectroscopy* [56], as it gives rise to local vibrational modes. It is suggested by HÖNNIGER [82], that the concentration of the I_2O-complex detected by DLTS gives information about the concentration of oxygen dimers. The activation energy for diffusion of O_i is E_a =2.5 eV while the diffusion energy for O_{2i} is E_a =1.5 eV. This leads to the assumption that oxygen dimers are able to diffuse at lower temperatures through the lattice than O_i. It seems likely, that oxygen dimers play a key role for the formation of *Thermal Donors* (TD) [6].
Thermal Donors
Thermal Donors (TD) are oxygen related defects, formed in oxygen rich material within a temperature range of 300°C - 550°C. Oxygen is a group 16 atom that can act as donor-like in some compound semiconductors, although oxygen interstitials are usually electronically inactive. Several types of TD have been discovered, *Thermal Double Donors* (TDD), shallow *Thermal Donors* (STD) and *New Donors* (ND). The formation of either of these donors depend on the oxygen concentration of the material and the heat treatment. For example annealing at high temperatures (450 °C) increases the concentration of *Thermal Double Donors* (TDD) in oxygen rich material. In order to avoid the formation of *Thermal Donors* in oxygen rich silicon a heat treatment at 800 °C is performed during the production process followed by a rapid cooling down to temperatures below 300 °C. This treatment is often called "thermal clean or kill" process. Further information about TDs can be found in [6].

7.1.2. Carbon

Carbon in silicon is present as substitutional (C_s) or less often as interstitial (C_i). C_s is electrically inactive and does not influence the electrical properties of silicon. It forms C_i via the *Watkins replacement mechanism* ($Si_i + C_s \rightarrow Si_s + C_i$). C_i is mobile at room temperature and forms instantly higher order defects like C_iC_s or C_iO_i.

[1] The index $_i$ denotes interstitials while $_s$ denotes substitutional

7.1.3. Phosphorus

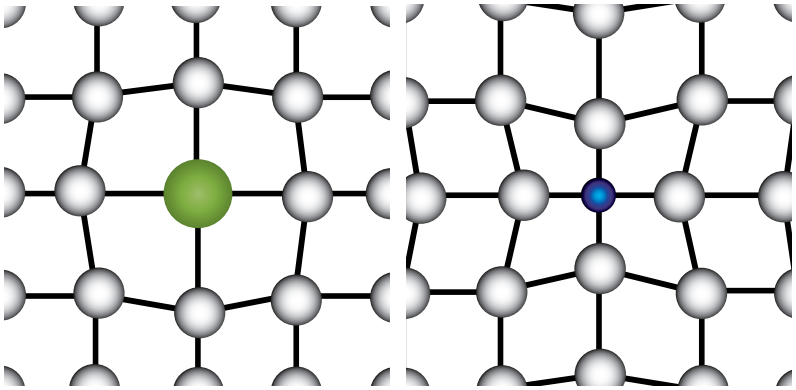

Figure 7.1.1.: Silicon lattice doped with phosphorus (a) and boron (b) illustration of the lattice distortion.

As a group 15 atom, phosphorus has five electrons in the outer shell and thus acts as a donor in silicon. It is the main dopant atom for *n*-type materials. Due to the fact that the size of the phosphorus atom is very similar to the silicon atom it deforms the silicon lattice only a little (see schematically in Fig. 7.1.1 (a)). The other dopant atoms used for this works' materials are boron for *p*-type silicon and antimony for very low resistivity *n*-type MCz substrate. Usually phosphorus is *built-in* as a substitutional atom, replacing silicon atoms. Furthermore phosphorus can form complexes with other defects or impurities for example carbon and form stable centres like the vacancy-phosphorus-centre (VP).

7.1.4. Boron

As a group 13 atom, boron has three electrons in the outer shell and thus acts as an acceptor. It is the main dopant atom for *p*-type materials. Due to the fact that the size of the boron atom is small compared to the silicon atom it deforms the silicon lattice (see schematically in Fig. 7.1.1 (b)).

7.1.5. Hydrogen

Hydrogen is commonly used to passivate dangling bonds at the SiO_2-Si interface during the processing. It is assumed that hydrogen also passivates other dangling bonds inside the silicon crystal [83]. In a first try, hydrogen was incorporated into silicon with the aim to reduce the damage due to multi-vacancies and cluster regions. Unfortunately, it is not easy to introduce this element into the silicon and keep it there. Due to its atomic properties it starts to diffuse. Latest results from measurements

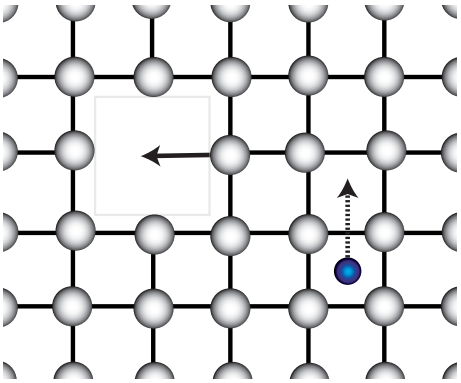

Figure 7.2.1.: Schematic process of vacancy and impurity migration.

performed at the University of Hamburg did not result in a sufficient quality of homogeneity and revealed further introduction of dislocations and stacking faults due to an implantation process.

7.2. Radiation induced defects

The irradiation mainly creates *Frenkel-pairs* as illustrated in Fig. 4.1.1 (a). They either recombine instantly or create vacancies (V) and interstitials (I). These irradiation induced defects can form complexes with the present impurities due to migration as illustrated in Fig. 7.2.1. Some of the resulting defects are responsible for the degradation of sensor properties after irradiation. Here a short survey of the main radiation induced defects is given, a detailed compilation can be found in the PhD thesis of Stahl [72].

7.2.1. Vacancy related point defects

Vacancies (and the corresponding interstitials) are the main result of *non ionising energy loss* in the silicon lattice after irradiation. The number of vacancies in a defined volume created during irradiation depends on the particle type, particle energy and dose, as explained in Sec. 4.1.

7.2.1.1. The single vacancy

The single vacancy has five different charge states $V^{++}, V^{+}, V^{0}, V^{-}, V^{=}$, here $^{+}$ and $^{-}$ denote the charge state of a defect. The single vacancy is highly mobile at room temperature and all single vacancies are trapped by other vacancies, forming the di-vacancy (V_2) or by material impurities, forming complexes like VO or VP.

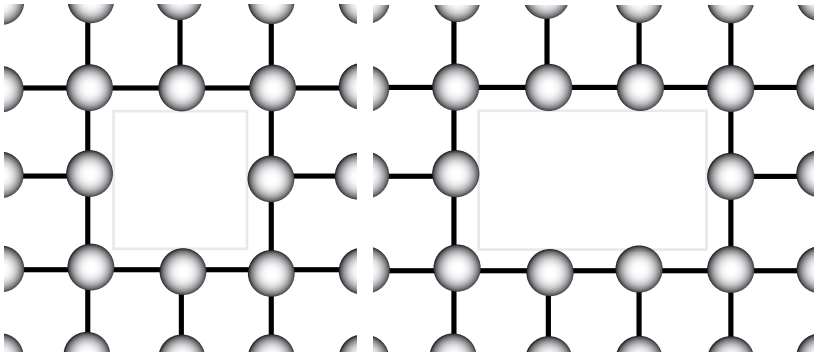

Figure 7.2.2.: Schematic illustration of the vacancy defect V (a) and the di-vacancy defect V_2 (b) in the silicon lattice.

7.2.1.2. The di-vacancy

The di-vacancy (V_2) consists of two single vacancies. V_2 has three levels in the forbidden band gap, two acceptor states $V_2^{=/-}$ at $E_C - 0.22$ eV and $V^{-/0}$ at $E_C - 0.42$ eV and a donor state $V_2^{+/0}$ at $E_V + 0.2$ eV [72]. The defect is created directly through irradiation or by formation of two single vacancies. Whether V_2 can be created directly depends on the energy of the impinging particle. The di-vacancy is not known to have a strong impact on the electrical properties of silicon sensors.
The main reaction channel of V_2 is via $V_2 + O_i \rightarrow V_2O$ via diffusion of V_2. Oxygen has an activation energy for migration of $E_a = 2.5$ eV (see Sec. 7.1.1) and stays fixed to its lattice site. For that reason, the temperature at which the annealing starts depends strongly on the oxygen concentration of the material. The annealing of V_2 starts at 250 °C (via $V_2 + O_i \rightarrow V_2O$) in oxygen rich material. On the other hand annealing starts at around 350 °C via dissociation in oxygen lean material.

7.2.1.3. The multi-vacancies

Multi-vacancy defects (V_n) like the V_3 or V_4 are created after fast hadron irradiation and high energy electron irradiation. Multi-vacancies only appear in clusters, whose structure is still relatively unknown. Some of the multi-vacancies can be tracked by DLTS measurements. They are the so-called *cluster related defects*[2] like $E5$ and $E205a$. Fig. 7.2.3 illustrates a simulation performed by Huthinnen [36] on the generation of the V_2 and V_3 defects after 10 MeV proton (left), 24 GeV/c proton (middle) and 1 MeV neutron (right) irradiation. The plots correspond exactly to the initial vacancy concentration of Fig. 4.1.4 and have the same fluence and depth scaling. The identification and assignment of V_3 to measurements performed in this work will

[2]Multi-interstitial are *cluster related defects* as well, but they were not identified so far.

be explained later in Sec. 8.5. Also the impact of multi-vacancies on detector properties

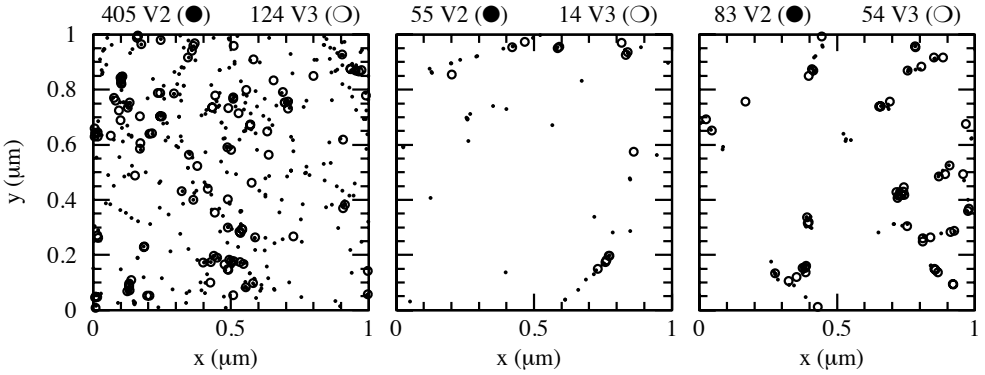

Figure 7.2.3.: Final distributionof V_2 (dots) and V_3 (circles) defects after 10 MeV proton (left), 24 GeV/c proton (middle) and 1 MeV neutron (right) irradiation. The plots correspond exactly to the initial vacancy concentration of Fig. 4.1.4 and have the same fluence and depth scaling. Taken from [36].

is not fully known. A detailed study about the impact of the tri-vacancy on sensor properties is given in chapter 8.

7.2.1.4. The *E*-centre

The *E*-centre (VP) consists of a vacancy coupling with a phosphorus dopant atom (see Fig. 7.2.4 (a)). The VP-complex does not act as donor anymore, but gives rise to an acceptor level at $E_C - 0.456$ eV [84]. Due to an overlap of the VP level with the levels of the cluster defects, it is not easy to be observed by DLTS and impossible by TSC. However, this mechanism can be described as *donor-removal*, as interpreted from macroscopic measurements of the fluence dependence of the effective doping concentration at low fluences. The microscopical observation suggests an annealing temperature of about 150°C.

7.2.1.5. The *A*-centre

Immobile oxygen atoms are able to catch mobile vacancies and form the *A*-centre (VO_i) via the process $V + O_i \rightarrow VO_i$ (see Fig. 7.2.4(b)). A saturation of the generation of VO_i is expected for materials with low oxygen concentration and very high irradiation fluences.
Although VO_i is electrically active (acceptor level at $E_C - 0.17$ eV), it does not influence the electrical properties of the detector at room temperature much. The VO_i starts to anneal out at 300°C, depending on the oxygen concentration of the material as explained in [49].

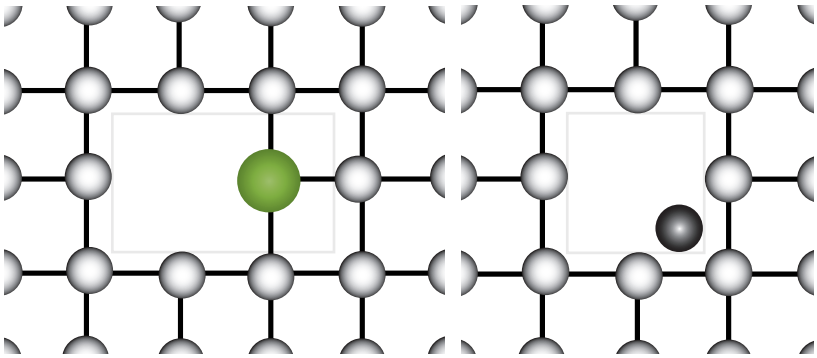

Figure 7.2.4.: Schematic illustration of the VP defect (a) and the VO defect (b) in the silicon lattice.

7.2.1.6. The di-vacancy-oxygen-complex

The di-vacancy-oxygen-complex (V_2O) is formed via the second order reaction $V + VO_i \rightarrow V_2O$. The defect was observed by LEE ET AL. [85] by *electron paramagnetic resonance* (EPR) (see page 46). It was found to introduce an very deep level, that was commonly supposed to be a current generator. In the recent years some studies were performed on this topic [72,77,86–91]. The Sec. 8.5.1 deals with the transformation of $V_2 \rightarrow V_2O$.

7.2.2. Interstitial related defects

7.2.2.1. The silicon interstitial

EPR (see page 46) investigations on low temperature irradiated diodes show no evidence for silicon interstitials (Si_i)[3] [52]. This can be explained by a very low activation energy for migration of interstitials, silicon interstitials seem to be mobile even at 4.2 K. The Si-interstitials interact mainly with the carbon impurities via the *Watkins replacement mechanism*. Here the Si-interstitial replaces a substitutional carbon atom from the lattice and produces a carbon interstitial (C_i). A reaction between Si_i and other impurities is also possible.

7.2.2.2. The carbon-oxygen-complex

The mobile carbon interstitial may couple with an immobile oxygen atom, forming the C_iO_i-centre. At room temperature it takes a few weeks to anneal out the carbon interstitial and form C_iO_i. In oxygen lean material, a competing process forming the C_iC_s takes place.

[3] Instead of I the silicon interstitial is also written as Si_i

The C_iO_i gives rise to a donor level at $E_V + 0.36$ eV. It is often considered to be responsible for trapping in simulations. One of the models using the defect is given in [92]. Yet, there is no indication that the C_iO_i defect has much of an influence on the electrical properties of silicon.

7.2.3. Clusters

Clusters are created when a high energy deposition leads to a cascade of displacements producing a high density of defects. The exact nature of defects inside the cluster is not known neither their electrical properties. There are models (e.g. [46]) which suppose silicon interstitials to diffuse very fast out of the cluster region while the vacancies remain there due to their low mobility. Thus, the production of vacancy-complexes of higher orders in the cluster core is possible. This core area might have a dimension of up to 15-20 nm and consist of 10^5 - 10^6 atoms [46].
Some defects are already attributed to clusters because they are not visible after gamma irradiation, but only after hadron irradiation ($E4$, $E5$ and $E205a$). Since it is not possible to observe the whole damaged region, *cluster related defects* are used as marker to track the damaged region. The labeling of unidentified defects is not straightforward, some defects were labelled according to the temperature of the peak maximum of a defect in the DLTS spectra, other defects were simply numbered. The labels of defects used in this work might differ from previous works, because the author tried to use names which are commonly used in literature.

7.2.4. The clustering effect

It is known that the damaged region effects the electrical properties of a semiconductor. Unfortunately, the mechanism leading to the effects is still unknown. According to Gossick [46] the damaged region in silicon can be of the size of 15-20 nm and consists of a densely packed cluster core and less dense outer regions. The high defect density leads to *coulomb interactions* which change the local properties of the defect levels. According to Svensson [51] the close conglomeration of defects inside the clusters give rise to strain fields which lead to a suppression of the DLTS signal of e.g. the doubly charged divacancy [93]. In addition to that, a high leakage current was observed in silicon detectors after fast hadron irradiation. This can be explained by the *intercenter charge transfer model* [52].
The effect of the cluster region can be explained by potential barriers surrounding the cluster, which shields the core region and defects inside. The effect can be nicely observed in the reduction of the DLTS and TSC signals in the presence of cluster defects (see Sec. 8.1) and the change of the filling conditions of defects inside the cluster region (see Sec. 8.5.4).

7.3. Overview of recent results on the identification of defects with impact on detector properties

A first breakthrough in understanding radiation damage in FZ and oxygen enriched FZ material after ^{60}Co-γ irradiation was achieved by Pintilie et al. [86,87,94,95]. It was seen in *macroscopic* studies that oxygen is very beneficial for the radiation hardness of the material concerning the effective doping concentration and the leakage current. It was assumed that a close to mid gap acceptor level can be correlated to the concentration of oxygen. This defect is necessarily a point defect due to the fact that interaction of ^{60}Co-γ with the silicon lattice works through the production of Compton electrons with a maximum energy of 1 MeV. The threshold energy for electrons to create clusters is about 8 MeV therefore only point defects can be created.
Pintilie et al. found the main reason for sensor degradation in the I_p defect [86]. The defect was found to be generated by a second order process [95]. The defect gives rise to a deep acceptor level ($E_C - 0.545$ eV) and a donor level ($E_V + 0.23$ eV). They correlates the I_p defect to the V_2O defect, revealing an influence on the leakage current and the effective doping concentration. On the other hand Alfieri et al. [96] assignes the X defect to V_2O, describing the transition of $V_2 + O \rightarrow V_2O$. The correct assignment is still under discussion, although it is commonly accepted, that the X defect can be assigned to V_2O. However, the I_p defect is the main defect, responsible for the space charge sign inversion after ^{60}Co-γ irradiation of standard FZ devices.
Two further defects with impact on the electrical properties were discovered by Pintilie et al.. On the one hand the very deep Γ defect was observed to be responsible for the increase of the leakage current and for change of the effective doping concentration [87], on the other hand she discovered the BD defect to be responsible for positive space charge at room temperature [87]. This bistable donor in the upper part of the gap is generated in oxygen rich material. It can even overcompensate the effect of the deep acceptors I_p and Γ. It was possible to associate the BD defect with the *thermal double donor 2* ($TDD2$) [87].
This breakthrough in understanding radiation damage was achieved for ^{60}Co-γ irradiated FZ samples. In the following years other materials like MCz and Epi were taken into consideration for HL LHC applications and further hadronic irradiations were performed. The sensor degradation after hadronic irradiation is much more severe than after ^{60}Co-γ irradiation. Latest results by the Hamburg group reveal the impact of three cluster related deep acceptors ($H(116K)$, $H(140K)$, $H(151K)$) in the lower half of the band gap on the effective doping concentration [55]. Additional to the BD defect, that can be observed also after hadronic irradiation, a shallow donor ($E(30K)$) in the upper half of the band gap with impact on the effective doping concentration was found [97]. Since these defects are also part of this works' investigations, these defects are introduced in chapter 9. Investigation on hadron irradiated samples are illustrated the chapters 8 and 9.
An overview of the most important defects and their properties (like ΔE_a, $\sigma_{n,p}$, anneal-

ing temperature, peak temperature in DLTS or TSC) that were not discussed in this work can be found in the PhD thesis of Moll. A brief review of the main important defect and their influence on detector properties is given in Tab. 7.3.1

Defect	Assign-ment	ΔE_a (eV)	σ_n (cm^2)	σ_p (cm^2)	Impact	Generated by	[O] dependence	Ref.
Point defects								
$I_P^{0/-}$	? (V_2O)	-0.545	1.7×10^{-15}	9.0×10^{-14}	I_{leak} + N_{eff} (-SC)	^{60}Co-γ (high generation) observed in 6, 15, 900 MeV e	suppressed in [O] rich Si	[86]
$BD^{0/++}$	$TDD2$	-0.224	6×10^{-15}		I_{leak} + N_{eff} (+SC)	^{60}Co-γ (high generation)	generation higher in [O] rich Si	[94]
		-0.26			N_{eff} (+SC)	23 GeV p (medium generation)		this work
					N_{eff} (+SC)	1 MeV n (low generation)		
Γ		+0.66	5×10^{-15}		I_{leak}	^{60}Co-γ	no	[94]
$V_2^{-/0}$	$V_2^{-/0}$	-0.422	2.2×10^{-15}		I_{leak}	^{60}Co-γ, e, p, n	no	[49]
Cluster defects								
$E5$	$V_3^{-/0}$	-0.46	7.8×10^{-15}		I_{leak}	6 MeV e, 23 GeV p, 1 MeV n	no	this work
$E205a$	? ($V_4^{-/0}$)	-0.395	1.7×10^{-15}		I_{leak}	23 GeV p, 1 MeV n	no	this work
$E(30K)$	donor	-0.1	2.3×10^{-14}		N_{eff} (+SC)	6, 15, 900 MeV e, 23 GeV p (high generation) 1 MeV n (low generation)	generation higher in [O] lean Si	[97]
$H(116K)$	accep.	+0.33		4.0×10^{-14}	N_{eff} (-SC)	23 GeV p, 1 MeV n	no	[55]
$H(140K)$	accep.	+0.36		2.5×10^{-15}	N_{eff} (-SC)	23 GeV p, 1 MeV n	no	[55]
$H(151K)$	accep.	+0.42		2.3×10^{-14}	N_{eff} (-SC)	23 GeV p, 1 MeV n	no	[55]

Table 7.3.1.: Influence of defects on leakage current (I_{leak}) and the effective doping concentration (N_{eff}). Although C_iO_i is frequently used in simulations (e.g. [92]) to explain trapping, there is no evidence found in microscopic measurements performed in this work. Candidates for trapping are $E205a$ and $H(151K)$. The influence of the clustering effect on the cross sections of defects is not clear. The "-" sign refers to electron traps with E_C- and the "+" sign refers to hole traps with E_V+. For defects with PF-effect the zero field ΔE_a is given. Complete lists of radiation induced defects are given in [32,72].

8. Cluster defects with impact on the leakage current

The results obtained during the CERN-RD48 (ROSE) collaboration [98] illustrated impressively the importance of microscopic studies on defects as shown in Sec. 7.3. The results achieved by DLTS and TSC measurements revealed a complete description of the degradation of the sensor properties after ^{60}Co-γ irradiation as function of dose on the basis of the radiation induced defects [86, 87, 94, 95]. For the first time it was possible to predict the behaviour of leakage current and the effective doping concentration on the basis of defect analysis after irradiation for specific materials. As a result the beneficial effect of oxygen enrichment on the radiation tolerance of silicon was approved.
A similar approach was started for HL LHC experiments within the framework of the RD50 collaboration [5] in which this work was carried out. This chapter addresses the identification of defects that are responsible for the increase of leakage current after hadron irradiation. Besides defect properties and the annealing behaviour also the knowledge of the chemical structure of defects with impact on the leakage current is a matter of interest. Those information increase the prospects for either developing future materials that are less susceptible for radiation damage or finding the best available material.
The radiation environment shown in Fig. 1.0.1 consists of mainly pions in the inner region of the silicon tracker followed by backscattered neutrons dominant in the outer layers. As explained in chapter 4, during neutron and charged hadron irradiation predominantly cluster defects are created in addition to fewer point defect (compared to ^{60}Co-γ irradiation).
We use the notation *cluster* as synonym for disordered regions with densely packed conglomerates of vacancies and/or interstitials. It is assumed that cluster defects are responsible for the increase of the bulk generation current. So far our present knowledge on clustering is very limited. Especially, neither the structure or components of the clusters nor their influence on the charge carrier capture characteristics of the extended defects are precisely known.
Unfortunately, it is very hard to get information about clusters, because they are huge conglomerations of multiple defects. The measurements do not provide enough information for a proper description of the whole damaged region. They merely hold information about parts of the cluster, therefore the *cluster related defects* have to serve as indicator or tracer for the damaged region. An example of the influence of the damaged region extracted from single point defect observations can be found in

Sec. 8.1. Later in this chapter, the investigation of the *cluster related defect* $E5$ yields information about the influence of the damaged region on the generation of leakage current.
The increase of leakage current after neutron and high energy proton irradiation has bee known for decades. In 1999 Moll [32] suggested a correlation between the $E4/E5$ defect and the leakage current. Since that time various studies were performed in order to find the origin of leakage current in silicon sensors after irradiation (eg. [49, 99]).

8.1. Influence of cluster defects on filling conditions

The importance of clusters can be clearly seen by their influence on the defect properties, that naturally also leads to a change of the diode properties. An example for the suppression of the defect signal in DLTS or TSC measurements in the presence of cluster defects can be observed in Fig. 8.1.1 (a). A comparison of the measured concentration of the VO defect during annealing at high temperatures, undisturbed by cluster defects is denoted with filled squares. The recovery of clusters after the annealing can be achieved by applying 1 A forward current for 20 minutes (open triangles) to the same sample. This treatment recovers the electrically active level of a bistable cluster defect from an electrically non-active configuration (see Sec. 8.4 for more information about the recovery of the bistable defect). As a result the "visible" VO concentration in the presence of the recovered clusters is given by open squares. The "visible" concentration of VO is reduced due to the impact of cluster defects.
A second example is illustrated in Figure 8.1.1 (b), illustrating the influence of the

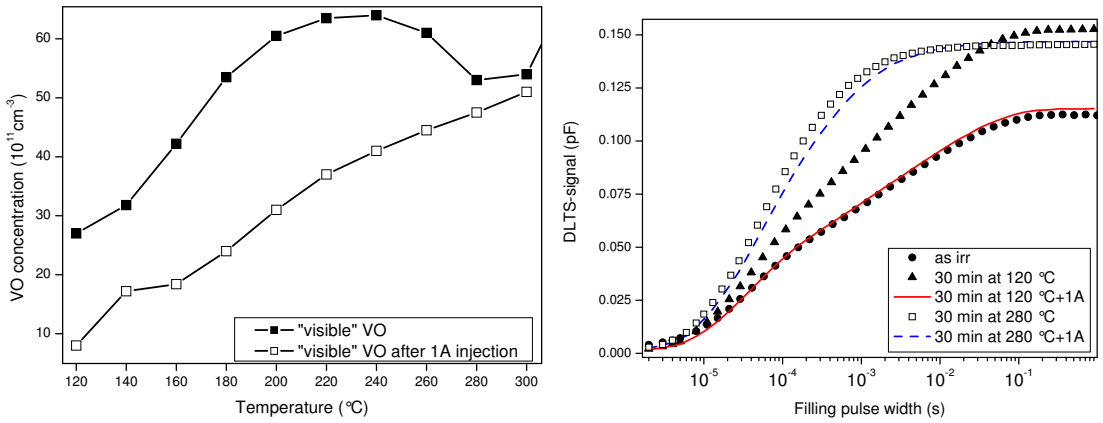

(a) **(b)**

Figure 8.1.1.: Concentration of the VO defect in presence of cluster defects and without measured by TSC (a). Influence of cluster defects filling conditions of the V_2 defect measured by DLTS (b).

cluster defects on the filling conditions of the V_2 defect. The measurement was per-

formed by taking DLTS transients for $U_B = -10$ V and $U_P = -0.1$ V. Filling times were varied from 5×10^{-6} s to 1 s, the filling improves with higher filling times. The data represent the condition directly after irradiation, where the signal is small (black squares) due to the presence of clusters. The filling process proceeds over two orders of magnitude with a non-sharp saturation. After annealing for 120 minutes at 80 °C (triangles) the signal heights increased which implies that the filling of more defects is possible. Furthermore, annealing at higher temperatures changes the shape of the filling curve towards a filling curve expected for point defects.

Location of point defects inside clusters

A reduction of the signal of point defects is clearly seen in DLTS and TSC measurements. A remaining question is the location of those defects, either inside the cluster region, outside or both. Calculations of Davis [100] show, that for the oxygen concentration of $1 \times 10^{18}\,\mathrm{cm}^{-3}$ only 1 oxygen atom will be trapped in the cluster resulting from a 50 keV PKA. Thus only one VO-complex can be located inside the cluster region. The general process of the signal reduction can be attributed to the shielding of defects inside the cluster region. However, there are some open questions whether the picture given here suits all observations. A detailed study on the influence of the cluster related defects and the influence of the damaged region on the the leakage current is given in the following.

8.2. The $E4/E5$ defect

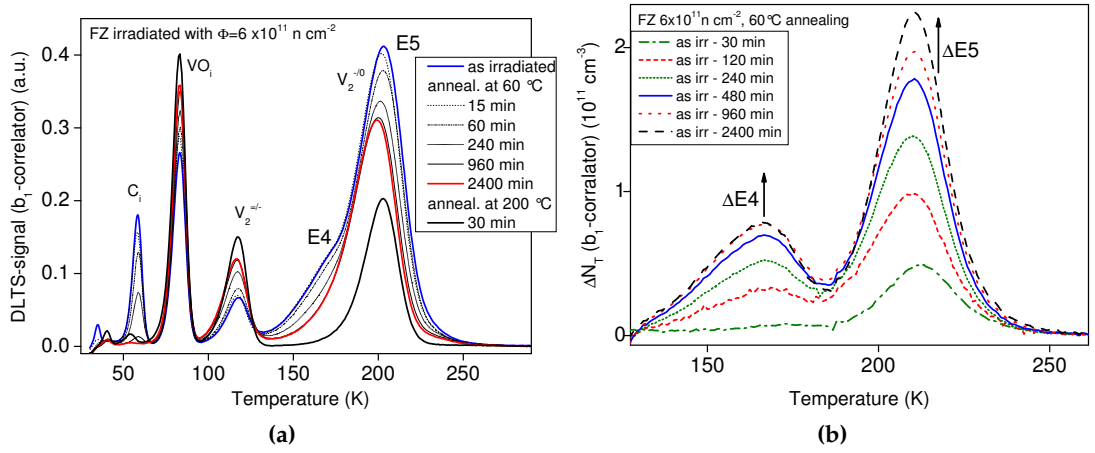

Figure 8.2.1.: Annealing behaviour of defects at 60 °C in a 100 µm thick FZ irradiated with $\Phi = 6 \times 10^{11}$ n cm^{-2} measured by DLTS (a) and corresponding difference spectra illustrating the change of the $E4/E5$ defect concentrations based on the annealed fraction during the annealing procedure (b). Measurement condition: $V_R = -10$ V, $V_P = -0.1$ V, $t_w = 200$ ms.

The increase of the leakage current is a severe problem for silicon sensors, because it leads to an increase of the noise and an increased power dissipation. The only way to minimise the leakage current during the operation of the experiments is cooling (see Sec. 5.2). During the maintenance periods at room temperature some beneficial current annealing will occur. Further information about HL LHC annealing scenarios can be found in HÖNNIGER [82].
It is known that the increase of the leakage does not depend on the oxygen content of the material. Unfortunately this is the only impurity that can be properly used for defect engineering. It is necessary to know the chemical structure of the defects in order to find ways for improving the radiation hardness. As mentioned before, some of the studies showed a correlation between the leakage current and the $E4/E5$ defect, in MOLL [32] labelled as $E170/E212$ Both defect levels $E4/E5$ cannot be evaluated from only one DLTS spectrum, but they can be well separated from other superimposed defects with similar energy levels by isothermal annealing measurements.
As an example Fig. 8.2.1 (a) shows the development of DLTS spectra for a 100 µm thick FZ irradiated diode with 6×10^{11} n cm^{-2} and annealed at 60 °C. The corresponding difference spectra are presented in Fig. 8.2.1 (b). $\Delta E4$ and $\Delta E5$ represent the annealed fraction of the defect concentration. The extracted concentration of $E4/E5$ as a function

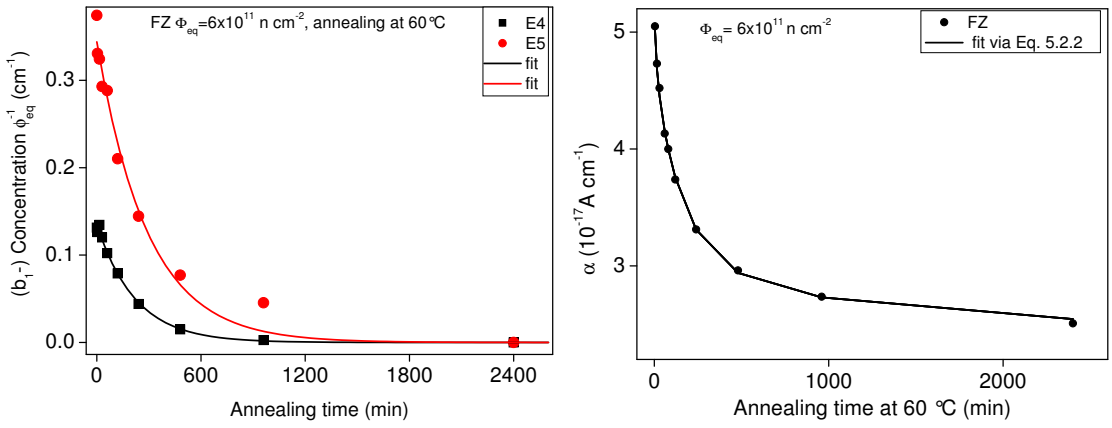

Figure 8.2.2.: Annealing behaviour of the concentration of the cluster related defect levels $E4$ and $E5$ (a) and leakage current (b) in 100 µm thick FZ material irradiated with $\Phi_{eq} = 6 \times 10^{11}$ n cm^{-2}.

of the annealing time is shown in Fig. 8.2.2 (a) and the corresponding annealing of the leakage current is shown in Fig. 8.2.2 (b). The annealing of the leakage current follows Eq. 5.2.2. Similar to the defect annealing, the first 1000 minutes of the leakage current annealing follow an exponential decay with the same time constant.
Suspecting the defect level to be correlated with the leakage current could be proven by a proportionality between the leakage current values and the defect concentrations

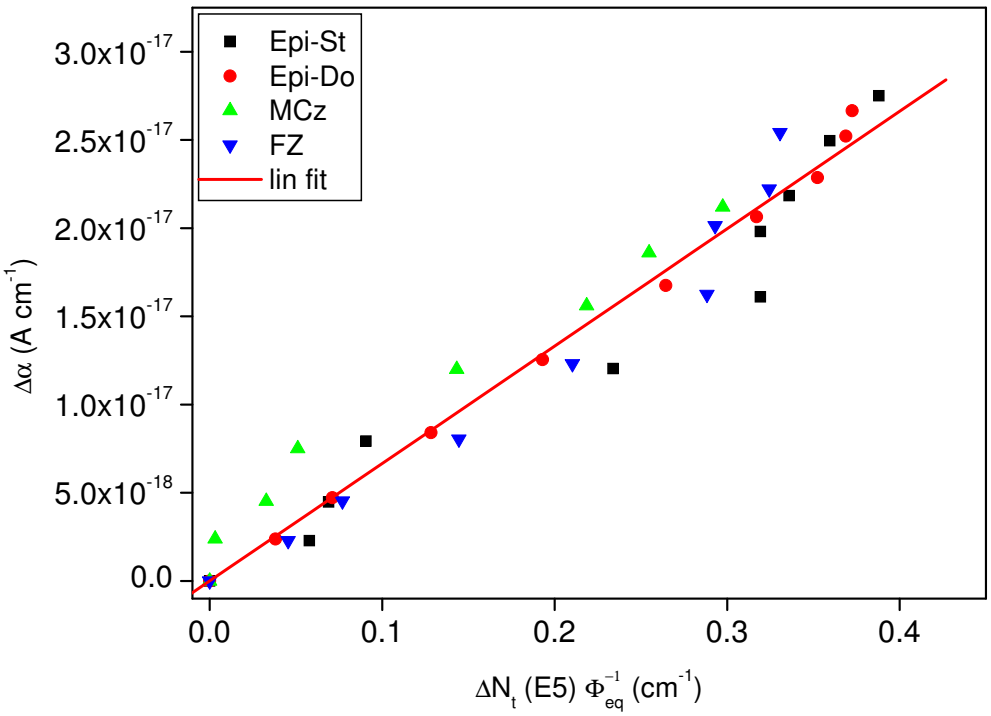

Figure 8.2.3.: Correlation of the $E5$ defect concentration with the change in the damage parameter α for Epi-St, Epi-Do, Mcz and FZ material all irradiated with 1 MeV neutrons, normalised.

during annealing studies. Figure 8.2.3 illustrates the change of the leakage current as a function of the change of the defect concentration of the $E5$ defect during annealing. Four different materials were analysed, irradiated with different fluences of 1 MeV neutrons. This figure was achieved by plotting the annealed fraction of the defect concentration as a function of the annealed fraction of the leakage current represented by the damage parameter α at the same annealing step. Values for the current related damage rate α and the corresponding defect concentration were obtained by:

$$\Delta\alpha = \alpha_0 - \alpha_n \quad , \quad \Delta N_t = N_{t,0} - N_{t,n}. \tag{8.2.1}$$

with α_0 denotes the value for the maximum current (directly after irradiation) and α_n the damage value corresponding to the current after the n^{th} annealing step. $N_{t,0}$ denotes the maximum (directly after irradiation) defect concentration and $N_{t,n}$ the concentration after the n^{th} annealing step.
The individual fluences were evaluated by using the damage rate $\alpha = 3.99 \times 10^{-17}$ A cm^{-1} for 80 minutes at 60 °C annealing [32]. This normalisation is supposed to minimise the errors resulting from uncertainties in annealing during irradiation and storage after irradiation. A linear dependance starting at zero can be observed. This is

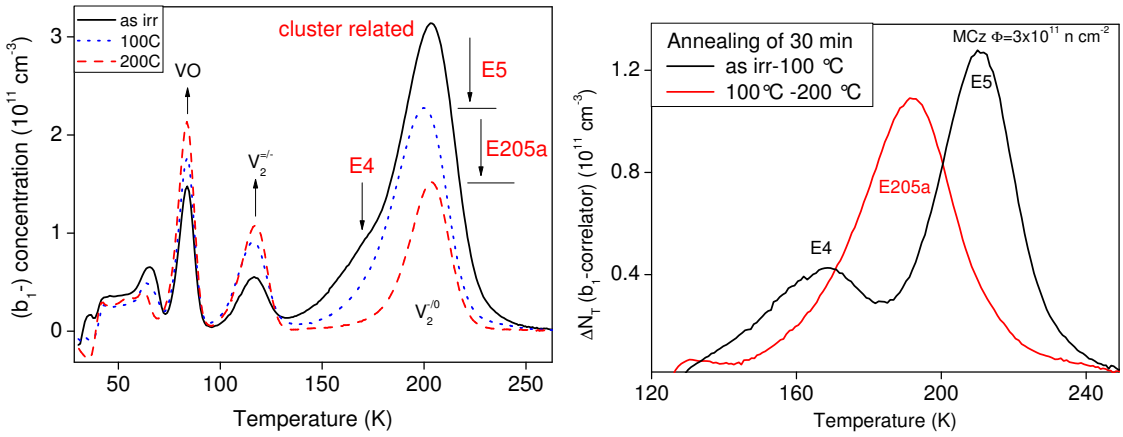

Figure 8.3.1.: Annealing behaviour of cluster defects at higher temperatures. The $E205a$ defect anneals out between about 100 °C and 180 °C (a), therefore an annealing step of 30 minutes at 200 °C was chosen. The defect is well visible in difference spectra and can be clearly distinguished from the $E4/E5$ defect (b). Measurement condition: $V_R = -10$ V, $V_P = -0.1$ V, $t_w = 200$ ms.

a strong evidence for $E4/E5$ being the origin of a large fraction of the leakage current increase after hadron irradiation (see next section). The relevance of this defect is discussed in the next section.

8.3. The $E205a$ defect

The DLTS signal of another cluster related defect $E205a$ with an energy level in the band gap of $E_C - 0.395$ eV overlaps with the $E4$ and $E5$ defect (see Fig. 8.3.1 (a) and (b)). This signal needs to be seperated from them before the annealing behaviour of the other cluster related defect can investigated at higher temperatures. As the $E205a$ defect is only stable up to 140 °C, the annealing process could affect the evaluation of other configurations of the $E4$ and $E5$[1] concentrations (see Sec. 8.4). An additional annealing for 30 minutes at 100 °C and 200 °C reduces the main cluster peak at around 200 K. This is shown in Fig. 8.3.1 (a). The corresponding difference spectra are illustrated before any annealing in Fig. 8.3.1 (b). It is possible to distinguish between three defect levels, although they overlap, because they anneal at different temperatures. $E205a$ starts to anneal out, when $E4$ and $E5$ are not visible any more.
For a dedicated annealing study of the defect $E205a$ and $E4/E5$ we used diodes which

[1] As the annealing of $E4$ and $E5$ was earlier mentioned to start at 60 °C, the $E205a$ defect does not seems to interfere, but this is not the full story. $E4$ and $E5$ exhibit a bistability and can be traced up to high annealing temperatures. For further information see Sec. 8.4.

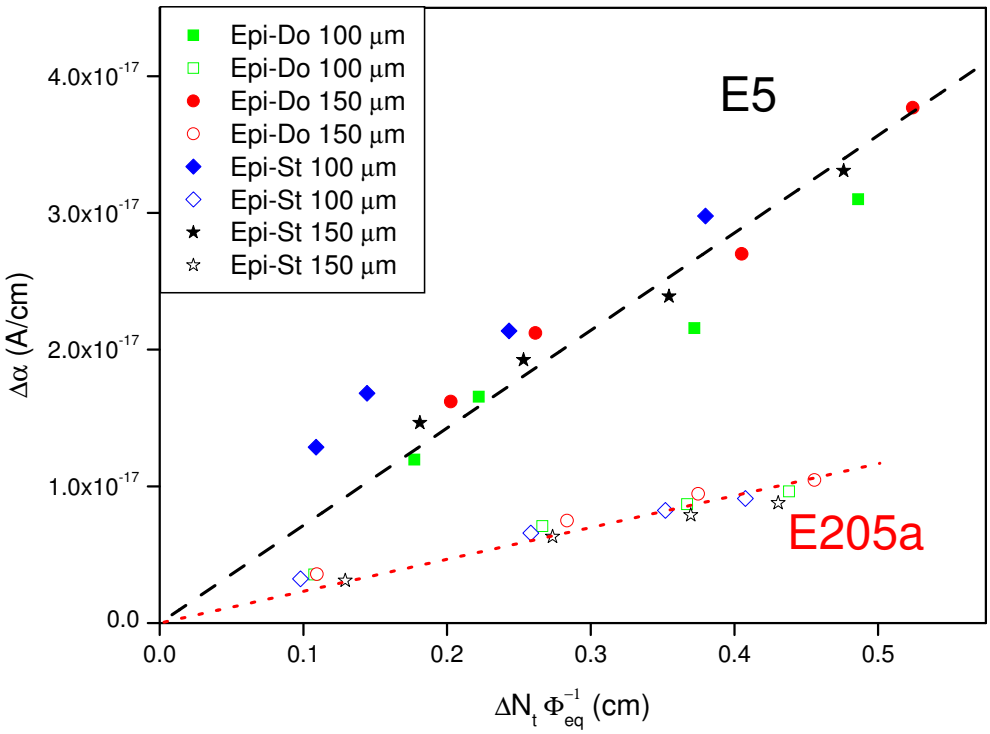

Figure 8.3.2.: Correlation of annealing of ΔN_t of $E4/E5$ and $E205a$ with the current annealing $\Delta\alpha$ for proton irradiated standard epitaxial and oxygen enriched epitaxial material with thicknesses of 100 µm and 150 µm recorded during the isochronal annealing between 80 to 180 °C.

were fabricated on standard and oxygen enriched epitaxial material and irradiated with 24 GeV/c protons. The annealing procedure for the $E4/E5$ defect annealing was isothermal annealing at 80 °C. On the other hand for the annealing of the $E205a$ defect an isochronal treatment was performed between 140 °C and 200 °C in temperature steps of 20 °C and a duration of 30 minutes each.
Following the same analysis procedure as described in Sec. 8.2 we derive the concentration differences ΔN_t for the $E4/E5$- and the $E205a$ defect and the corresponding change of the current related damage rate $\Delta\alpha$. The data are shown in Fig. 8.3.2. Indeed, a nice correlation between the annealing of both defects ($E5$ and $E205a$) and the leakage current in different temperature ranges can be stated. Furthermore, the current generation rate of the $E205a$ defect is smaller than that of $E5$ which is obvious from the different slopes of both curves.
These different contributions in the current generation can also be deduced from Fig. 8.3.3. Here the annealing of $E5$ is shown. As can be seen 60 % of the leakage current decreases due to the annealing of the $E5$ defect and only 30 % decreases due to the $E205a$-annealing.

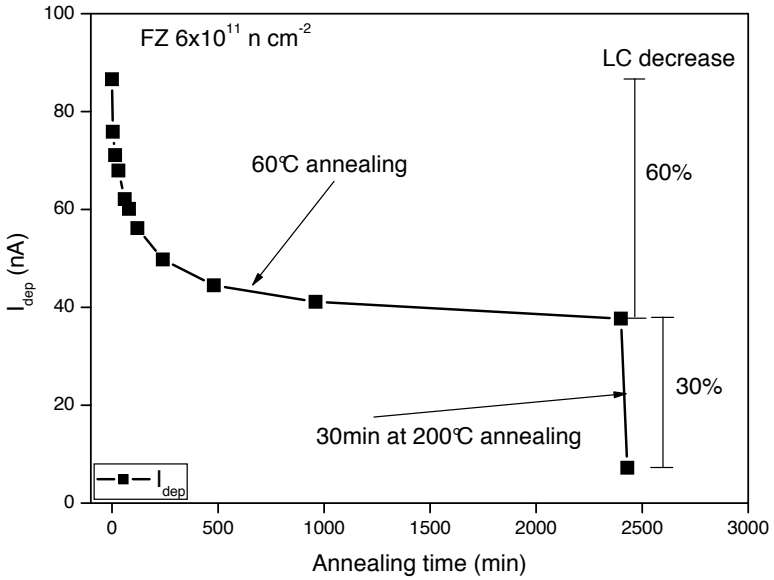

Figure 8.3.3.: Current decrease during the annealing at 60°C and 200°C. A major portion of 60 % of the initial leakage current anneals out during 60°C annealing for 2400 min and additional 30 % anneal during 30 minutes at 200 °C.

8.4. Direct correlation between *E5* and the leakage current

After the annealing at 200 °C most of the cluster defects overlapping with the singly charged state of the divacancy ($V_2^{-/0}$) have been annealed out. As a result, the "visible" concentration of the doubly ($V_2^{=/-}$) and singly charged states ($V_2^{-/0}$) of the divacancy become similar. Figure 8.4.1 shows the DLTS spectra of 300 µm thick MCz sensors irradiated with $\Phi = 3 \times 10^{11}$ n cm^{-3}. The blue squares illustrates the annealing stage at 200 °C. Fleming et al. found on irradiated transistors that $E4/E5$ do not really anneal out, but change the configuration [101, 102]. They observed a recovery of this defect by injecting a forward current density of J =12.5 A cm^{-2}. We performed a similar treatment on a MCz sample and the result is illustrated in Fig. 8.4.1. The red circles denote the DLTS measurement after the treatment with I =1 A (J =4 A cm^{-2}) forward current for 20 minutes.
Successive annealing at 80 °C anneals the concentration of $E4/E5$ again to the former situation (black line). If the $E4/E5$ defect is the origin for the leakage current, then the current should behave similar to the defect concentration. Figure 8.4.2 shows a comparison between the measured leakage current on the left hand side (open black squares) and the $E4/E5$ defect concentration on the right hand side (red circles). The treatment with I =1 A forward current injection leads to an increase of both, current and concentration. Successive annealing again leads to a decrease of current and concentration. The situation is reproducible, as is shown for the second peak. This is a direct proof that the leakage current and the concentration of $E4/E5$ are directly

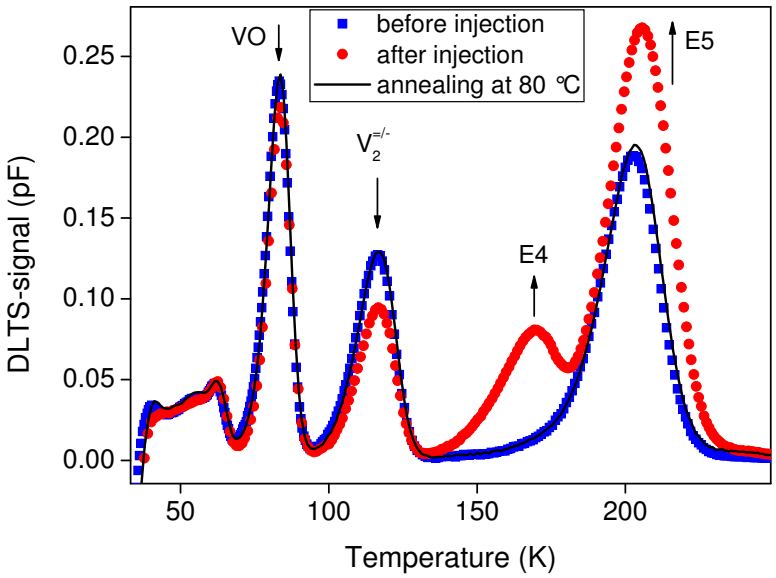

Figure 8.4.1.: Recovery of $E4/E5$ after I =1 A forward current injection. Material: MCz, d =300 µm with $\Phi = 3 \times 10^{11}$ n cm^{-3} (for details see text). Measurement condition: $V_R = -10$ V, $V_P = -0.1$ V, $t_w = 200$ ms.

correlated. The effect is reproducible and can be used for further studies. In Sec. 8.5 we make use of this bistability in order to follow the out-annealing of the $E4/E5$ defect.

8.5. Identification of *E4/E5* as V_3

Since the DLTS method only provides information about the electrical properties of defects, the direct identification of the chemical structure is not possible. In order to contribute to the assignment, we need to perform annealing studies and compare the results with the annealing behaviour of known defects or with results achieved by other methods like EPR or IR measurements (see page 46).
Our contribution to the identification of the $E4/E5$ could be achieved by a comparison of the defect properties and the annealing behaviour of $E4/E5$ to V_2. Within the WODEAN collaboration [103], the results of this study were also correlated to results obtained by IR-*spectroscopy* (see page 46) and *Laplace* DLTS [104] (see Sec. 8.5.2).
The following measurements concerning the annealing behaviour of $E4/E5$ defect at higher temperatures were obtained with the following scheme:

- isochronal annealing step
- injection of 1 A forward current
- further annealing at 80 °C or a further annealing step at higher temperature

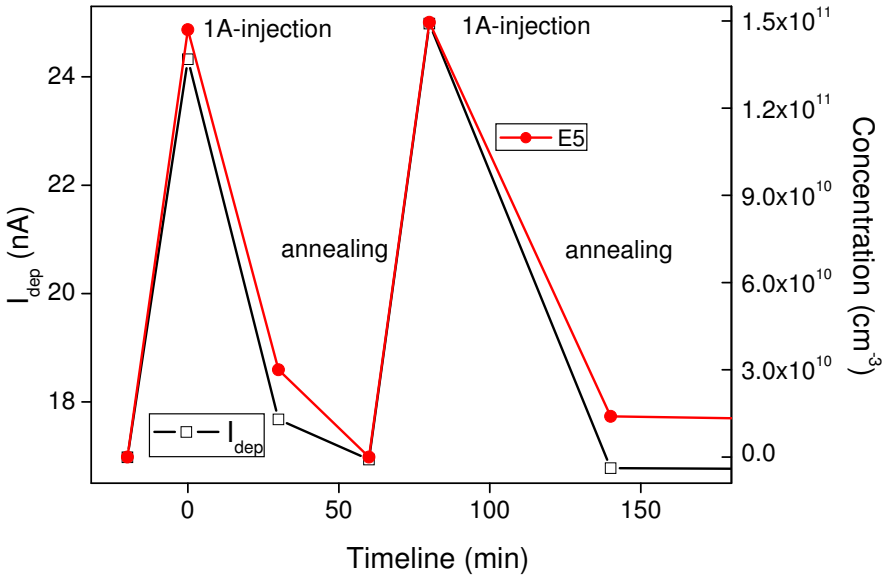

Figure 8.4.2.: Direct correlation of $E4/E5$ and the leakage current by analysing the bistability of $E4/E5$.

After each step C-V and I-V measurements and DLTS or TSC measurements were performed.

8.5.1. Annealing behaviour of V_2 and transition to X defect

The annealing behaviour of $E4/E5$ is very similar to the annealing of the V_2 defect (as presented in Sec. 8.5.2). Therefore it is useful to recapitulate the annealing behaviour of V_2. Figure 8.5.1 illustrates the isothermal annealing of the concentration of the doubly charged state of the divacancy ($V_2^{=/-}$) measured by means of DLTS during isothermal annealing. The annealing temperature was chosen to be 300 °C.
The annealing of V_2 depends strongly on the oxygen content of the silicon material. The higher the [O] of the material, the faster the annealing already at lower temperatures. Information about the annealing of the V_2 defect can be found in [49, 90, 96, 105]. Fig. 8.5.1 illustrates the annealing of the V_2 defect in FZ (circles) and Epi-Do (squares) diodes. The defect concentration was obtained by DLTS measurement and normalised to the fluence. The annealing of V_2 starts at 5 min at 300 °C in oxygen rich Epi-Do material, whereas the annealing of V_2 starts later in FZ material (low oxygen content), in this case around 10 minutes at 300 °C.
This behaviour shows the influence of the oxygen content and the resulting defect

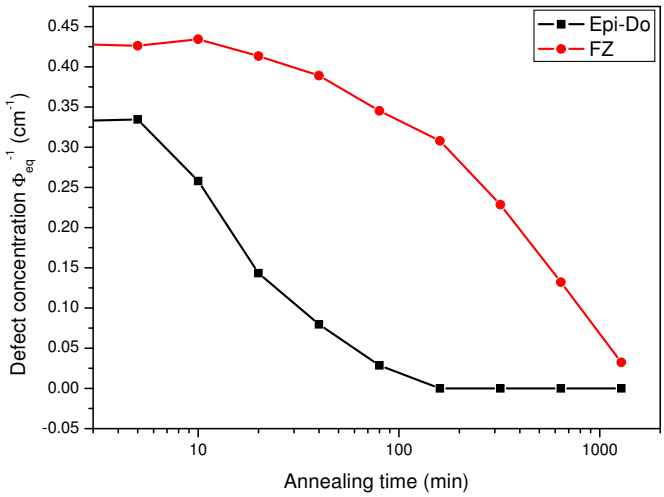

Figure 8.5.1.: Isothermal annealing of V_2 in Epi-Do and FZ material, both samples were irradiated with Φ =6×10^{11} n cm^{-2}. Defect concentrations were obtained by DLTS measurements. The fluence was normalised with help of the α-value for 80 minutes at 60 °C annealing.

reactions due to migration and/or dissociation. Possible defect reactions are:

$$V_2 \rightarrow V + V \tag{8.5.1}$$
$$V_2 + O \rightarrow V_2O \tag{8.5.2}$$
$$V_2 + O_2 \rightarrow V_2O_2 \tag{8.5.3}$$
$$V_2 + V \rightarrow V_3 \tag{8.5.4}$$
$$V_2 + VO \rightarrow V_3O \tag{8.5.5}$$

The latter three reactions are unlikely even in oxygen rich material, because the concentrations of the reaction partners are much lower than the concentration of oxygen: $[O_2]$, $[V]$, $[VO_i] \ll [O_i]$. As an example, $V_2 + VO \rightarrow V_3O$ is not the preferred path due to the fact that $[VO_i] \ll [O_i]$. The VO defect concentration stays stable while V_2 starts to migrate, thus finding oxygen for a reaction is much more likely than finding VO.
Moreover the reaction $V_2 + O_2 \rightarrow V_2O_2$ is very unlikely because oxygen dimers are less likely than single oxygen interstitials. Murin et al. investigated the concentration of oxygen dimers with IR-*spectroscopy* and found a quadratic dependence of the oxygen dimer concentration on the concentration of oxygen in silicon [106]. Also Hönniger investigated the presence of oxygen dimers with DLTS. Hönniger assumes the IO_2 defect [107] as indicator for the concentration of oxygen dimers [82]. The main concentration of the IO_2 defect is represented in Fig. 8.5.2. For the materials used in this work, the presence of $[IO_2]$ does not exceed 1×10^{12} cm^{-3}. This is about 5 orders of magnitude less than [O]. Thus the most probable reaction is $V_2 + O \rightarrow V_2O$ in

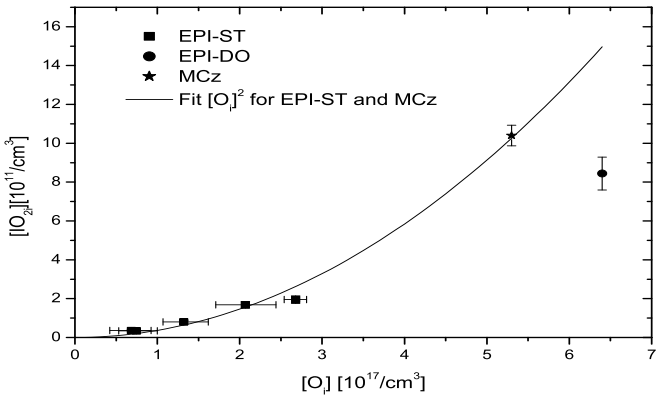

Figure 8.5.2.: Concentration of the IO_{2i} defect in Epi-St 72 µm, Epi-Do 72 µm and MCz detectors as function of the oxygen concentration. The solid line represents a fit with a quadratic function based on the observation of Murin et. al. [106]. The figure was taken from [82].

oxygen rich material. The complex which was recently assigned to V_2O ([89,96]) was first called X defect [88], a defect which is supposed to form during the migration of V_2 that combines with an immobile O_i [91]. This defect only builds up in oxygen rich material, as expected.
However, the annealing of V_2 and transition to the X defect is suppressed in oxygen lean material. Due to the lack of any other reaction partner, the annealing is dominated by dissociation processes. In the recent time a large number of studies were performed on the transition of V_2 to X defect [49,82,88–91,96,105,108].
Figure 8.5.3 shows the transformation of $V_2^{=/-} \rightarrow X^{=/-}$ in detail, supposing that the X defect is V_2O. The left hand side (a) shows a close-up view of the DLTS spectra of the $V_2^{=/-}$ defect during the isothermal annealing at 300 °C. In the same way that the V_2-concentrations decreases an increase of the X defect can be observed. The $V_2^{=/-}$ defect anneals out completely at $\approx$ 160 minutes at 300 °C, while the maximum $X^{=/-}$ defect concentration can be found between 40 min and 160 min at 300 °C. It is possible to observe the annealing process as a superposition of *annealing-in* and *-out* of the $X^{=/-}$ defect.
The overlap of both defects during the transformation was determined by fitting two defect levels to the DLTS spectra. Concentrations obtained by this procedure are presented on the right hand side in Fig. 8.5.3 (b). The simulated results of the relevant reactions are included into this figure by solid lines.
The annealing was simulated by using reaction kinetics explained in Sec. 4.8. The process of $V_2^{=/-} \rightarrow X^{=/-}$ is a single diffusion driven reaction [57,91,108] for which Eq. 4.8.4 (see Sec. 4.8) holds. Using the *Arrhenius relation* (Eq. 4.8.3) and Eq. 4.8.6 for the dissociation of the V_2 follows:

$$[V_2] = [V_2]_{t=0} \exp(-4 \cdot \pi \cdot R(D_{V_2} + D_{O_i}) \cdot [O_i] \cdot t). \tag{8.5.6}$$

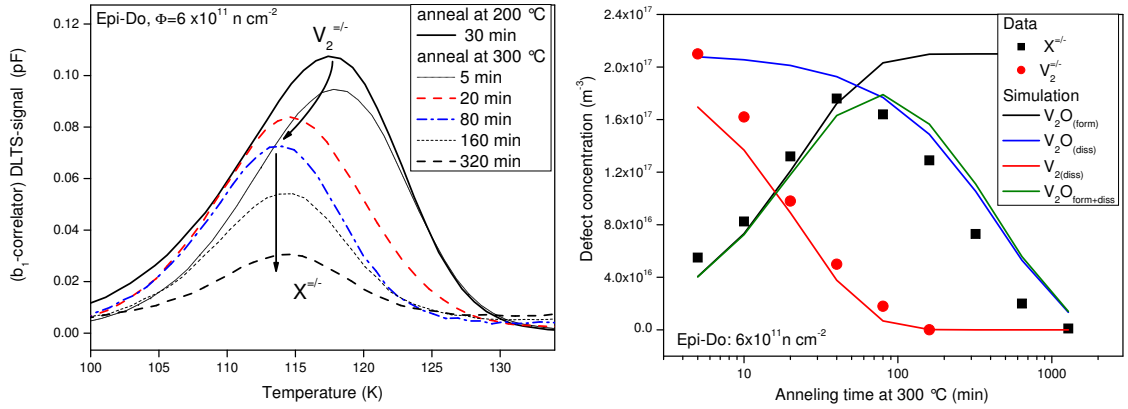

Figure 8.5.3.: DLTS spectra of the annealing behaviour of V_2 to V_2O during annealing (a) and evaluated defect concentrations with simulation of the transformation (b). Material: Epi-Do irradiated with $\Phi = 6 \times 10^{11}$ n cm^{-2}. Measurement condition: $V_R = -10$ V, $V_P = -0.1$ V, $t_w = 200$ ms.

The transition of $V_2^{=/-} \rightarrow V_2O^{=/-}$ can be calculated by:

$$[V_2O] = [V_2]_{t=0} - [V_2]_{t=0} \exp(-4 \cdot \pi \cdot R(D_{V_2} + D_{O_i}) \cdot [O_i] \cdot t), \tag{8.5.7}$$

The *out-annealing* of V_2O can be simulated by

$$[V_2O] = [V_2O]_{t=0} \exp(-k_2 t), \tag{8.5.8}$$

with $k_2 = k_0^{V2O} \cdot \exp\left(-\frac{E_a^{V_2O}}{k_B T}\right)$ for a dissociation.

The simulation of the reaction kinetics of $V_2^{=/-} \rightarrow V_2O^{=/-}$ was performed with parameters displayed in Tab. 8.5.1.

Defect / Impurity	E_a (eV)	k_0 (s^{-1})	D_0 (cm^2 s^{-1})
O_i	2.54 [109]		0.17 [109]
V_2	1.3 [91]		3×10^{-3} [91]
V_2O	2.02 [108]	2×10^{13} [108]	

Table 8.5.1.: Parameters for the $V_2 \rightarrow V_2O$ transformation and out-annealing of the V_2O defect. Given are activation energy for migration E_a, the pre-exponentioal factor k_0 and the *diffusion constant* D_0.

Using these values the simulation only reproduces the measured data if the oxygen concentration of this material is assumed to be a factor of two lower compared to the data measured by SIMS (see Sec. 2.2), which is [O]=6×10^{17} cm^{-3}.

The reason for this deviation may result from differences in materials and radiation sources used in this work compared to those used for the extraction of the defect parameters in [110] and [91]. In particular, V_2's diffusion constant and activation energy for migration obtained by PELLEGRINO ET. AL. was extracted from low resistivity silicon material irradiated with low doses 5.6 MeV Si-ion. This ion-implantation leads to a defect layer 3.8 µm below the surface, that differs strongly from the homogeneous distribution of vacancies after $^{60}Co - \gamma$, electron and proton irradiation, and from the homogeneous distribution of clusters inside the silicon created by protons and neutrons.
Although it is common opinion, that the X defect can be assigned to V_2O, there are still some questions about this assignment. The main capture for vacancies in oxygen rich silicon is via the reaction $V + O_i \rightarrow VO_i$. The reaction $V + VO_i \rightarrow V_2O$ is therefore suppressed in material where $[O] \gg [VO_i]$. PINTILIE ET. AL. on the other hand describe the I_p defect to be V_2O. The I_p defect is generated via second order generation and suppressed in oxygen rich material, as expected for V_2O. Moreover, EPR (see page 46) studies performed by LEE [85] observed the V_2O to be a deep defect level, with possible influence on the current generation. The I_p defect is a current generator, whereas no influence on the leakage current was observed for the X defect [49].
HÖNNIGER [82] studied the transformation of $V_2 \rightarrow X$ for FZ material with three different oxygen concentrations and irradiated with ^{60}Co-γ. He simulated the measured annealing curve with the values listed in Tab. 8.5.1. The simulation did not fit to the measured data points, unless he increased the oxygen concentration of the materials by 10 % to 30 %. The question, whether the X defect can be attributed to V_2O is therefore not fully answered. The activation energy for migration of V_2 may be a source for errors in the simulation of HÖNNIGER [82], as well as in the earlier described deviation of measurements performed in this work.

8.5.2. Annealing behaviour of *E4/E5* and transition to the *L* defect

As mentioned before, an identification of the chemical structure of defects with the DLTS technique is not possible, but DLTS indirectly provides information about a possible defect assignment. For the $E4/E5$ defect the information is mainly derived from a comparison of its annealing behaviour with that of the divacancy. The transition of the $E4/E5$ defect to another defect during annealing and in particular the dependance on the oxygen concentration of the studied material of the reaction, equals that of the transition of $V_2 \rightarrow V_2O$.
Further similarities in the properties of the $E4$ and the $E5$-levels to those of the V_2 charge states, level position and DLTS peak suppression of the $E4$-level compared to the level of $E5$, are analog to the observation of the two different charge states of the V_2.
The transformation of the $E4/E5$ defect into a new defect during high temperature annealing can be observed in oxygen enriched material, see Figs. 8.5.4 (a) and (b). Both

figures represent the same annealing steps, (a) before and (b) after the injection of $I = 1$ A forward current. The left hand side illustrates the transformation of the V_2 defect to X and the in-annealing of the L defect during isochronal annealing steps of 20 °C for 30 minutes. The right hand side figure illustrates the recovered $E4/E5$ defect levels after injection with $I = 1$ A that overlap with the defect signals illustrated in (a). Due to the bistability of the $E4/E5$ defect it is possible to follow the transformation

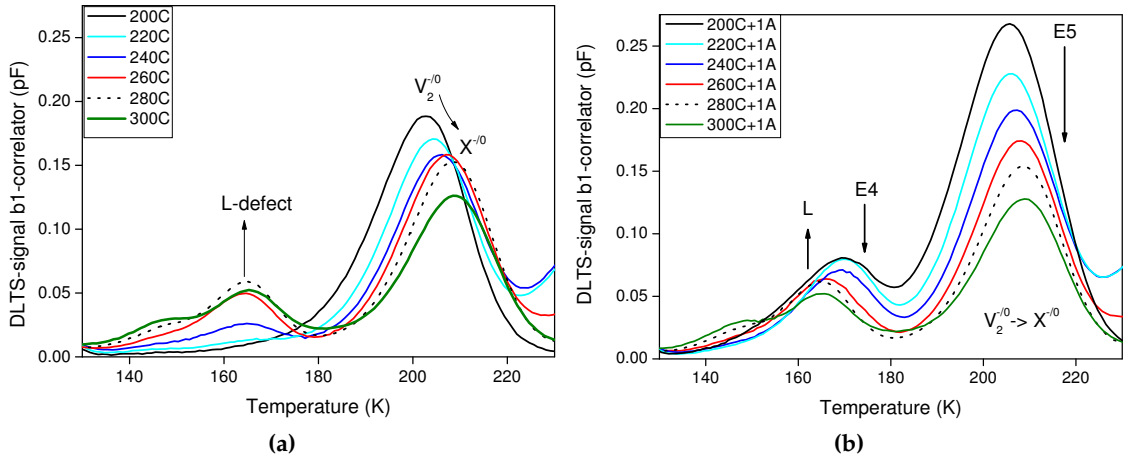

Figure 8.5.4.: Annealing behaviour of $d = 300$ µm thick MCz material irradiated with $\Phi = 6 \times 10^{11}$ n cm^{-2} illustrating the transformation of the V_2 defect to X and the in-annealing of the L defect during isochronal annealing steps of 20 °C for 30 minutes (a). Overlapping with the results from (a) are the recovered $E4/E5$ defect levels after injection with $I = 1$ A during the same annealing steps (b). Note that the axis scale is similar for both figures (further description see text). Measurement condition: $V_R = -10$ V, $V_P = -0.1$ V, $t_w = 200$ ms.

$V_2 \rightarrow V_2O$ and the in-annealing of the L defect separately from the out-annealing of the $E4/E5$ defect. This can be followed when plotting the difference in DLTS signals of Figs. 8.5.4 (a) and (b), revealing the transformation of $E4/E5$ into the L defect. It should be noted, that the annealing of the V_2 defect is delayed and the transition to the X defect is suppressed in oxygen lean materials. This is an expected result of the lack of reaction partners.

As a result of the similarity the $E4/E5$ defect can be suspected to be the *tri-vacancy* - V_3. In order to obtain an assignment of the $E4/E5$ defect is necessary to compare also the annealing behaviour and the electrical properties of both defects. If $E4/E5$ is V_3, the annealing behaviour must appear very much like V_2. With this assumption in mind, this study may contribute to the identification of the chemical structure of the $E4/E5$ defect. As mentioned in the previous section, the annealing of $E4/E5$ is similar to the annealing of the V_2. The reaction for the out-annealing of the $V_2 \rightarrow X$ is assumed to be $V_2 \rightarrow V_2O$. A similar reaction can be assumed for the $E4/E5$ defect: $E4/E5 \rightarrow V_3O$. Both reactions should be strongly depending on the oxygen concentration. In fact this

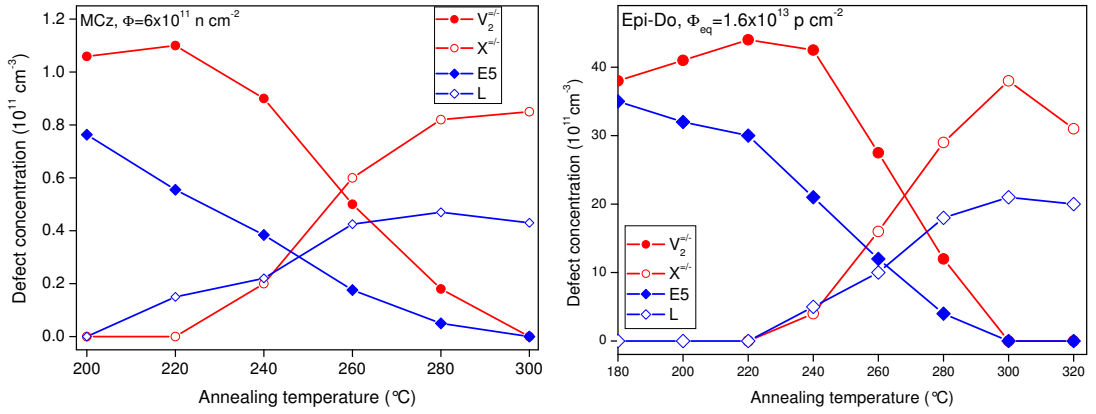

Figure 8.5.5.: Annealing behaviour of $E4/E5$ compared to the V_2 defect for Φ =6×10^{11} n cm^{-2} irradiated MCz-material (a) and Φ =1.6×10^{13} p cm^{-2} irradiated Epi-Do-material (b). Concentrations were obtained by means of DLTS (a) and TSC (b) measurements.

is reflected in the observation of the annealing behaviour. In oxygen rich material, the annealing starts earlier than in oxygen lean silicon, and in oxygen rich material the $E4/E5$ defect transforms into another complex, which was called L-centre [111]. This is demonstrated in Fig. 8.5.5. The annealing behaviour of the $E4/E5$-concentration compared to the V_2-concentration is shown for neutron irradiated MCz-material (a) and proton irradiated Epi-Do material (b).

The concentrations were obtained by means of DLTS (a) and TSC measurements (b). Circles represent the transformation of $V_2 \rightarrow V_2O$ (or the X defect) and diamonds $E4/E5 \rightarrow L$ defect. Both, the transformation of $V_2 \rightarrow V_2O$ and $E4/E5 \rightarrow L$ show a very similar behaviour. The main differences for both reactions are the higher defect concentrations for the V_2 and V_2O.

The materials illustrated in this section are oxygen rich materials. For oxygen lean material there is neither the transformation of $V_2 \rightarrow V_2O$ nor $V_3 \rightarrow V_3O$ anticipated. Figure 8.5.6 represents the annealing behaviour of FZ (a), a material which exhibits a low oxygen concentration, and Epi-St (b) where [O] lies in between that of FZ and Epi-Do (see Sec. 2.2). In FZ material the transformation of $E4/E5 \rightarrow L$ is not seen. We therefore conclude, that the L-centre can be attributed to the V_3O.

It was reported by Mikelsen et al. ([111]) that the L-centre was only found in oxygen rich material, this can be confirmed by the measurements presented here. The striking similarity of the $E4/E5$ annealing compared to the V_2 annealing up to the point of the transformation in oxygen rich materials supports the assumption, that the $E4/E5$ defect can be assigned to the V_3 and the L-centre to V_3O.

Very recently also Markevich et. al. correlated $E4/E5$ to the V_3 by means of IR-*spectroscopy* [112]. A comparison to the results of IR-*spectroscopy* investigations

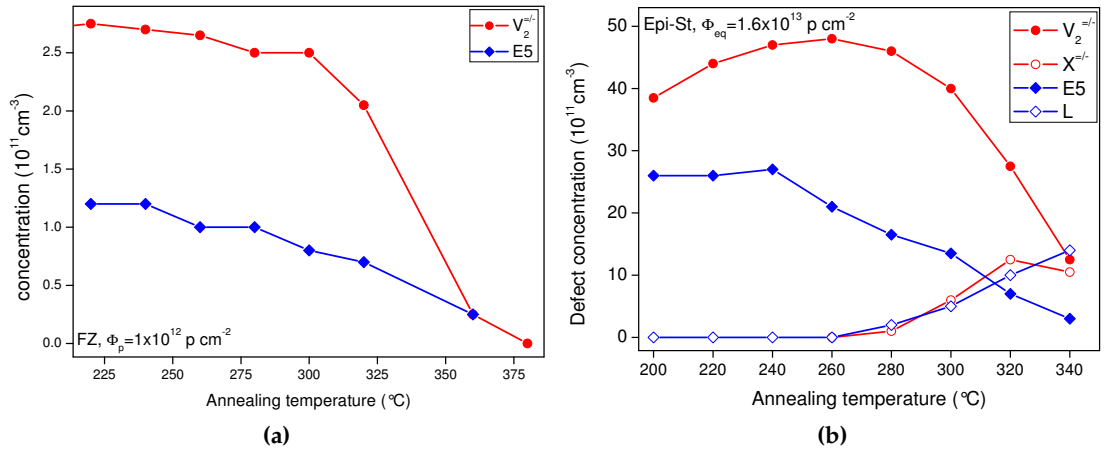

Figure 8.5.6.: Annealing behaviour of $E4/E5$ compared to the V_2 defect for FZ material (a) and Epi-St material (b).

on neutron irradiated Cz silicon-crystals illustrated in Fig. 8.5.7 reveals the striking similarity of the annealing behaviour observed by IR-*spectroscopy* and DLTS or TSC. As for IR-*spectroscopy* a direct correlation to the defect's chemical structure is possible,

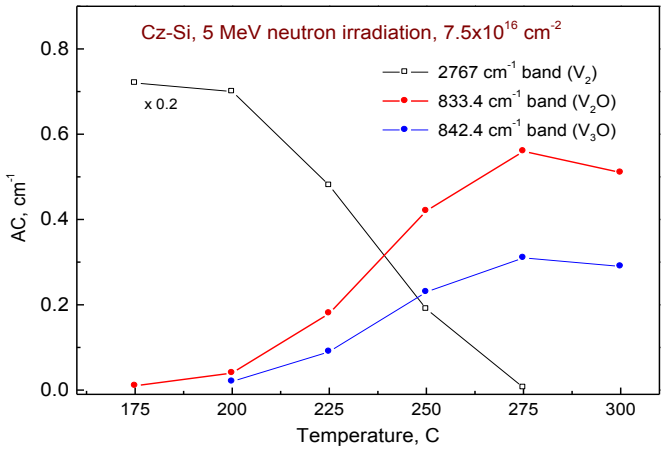

Figure 8.5.7.: Annealing behaviour of the concentrations of V_2, V_2O and the V_3O obtained via IR-*spectroscopy*. Taken from [112].

a correlation of the V_3 and V_3O-complexes with $E4/E5$ and the L defect is confirmed. Moreover, Markevich et al. [104] performed measurements with Laplace DLTS on electron irradiated Cz silicon, investigating the $E4/E5$ defect levels. There, also ab initio modeling was performed resulting in the atomic structure of V_3 and V_3O and their energy levels in the band gap. This will be reported here for completeness. As we already know from Sec. 8.4, the V_3 exhibits a bistability. This is reflected in the

atomic structures of V_3 which is shown in Fig. 8.5.8. The planar configuration 8.5.8 (a) gives rise to the known $E4$ ($V_3^{=/-}$) and $E5$ ($V_3^{-/0}$) defect levels. The silicon lattice is well recognisable: silicon atoms are represented by grey spheres, the covalent bonds as black lines and the three vacancies by white spheres. The defect levels in the band gap are represented in Fig. 8.5.10 labelled as b_1 and b_2 in the column $V_3(C_{2v})$.
The *four-fold* configuration of V_3 is displayed in 8.5.8 (b). There the lattice is distorted

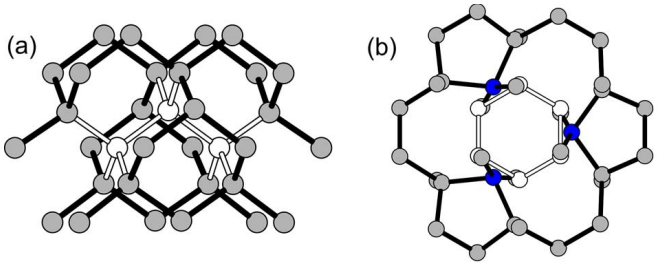

Figure 8.5.8.: Chemical structure of V_3 in the planar (a) and the four-fold (b) configuration. Taken from [104].

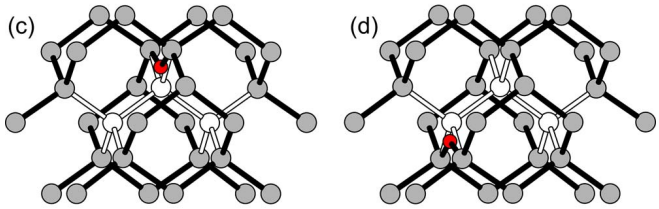

Figure 8.5.9.: Chemical structure of V_3O in two different states, planar stable (c) and metastable (d). Taken from [104].

and the three vacancies can be found at dislocated lattice positions. Three interstitial silicon atoms, represented as dark blue circles changed position and therefore the electrical properties of the defect. This configuration gives rise to a shallow defect level labelled $E75$ [104]. The ab initio modelling of the charge states of the V_3 is shown in Fig. 8.5.10. The *four-fold* configuration gives therefore rise to defect levels at the edge of the band gap labelled as a_1 in column $V_3(D_3)$.

Also the energy in the band gap of the V_3O (L-centre) was calculated from the atomic structure by MARKEVICH ET AL. [104] and is displayed in Fig. 8.5.9. Like in Fig. 8.5.8 the silicon atoms are represented by gray circles, the vacancies in white and the bonds with black lines. Additionally the oxygen impurity is shown as a red circle. As we can see, the V_3O can appear in a planar stable structure (c) and in a metastable structure (d). In Fig. 8.5.10 the simulated levels in the band gap are shown. The levels of the stable structure (c) are displayed in column $V_3O(C_{2v})$ labelled a_1 and b_1. They are attributed to the levels $V_3O^{-/0}$ at $E_C - 0.42$ eV and $V_3O^{=/-}$ at $E_C - 0.28$ eV corresponding to the experimental values of $E_C - 0.455$ eV and $E_C - 0.337$ eV respectively.

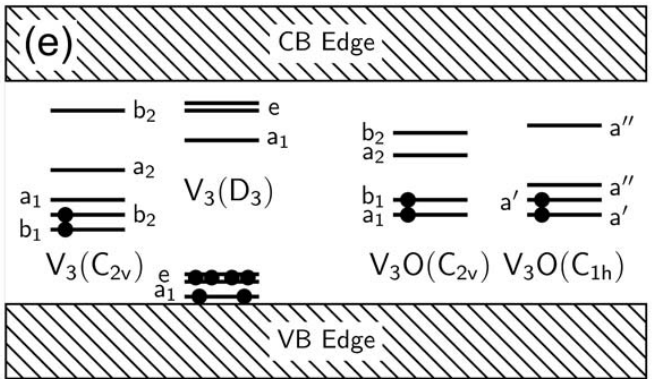

Figure 8.5.10.: Simulation of possible levels of the different configurations of the V_3 and the V_3O. Taken from [104].

Short summery of evidence found in this work for the correct assignment of the $E4/E5$ defect to the V_3 defect and L to V_3O:

- The annealing behaviour of $E4/E5$ is similar to the annealing behaviour of the V_2
  - Similarity found in temperature dependence of the annealing
  - Similarity found in the oxygen dependence of the defect
  - Confirms vacancy-like character of the $E4/E5$ defect
- Transformation of $E4/E5 \rightarrow L$-centre similar to $V_2 \rightarrow V_2O$
  - Similarity found in temperature dependance of reaction
  - Similarity found in the oxygen dependence of the reaction
  - L-centre can be attributed to the V_3O-complex
- V_3 exhibits a bistability, so does $E4/E5$
- Simulation of the reaction kinetics of the $E4/E5$ annealing will be shown in Sec. 8.5.3

8.5.3. Activation energy for migration of the V_3 defect

The V_3 is a defect with two configurations, which lead to several levels in the band gap. The planar configuration is created during irradiation and gives rise to the defect levels $E4/E5$. These two levels change their configuration to the *four-fould* configuration with the level $E75$ [104] during low temperature annealing (eg. 80 °C). The activation energy, needed to form the $E75$-configuration was analysed by Bleka et al. [99]. In his work it was assumed that the $E4/E5$ defect was annealing out. The configurational change was described in 8.4. The "real" annealing-out of the V_3 defect happens at high temperatures above 200 °C, and the defect transforms into the L defect (V_3O) in oxygen rich material, as discussed in Sec. 8.5.2. The activation energy for the annealing of the V_3 could not be obtained so far without the knowledge of the bistability. This is essential for simulations of reaction kinetics of defects in silicon.
There might be no direct application of the results achieved by annealing studies above 200 °C, concerning HL LHC experiments. However, the knowledge of activation energies and annealing dependencies helps to understand the reason for the changes of sensor properties during the lifetime of such detectors.
The temperature dependence of the rate constant for an annealing process is given by the *Arrhenius relation* (see Eq. 4.8.3)

$$k_1 = k_0 \exp\left(-\tfrac{E_a}{k_B T}\right),$$

with the frequency factor k_0 and the *activation energy* E_a for *migration* or *dissociation*. The effect of temperature on the rates of chemical reactions, can be deduced from *Arrhenius plots*. This plot displays the logarithm of a rate constant ($\ln(k_1)$) as function of the inverse temperature ($1/T$). For a single rate-limited thermally activated process, the *Arrhenius plot* is a straight-line, from which the activation energy (E_a) and the frequency factor can both be determined. We can follow the formation and the dissociation process of the V_3O via the reaction

$$V_3 + O \rightarrow V_3O \rightarrow \text{dissociation fragments} \tag{8.5.9}$$

with the annealing techniques explained in Sec. 8.5. This includes annealing at a fixed temperature and subsequent injection of a high forward current in order to restore the planar configuration of the $E4/E5$ defect. With the help of Eq. 4.8.6 it is then possible to describe the full reaction.
In order to obtain the rate constant, three 300 µm thick MCz sensors irradiated with $\Phi = 6 \times 10^{11}$ cm^{-2} 1 MeV neutrons were isothermally annealed at 220 °C, 230 °C and 240 °C. The temperature dependence of the reaction is reflected in the change of the time constant of the annealing process. The concentration deduced from the $E4$ defect vs. the annealing time can be fitted by the expression

$$[Y] = [A] + [E4]_0 \cdot \mathrm{e}^{-k \cdot t}, \tag{8.5.10}$$

where A denotes the background signal in the DLTS spectra, $[E4]_0$ is the $E4$ defect concentration, $\tau = 1/k$ is the annealing time constant, Y the concentration and t the annealing time. The annealing is illustrated in Figs. 8.5.11 (a) for 220 °C, (b) 230 °C and (c) 230 °C. Parameters from the fit are given in Tab. 8.5.2. The resulting time constants τ of the annealing and the fit parameters are presented in Tab. 8.5.2.

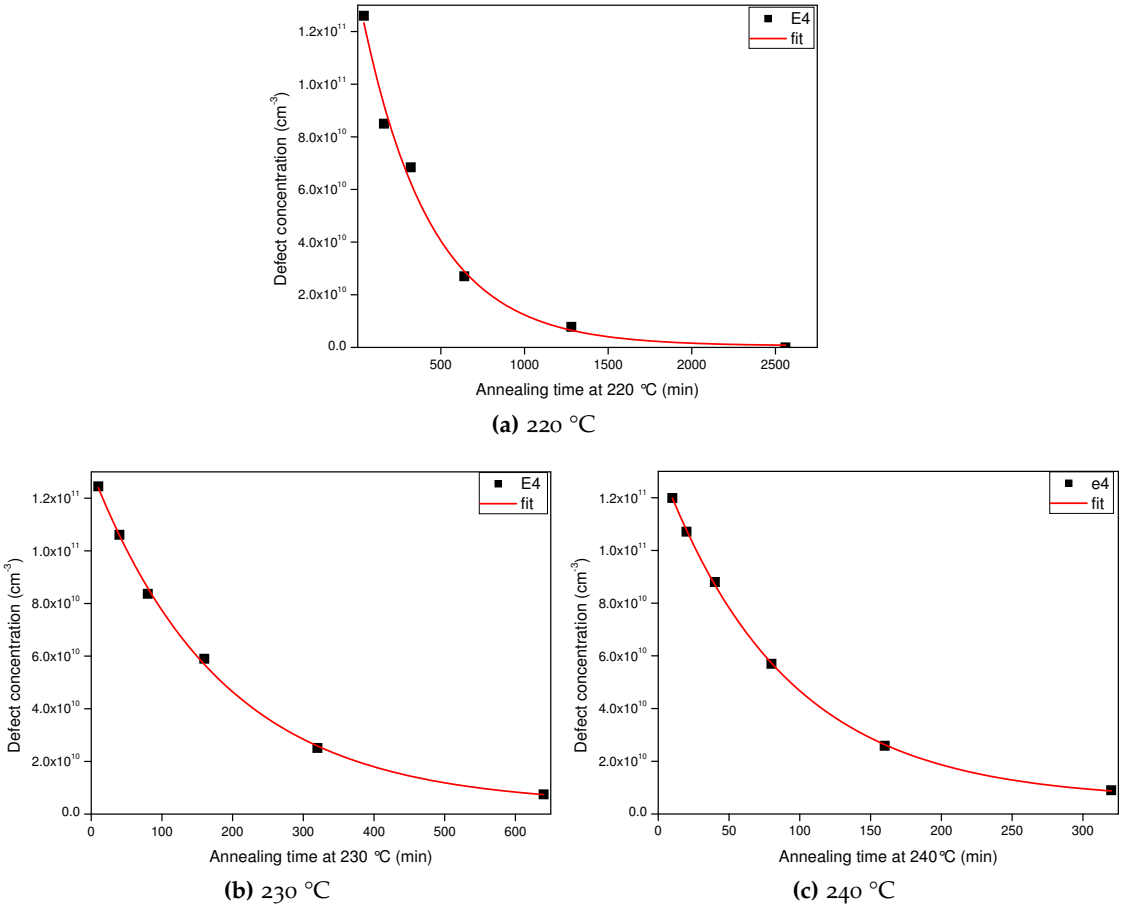

(a) 220 °C

(b) 230 °C

(c) 240 °C

Figure 8.5.11.: Annealing out of the $E4$ defect during isothermal annealing. Further information see text. Fitting results are given in Tab. 8.5.2.

T_{ann} (°C)	[A] (10^9 cm^{-3})	$[E4]_0$ (10^{11} cm^{-3})	τ (min)
220	1 ± 3	1.24 ± 0.03	475 ± 38
230	4 ± 2	1.30 ± 0.03	184 ± 10
240	5 ± 1	1.28 ± 0.01	88 ± 2

Table 8.5.2.: Parameters for the out-annealing of the $E4$ defect obtained by fitting of Eq. 8.5.10 to the experimental data in Fig. 8.5.11. T_{ann} is the annealing temperature and the errors result from the parameter fit.

Fig. 8.5.12 illustrates the *Arrhenius plot* for the evaluated MCz samples, providing the activation energy E_a from the slope of the linear fit, and the pre-exponential factor from the intersect with the ordinate axis. The results for the activation energy E_a and the frequency factor k_0 are summarised in Tab. 8.5.3.
The fitting-error of the *Arrhenius plot* takes into account the fitting-errors of the annealing out of the $E4$ defect which are lower than 10 %. However, it is still the dominating cause of error, as the accuracy of the annealing temperature is about 2 K (about 1 %). The accuracy may benefit from a fourth data point for the *Arrhenius plot* from

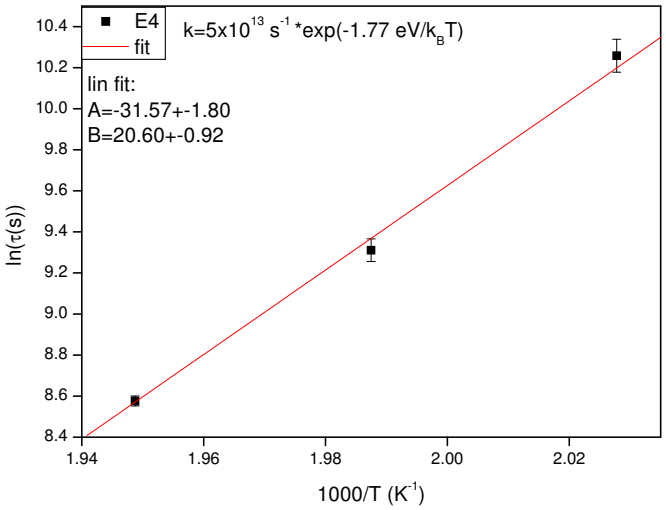

Figure 8.5.12.: Annealing kinetics of the $E4$ defect at three different temperatures. The linear fit indicates a first- order kinetics.

the annealing of a sensor at 250 °C. This fourth measurement process is already in progress, but since it takes monthes to perform these test measurements it could not be finished in time for this work.

Defect	E_a (eV)	k_0 (s^{-1})	
V_3 migration	1.77 ± 0.08	5×10^{13}	$+8 \times 10^{12}$ -3×10^{14}

Table 8.5.3.: Results for the out-annealing of the V_3 from a fit to the data points shown in Fig. 8.5.12. Given are the activation energy for migration E_a and the pre-exponentioal factor k_0.

The energy barrier for migration of the $E4/E5$ defect (V_3) differs strongly from the activation energy of the migration of the V_2 of $E_a = 1.3$ eV given by Pellegrino et al. [110]. In principal, the value of $E_a = 1.77$ eV matches the expected values for the studied reaction. It is lower than the activation energy for migration of V_2O

of $E_a = 2.02$ eV presented in [108] and higher than the activation energy $E_a = 1.3$ eV for the change of the V_3 defect configuration from planar to four-fould, given by Bleka [99]. As mentioned earlier, the activation energy for migration of the V_2 was obtained by Pellegrino et al. from silicon irradiated with 5.6 MeV ^{28}Si ions, which leads to a defect layer directly beneath the surface. This may lead to a deviation from the values obtained by a homogeneously irradiation with neutron irradiation, performed in this work.
The frequency factor $k_0 = 5 \times 10^{13}$ s^{-1} gives further information about the nature of the process because k_0 is related to the *attempt-to-escape frequency*. It can be approximated with help of the *Debye frequency* which is given by $\approx k_B T/h = 2.1 \times 10^{10} \times T$ [K] s^{-1} [113, 114]

$$k_0 = \delta \cdot \frac{k_B T}{h} \tag{8.5.11}$$

The δ describes the character of the reaction, whether it is due to a dissociation process ($\delta \approx 1$ stands for a single jump process) or due to migration of one defect over long distance ($\delta \ll 1$). Moreover, $1/\delta$ indicates the number of jumps needed to fulfill the reaction. The value found in this work ($k_0 = 5 \times 10^{13}$ s^{-1} and T=220 °C), results in $\delta = 5$. Because oxygen is quite stable, the trivacancy-defect migrates until it finds an oxygen atom. Thus this value is very unlikely and a value far below 1 is expected. The frequency factor is not very reliable due to the large extrapolation in the *Arrhenius plot*. An error of one order of magnitude is normal. However, a fourth point in the *Arrhenius plot* would increase the reliability of the frequency factor and probably improve the possibility to draw a conclusion from this information.

8.5.4. Properties of the bistability

An important question about the configurational change of the V_3 defect is, whether the parameters of the forward current injection are optimal. Therefore a study was performed, investigating the properties of the reconfiguration of the defect. The following data were obtained during the co-supervision of the bachelor thesis of C. Neubüser [115].
R. M. Fleming et al. treated the transistors with 1 A forward current (12.5 A cm^{-2}) for 20 minutes, in order to get back the full concentration of the $E4/E5$ defect [101]. For diodes these parameters may differ. The parameters for diodes can be obtained from C-V/I-V measurements on samples injected with different filling times and filling currents. The knowledge of the parameters may also hint at the mechanisms for the change of the configuration. As one of the configurations produces current, whereas the other one does not, it also may give information about the current generation mechanism.
Test proceedure
The study was performed, based on the systematic explained in the following. First, the diode needs to be in a stable annealing situation. In a next step it must be verified

that V_3 is in the non-current-generating *four-fold* configuration $E75$. Then a forward current is applied under cooling, to suppress annealing of the planar configuration due to the temperature increase caused by the power dissipation during forward injection. The temperature was chosen to be 0 °C. Subsequently C-V/I-V measurements at 20 °C have been performed, followed by further annealing at 80 °C, reestablishing the stable situation. Then the next injection can be performed on the same diode.

Results

Four 300 µm thick MCz diodes irradiated with 1-3 $\Phi = \times 10^{11}$ n cm^{-2} were used to investigate the recovery of the planar configuration of the $E4/E5$-levels. All diodes were pre-annealed for 30 minutes at 180 °C in order to remove the $E205a$ defect and to obtain a stable situation for further 80 °C annealing. The first parameter under investigation is the magnitude of the injected forward current, for injection times of 10 and 20 minutes. Table 8.5.4 shows the chosen forward current values for two different time intervals.

time (min)	forward current (A)								
10	0.001	0.010	0.020	0.050	0.100	0.200	0.500	1.000	2.000
20	-	0.010	0.020	0.050	0.100	0.200	0.500	1.000	-

Table 8.5.4.: Forward current pulses for 10 and 20 minutes current injection.

The result of the treatment is shown in Fig. 8.5.13 (a). Black squares illustrate the leakage current recovery as function of the injected forward current for 10 minutes while the red circles represent the condition for 20 minutes. For 10 minutes injection the leakage current starts to be recovered at about 20 mA. For 1 and 10 mA no sign of recovery is observed, and therefore, 10 mA can be seen as a lower limit. By increasing the forward current also the fraction of recovered leakage current increases. At around 1 A a saturation is found.

Increasing the forward current to 2 A does not further increase the recovery of the defect, which is most likely due to annealing effects. Although the diode was kept at 0 °C during the injection, at about 8 V and 2 A forward current the power dissipation in the diode is about 16 W. At 16 W the heat production is high enough for self-annealing effects.

The 20 minutes injection shows a slightly faster increase of the recovered leakage current compared to the values found after 10 minutes in the range of 20 mA to 200 mA. Already at 500 mA the prolonged treatment shows no change of the value reached after 10 minutes. This supports the idea of a saturation value. The next question is how long the current needs to be applied to recover the maximal leakage current or the full concentration of $E4/E5$. For that reason two fixed forward current values were chosen whereas injection times were varied. Table 8.5.5 shows the injection times that were used.

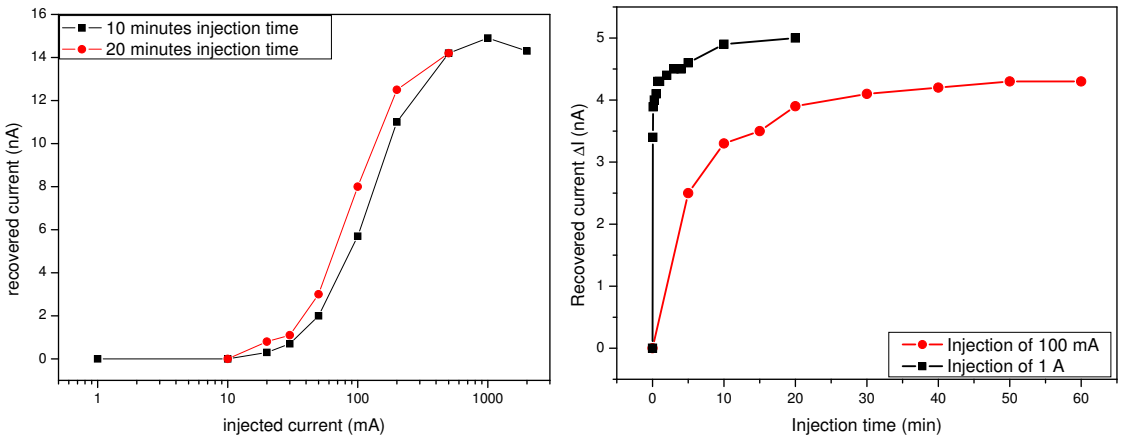

Figure 8.5.13.: Recovery of leakage current as function of the variation of current filling pulses for 10 and 20 minutes (a) and for the variation of the filling time for 100 mA and for 1 A (b) in order to recover the planar configuration of the V_3. Material: MCz 300 µm irradiated with 3 $\times 10^{11}$ n cm^{-2} (a) and 1 $\times 10^{11}$ n cm^{-2} (b).

forward current (A)	injection time (min)									
1	0.05	0.10	0.75	1	2	3	5	8	10	20
0.1	5	10	15	20	30	40	50	60		

Table 8.5.5.: Variation of the forward current injection times for 100 mA and 1A.

The result is displayed in Fig. 8.5.13 (b). The 1 A injection is given by the black squares and the 100 mA is shown as red circles. Already the first injection step after 3 seconds at 1 A causes a recovery of the leakage current of more than 50 %, after 1 minute it is more than 80 %. Since the recovery of the leakage current is also a measure for the recovery of the $E4$ and $E5$ defect, it can be supposed, that the defect concentration was recovered in the same way. No significant change can be observed between 10 minutes and 20 minutes injection time at 1 A. Again the information we obtain from this measurement is a saturation value for the 1 A forward current injection. In comparison to the 1 A, the 100 mA recovery is reduced and much slower. 50 % of the current compared to the 1 A measurements is recovered after 5 minutes forward current. The increase of the leakage current continues up to 50 minutes and seems to stay constant beginning from 50 minutes. Extrapolating from the slope, the level of 100 % current recovery is never reached.
A comparison of the total number of injected charge carriers $[N]$ during 10 minutes at 1 A and 100 minutes at 100 mA is calculated to $[N] = 3.7 \times 10^{21}$ charge carriers (see Tab. 8.5.6) for both procedures. But as can be seen in Fig. 8.5.13 (b) The extrapolation of the 100 mA curve to 100 minutes will never reach the same value like it is seen after

10 minutes at 1 A. The interpretation of the behaviour is given by the clustering effect which is explained in Sec. 7.2.4. The electrical potentials of the surrounding damaged region shields the $E4/E5$ defect from being filled by electrons. Both curves show a dip in the rising edge, around 4-5 minutes in the 1 A curve and 15 minutes in the 100 mA curve. The dip is not a measurement artifact but something which points to other processes in the filling behaviour. This again hints to a clustering effect.
The charge carrier density per second $[n]$ in the diode can be roughly estimated by

$$[n] = \frac{I}{Vol \cdot q_0}, \tag{8.5.12}$$

and the total number of charge carriers N being injected by the current I or the current density $J = I/A$:

$$[N] = \frac{I \cdot t}{q_0}, \tag{8.5.13}$$

for the given volume $Vol = A \cdot d$ of the diodes.
The results for $[n]$ and $[N]$ for t=10 min and t=20 min for a 280 µm thick diode are displayed in Tab. 8.5.6. A comparison of the calculated charge carrier densities and the total number of charges with Figs. 8.5.13 (a) and (b) reveals that the carrier density $[n]$ strongly influences the filling conditions of the sensor. The total injected charge $[N]$ does not influence the saturation value in the same way, as the saturation value is different even if the total injected charge is similar. The charge carrier density $[n]$ has a higher impact on the recovered current than the total number of charge carriers $[N]$. Again the clustering effect is considered to be responsible for the behaviour.

I (A)	J [A· cm^{-2}]	n (mm^{-3}s^{-1})	N (t=10 min)	N (t=20 min)
0.01	0.04	9.01 $\times 10^{15}$	3.74 $\times 10^{19}$	7.49 $\times 10^{19}$
0.02	0.08	1.80 $\times 10^{16}$	7.49 $\times 10^{19}$	1.50 $\times 10^{20}$
0.1	0.40	9.01 $\times 10^{16}$	3.74 $\times 10^{20}$	7.49 $\times 10^{20}$
0.2	0.80	1.80 $\times 10^{17}$	7.49 $\times 10^{20}$	1.50 $\times 10^{21}$
0.5	2.00	4.51 $\times 10^{17}$	1.87 $\times 10^{21}$	3.74 $\times 10^{21}$
1.0	4.00	9.01 $\times 10^{17}$	3.74 $\times 10^{21}$	7.49 $\times 10^{21}$
2.0	8.00	1.80 $\times 10^{18}$	7.49 $\times 10^{21}$	-

Table 8.5.6.: Charge carrier density $[n]$ and total number of injected charges $[N]$ for various injected currents I and current densities J for injection times t, calculated for a diode with area $A = 25$ mm^2 and thickness $d = 277$ µm.

The potentials of the surrounding damaged region needs to be overcome which is only possible with high current densities. The dips in the beginning of the recovered current curves in Fig. 8.5.13b might be related to a clustering effect.

8.5.5. Influence of the disordered region on leakage current generation

It was shown in Sec. 8.4 that the leakage current after fast hadron irradiation is caused by defects in the detector bulk. The identification of the defects could be achieved by performing isochronal annealing studies on irradiated sensors. The annealing out of the leakage current was correlated with the defect concentrations of two defects. A major quantity of the current generation was attributed to the *E*5 level. Due to a bistability this level anneals even at moderate temperatures between 20 °C and 100 °C into another configuration (*E*75). It was possible to assign this defect level to the tri-vacancy-complex in the previous chapter. The stable *E*75 level was attributed to the *four-fold* configuration, leading to a level in the band gap which does not generate current since it is too shallow.
Between 140 °C and 180 °C the defect labelled as *E*205*a* anneals out. This defect is also

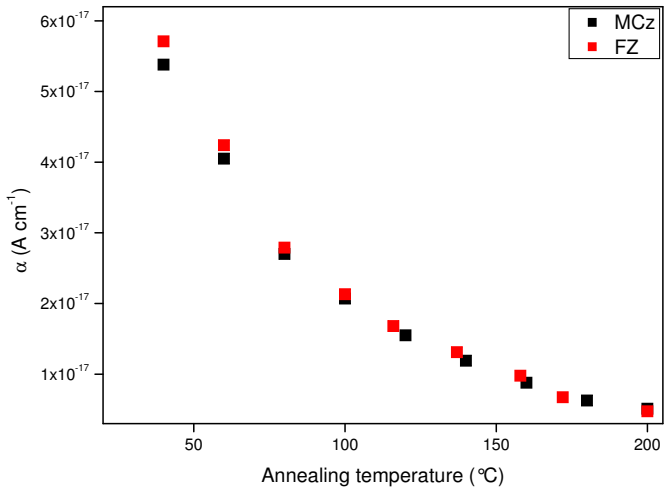

Figure 8.5.14.: Comparison of the normalised current related damage rate obtained from the current at full depletion in 280 µm thick standard FZ and MCz material. Original fluences MCz: $\Phi = 6 \times 10^{11}$ n cm^{-2}, FZ: $\Phi = 3 \times 10^{11}$ n cm^{-2}

correlated to the annealing of leakage current. It was found, that this defect is less effective in the current production. The chemical structure of the *E*205*a* level was not revealed so far, but due to the similarity of the defect properties with that of V_2 and V_3 it is assumed that this defect is V_4 or another multi-vacancy.
Different from the two defects that anneal at defined temperatures, the leakage current shows a continuous decrease between 80 °C to 200 °C. Figure 8.5.14 illustrates the annealing of the current related damage rate α calculated from the leakage current at full depletion for 280 µm thick FZ (red) and MCz (blue) material. The isochronal annealing was performed in steps of 20 °C. The curves look very similar, this behaviour is in accordance with the assumption that the *E*4/*E*5 defect (V_3) is created with the same introduction rate in oxygen rich and oxygen lean material ([49, 82]).
There is no defect observed by DLTS that can be correlated to the decrease of leakage

current between 100 °C and 140 °C annealing, as displayed by the current related damage rate illustrated in Fig. 8.5.14. The decrease of the leakage current (and thus α) must be a result of either an unknown defect that is not visible in DLTS or an unaccounted further reason.
The first option is unlikely, for the latter more insight into this problem may be given by looking at the behaviour of the recovery of $E5$ and the corresponding current at full depletion I_{rec} or α_{rec} after 1 A forward current injection.
We already know from the previous section, that V_3 anneals out differently for oxygen rich and oxygen lean material. Figure 8.5.15 illustrates the annealing behaviour and

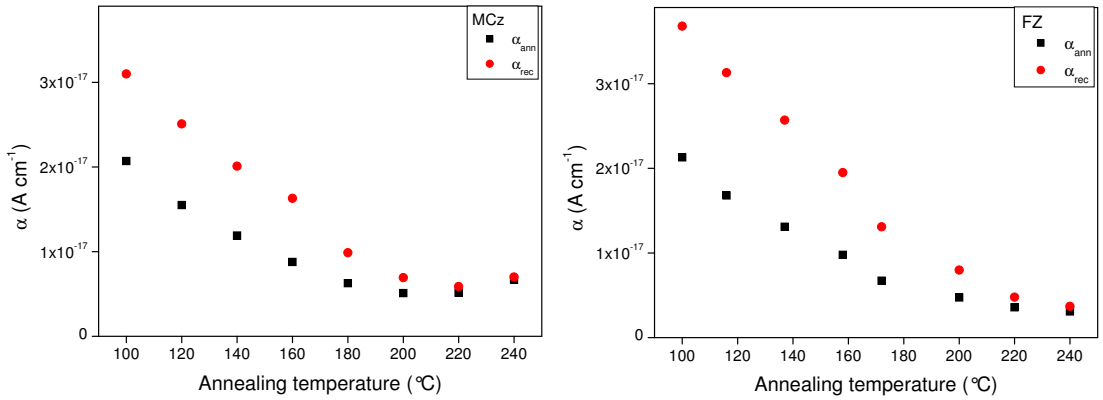

(a) MCz **(b)** FZ

Figure 8.5.15.: Current related damage rate α versus annealing temperature for isochronal annealing steps for MCz (a) and FZ (b) material. α_{ann} denotes the situation directly after the annealing step and α_{rec} after the injection of 1 A, when the current is recovered.

the recovery of the current related damage rate α calculated from the leakage current for oxygen rich MCz material (a) and oxygen lean FZ material (b) as function of the annealing temperature. The annealing procedure explained in chapter 8.5 was used, with the difference that the microscopic measurements were omitted. The black squares present the behaviour directly after annealing (α_{ann}), while the red circles denote the result after the injection with 1 A forward current and the resulting recovery of $E4/E5$ (α_{rec}). For both materials it is observed that $\alpha_{rec} > \alpha_{ann}$ between 100 °C and 200 °C. Furthermore it is seen that α_{ann}(MCz)$\simeq$ α_{ann}(FZ) and α_{rec}(MCz)$<$ α_{rec}(FZ). α_{ann} continuously decreases as expected from Fig. 8.5.14 but also α_{rec} continuously decreases between 100 °C up to 200 °C.
For a more detailed comparison of the recovery of the current related damage rate α_{rec} the difference between α_{ann} and α_{rec} was calculated: $\Delta\alpha = \alpha_{rec} - \alpha_{ann}$. In this way the annealing of the $E205a$ is disregarded between 140 °C and 180 °C. The resulting $\Delta\alpha$ is illustrated as a function of the annealing temperature T_{ann} in Fig. 8.5.16. FZ is illustrated with blue squares, MCz with red circles.

$\Delta\alpha$ decreases between 100 °C to 200 °C. In general, it is observed, that the recovered

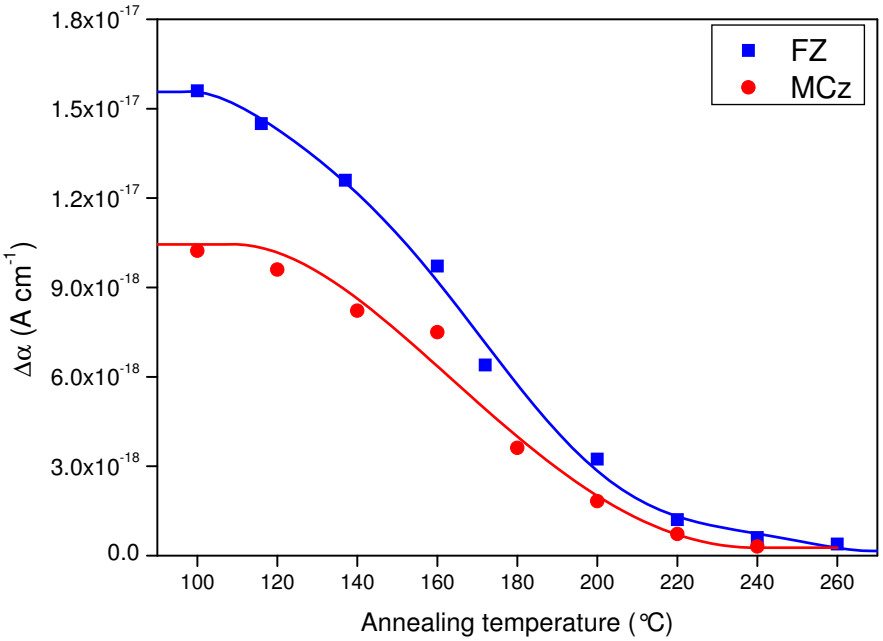

Figure 8.5.16.: Difference of the damage parameter α during isochronal annealing before and after the recovery of I_{leak} for FZ and MCz samples as shown in Fig. 8.5.15. In contrast to this result, the concentration of $E4/E5$ stays constant up to 200 °C.

current in the FZ material is higher than in MCz material $\Delta\alpha$(MCz)<$\Delta\alpha$(FZ), but with a similar slope.
In conclusion, the $E5$ defect concentration measured by DLTS after the recovery stays constant up to $T_{ann} \approx 200$ °C, depending on the oxygen concentration of the material. However, $\Delta\alpha$ does not stay constant and the recovered part of the leakage current decreases independent of the material. This indicates, that the efficiency of the $E5$ generation rate decreases with increasing T_{ann}.
A possible explanation can be found in the clustering effect, which was introduced in Sec. 7.2.4. Vacancy defects like V_3 or V_2 are mainly created inside the disordered regions (cluster) after hadron damage. This is simulated in *Monte-Carlo* calculations performed by HUTHINEN [36]. The charge carrier generation rate of V_3 inside the cluster is different from those being outside due to processes like the *inter-center charge transfer*. It can be assumed that with increasing temperature also the disordered regions partly anneal out in such a way that the probability for *inter-center charge transfer* decreases, without changing the total number of defects visible in DLTS. The defect properties (capture cross section and emission rates) approaches the values for isolated point defects during this annealing process.
The suppression of the signal heights of point defects like VO or V_2 as indicated in Sec. 8.1 is a consequence of the influence of the disordered region on the defect properties.

Similarly, it is well visible for the suppression of the signal heights of the doubly charged states of the divacancy ($V_2^{=/-}$) or the trivacancy ($V_3^{=/-} = E4$) compared to their signal heights after some annealing.

9. Defects with impact on the effective doping concentration

The operational bias voltage of silicon sensors in HEP experiments is an important parameter for the design of a detector. Powering, cabling and electronics need to be designed for the requirements of electronics and the biasing voltage of the sensors. Currently bias voltages up to 500 V are used in the silicon tracker of the CMS detector, but the possibility of higher voltages for future experiments is under discussion, due to the finding of charge multiplication effects at high voltages in silicon sensors [20–23]. High voltage concepts need to be taken into account during the design phase of the experiment. A belated upgrade of the requirement, e.g. a change of the max. voltage, is difficult. Therefore it is very important to know the change of the depletion voltage due to radiation damage and the requirements of the silicon sensors during the operating time of the LHC.
In chapter 4 we learned that the impact of radiation damage on the leakage current is the same for neutrons and pions when normalised to 1 MeV equivalent fluence. In contrast to that it was shown that the radiation induced change of the effective doping concentration and thus the voltage for total depletion depends on the particle type and the oxygen content of the sensor material. Therefore the particle composition of the radiation environment inside the silicon tracker will have an impact on the long term changes of the full depletion voltage. From Fig. 1.0.1 in chapter 1 it can be seen that the total fluence of the HL LHC experiments as well as the particle composition depend on the distance to the interaction point. In the first 10 cm, the damage is mainly created by pions, while in the more outer layers, the backscattered neutrons dominate.
A precise knowledge of the peculiarities of damage created by neutrons and pions allows to predict the evolution of the depletion voltage V_{dep} and therefore the effective doping concentration N_{eff} during the operating time of the detector.
The sensors are cooled to low temperatures (planned for example -10 °C for CMS tracker, -10 °C for ATLAS pixel) during operating times, while kept at room temperature during short maintenance times. This thermal energy is sufficient to start defect migration and the formation of new complexes. A prediction of the impact of defect creation due to annealing will help to optimise the detector concept for specific radii.
A big step towards the understanding of the change of the N_{eff} was recently achieved by Pintilie et al. in [55, 97] and subsequently during this work. Pintilie discovered a group of cluster defects created by fast hadron irradiation that were found to be the origin of the change of the space charge. The understanding of these crystal

defects will help to improve the stability of the voltage needed to operate the sensors properly. Furthermore, the knowledge of the chemical structure of these defects could help to find ways to deactivate harmful defects via defect engineering.
In contrast to the increase of the leakage current after hadron irradiation, the depletion voltage and (via Eq. 3.4.5) also the effective doping concentration N_{eff} does not increase linearly with the fluence. A detailed comparison of neutron irradiated epitaxial, FZ and MCz materials for a large fluence range can be found in the diploma thesis of Koch [116].
As explained in chapter 5, N_{eff} is composed of the initial phosphorus concentration ($N_{eff,0}$) and the radiation induced donors (N_D) and acceptors (N_A):

$$N_{eff} = N_{eff,0} + \sum N_D - \sum N_A. \tag{9.0.1}$$

The impact of neutron and proton irradiation on N_{eff} as a function of the fluence is illustrated in Fig. 9.0.1. The samples used for this figure are 75 µm thick oxygen enriched Epi-Do diodes. The N_{eff} was obtained from C-V measurements, taken after 8 minutes

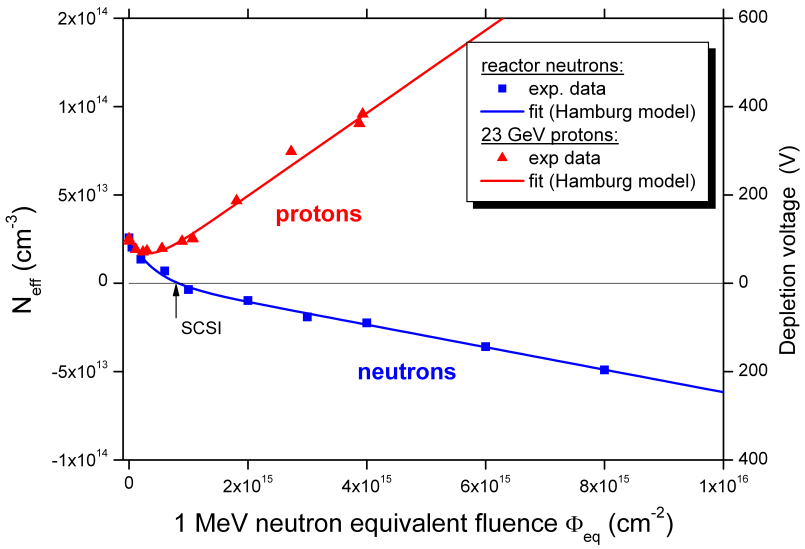

Figure 9.0.1.: Effective doping concentration of 75 µm thick Epi-Do diodes after irradiation with neutrons and protons. Data originally published in [97].

at 80 °C annealing. Blue squares present the dependence of the neutron irradiated samples on the fluence. They experience type inversion after $\Phi_{eq} \approx 8 \times 10^{14}\,\mathrm{cm}^{-2}$. In contrast, the proton irradiated samples, denoted in red, show no type inversion. After $\Phi_{eq} = 2 \times 10^{14}\,\mathrm{cm}^{-2}$ irradiation a compensation of the irradiation induced acceptors occurs and the positive space charge increases.
It has been proven also by charge collection measurements that the proton irradiated

diodes do not undergo type inversion (see Diploma thesis by LANGE [15]), but looking at the right hand side scale of Fig. 9.0.1 a strong increase of the depletion voltage can be observed. An extrapolation of the depletion voltage results in around 1000 Volts after Φ_{eq} =1 $\times$ 10^{16} cm^{-2} proton irradiation. For HL LHC experiments, this high depletion voltage would lead to severe problems operating those structures. However, after neutron irradiation the depletion voltage increases only moderately.
The opposite behaviour of the proton and neutron irradiated diodes can only be explained by the different generation rates of defects created by each type of irradiation. The following chapter deals with the results of microscopic analyses of irradiated samples. The general idea behind those defect studies is to identify the differences in the defect creation induced by neutron and proton irradiation. With this knowledge it will be possible to predict the evolution of the N_{eff} for HL LHC scenarios and select the optimal material for the application.
Defects which are charged at room temperature contribute to the space charge, acceptors contribute negatively while donors contribute positively. PINTILIE [55] found a group of deep acceptors, which are negatively charged at room temperature. Two overlapping deep acceptors labelled $H(140K)$ and $H(151K)$ were earlier assigned to the C_iO_i defect. Those two defects and the $H(116K)$ labelled third deep acceptor are created only by hadronic and high energy electron irradiation, hence can be attributed to extended or cluster related defects. Another two defects were found to be donors which contribute with positive sign to the effective space charge. In this work, highly neutron irradiated samples will be analysed referring to those defects, revealing a more complex picture of the formation and analysis of defects after high irradiation fluences.
From former investigations of the ROSE collaboration [98] it is known, that the oxygen content of silicon material influences the change of the effective doping concentration of silicon sensors after ^{60}Co-γ and charged hadron irradiation. A brief review of ^{60}Co-γ results (from ROSE) is given in section 7.3. The impact of oxygen on the formation of defects was a very important result of the previous investigations. The influence of oxygen on the N_{eff} after hadron irradiation will as well be discussed in the following chapter.

9.1. Change of the N_{eff} with particle type and impurity content

Fig. 9.0.1 already illustrated the influence of irradiation with different particle types on the N_{eff} in oxygen rich epitaxial sensors. The data points achieved during this work were added and are pictured in Fig. 9.1.1 (a). Data points that were published in Fig. 9.0.1 are denoted with small symbols, while newly added points are denoted with large symbols. The Epi-Do data points (protons: red triangles, neutrons: blue squares) are compared with oxygen lean Epi-St samples (open stars in the same colour-code).

The fluences values of the former neutron data are not corrected with the current related damage rate α and have an error of ten percent, the fluence of the newly added neutron data and all proton data points were corrected with the help of Eq. 5.2.1 and the current related damage rate $\alpha = 4 \times 10^{-17}$ A $\cdot$ cm^{-1}.
Overall, the Epi-St samples behave quite similar to the Epi-Do samples for neutron irradiation[1]. However, the Epi-St samples show a slightly faster negative increase of the space charge and undergo type inversion earlier than the corresponding Epi-Do samples, as can be seen in the close-up view in Fig. 9.1.1 (b). The situation is different for proton irradiated diodes. Here, N_{eff} of the Epi-St and Epi-Do samples reveal no dependance on the oxygen concentration of the test-materials for fluences up to Φ=1 $\times$ 10^{15} cm^{-2}, see Fig. 9.1.1 (b). For high fluences for Epi-St, there is only one data point available, at Φ=4 $\times$ 10^{15} cm^{-2}. This value yields a much lower effective doping concentration compared to the Epi-Do samples. Further points need to be added, in order to confirm this trend. Moreover, a study with mixed irradiation of protons and neutrons combined would be interesting, to show if the damage adds up, or if compensation effects would result in a much more moderate increase of the effective doping concentration after high irradiation fluences. Studies concerning the collected charge after mixed irradiations were performed by Kramberger et al. on MCz and FZ material [117]. The author suspects compensation processes in MCz material to be the reason for the results of the collected charge measurements.
In conclusion, the difference observed between oxygen rich and oxygen lean neutron irradiated samples is small. Nevertheless, for proton irradiated sensors, the one oxygen rich sample results in a higher change of the depletion voltage. Unfortunately, there is only one oxygen lean sample irradiated with high proton fluences available for this study.
The isothermal annealing behaviour at 80 °C of the N_{eff} of Epi-Do and Epi-St samples irradiated with three neutron fluences is illustrated in Fig. 9.1.2 (a). The lowest fluence of Φ =5 $\times$ 10^{13} cm^{-2} is pictured with red dots, the intermediate fluence of Φ =2 $\times$ 10^{14} cm^{-2} is shown in blue squares and the highest fluence of Φ =1 $\times$ 10^{15} cm^{-2} is illustrated with black triangles. It is well visible, that the samples irradiated with the highest fluence are type inverted from the beginning while both lower fluences do not undergo type inversion. A more detailed study of the behaviour of N_{eff} during isothermal annealing at 80 °C with respect to its initial value $\Delta N_{eff}(\Phi_{eq,t})$

$$\Delta N_{eff}(\Phi_{eq,t}) = N_{eff,0} - N_{eff}(\Phi_{eq,t}) \tag{9.1.1}$$

is illustrated in Fig. 9.1.2 (b). From this illustration, the lowest fluence of Φ =5 $\times$ 10^{13} cm^{-2} (red dots) shows no difference between Epi-Do and Epi-St samples. In a close view a small difference would appear which might find a reason in the fluence uncertainty. A significant difference is found for the highest fluence of Φ =1 $\times$ 10^{15} cm^{-2}. Note, that the fluences are non-corrected and have an error of about 10 %. The results are

[1] The experimental data at Φ=1.6 $\times$ 10^{15} cm^{-2} and Φ=3.6 $\times$ 10^{15} cm^{-2} after neutron irradiation are taken from Koch [116].

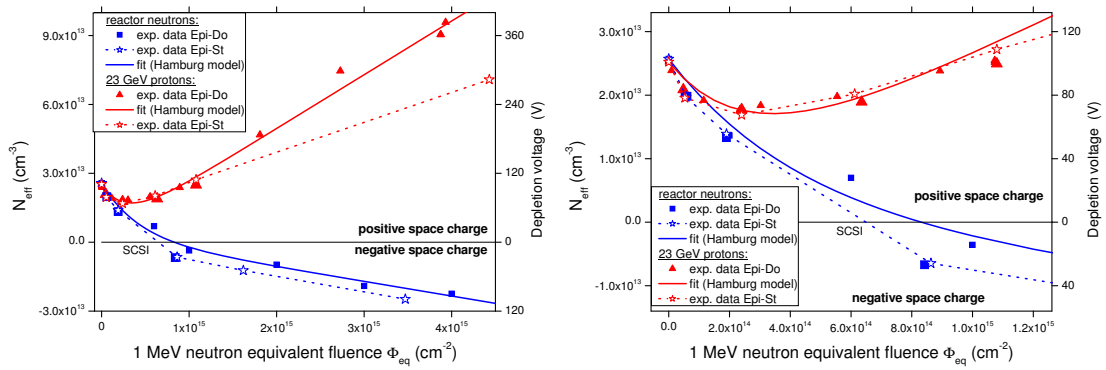

Figure 9.1.1.: Evolution of N_{eff} as function of fluence for neutron (blue) and proton (red) irradiated samples. Oxygen lean Epi-St (open stars) material is compared to oxygen rich Epi-Do (blue squares and red triangles). Most of the data points for Epi-Do were published in [97] and are displayed in Fig. 9.0.1, these data points are denoted with small symbols. Newly measured data points are represented by large symbols.

illustrated with black triangles. While the short term annealing is similar for both samples, the long term annealing for Epi-St starts earlier and is more pronounced. The minimum in ΔN_{eff}, which is attributed to the stable damage constant g_C, is shifting towards higher times for higher irradiations.
For Epi-diodes irradiated with 23 GeV protons the annealing behaviour is shown in Fig. 9.1.3 (a). The presented fluences are 1 MeV neutron equivalent values. The colour code and sym- bols were chosen in the same way as in Fig. 9.1.2. It can be observed that in difference to the neutron irradiated samples, none of the samples undergoes type inversion during the irradiation and during the annealing. For the highest fluence it can be estimated, that the Epi-St sample will undergo type inversion at an annealing time of about 700 minutes at 80 °C. Fig. 9.1.3 (b) illustrates the behaviour of ΔN_{eff}. Here, the difference between Epi-St and Epi-Do is striking. The Epi-St samples show a higher ΔN_{eff} than the Epi-Do samples before or shortly after the start of the annealing. The influence of the oxygen in silicon on the radiation hardness of neutron and proton irradiated diodes during the annealing is not obvious for low fluences. However, for higher fluences (at about $\Phi_{eq} = 1 \times 10^{15}$ cm^{-2}) the difference between the N_{eff} of Epi-St and Epi-Do samples is evident. In particular for proton irradiated samples, the difference between the annealing of Epi-Do and Epi-St is visible throughout the whole annealing procedure (see Fig. 9.1.3). Starting with a difference in the short term annealing followed by a different stable damage constant and a different long term annealing. The neutron irradiated samples show only a deviation between Epi-Do and Epi-St in the long term annealing behaviour (see Fig. 9.1.2).

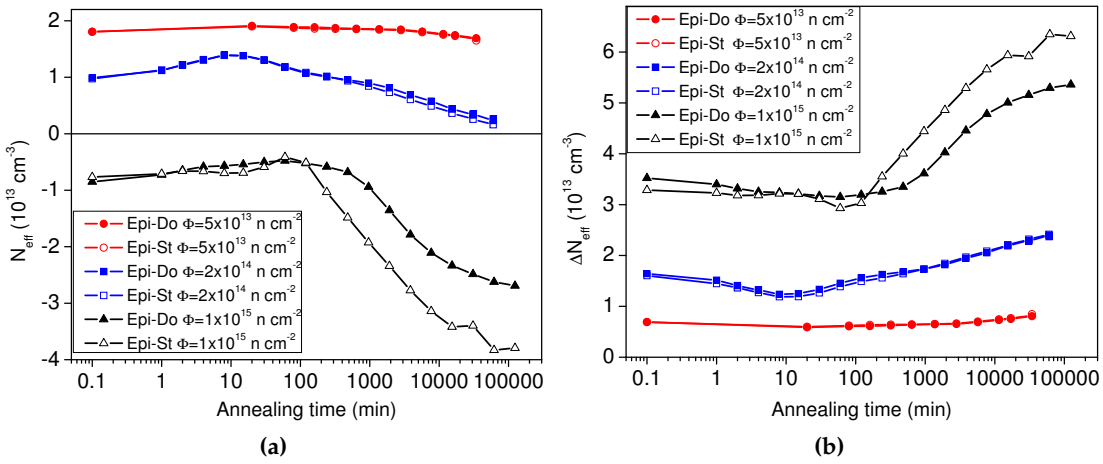

Figure 9.1.2.: Comparison of the annealing behaviour for isothermal annealing studies at 80 °C of the N_{eff} (a) and ΔN_{eff} (b) of neutron irradiated Epi-St (open symbols) and Epi-Do diodes (closed symbols). Three different fluences are presented: $\Phi_{eq} = 5 \times 10^{13}$ cm^{-2} (red), $\Phi_{eq} = 2 \times 10^{14}$ cm^{-2} (blue) and $\Phi_{eq} = 1 \times 10^{15}$ cm^{-2} (black). 0.1 minutes stands for as irradiated.

9.1.1. The Reason for Negative Space Charge - Acceptors

Only defects which are charged at room temperature can contribute to the space charge at room temperature. Those defects which are the reason for the increase of the negative space charge after fast hadron irradiation, and thus cluster related, were recently discovered by Pintilie et al. [55,97]. Three deep acceptor-like hole traps with energy levels in the lower half of the band gap were found to be charged at room temperature.

A Group of Deep Acceptors *(H(116K), H(140K) and H(152K))*

Pintilie [55] investigated neutron and proton irradiated n-type oxygen enriched epitaxial material with a thickness of 75 µm. Three deep acceptors with impact on the space charge at room temperature were discovered. They are presented in Fig. 9.1.4 (a). One of the deep acceptors, labelled $H(116K)$ was previously reported in Moll [32] to be an acceptor with impact on N_{eff}. The two other defects were labelled $H(140K)$ and $H(152K)$ and formerly assigned to the C_iO_i defect, which has no impact on the N_{eff}. Pintilie reported for ^{60}Co-γ-irradiated samples, that the C_iO_i-complex cannot be filled at temperatures below 30 K (see Fig. 9.1.4 (b)). Thus, after filling at low temperatures (T<10 K), the remaining two defects in neutron and proton irradiated test-structures are cluster related and can be analysed properly without the influence of the C_iO_i defect.

Studies performed by Pintilie were carried out on samples with rather moderate neutron fluences of $\Phi = 5 \times 10^{13}$ cm^{-2} and proton fluences of $\Phi_{eq} = 2 \times 10^{14}$ cm^{-2}. For HL LHC applications the most important fluences are above $\Phi = 1 \times 10^{15}$ cm^{-2}. As

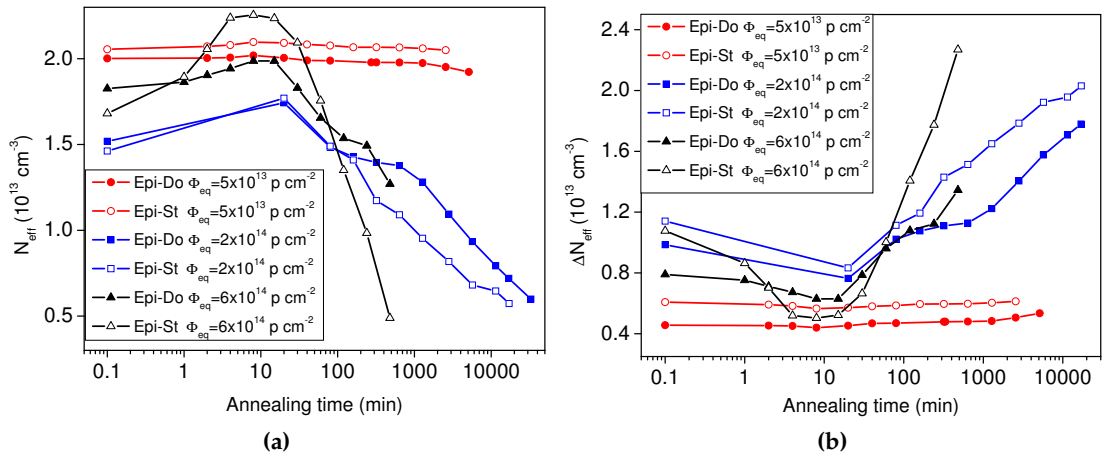

Figure 9.1.3.: Comparison of N_{eff} (a) and ΔN_{eff} (b) of proton irradiated Epi-St (open symbols) and Epi-Do (closed symbols). Three different fluences are presented: $\Phi_{eq} = 5 \times 10^{13}$ cm^{-2} (red), $\Phi_{eq} = 2 \times 10^{14}$ cm^{-2} (blue) and $\Phi_{eq} = 6 \times 10^{14}$ cm^{-2} (black). Note that 0.1 minutes stands for as irradiated and the fluences are not corrected for α.

illustrated in Fig. 9.1.2 (a) the N_{eff} measured by C-V already shows different results for the same material after $\Phi = 1 \times 10^{15}$ cm^{-2} neutron and proton irradiation. Neither a dependence on the oxygen concentration, nor a dependence on the particle type was found so far for the deep acceptors.

Influence of VP

The E-center is the vacancy-phosphorus-complex VP, which builds up during irradiation. This point-defect inactivates the phosphorus doping and reduces the positive space charge, sometimes referred to as *donor removal*. The formation of VP is suppressed in oxygen rich material, because the vacancy couples with the excessive supply of oxygen, forming the VO_i-complex.

$V + P \rightarrow VP$ preferred path for low $[O_i]$ and high $[P_s]$,

$V + O_i \rightarrow VO_i$ preferred path for high $[O_i]$.

It is not possible to determine the concentration of VP by means of TSC measurements, because the defect-signature is located in the cluster shoulder at around 170 K. It is not possible to extract proper concentrations of defect levels in this region by simulation with known levels or by the analysis of difference spectra.

9.1.2. The Reason for Positive Space Charge - Donors

The creation of positive space charge after irradiation can be correlated to the formation of donors. During the investigations of the ROSE collaboration [98], a bistable donor was found and labelled BD defect, which can exist in two different configurations with

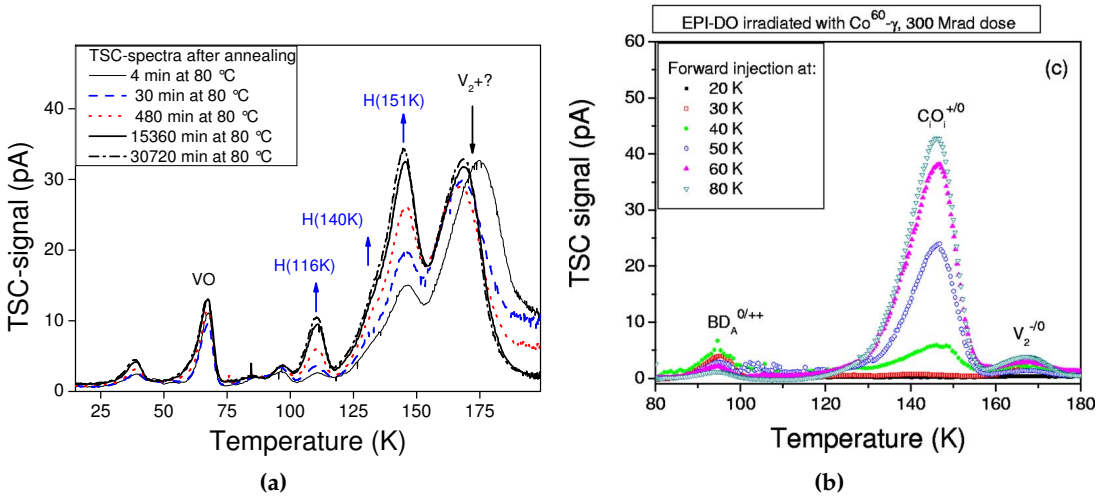

Figure 9.1.4.: TSC spectra illustrating the increase of deep acceptors ($H(116K)$, $H(140K)$ and $H(151K)$) during annealing at 80 °C. Material: Epi-St, fluence: $\Phi = 2 \times 10^{14}$ n cm^{-2}, measurement at $V_{bias} = 300$ V (a). Suppression of the C_iO_i defect in TSC spectra with charge carrier filling at low temperatures in Epi-St material after ^{60}Co-γ irradiation (b), this figure is taken from [55].

different energy levels and charge states $BD_A^{0/++}$ at $E_C - 0.255$ eV [94] and $BD_B^{+/++}$ at $E_C - 0.12$ eV. The bistability and the *double donor* character resulted in the identification with the known *thermal double donor* $TDD2$ [86]. This defect is strongly depending on the oxygen content of the material, and suppressed in oxygen lean material. It is created after ^{60}Co-γ as well as after hadron irradiation, thus it is no cluster defect and will not be investigated in detail. However, in order to correlate the N_{eff} measured by C-V with microscopic results, this defect has to be taken into account with its full concentration.

The shallow *E(30K)* defect

A second donor was recently discovered by Pintilie [97], which exhibits the *Poole-Frenkel* effect. This defect is supposed to be the reason for the main difference in the behaviour between neutron and proton irradiated sensors. This defect is labelled $E(30K)$. Unfortunately it was not possible to measure electron traps with $T < T_{VO}$ for ^{60}Co-γ irradiated samples, due to the fact that the concentration of VO is so high, that no free electrons are left to fill further defects. Therefore it was so far not possible to determine, if $E(30K)$ is cluster related or not. It was also not known if it depends on the oxygen concentration of the material. In this work new studies concerning the oxygen dependence are presented. The question whether the $E(30K)$ is cluster related or a point defect seems to be solved. It was not possible to observe the $E(30K)$ defect after 1.5 MeV electron irradiation in latest measurements, which points to a

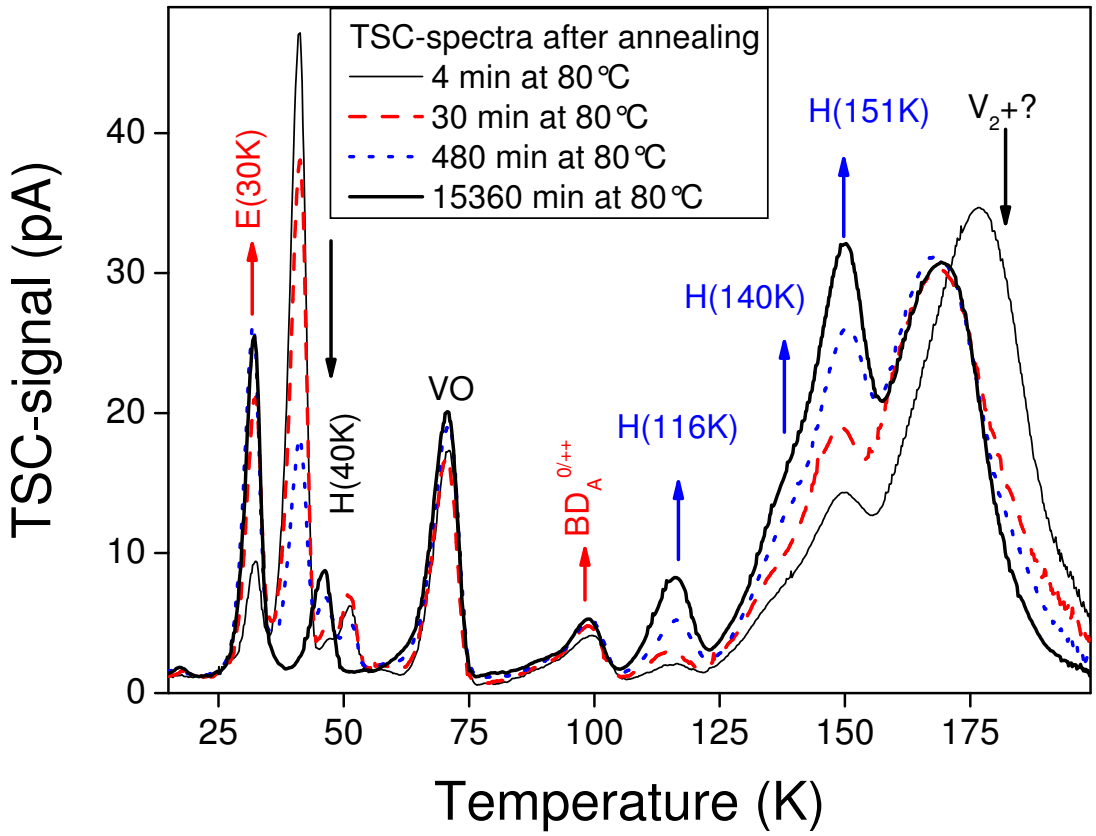

Figure 9.1.5.: TSC spectra illustrating the shallow donors during annealing at 80 °C. Material: Epi-Do, fluence: Φ =2 $\times$ 10^{14} n cm^{-2}, measurement at V_{bias} = 100 V.

cluster-type character. Fig. 9.1.5 represents the shallow donors $E(30K)$ and BD and the deep acceptors $H(116K)$, $H(140K)$ and $H(152K)$ at a bias voltage of V_{bias} = 100 V.

9.2. Correlation of defects with the change of N_{eff}

The radiation induced defects which are responsible for the change of the N_{eff} were discussed in the previous section. A more detailed analysis of the influence of the oxygen concentration and the defect creation by different particles used for irradiation is treated in this section.

9.2.1. Particle dependence of defects with impact on N_{eff}

The influence of oxygen on the creation of defects with impact on the N_{eff} is illustrated in Fig. 9.2.1. Proton (dotted line) and neutron (solid line) irradiated Epi-Do (blue line)

and Epi-St (red line) diodes were measured by TSC at V_{bias} =100 V at a rather stable annealing step of more than 30 000 minutes at 80 °C. The neutron fluence of $\Phi_{eq} = 1.9 \times 10^{14}\,\mathrm{cm}^{-2}$ was scaled to be comparable to the proton fluence of $\Phi_{eq} = 2.4 \times 10^{14}\,\mathrm{cm}^{-2}$. The uncertainty of the nominal fluence error is the main problem for such a comparison, therefore a fluence nomalisation was performed using the current related damage rate α. The main differences of the important defects can be found in the concentration of donors. Both, the $E(30K)$ and the BD TSC defect peaks are smaller after neutron irradiation compared to the proton irradiation, while the deep acceptors are mostly similar. The $H(151K)$ defect concentration is slightly larger for proton irradiation. Effects on defects which were not correlated to the change of the N_{eff} can be found in the VO_i-complex. The introduction rate of this defect by protons is larger compared to that in neutron irradiated material due to the excessive supply of single vacancies created by protons. In contrast to that, the cluster related defect shoulder at 170 K is suppressed after proton irradiation, due to the lower generation rate of higher order vacancies.

9.2.2. Influence of the oxygen concentration on the defect creation

The influence of oxygen on the observed defects with impact on the effective doping concentration N_{eff} is prominent for the donor-like defects (see Fig. 9.2.1). The BD behaves like expected from [86], it is suppressed in oxygen lean Epi-ST material. In contrast to that, it seems that the $E(30K)$ is enhanced in oxygen lean Epi-St material. The deep acceptors $H(116K, 140K)$ appear independent of the oxygen concentration, while the $H(151K)$ shows a small increase for proton irradiated samples at fluences of $\Phi_{eq} = 2 \times 10^{14}\,\mathrm{cm}^{-2}$.
The difference of the creation of defects in highly neutron irradiated samples in the reverse annealing can be observed in Figs. 9.2.2 at the annealing step of 1920 minutes at 80 °C. The comparison of Epi-St (red) and Epi-Do (blue) at 100 V (a) reveals the same dependence of the $E(30K)$ and BD defects on the oxygen as illustrated in Fig. 9.2.1. $E(30K)$ is suppressed for material with high oxygen concentration, whereas the BD (as the VO) is enhanced for oxygen enriched material.
In contrast to the samples irradiated with $\Phi_{eq} = 2 \times 10^{14}$ cm^{-2} neutrons, where only small variations of the $H(151K)$-peak can be observed, the highly irradiated samples with $\Phi_{eq} = 1 \times 10^{15}$ cm^{-2} show a difference in the concentration of the $H(151K)$ and the V_2-peaks. Due to the overlap of defects in the V_2-peak, it is not possible to evaluate the single defects inside this cluster properly. Since the *Poole-Frenkel* effect indicates the defect to be charged at room temperature, only concentrations of defects that exhibit this effect influence the effective doping concentration. The V_2-cluster shoulder did not show the *Poole-Frenkel* effect, so far. However, due to the earlier mentioned composition of the peak of different defects, it is most likely not possible to resolve a *Poole-Frenkel* effect inside the V_2-shoulder.
Unfortunately, it seems that not only defects which are charged at room temperature

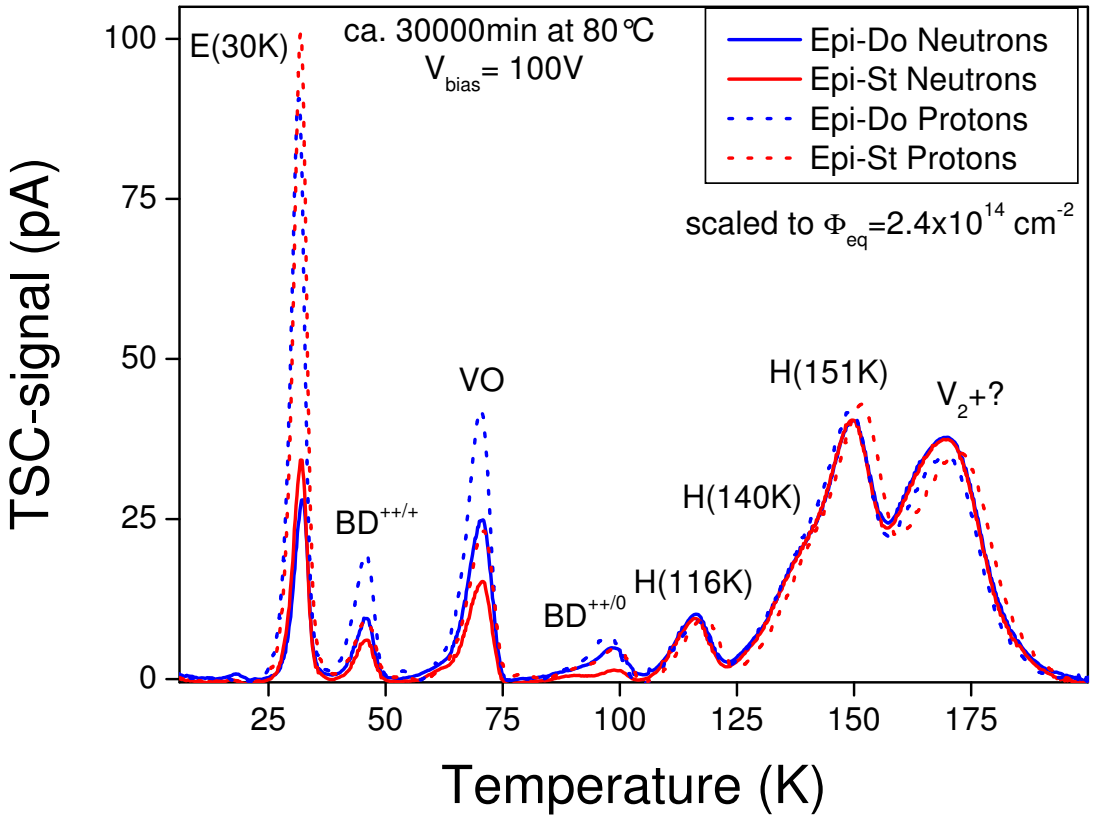

Figure 9.2.1.: Comparison of TSC spectra of proton (dotted line) and neutron (straight line) irradiated Epi-Do (blue) and Epi-St (red) samples. Spectra for neutron irradiation are scaled by a factor of 1.2 (see text).

are affected by the electrical field distribution at high fluences. Even defects which are not supposed to show the *Poole-Frenkel* effect, like the VO_i, show a shift of the peak depending on the applied bias voltage. The origin of this effect is not identified, yet. In summary, it has been verified the enhanced production of $E(30K)$ after proton irradiation and add the observation, that BD is also enhanced after proton compared to neutron irradiation. BD and $E(30K)$ both depend on the oxygen concentration of the material, but with the BD enhanced and the $E(30K)$ suppressed for high oxygen concentrations. For a quantitative description further analysis is necessary. The large difference between Epi-Do and Epi-St in the reverse annealing can be explained by this rather small difference of the $E(30K)$ and the $H(151K)$ defects, when adding the influence of the VP defect. The VP is not supposed to build up during the annealing. It can lead to an offset, only, which should be larger for oxygen lean material. A detailed comparison of Epi-Do and Epi-St samples irradiated with $\Phi = 2 \times 10^{14}$ cm^{-2} and $\Phi = 1 \times 10^{15}$ cm^{-2} neutrons is given in the next section (9.2.3).

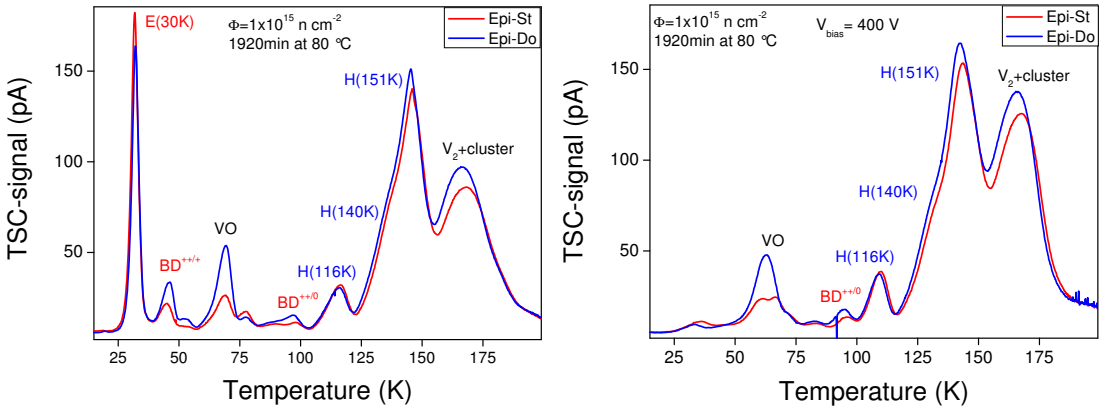

(a) 100 V **(b)** 400 V

Figure 9.2.2.: TSC spectra after irradiation with $\Phi_{eq} = 1 \times 10^{15}$ cm^{-2} neutrons for Epi-St (red) and Epi-Do (blue) for $V_{bias} = 100$ V (a) and $V_{bias} = 400$ V (b) at an annealing step of 1920 minutes at 80°C illustrating the difference between Epi-Do and Epi-St.

9.2.3. Highly neutron irradiated Epi material

The N_{eff} does not scale linearly with the particle fluence. Therefore it is necessary to look at higher irradiation fluences in order to find the defects with impact on the N_{eff} and hence on the depletion voltage. Fluences of interest for the HL LHC start around a few 10^{15}. At these fluences DLTS is not applicable any more, because the original doping concentration is compensated by acceptor-like defects.
The TSC method is a good alternative for defect studies for highly irradiated samples. As explained previously, this method depends strongly on the filling of the defects in the sensor. During this work some studies could not be completed because the filling of defects could not be performed properly. The data presented in this chapter are checked for errors and filling-problems. Tab. 9.2.1 illustrates the current-normalised fluence and the material of the used samples.

Φ_{nom}		Epi-St	Epi-Do
2×10^{14} cm^{-2}	Diode number	8364-02-40	8364-05-58
	Φ_{eq} [cm^{-2}]	1.9×10^{14}	1.9×10^{14}
1×10^{15} cm^{-2}	Diode number	8364-02-43	8364-05-61
	Φ_{eq} [cm^{-2}]	8.6×10^{14}	8.4×10^{14}

Table 9.2.1.: Overview of highly neutron irradiated Epi-St and Epi-Do samples that are presented in this section. The nominal fluences are given as Φ_{nom}, the equivalent values Φ_{eq} are determined from a normalisation to the α-value at 8 minutes at 80°C.

Samples irradiated with $\Phi_{nom} = 2 \times 10^{14}$ cm^{-2}

Figs. 9.2.3 illustrate the TSC spectra taken during an isothermal annealing study of an Epi-St sample for bias voltages of $V_{bias} = 100$ V (a) and $V_{bias} = 300$ V (b). It is well visible, that the shallow defects like $E(30K)$ and $H(40K)$ are suppressed at high voltages (b). Therefore, in the following analysis defect concentrations for the shallow defects were taken from TSC spectra at $V_{bias} = 100$ V, while the defects with $T > 80K$ were analysed from high bias measurements. Note that at this fluence, the diode is depleted even at $V_{bias} = 100$ V. A comparison of concentrations extracted at both bias voltages results in similar values.

The acceptors with impact on the N_{eff} are marked in blue ($H(116K)$, $H(140K)$ and $H(151K)$), donors in red ($E(30K)$ and BD). Both, the concentration of acceptors and donors increase with annealing at 80 °C. The corresponding TSC measurements for the Epi-Do sample are presented in Figs. 9.2.4 (a) for $V_{bias} = 100$ V and (b) $V_{bias} = 300$ V. The results are very similar to the findings concerning Epi-St sample. In comparison, the expected increase of the oxygen dependent BD defect can be observed in the Epi-Do sample. The donors (red) and acceptors (blue) with impact on the N_{eff} are marked with their labels.

The results of the evaluation of the TSC spectra are presented in Figs. 9.2.5 for Epi-St

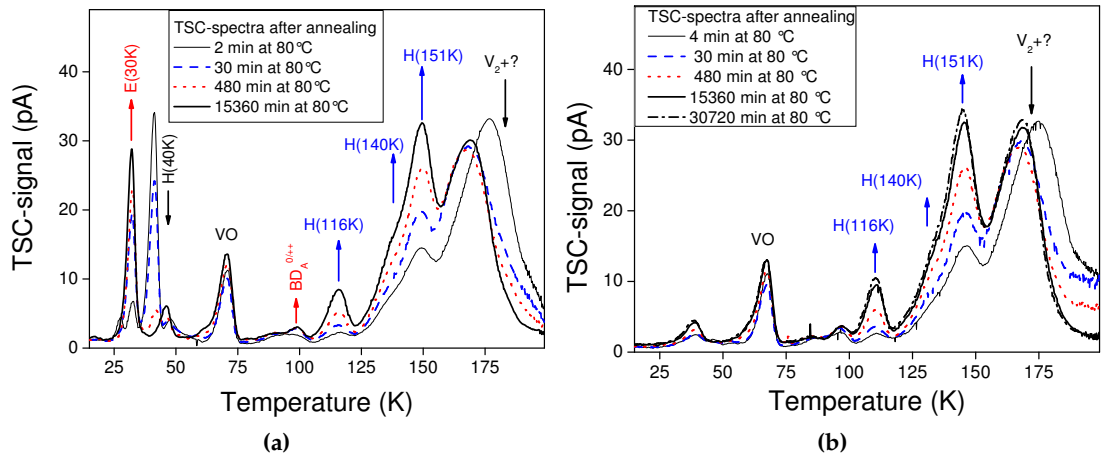

Figure 9.2.3.: TSC spectra of 2×10^{14} cm^{-2} neutron irradiated Epi-St material, measurement during heating at $V_{bias} = 100$ V (a) and $V_{bias} = 300$ V (b).

(a) and Epi-Do (b). The concentrations for the known donors were summed up and displayed as positive concentration by red triangles, while the sum of the concentration of acceptors is illustrated by blue circles. Since acceptors contribute negative to the space charge, they are represented on a negative scale.

The effective doping concentration calculated from the sum of the original doping $N_{eff,0}$, the concentration of all acceptors, donors and the E-center is illustrated by green stars. The result is compared to the N_{eff} measured by C-V at room temperature. The

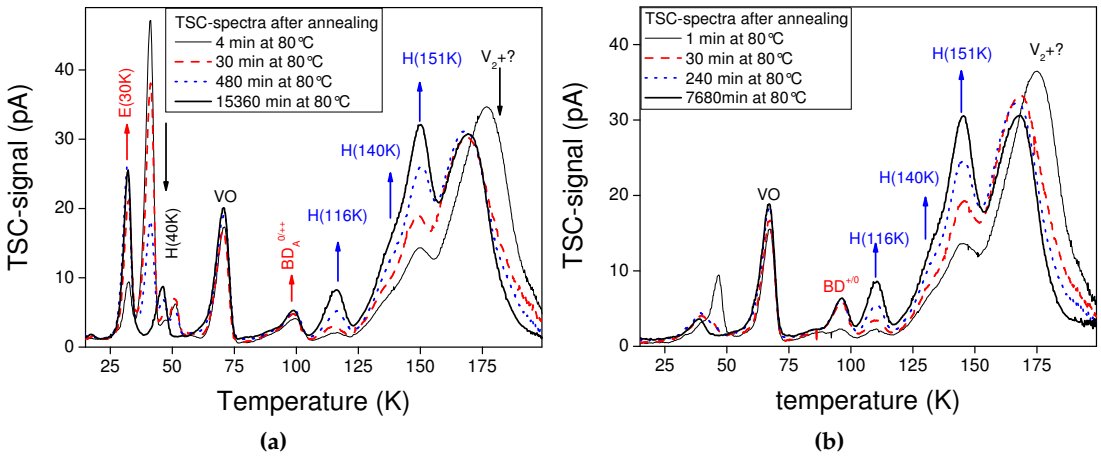

Figure 9.2.4.: TSC spectra of 2×10^{14} cm^{-2} neutron irradiated Epi-Do material, measurement during heating at $V_{bias} = 100$ V (a) and $V_{bias} = 300$ V (b).

results for the Epi-St (a) sample demonstrate that the characteristics of the annealing behaviour can be reproduced very accurately. Both, the short term annealing, and the long term annealing are reproduced very nicely. However, the E-center cannot be resolved by the TSC technique and was added as a constant value. This value was "chosen" to be $[VP] = 3 \times 10^{12}$ cm^{-3}.
Similarly, a good agreement between the defect concentrations and the N_{eff} from C-V at room temperature can be observed for the Epi-Do sample illustrated in Fig. 9.2.5 (b). Here however, it is obvious that the short term annealing from C-V at room temperature is not reproduced properly by the evaluated defect concentrations. Nevertheless, the reverse annealing can be described by the evaluated defect concentrations. The E-center was added with a supposed concentration of $[VP] = 3.5 \times 10^{12}$ cm^{-3}.
The influence and the concentration of the VP defect is an assumption, based on the observation of donor removal in C-V and I-V annealing studies. The concentration of the VP for the studied Epi-Do and Epi-St samples that is necessary to reproduce the C-V measurements at room temperature is in contrast to the known dependence of the VP defect on the oxygen concentration. The concentration of the E-center should be lower for the Epi-Do sample than for Epi-St. This discrepancy could be resolved assuming the existence of another, yet not identified defect with an impact on the effective doping concentration.

Samples irradiated with $\Phi_{nom} = 1 \times 10^{15}$ cm^{-2}
The next higher neutron irradiation that was analysed by microscopic means was $\Phi_{nom} = 1 \times 10^{15}$ cm^{-2}. According to the results from Fig. 9.1.2, at this fluence the samples have undergone type inversion. Proton irradiated epitaxial samples do not undergo type inversion, therefore a detailed study of defects created in proton ir-

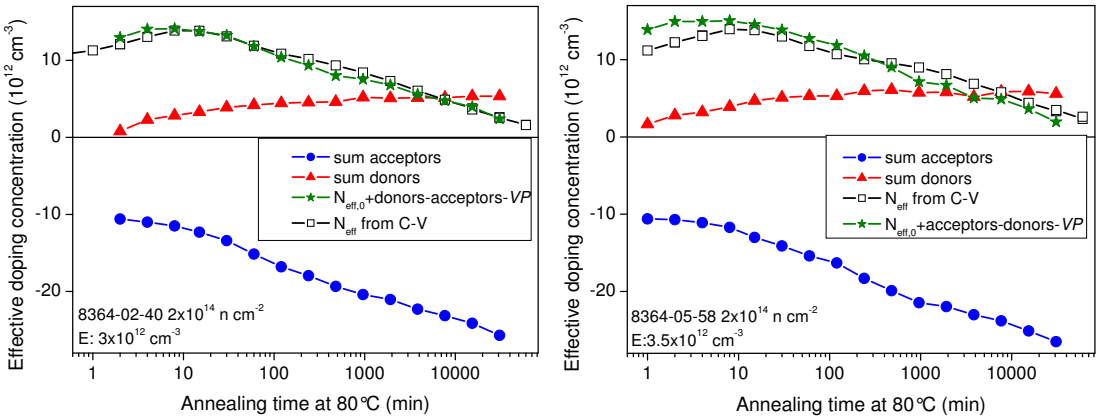

Figure 9.2.5.: Concentrations of defects influencing the N_{eff}, evaluated from TSC spectra of $\Phi_{nom} = 2 \times 10^{14}$ cm^{-2} neutron irradiated Epi-St (a) and Epi-Do (b) material. The sum of the concentrations (green stars) deduced from concentrations of acceptors (blue circles), donors (open black squares) and the E-center and $N_{eff,0}$ is compared to the N_{eff} from C-V at room temperature for isothermal annealing studies at 80 °C.

radiated material in comparison with the results obtained in this work would be very interesting. Furthermore, for this fluence, there is a large difference between the long term annealing of Epi-St and Epi-Do, as it was shown in 9.1.2. This difference is supposed to be reflected in the defect concentrations relevant for the N_{eff}. On the other hand, problems due to missing information about the electrical field inside the diode volume deteriorate the quality of the evaluation of defect concentrations.
TSC spectra of an isothermal annealing study of the Epi-St sensor are illustrated in Fig. 9.2.6. The shallow donor $E(30K)$ is only visible at low bias voltages. It is shown for $V_{bias} = 100$ V in Fig. 9.2.6 (a), while the full concentration of the deep acceptors $H(116K)$, $H(140K)$ and $H(151K)$ can be determined from higher bias voltages ($V_{bias} = 400$ V), see Fig. 9.2.6 (b). The corresponding TSC spectra for the isothermal annealing study of an Epi-Do sample is presented in Figs. 9.2.7, for $V_{bias} = 100$ V (a) and $V_{bias} = 400$ V (b).
As before for the lower irradiated sensors, the identified donors are labeled in red, the acceptors in blue. The concentrations of $E(30K)$, BD and the H defects increase during the annealing treatment. From the shape of the TSC spectra at $V_{bias} = 100$ V, it is well visible that the sensor was undepleted at temperatures $T > 120$ K. Hence, the concentrations for the deep acceptors and the BD defect were always obtained from the $V_{bias} = 400$ V TSC measurements. The isothermal annealing study of the defect concentrations obtained for the $\Phi_{nom} = 1 \times 10^{15}$ cm^{-2} neutron irradiated samples is presented in Figs. 9.2.8 (a) for Epi-St material and (b) for Epi-Do material. The samples became type-inverted during the irradiation. That is the reason why the C-V measured

at room temperature counts as negative space charge, and therefore is illustrated as negative effective doping concentration N_{eff} by open black squares. The defect concentrations of all identified acceptors (blue circles) and donors (red triangles) were summed up and illustrated, too. Finally, the sum of acceptors, donors, the VP and $N_{eff,0}$ is presented by green stars.

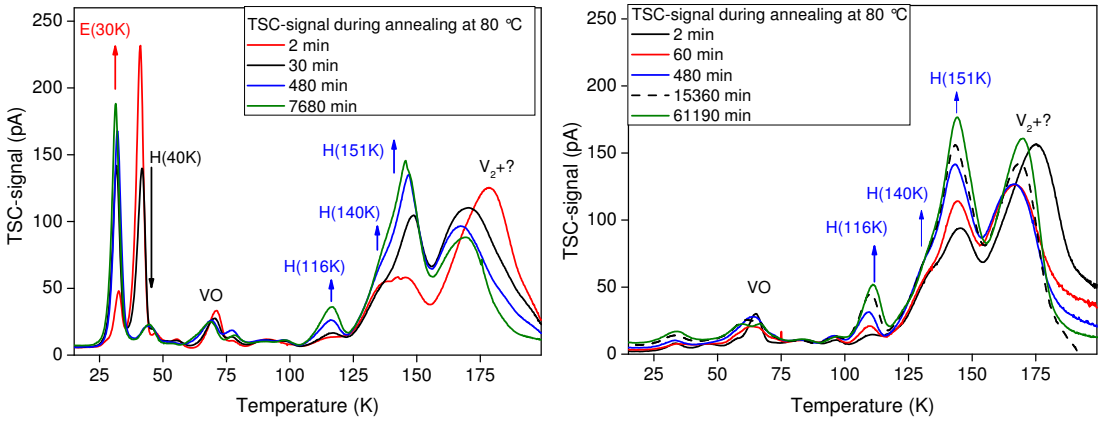

(a) Epi-St: V_{bias} =100 V **(b)** Epi-St: V_{bias} =400 V

Figure 9.2.6.: TSC spectra of $\Phi_{nom} = 1 \times 10^{15}$ cm^{-2} neutron irradiated Epi-St material, measurement during heating at $V_{bias} = 100$ V (a) and $V_{bias} = 400$ V (b).

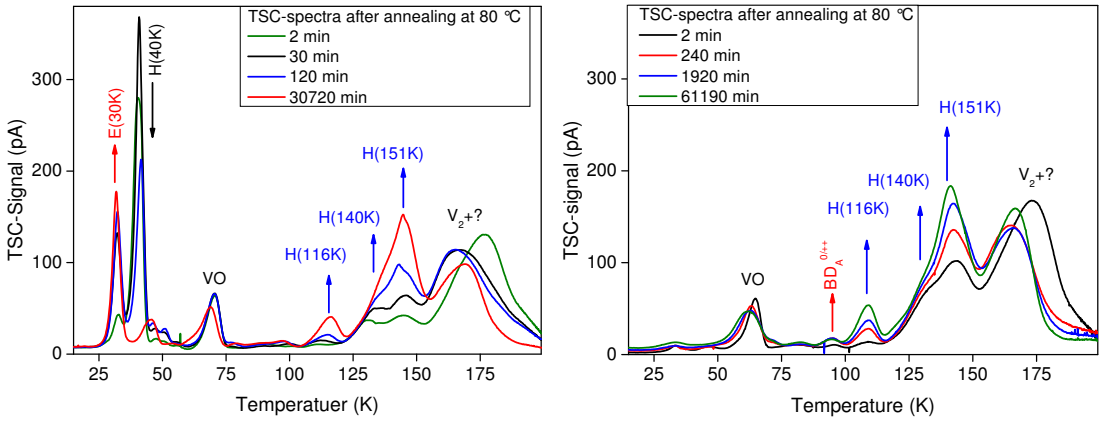

(a) Epi-Do: V_{bias} =100 V **(b)** Epi-Do: V_{bias} =400 V

Figure 9.2.7.: Concentrations of defects influencing the N_{eff}, evaluated from TSC spectra of $\Phi_{nom} = 1 \times 10^{15}$ cm^{-2} neutron irradiated Epi-Do material, measurement at $V_{bias} = 100$ V (a) and $V_{bias} = 400$ V (b) during heating.

The comparison of the effective doping concentration deduced from defect concentra-

tions with the concentrations obtained from C-V measurements at room temperature shows a deviation of both curves for the first 120 minutes of annealing. At higher annealing times the concentrations measured by TSC reproduce the data measured by C-V very well. This again means, the long term annealing can be described very nicely. It is not clear, why the extended short term annealing cannot be reproduced by microscopic defects. As concluded from the strange E-center concentration in the $\Phi_{nom} = 2 \times 10^{14}$ cm^{-2} irradiated diodes, a further defect might be created during irradiation which was not identified, yet.
Looking at the E-center for $\Phi_{nom} = 1 \times 10^{15}$ cm^{-2} irradiated sensors, a concentration of [VP]$= 2.5 \times 10^{13}$ cm^{-3} can be observed in oxygen lean material, whereas in oxygen rich material it results in a 5 times lower concentration of [VP]$= 5 \times 10^{12}$ cm^{-3}. This observation would fit to the formerly mentioned oxygen dependence of the VP creation. However, this is in contrast to the findings for lower irradiated samples, where the assumed concentration of VP does not fit to the expected dependence on oxygen. There are hints that there might be another defect overlapping with the VO_i

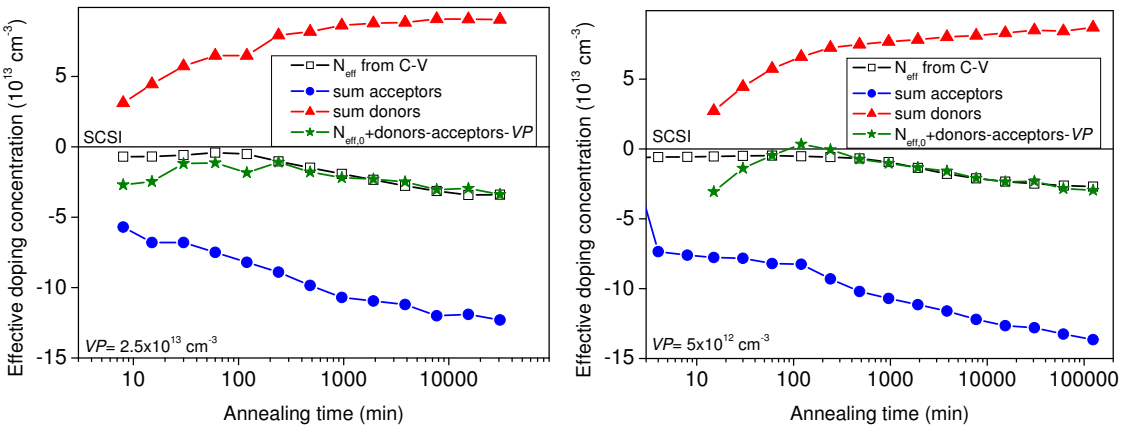

(a) Epi-St **(b)** Epi-Do

Figure 9.2.8.: Concentrations of defects influencing the N_{eff}, evaluated from TSC spectra of $\Phi_{nom} = 1 \times 10^{15}$ cm^{-2} neutron irradiated Epi-St (a) and Epi-Do (b) material, filling with $V_{fill} = -60$ V at $T_{fill} = 5$ K for $t_{fill} = 30$ s and measurements at various reverse bias voltages during heating.

defect. Some measurements revealed a double-peak (see Fig. 9.2.6 (a) and (b)). It is not clear yet, whether this is an overlap of the VO_i defect with a second defect, or a field effect. However, both defect-peaks shift with applied bias voltage, which would usually indicate the *Poole-Frenkel* effect. Another defect could also be located in the shoulder of the V_2+cluster-peak. Currently, no further information about the topic is available.
In summary, the reverse annealing of highly neutron irradiated sensors can be explained by microscopic means, although there are still some open questions.

9.2.4. Measurement of shallow and deep defects

Two very important parameters of the TSC measurements are the filling pulse and the reverse bias during temperature ramping up. If the applied filling pulse at the chosen filling temperature is not high enough, only a part of the defects is filled and thus the full concentration cannot be observed (see also section 6.4).
Typically, for a TSC measurement the sensor is cooled to low temperatures (between 5 K and 30 K). If the sensor is filled with charge carriers, by forward current for example, the charge carriers that are trapped in the defects, cannot be emitted due to a lack of thermal stimulation. At these temperatures, the charges get *frozen-in*. When the diode is heated up with a constant heating rate, the defects will emit the charges at a temperature which corresponds to the energy level of the defect in the band gap. The current due to the charge carrier emission is a measure for the defect concentration. It can be evaluated by fitting the TSC peak. The TSC measurements only deliver reliable concentrations, if all defects that we want to observe are completely filled inside the total detector volume. This is one reason, why injection with light only leads to qualitative defect concentrations. In case of illumination with light, only the silicon atoms inside the light cone are being ionised and produce electron hole pairs. Thus, the volume is not well-defined. Moreover, if the applied filling pulse was not chosen to be high enough or applied for enough time, the defects may be filled inhomogeneously. Depending on the capture cross sections, also the filling of different defects may be inhomogeneous. This will lead to a completely misleading picture. It is vital to completely fill the total volume of the sensor.
For example, the filling of highly irradiated sensors by forward current at low temperatures can be a problem, if internal barriers build up highly ohmic layers. Then, even the filling with a forward bias of $V_{bias} = -450$ V may not lead to a high current inside the silicon and thus the defects will not be filled completely at 20 K. Fig. 9.2.9 illustrates the TSC spectra of an Epi-Do sensor irradiated with $\Phi_{eq} = 6 \times 10^{14}$ cm^{-2} protons for various filling times at $T = 20$ K, a forward bias of $V_{fill} = -450$ V and a reverse bias during heating of $V_{bias} = 100$ V. Apart from filling conditions we always need to be sure, that the diode is completely depleted during the measurement. If this is not the case, the result of the concentration of defects is not correct. In the worst case, the type inverted diode would deplete from the rear side and the guard ring would not be active. The active volume would then be undetermined and the evaluation of the concentrations not useful.
The V_{dep} at room temperature from C-V does not represent the V_{dep} at lower temperatures. Depending on the charge properties of the defects, they capture charge and either start to contribute, or stop contributing to the effective doping concentration at low temperatures. As an example, the $V_2^{-/0}$ is not charged at room temperature, but at low temperatures charge gets trapped, and the defect contributes to the space charge. As a result the V_{dep} increases at low temperatures. For the deep acceptor $H(151K)$ it is the opposite. At low temperatures, this defect becomes neutral due to hole trapping and does not contribute to the space charge. As a result the V_{dep} decreases. It is most

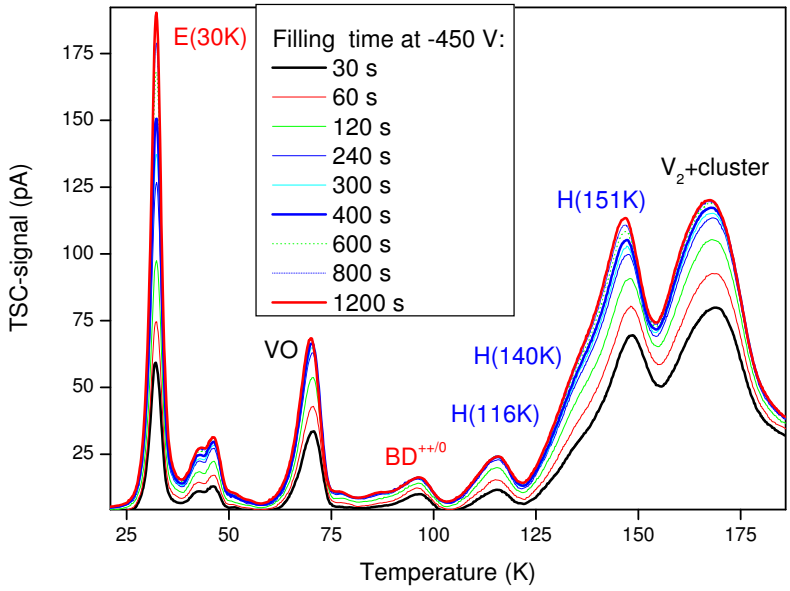

Figure 9.2.9.: TSC spectra of an Epi-Do diode measurement after irradiation with $\Phi = 6 \times 10^{14}$ cm^{-2} protons for various filling times t_{fill}, the filling voltage $V_{fill} = -450$ V and an annealing step at 640 minutes at 80 °C.

essential to fully deplete the diode during ramping up in the full temperature range. A comparison between Fig. 9.2.2 (a) and (b) reveals another problem. In the low temperature regime, some defects are visible in (a), measured at $V = 100$ V which can not be found in (b) measured at $V = 400$ V. These shallow defects are suppressed for high-bias measurements. The reason for this behaviour is not clear, yet. It is possible, that phonon assisted tunneling (see [2]) leads to unobserved emission.
In conclusion, the shallow defects need to be analysed for low-bias measurements[2], while the deep defects only deliver reliable concentrations for high-bias measurements.

9.2.5. Résumé

Some problems inherent to the TSC measurement technique have been observed during the preparation of this work. On the one hand the importance of the filling time and filling current for highly irradiated sensors should be mentioned. This factor must be controlled during the whole measurement process. The complete filling of the defects is essential for the reliable evaluation of absolute concentrations.
Moreover, the field-dependence of the peak position in TSC spectra gives rise to

[2]Fortunately, the depletion voltage is very low at low temperatures.

questions. Both, the suppression of shallow donors at high bias voltages (high electric fields) and the peak-shift, which appears to be similar to the *Poole-Frenkel* effect, are unexplained and can only be assumed as to be related to effects like *phonon-assisted-tunneling*. This effect may lead to emission too fast to be observed by TSC.
The deep acceptors $H(116K)$, $H(140K)$ and $H(151K)$ are responsible for the reverse annealing of sensors also at high neutron fluences ($\Phi_{eq} = 1 \times 10^{15}$ cm^{-2}). However, at that high fluences, some inconsistencies concerning the temperature dependence of the *E*-center (VP) and the short-term annealing hint to the existence of another defect with influence on the N_{eff}, that is not identified, yet.
The impact of defects on the space charge in a silicon material as presented in Fig. 9.0.1 can be demonstrated by a simple picture. The counteraction of acceptors and donors on the effective doping concentration is like a balance, with the type of material (*n*-type or *p*-type) resulting from the larger concentrations of one of the two *dopants*. Figs. 9.2.10 (a)-(h) illustrate this correlation by using a pair of scales, presenting the impact of defects as *weight* that turns the indication either to the *n*-type or to the *p*-type side. Please note that the defect concentrations are not to scale. The left hand side column presents the neutron damage case, while on the right hand side proton damage is presented. Fluences increase from top to bottom. Although both cases start with a similar N_{eff}, the difference between proton and neutron irradiation is clearly seen for the fluence of $\Phi_{eq} = 4 \times 10^{14}$ cm^{-2}. There, the increase of the positive space charge due to the $E(30K)$ defect in proton irradiated silicon over-compensates the negative space charge due to the deep acceptors, eventually preventing type inversion for proton irradiated samples at a fluence of $\Phi_{eq} = 8 \times 10^{14}$ cm^{-2}. For higher fluences, illustrated here at $\Phi_{eq} = 2 \times 10^{15}$ cm^{-2}, the neutron irradiated sample becomes more *p*-type, while the proton irradiated sample becomes more *n*-type.
In conclusion, the oxygen enrichment seems to act beneficial for the radiation hardness of neutron irradiated samples, while first results for purely proton irradiated samples illustrate a lower full depletion voltage for oxygen lean materials, which could prevent very high depletion voltages.
In actual HL LHC experiments, there will be a mixture of pions and neutrons, with a composition depending on the distance to the interaction point. The impact of the oxygen concentration on the evolution of the effective defect concentration should therefore also be analysed for mixed irradiations.

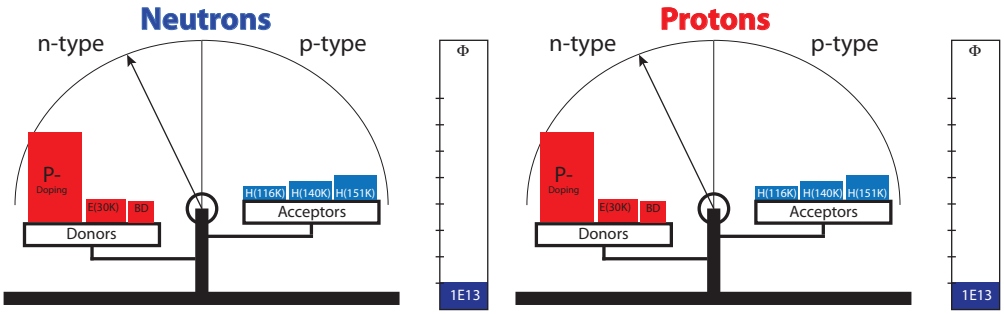

(a) $\Phi_{eq} = 1 \times 10^{13}$ cm^{-2}

(b) $\Phi_{eq} = 1 \times 10^{13}$ cm^{-2}

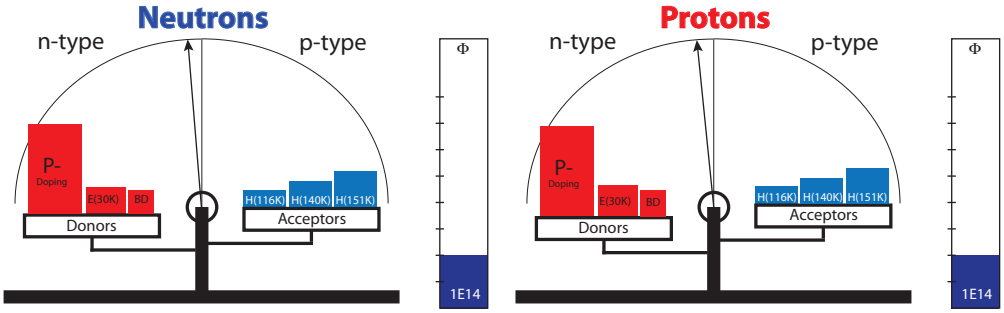

(c) $\Phi_{eq} = 4 \times 10^{14}$ cm^{-2}

(d) $\Phi_{eq} = 4 \times 10^{14}$ cm^{-2}

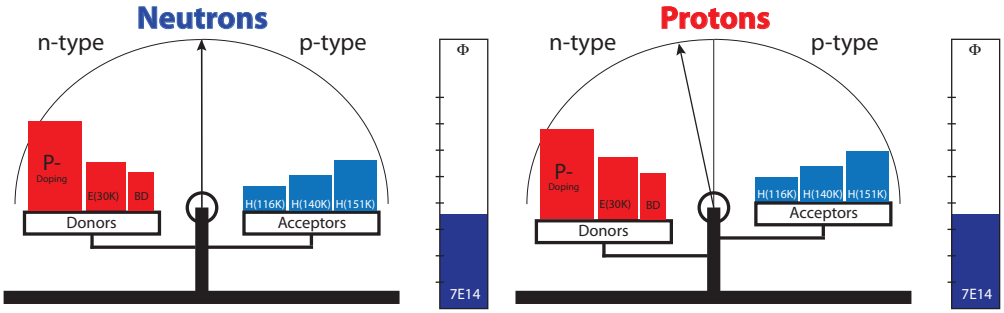

(e) $\Phi_{eq} = 8 \times 10^{14}$ cm^{-2}

(f) $\Phi_{eq} = 8 \times 10^{14}$ cm^{-2}

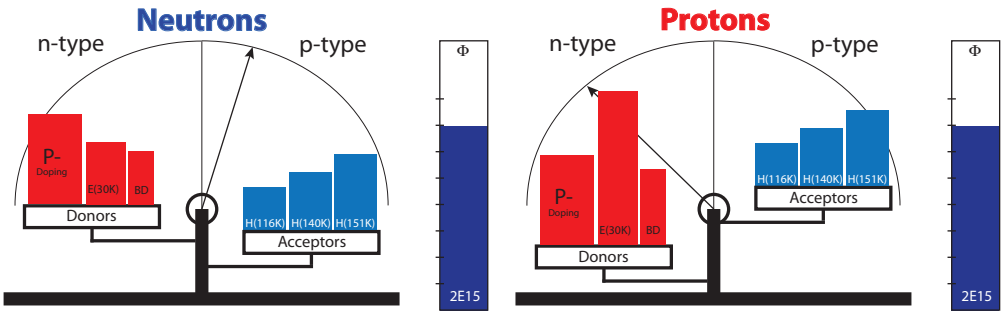

(g) $\Phi_{eq} = 2 \times 10^{15}$ cm^{-2}

(h) $\Phi_{eq} = 2 \times 10^{15}$ cm^{-2}

Figure 9.2.10.: Impact of acceptor and donor defects on the evolution of the space charge depending on fluence and particle used for irradiation illustrated with use of a defect balance. For description see text.

10. Characterisation of test-diodes for future CMS-detectors for the *high luminosity* LHC phase

10.1. Introduction

A comprehensive R&D campaign for future CMS-detectors was started in the framework of the CMS collaboration. This campaign covers a full programme of test-sensors including diodes, strip-sensors and test structures made from the available common technologies like *n*-type and *p*-type FZ, MCz and Epi silicon with *p*-stop and *p*-spray isolation. The programme enables a comparison of the available materials, and of sensor geometries and technologies before and after irradiation.
It is planned to irradiate the test-structures with both 1 MeV neutrons at the TRIGA reactor in Ljubljana and with 25 MeV protons in Karlsruhe, thus allowing to evaluate the optimal polarity of material, *n*- or *p*-type and sensor design, radiation hardness and annealing behaviour. A brief overview about the campaign can be found in [118]. In total 13 institutes are involved in the campaign, Hamburg University participates in the characterisation of the radiation hardness of diode-structures.
Before starting the irradiation, it is necessary to understand the material and properties of the newly produced test-structures. For that reason it was decided to characterise all diodes by measuring C-V characteristics and I-V characteristics. Moreover, some diodes were measured by the *Transient Current Technique* (TCT) and some by DLTS in order to characterise material or process induced defects.
The first batch of unirradiated diodes for characterisation contained FZ-*n*-type and *p*-type sensors, the *p*-type manufactured with *p*-spray and *p*-stop isolation, each sensor type in three different thicknesses. The results presented in this work deal with the investigation of 120 µm, 200 µm and 320 µm thick *n*-type and *p*-spray sensors.

10.2. Macroscopic behaviour

The fist supply of diodes consisted of FZ sensors in three different active thicknesses (120 µm, 200 µm and 320 µm) in three different device designs (*n*-type, *p*-type with *p*-spray and *p*-stop). In this work only the *n*-type FZ and the *p*-type FZ with *p*-spray between PAD and guard ring (GR) were analysed. Another set of *p*-type diodes was not included in this work, because the isolation between pad and guard ring was not working properly.

Type	Active thickness	Geometry	Diode label
P-in-N FZ	120 µm	diode with GR	FZ120N Wx Diode y
P-in-N FZ	200 µm	diode with GR	FZ200N Wx Diode y
P-in-N FZ	320 µm	diode with GR	FZ320N Wx Diode y
N-in-P FZ	120 µm	diode with GR and *p*-spray	FZ120Y Wx Diode y
N-in-P FZ	200 µm	diode with GR and *p*-spray	FZ200Y Wx Diode y
N-in-P FZ	320 µm	diode with GR and *p*-spray	FZ320Y Wx Diode y

Table 10.2.1.: Diode types and materials of test-samples. Oxygen content [O]$\approx 1 - 10 \times 10^{17}$ cm^{-3}.

The physical thickness of all sensors is measured to be 320 µm $\pm$ 6 µm with an sensor PAD area of 0.25 cm^2 surrounded by a guard ring structure. The active thickness of the sensors is achieved by *in-diffusion* of a layer of high doping concentration from the rear side.

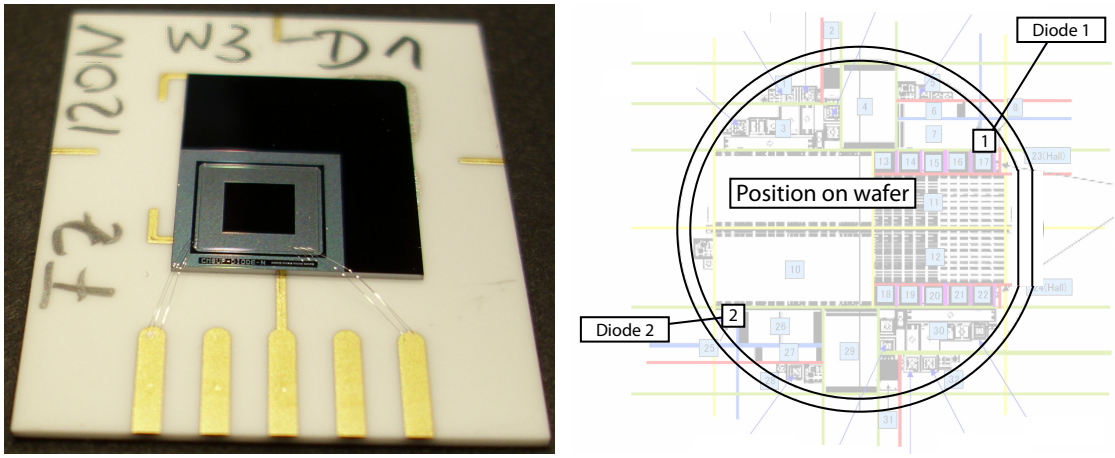

(a) **(b)**

Figure 10.2.1.: Picture of an *n*-type diode mounted on a carrier ceramic for DLTS measurements and bonded to gold pads (a). Overview of location of test-structures on the wafer (b) for Diode 1 and Diode 2.

This process is a new method called *deep-diffusion* process. Unfortunately, there is not much information about this process available from the company. Common information about the process can be found in [119]. Tab.10.2.1 shows an overview of the materials used in different thicknesses, geometries and labeling of the diodes. A picture of an *n*-type diode is shown in Fig. 10.2.1 (a).
The diode labels, as given in Tab. 10.2.1, derive from the material type, the wafer and the location on the wafer: Type+active thickness+Wafer no.x+Diode no.y. Fig. 10.2.1 (b) shows the wafer mask and the diode positions on the wafer. The diodes used in this

work are Diode 1 and Diode 2 from different positions located opposite to each other at a similar radius.
The characterisation of diode properties before irradiation is very important in order to understand production induced effects on the electrical properties. Problems that derive from current generating defects, additional acceptor or donor generation due to impurities (like *TDD*s see chapter 7) and inhomogeneity effects could affect the results after irradiation. Therefore it is very useful to analyse the electrical properties of the unirradiated sensors and estimate the impact of crystal defects on them. The oxygen content of [O]$\approx 1 - 10 \times 10^{17}$ cm^{-3} communicated by the company seems very high for a pure FZ material, which usually is oxygen lean.

10.2.1. Comparison between 120 µm, 200 µm and 320 µm thick n-type and p-spray diodes

The diode properties were measured for the available FZ 120 µm, 200 µm and 320 µm thick n-type and p-spray diodes. In order to give an overview of the main properties of each material, one sample per diode-type and thickness was chosen representing the average results found during C-V and I-V characteristics. The spread inside the material and thickness will be discussed in Sec. 10.2.2. The measurements presented here were taken at 20 °C and a frequency of 10 kHz for the C-V measurements. A frequency dependence of the capacitance was not observed for unirradiated sensor.
Fig. 10.2.2 represents the main results of the three different thicknesses of n-type diodes. C-V measurements (a), $1/C^2$ normalised to 1 (b) and results for I-V measurements for PAD and guard ring (c) are displayed. It is well visible that the C-V curves for the thinner diodes do not show the *ideal* behaviour that was illustrated in Fig. 3.4.3 (a). The capacitance does not saturate at full depletion and the *ideal* sharp kink is not seen. Only for the 300 µm diode the measurement shows the expected behaviour. In the $1/C^2$ plot (b) the difference is more pronounced and it is obvious, that this effect becomes worse the thinner the diode becomes. The leakage current in the n-type diodes is generally very low (c). However, like the capacitance the current shows no saturation value at the expected full depletion voltage for the thinner diodes. Furthermore, the current is higher in thinner diodes. This is in contrast to the expectation, because the current should decrease with the material thickness if the current is generated by defects in the active detector bulk.
A similar feature is found for the three different thicknesses of the p-spray samples. In Fig. 10.2.4 again C-V (a), $1/C^2$ (b) and the I-V characteristics for pad and guard ring (c) are shown. As for the n-type material the C-V characteristics reveals for thinner diodes a non saturating behaviour of the end capacitance. In addition, the variation of the curve shapes for the diodes of one thickness is high. Two samples are shown in order to illustrate the diode behaviour. A bump shortly before depletion can be observed in the thinner materials (a) (further analyses see Fig. 10.5.1b). In the $1/C^2$-plot (b) the effect of the non-saturation of the C-V curve for 120 µm and 200 µm samples are

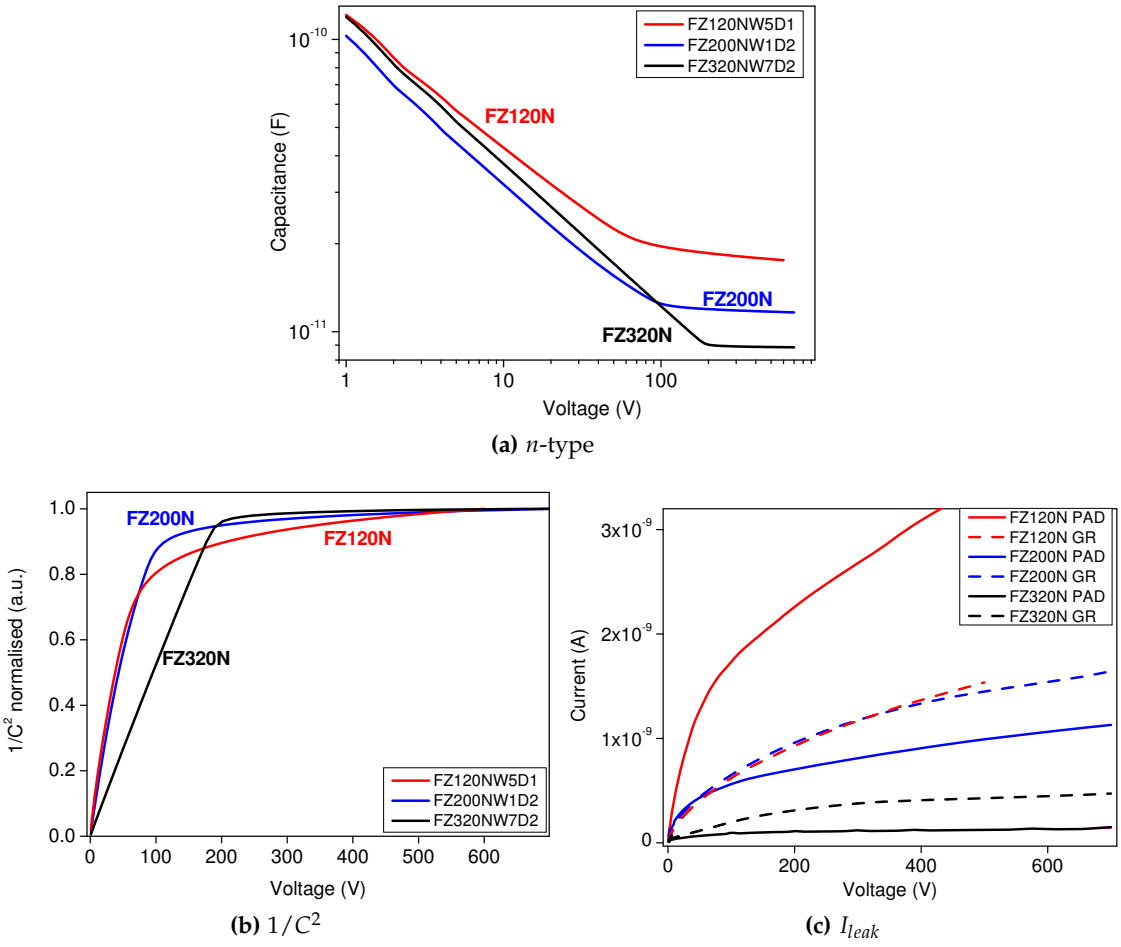

(a) n-type

(b) $1/C^2$

(c) I_{leak}

Figure 10.2.2.: Comparison of three thicknesses of n-type material. C-V characteristics (a), $1/C^2$ normalised to unity (b) and I-V characteristics (c)

more pronounced. Like in the n-type material, the effect is stronger for the 120 µm sample whereas the 320 µm diode shows a rather *ideal* curve. The I-V characteristics (c) illustrates the same thickness dependence of the current as the n-type material. The current is higher for thinner sensors. Over-all we can see, that the current in the p-spray sensors is higher than for the n-type sensors (compare Fig. 10.2.2 (c)).

A comparison between the C-V characteristics of n-type and p-spray sensors is shown in Fig. 10.2.3 for each of the three thicknesses. For 120 µm sensors (a) differences in the shape of the curve are seen, both have the same non-saturating behaviour, but with slightly different end-capacitance values, implying different active thicknesses. The p-spray characteristic shows a step behaviour in the first $V_{bias} = 10$ V. This step can be found in the 200 µm p-spray sensors (b) as well. The non-saturation effect is less pronounced for the 200 µm sensor than for the 120 µm sensors. The 320 µm p-spray sensor (c) also shows the bump in the first $V_{bias} = 10$ V, which is not as pronounced

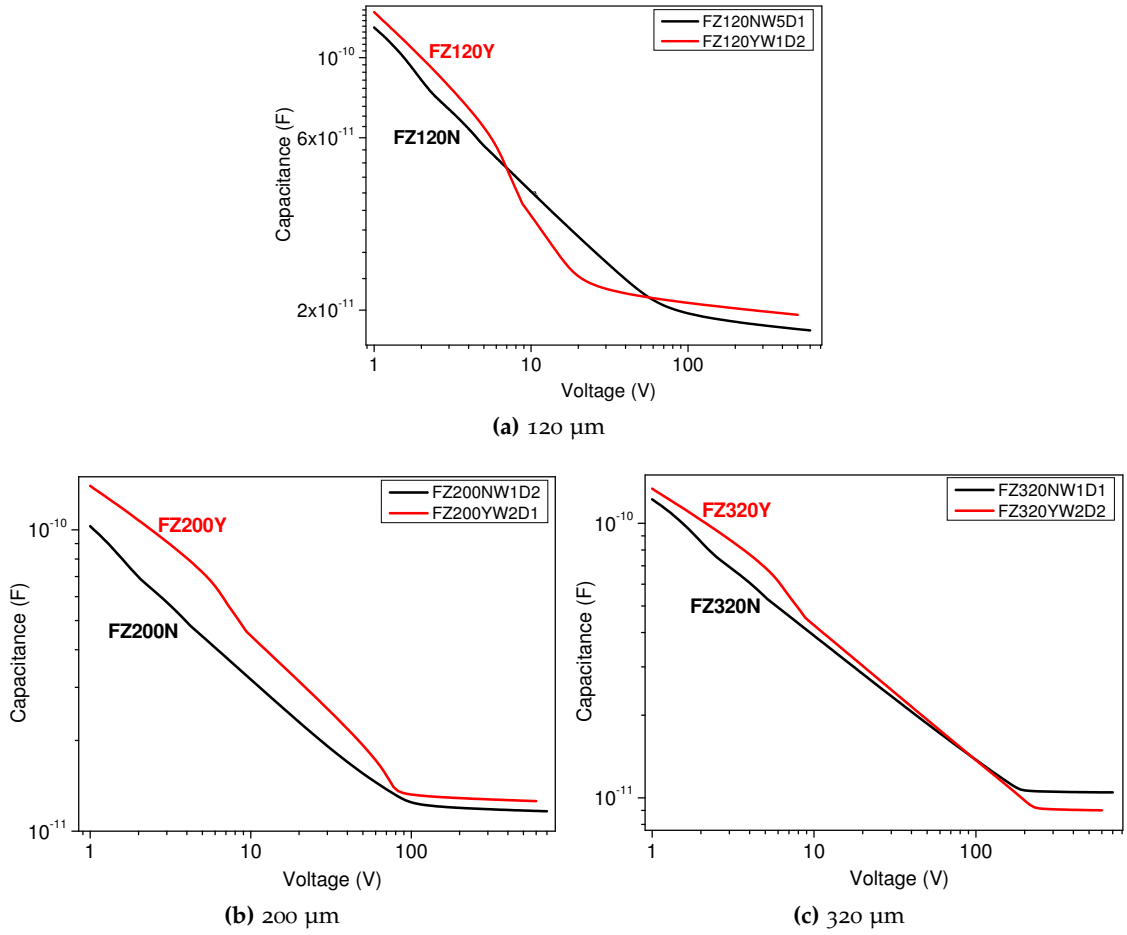

(a) 120 µm

(b) 200 µm

(c) 320 µm

Figure 10.2.3.: Comparison of C-V results for *n*-type (black) and *p*-spray (red) material for three thicknesses: FZ120 (a), FZ200 (b) and FZ320 (c).

as in *n*-type material. For the 320 µm the end-capacitance is quite similar for the two different diode types [1].
Generally, the *p*-spray sensors show a higher deviation from the *ideal* C-V characteristic (illustrated in Fig. 3.4.3 (a)). As the C-V characteristic is depending on the doping concentration (see Eq. 3.4.7), a detailed study of depth profiles of the N_{eff} using Eq. 3.4.9 is performed and will be shown in Sec. 10.2.3.

10.2.2. Wafer-position dependence of the diode characteristics

A comparison of several 120 µm thin sensors of the same type reveals a small difference between the diodes located at position Diode 1 and Diode 2 on the wafer. The diode

[1] Note that the capacitance scale is plotted logarithmically.

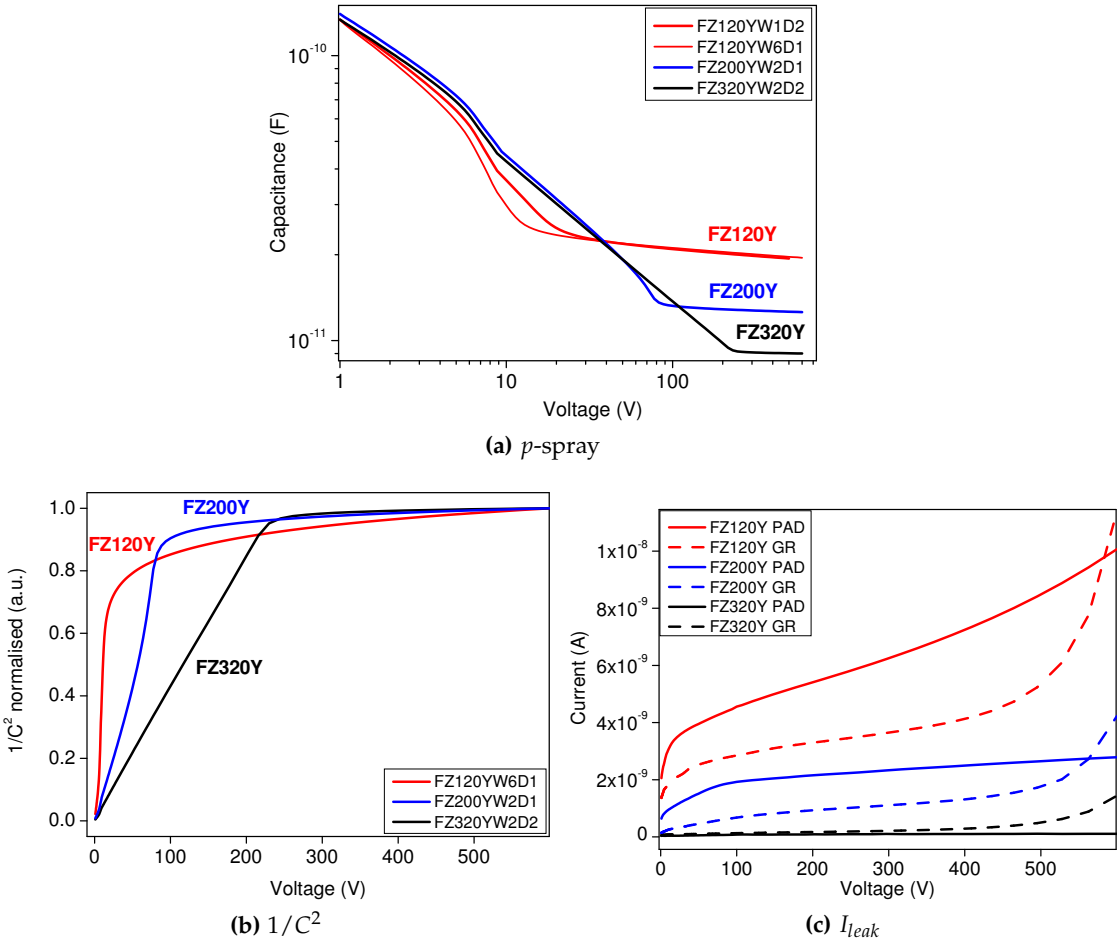

(a) p-spray

(b) $1/C^2$

(c) I_{leak}

Figure 10.2.4.: Comparison of three thicknesses of p-spray material. C-V characteristics (a), $1/C^2$ normalised to unity (b) and I-V characteristics (c)

positions are marked in Fig. 10.2.1 (b). Fig. 10.2.5 (a,b) represent the C-V measurements for 120 µm thick diodes of position Diode 1 and Diode 2. The capacitance characteristics of Diode 2 is shown in red, while Diode 1 is shown in black. C_{end} is similar for both diode positions and for both diode types. Nevertheless, there is a difference of the end capacitance between the diodes from position 1 and 2 up to $V_{bias} = 100$ V for n-type (a) and $V_{bias} = 40$ V for p-spray (b). The position dependence of the C-V characteristic is even more pronounced for p-spray sensors, but also clearly visible in the n-type sensor. The reason for this position dependence can be related to the production process. Consequences of the production process will be discussed in detail in Sec. 10.3.
Since the slope of the C-V characteristic depends on the N_{eff}, there seems to be a small difference in the doping profile of Diode 1 and Diode 2, which is not reflected in the I-V characteristics, but generally the p-spray sensors shows higher current values.

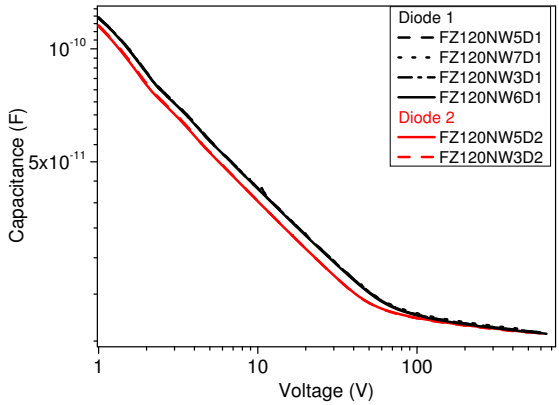

(a) *n*-type 120 µm

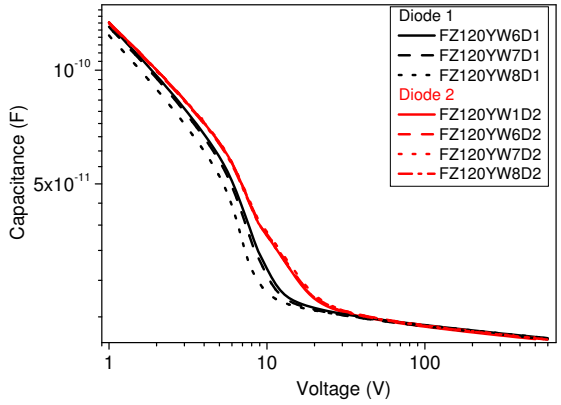

(b) *p*-spray µm

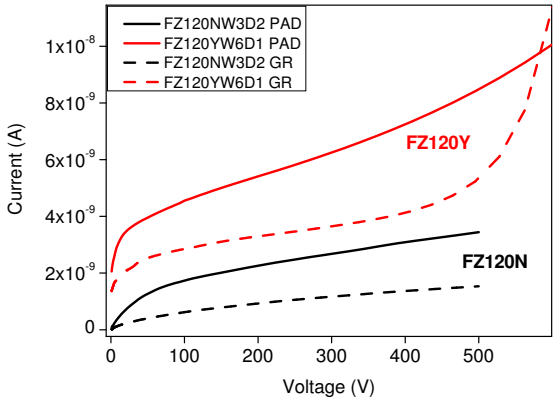

(c) I_{leak} 120 µm

Figure 10.2.5.: Comparison of C-V measurements of Diode 1 and 2 for FZ120N (a) and FZ120Y (b) and comparison of I-V characteristics (c).

The difference for the diode position is visible for the 200 µm diodes as well, but less pronounced as shown in Fig. 10.2.6 for *n*-type (a) and for *p*-spray (b) sensors. The spread is higher for the *p*-spray samples which is better visible in the $1/C^2$ plot in Fig. 10.2.6 (c). Eventually the diodes reach a similar C_{end} except for one outlier. The current profiles of the 200 µm diodes (c) show again no obvious dependence on the diode position, though like for 120 µm thickness, *p*-spray samples usually show higher current values.
The 320 µm diodes exhibit generally the expected C-V characteristics for *n*-type 10.2.7 (a) and for *p*-spray 10.2.7 (b). The I-V characteristics also show very low values of leakage current.
As mentioned earlier in this section, the C-V characteristic depends on the doping concentration (see Eq. 3.4.7). This is only quantifiable if the diode area is known. Therefore, all C-V and I-V measurements were performed with the guard ring connected

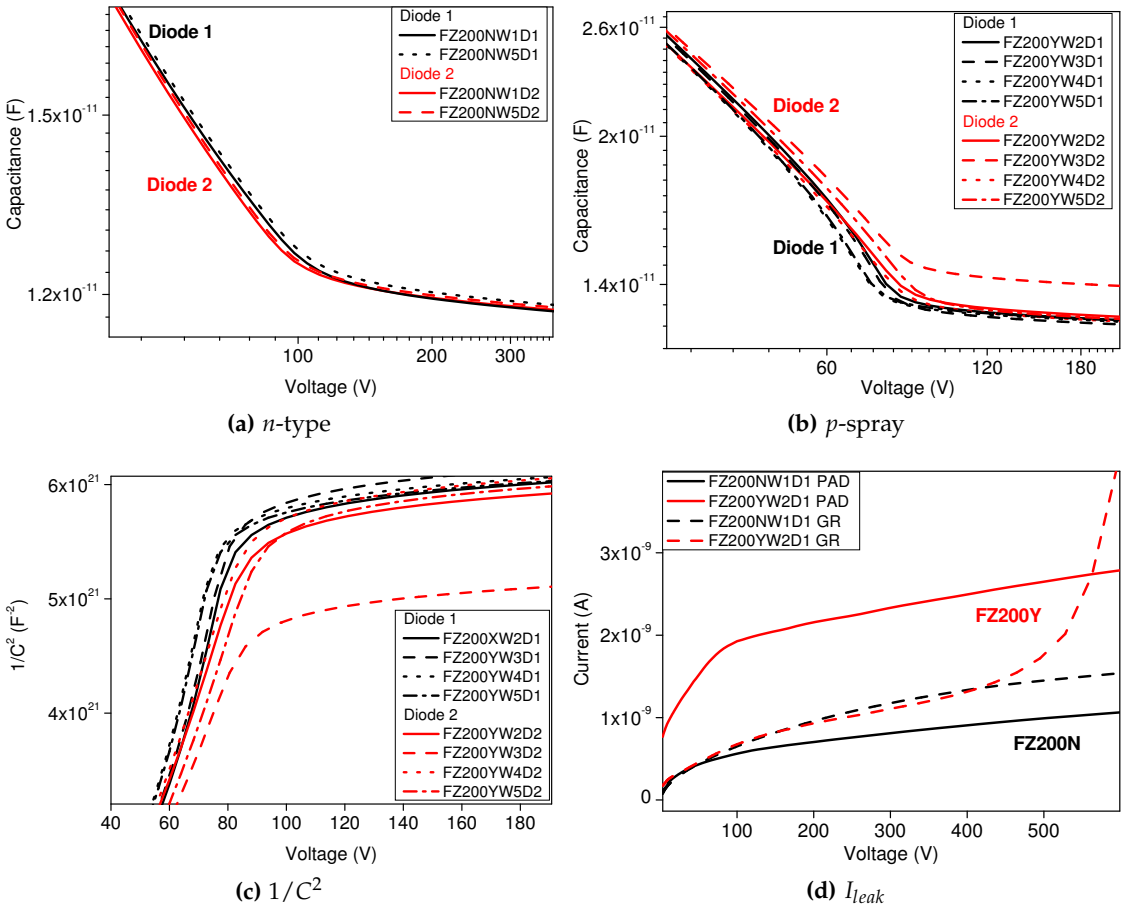

(a) n-type **(b)** p-spray

(c) $1/C^2$ **(d)** I_{leak}

Figure 10.2.6.: Comparison of the C-V characteristics of Diode 1 and 2 for FZ200N (a) and FZ200Y (b), a detailed picture of the $1/C^2$ (c) and a comparison of I-V characteristics for 200 µm n-type and p-type material (d).

to ground. Nevertheless, if the guard ring would not work properly this could be an explanation for the saturation behaviour of the C-V characteristics. In order to check the effective operation of the guard ring, measurements were performed with guard ring floating and the result compared to the measurements performed with guard ring grounded. There is a difference for C_{end} observed with and without guard ring connected and the measurements are reproducible. This implies that the guard ring is active.

10.2.3. Depth profiles of the effective doping concentration

The results of the C-V characteristics leads to the impression, that the 120 µm and 200 µm sensors exhibit a non-uniform doping profile. The depth profile of the effective

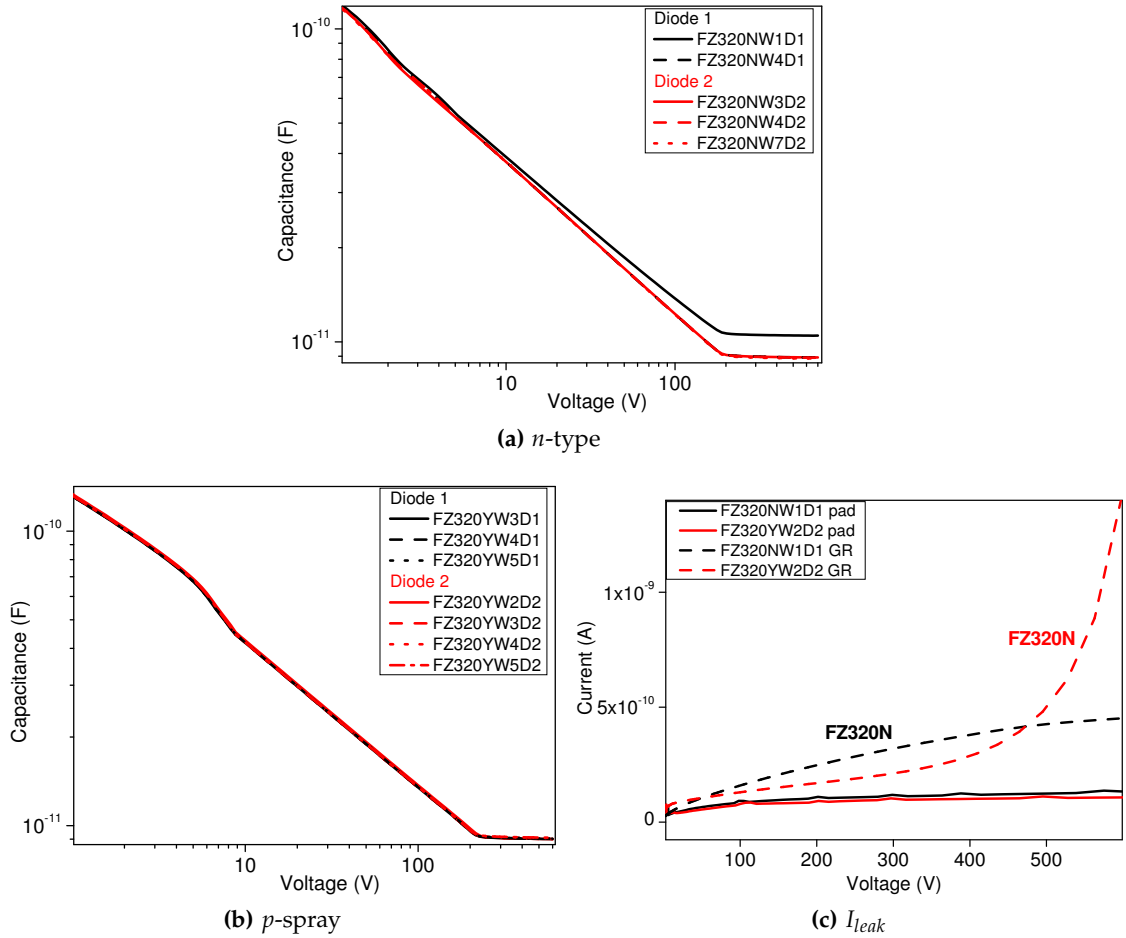

(a) n-type

(b) p-spray

(c) I_{leak}

Figure 10.2.7.: C-V characteristics of FZ320N (a) and FZ320Y (b) with comparison of I-V characteristics (c).

doping concentration N_{eff} can be calculated from the C-V characteristics by the approximation of Eq. 3.4.9. In this work, only one diode of each type and thickness is illustrated, as a representative of the main results for each diode type. Fig. 10.2.8 illustrates the N_{eff} depth profile for 120 µm diodes in red, the 200 µm diodes in blue and the 320 µm diodes in black, n-type is always denoted with solid lines, while p-spray is illustrated with a dashed line. The front side of the sensor is located at 0 µm.

In the first 40 µm a behaviour is seen, which is not quite understood. Fig. 10.2.8 shows low N_{eff} (dip) in the front region of the n-type sensors, while the p-spray show higher values of N_{eff} at the surface. This points to an *in-diffusion* of an acceptor-like impurity or defect from the surface. A defect found by means of *Deep Level Transient Spectroscopy* measurements in Sec. 10.3 can be used to explain this effect. However, the DLTS technique does not reach the very shallow edges of the band gap, due to a

temperature limitation of the setup of about $T_{min} \approx 28$ K. Since levels of doping atoms can also be found at the edges of the band gap, some defect may remain undetected due to the temperature limitation.
The behaviour of the depth profile of N_{eff} for the 120 µm *n*-type sensor (red) presents an increase of N_{eff} towards the rear side of the material, whereas *p*-spray shows a strong decrease towards the backside, which leads to a very non-uniform doping profile in the *p*-spray sensors. P-spray sensors also appear to be 10 µm thinner than the corresponding *n*-type sensors.
The 200 µm sensors (blue) show the same tendency as the 120 µm thick sensors. The doping profile of the *n*-type sensor increases constantly towards the rear side while the N_{eff} for the *p*-spray sensor shows a dip towards the substrate in the region between 110 µm and 190 µm. As for the *n*-type material, the *p*-spray is 10 µm thinner than the *n*-type sensor. Considering the opposite behaviour of the N_{eff} for *n*- and *p*-type sensors, the reason for the inhomogeneous doping profile could be found in a donor-like impurity or defect which increases towards the rear side of the sensor. Since it shows a depth dependence it seems possible that this donor has been introduced during the wafer-processing of the rear side.
Although the 320 µm sensors (black) show a very homogeneous doping profile for both, *n*-type (solid line) and *p*-spray (dashed line), the same tendency like in the thinner materials can be observed towards the rear side. Directly before the steep increase at the rear side, a slight increase can be observed for the *n*-type sensor whereas for the *p*-type a very small dip at the rear side is observed.
The impression that an active donor was introduced during the processing of the rear side is also supported by information from the company that produced the diodes. The different thicknesses were obtained by *deep-diffusion*. Further information about the process cannot be provided by the company, only common information about the *deep-diffusion* is available from literature. Either P- or B-rich material is fixed or created at the rear side of the material (e.g. poly silicon) or a highly doped layer at the rear side is created by implantation. In order to accelerate the diffusion of the dopants, the silicon is heated up to temperatures of about 800 - 1200 °C (further information see [119]). The consequences of this treatment are explained in the following section.

10.3. Introduction of bulk defects due to the *deep-diffusion* process

As explained in the previous section, the different thicknesses of the active diode volume of the sensors on the FZ-wafers were obtained by a newly applied *deep-diffusion* process. As a result of this new process, the transition between the very high rear side doping and the low doped active volume is not as sharp as it can be observed after e.g. rear side implantation. Due to the long diffusion times of the dopants, the transition is not abrupt. A doping profile as expected from a *deep-diffusion* process is illustrated with a red line in Fig. 10.3.1. As a comparison the doping profile resulting

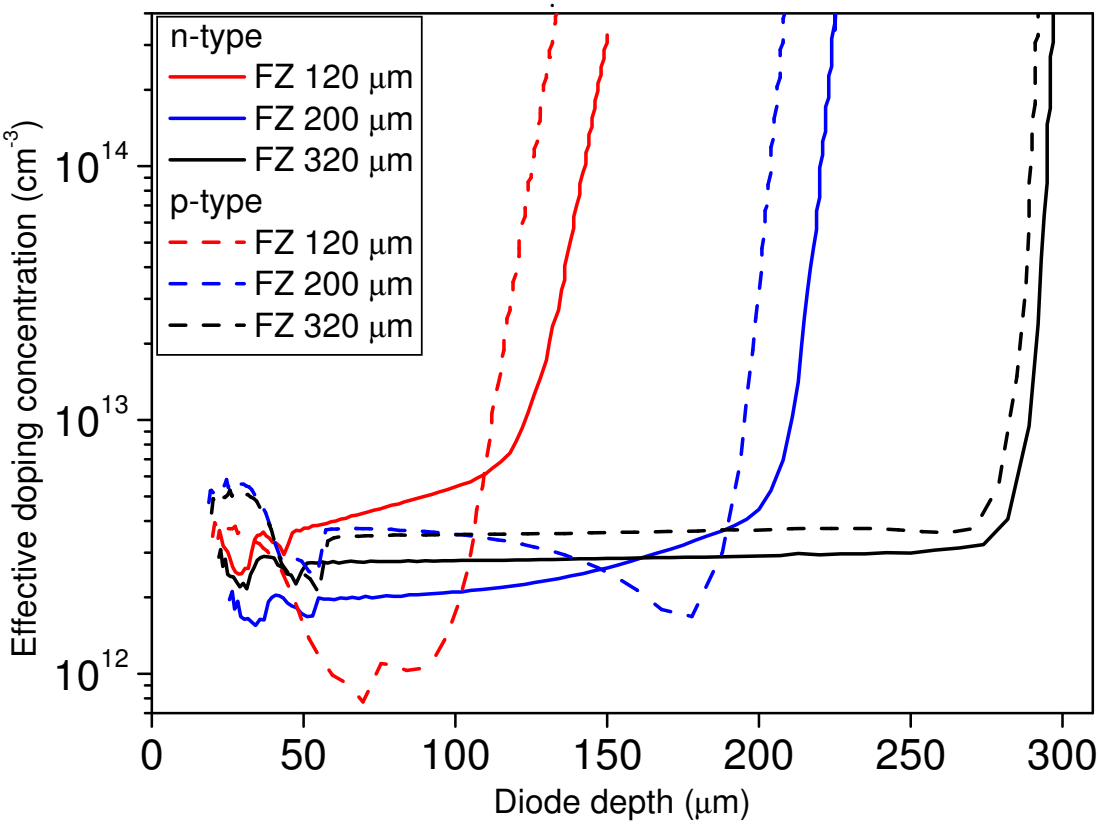

Figure 10.2.8.: Depth profiles of the doping concentration of the analysed diode types from C-V measurements at room temperature. The *p*-type sensors are depicted by dashed lines while the *n*-type sensors are illustrated by solid lines. The *built-in voltage* was analysed and taken into account.

from *wafer-bonding* technology is illustrated in blue. In the *wafer-bonding* technology the ohmic contact at the rear side is commonly produced by implantation and afterwords the material is bonded to a handling wafer with low resistivity. This results in a much sharper transition between low doped active sensor volume and highly doped rear side. However, neither the non-saturation and the high leakage current nor the depth profile can be explained by the non-uniformity of the *deep-diffusion* process.
The *deep-diffusion* of the doping atoms would only result in an increase of the N_{eff}, but not in a decrease, like found for the *p*-spray samples in Fig. 10.2.8. A reason for the change of the ideal doping profile can be found in the introduction of a donor, which can be identified by the *Deep Level Transient Spectroscopy* (DLTS) if the defect is not too shallow.
Five so far unobserved defects were found in the materials by means of DLTS. The spectra for electron traps in *n*-type material (red line) and hole traps in *p*-type material (black line) are illustrated in Fig. 10.3.2. The most prominent defects are observed at 61

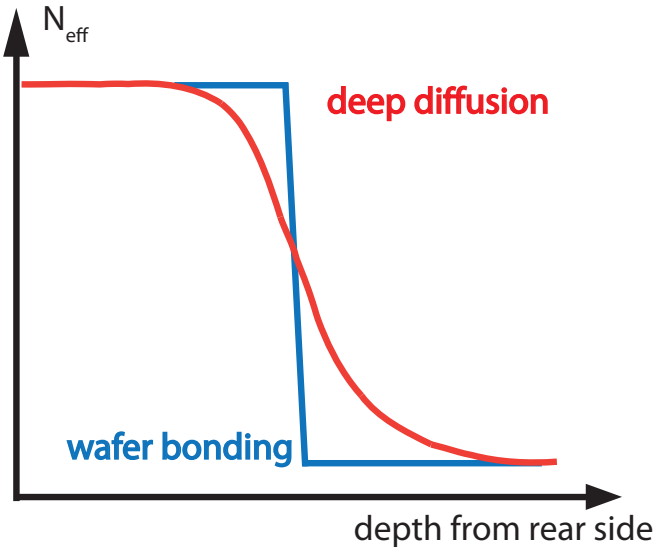

Figure 10.3.1.: Schematic illustration of the new *deep-diffusion* process starting from the rear side (red). For comparison the same profile is shown for the commonly used *wafer-bonding* technology (blue).

K and at 220 K. The first defect called $E(61K)$ is an electron trap, while the $H(220K)$ labelled defect is a hole trap. Two further hole traps have been found at 160 K and 50 K, therefore labelled $H(160K)$ and $H(50K)$. One additional electron trap at around 28 K was found in the n-type material and labelled $E(30K)$. The $E(30K)$, $H(50K)$ and $E(61K)$ have been detected in both diode types, the presence of $H(220K)$ in n-type could not be verified due to defect-filling limitations (e.g. with 200 µm non-active silicon at the rear side, filling with light from the rear side, and thus injecting only holes is not possible).

Electron traps

The $E(61K)$ is a donor with impact on the space charge, which is nicely demonstrated by the *Poole-Frenkel* effect in Fig. 10.3.3. The depth profile of this defect was obtained by measuring DLTS transients at a fixed temprature with bias voltage and pulse voltage chosen in such a way that only defects in a thin region inside the sensor are filled. From the transient it is possible to obtain the defect concentration in that volume of the detector. By varying the bias voltage and pulse voltage a profile of the defect concentration can be observed.

The result is presented in Fig. 10.3.3 (b). The red circles represent the concentration of the $E(61K)$ defect as a function of the depth inside the silicon bulk. The measured concentration is generally high and rises towards the rear side. This measurement assumes a homogeneous doping concentration throughout the sensor depth. Due to the fact that the doping concentration increases towards the rear side, this measurement underestimates the defect concentration towards the rear side.

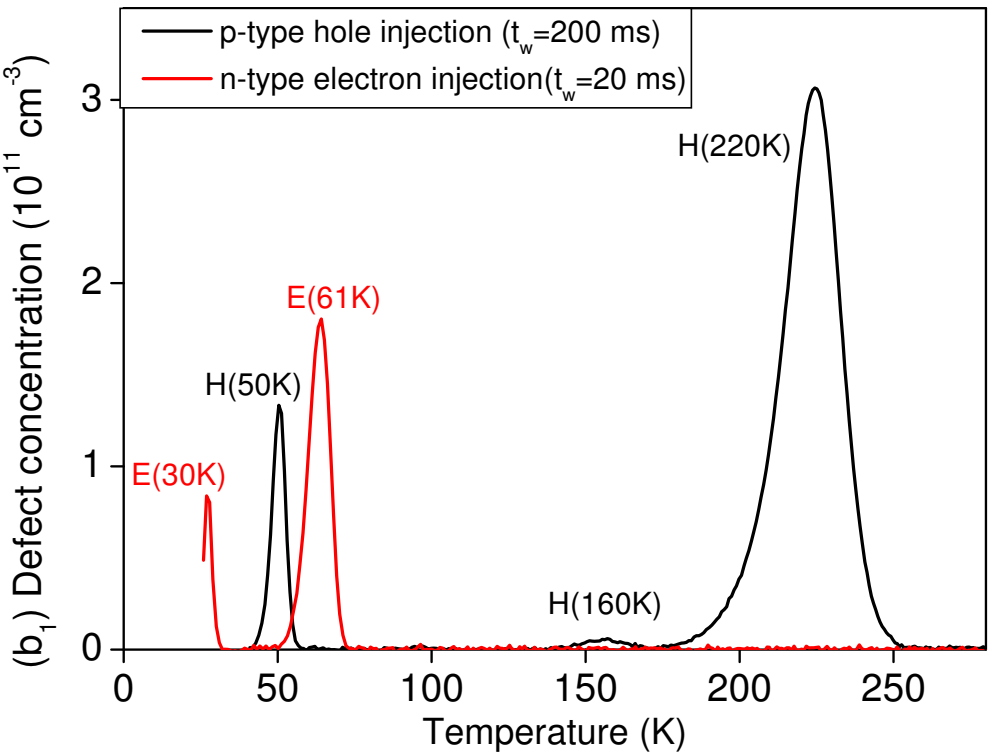

Figure 10.3.2.: Electron and hole traps found in the unirradiated material by DLTS. Majority carrier traps in FZ120N (n-type) are shown in red, majority carrier traps in FZ120Y (p-spray) are illustrated in black.

The donor $E(30K)$ is a very shallow electron trap located at the lower edge of the temperature range of the DLTS cryostat. Unfortunately it was not possible to gather information about the defect properties and the impact on the space charge, as the temperature of the peak maximum is too low. Yet, it was possible to measure a depth profile of the defect, which is presented in Fig. 10.3.3 (b). The black squares show the concentration of the $E(30K)$ defect as a function of the depth inside the silicon bulk. The defect concentration rises towards the rear side, reaching a value of about $1 \times 10^{12}\,\mathrm{cm}^{-3}$. Like for the $E(61K)$ defect the inhomogeneity of the material leads to an underestimation of the defect concentration.

Hole traps

The shallow $H(50K)$ defect was seen in p-type as well as in n-type material. First measurements of the depth dependence of this defect revealed a maximum concentration directly beneath the front surface. This defect is an acceptor and can most likely be correlated to the change of the N_{eff} at the front measured by C-V in the first 50 µm (see Fig. 10.2.8). It is very likely that this acceptor contributes with negative sign to the space charge, which leads to an increase of the N_{eff} in p-type material, and a decrease in the n-type material, as observed in the N_{eff} depth profile in Fig. 10.2.8.

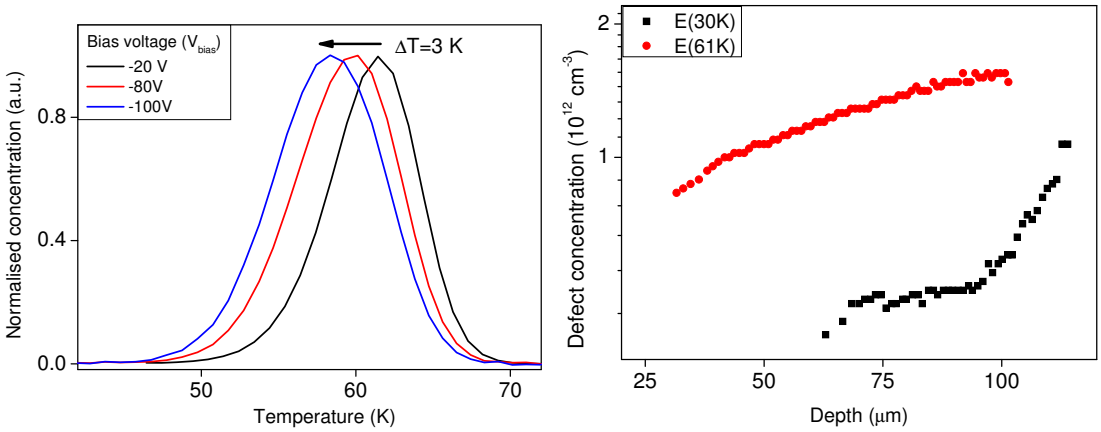

Figure 10.3.3.: *Poole-Frenkel* effect of the $E(61K)$ defect in FZ120N 03 Diode1. A normalisation to unity was performed for better visibility (a). Depth profile of the $E(30K)$ and $E(61K)$ in FZ120N 03 Diode1 (b).

The $H(220K)$ defect is a deep trap level, which was exclusively seen in *p*-type material. Measurements with applying forward current, injecting both holes and electrons, revealed a suppression of the $H(200K)$ defect. This result is only reasonable for a hole trap with a very high electron capture cross section which is 1-2 orders of magnitude higher than the capture cross section of holes. That means, the defect can not be filled with holes in the presence of electrons and, therefore, cannot be seen by forward biasing in DLTS. Fig. 10.3.4 (a) shows two measurements of a *p*-spray detector filled with holes (black) and holes and electrons (red). It is well visible that the $H(220K)$ defect is suppressed in the presence of electrons.
Generally it is only possible to fill minority carriers electrically by forward current, but then there are always majority carriers present. As in *n*-type material the majority carriers are electrons and the minority carriers are holes it is not possible to fill holes exclusively. Unfortunately, illumination with light from the rear side is not a possibility either, because the 200 µm highly doped rear side absorbs the light. Therefore the $H(220K)$ defect cannot be filled in *n*-type material and thus the question if this defect is also found in *n*-type material remains open.
Concerning the capture cross section of holes of the $H(220K)$ defect some strange results were found. Both the capture cross section for electrons is much larger than for holes, and on top of that it seems, that the capture cross sections for holes is not constant, but depends on the applied voltage. Additionally, the defect shows an electron-like character in some DLTS measurements, which could not be related to an overlapping electron trap. In the end, this problem can not be solved and the correct capture cross sections could not be determined due to the limitations in filling with holes, see above. The upper and lower limits are given in Tab. 10.3.1.

One way to perform further analyses on n-type material could be done by injecting light from the rear side of the sensor. For that purpose, a thinning of the substrate would be necessary.

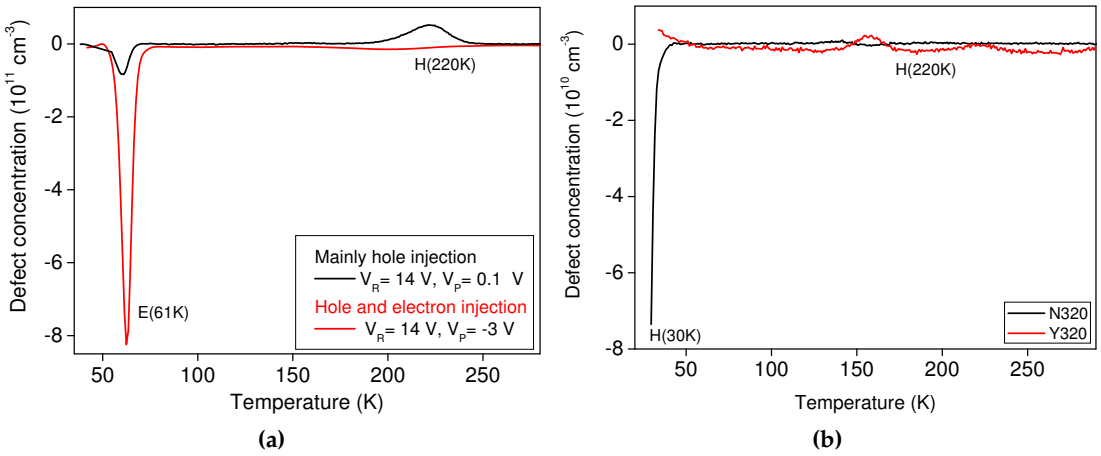

Figure 10.3.4.: DLTS spectra of p-spray diodes filled with majority carriers (holes) only (black line) and holes and electrons (red line). The $H(220K)$ is suppressed in the presence of electrons (a). The 320 µm thick n and p-type (p-spray) material is devoid of defects (b).

Thickness dependence of defect concentrations

A comparison of the concentration of the main defects in the sensors revealed a dependence on the thickness of the sensor. Fig. 10.3.4 (b) presents a comparison of DLTS spectra of p-type (p-spray) and n-type diodes with 320 µm thickness, revealing, that the material is nearly free of defects. Note, that the DLTS setup is limited to a bias voltage of 100 V which depletes only the first 180 - 200 µm of bulk material. This means the achievable depletion region with this DLTS setup does not reach the rear side ($w < d$). In contrast to that it is possible to fully deplete the 200 µm and 120 µm thick sensors with 100 V, and therefore to measure the concentration of the defect over the full sensor volume.

A comparison of the defect concentrations of the two most prominent defects in the material is represented in Fig. 10.3.5 (a) for the $E(61K)$ defect and (b) for the $H(220K)$ defect. The defect concentration shows a strong dependence on the thickness of the material.

Defect	ΔE_a (eV)	σ_n (cm^2)	σ_p (cm^2)	T$_{max}$ (K) ($t_w = 200$ ms)
$E(30K)$	≈-0.04	$\approx 1 \times 10^{-17}$	-	≤ 26
$E(61K)$	-0.125	2×10^{-15}	-	61
$H(50K)$	0.101	-	3×10^{-14}	50

Continued next page ...

Defect	ΔE_a (eV)	σ_n (cm^2)	σ_p (cm^2)	T$_{max}$ (K) ($t_w = 200$ ms)
$H(160K)$	0.301	-	9×10^{-16}	156
$H(220K)$	0.388 - 0.442	$\ll \sigma_p$	$1 \times 10^{-15} - 6 \times 10^{-17}$	220

Table 10.3.1.: Properites of defects found in new FZ CMS test-structures: Name, activation energy ΔE_a where a negative sign refers to $E_C - \Delta E_a$ and positive sign refers to $E_V + \Delta E_a$, capture cross section for electrons and holes $\sigma_{n,p}$, peak temperature T_{max} observed in DLTS with a time window of $t_w = 200$ ms.

The highest concentration can be found in 120 µm (red), followed by the 200 µm diode (black). As mentioned earlier, the defect concentration of the two defects is negligible in the 320 µm thick samples. But due to the fact that the rear part cannot be depleted, it is not possible to obtain defect concentrations at the rear side.
However, from C-V measurements taken at room temperature it can be assumed that small amounts of these defects with impact on the N_{eff} are located near the interface of the *in-diffused* n^+ or p^+ layers. Table 10.3.1 shows the main properties of the defects found in this material.

10.4. Influence of deep $H(220K)$ defect on the leakage current

The p-spray diodes exhibit a high leakage current compared to the n-type diodes. If it is generated by a defect in the crystal lattice, a possible candidate is the deep hole trap $H(220K)$. For the time being we will neglect the strange behaviour of the capture cross section for holes and discuss a possible correlation of this defect and the leakage current in the p-type sensors.
Fig. 10.4.1 (a) presents the volume generation current for three different p-spray diodes. Black diamonds represent FZ120Y-06 Diode1, red circles show FZ200Y-03 Diode2. It is clearly seen, that the 120 µm has a volume generation current similar to the 200 µm sample. This is a very nice situation for a comparison of defect concentrations, because the current should scale with the defect concentration. A second 200 µm sample with much less current is shown in blue (FZ200Y-02 Diode1). For this diode, the defect concentration should be much lower.
Corresponding DLTS measurements are illustrated in Fig. 10.4.1 (b). The *colour-code* for the DLTS spectra was chosen similar to that of the volume generation current as function of the applied voltage in Fig. 10.4.1. The correlation between the defect concentration is obvious: $[H(220K)]$ (FZ120Y-06 Diode1) $\approx 3 \times 10^{11}$ cm^{-3} which is similar to $[H(220K)]$ (FZ200Y-03 Diode2) $\approx 3 \times 10^{11}$ cm^{-3}. The diode with lower current also shows a lower defect concentration: $[H(220K)]$ (FZ200Y-02 Diode1) $\approx 1.5 \times 10^{11}$ cm^{-3}. Qualitatively the obtained defect concentrations scale with the observation

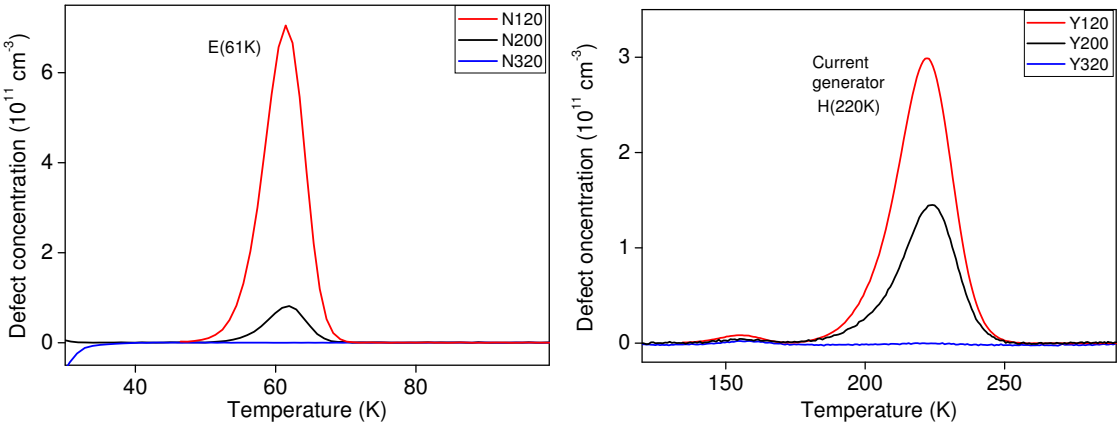

(a) **(b)**

Figure 10.3.5.: $E(61K)$ defect (a) and $H(220K)$ defect (b) for different diode thicknesses.

of the volume generation current very nicely[2]. Calculations of the current generation

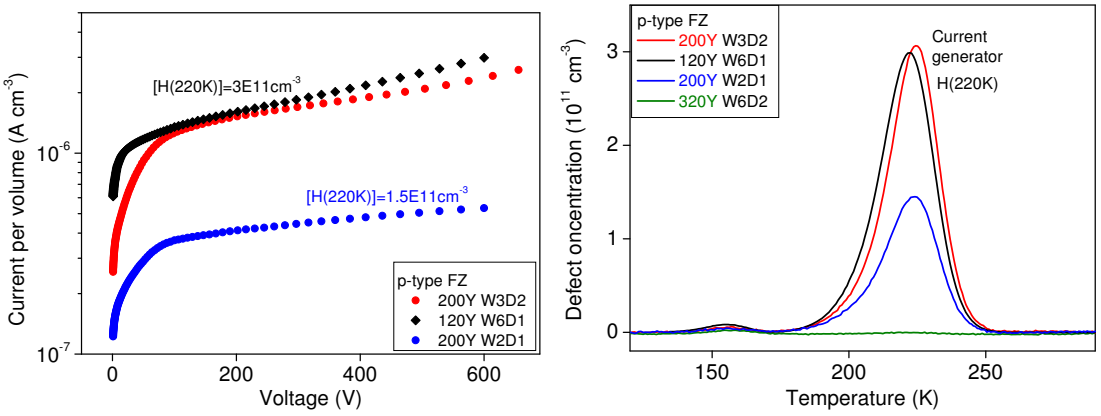

(a) $E(61K)$ **(b)** $H(220K)$

Figure 10.4.1.: Volume generation current for p-spray diodes of 120 µm and 200 µm thickness (a) and corresponding DLTS spectra illustrating the defect concentration measured in the respective diodes (b).

ΔI due to the $H(220K)$ defect were performed via Eq. 4.5.6 in order to find lower and upper limits of the current generation. Necessary values for the activation energy of

[2]Note that the guard ring was not used for DLTS measurements, therefore the active volume of the diodes is not well-defined and the defect-concentrations can only be used qualitatively. But on the other hand, one can see from Fig. 10.4.1 that the defect concentrations of diodes of different thickness match very well, implying that the active volume does not differ very much although the guard ring is not connected.

hole emission ΔE_a and the hole and electron capture cross sections $\sigma_{p,n}$ are listed in Tab. 10.3.1. As mentioned earlier, the hole capture cross section is much smaller than the electron cross section. Calculations were carried out with σ_n and σ_p different by two orders of magnitude. Calculated currents ΔI for different values for ΔE_a and $\sigma_{n,p}$ are listed in Tab. 10.4.1 for 120 µm and 200 µm. Since the guard ring could not be connected, the extracted defect concentrations are very rough estimations. The value cannot serve as a quantitative prediction of the absolute current.

ΔE_a eV	σ_n cm^2	σ_p cm^2	N_D cm^{-3}	thickn. µm	ΔI nA	I from I-V nA
0.388	6×10^{-17}	6×10^{-15}	3×10^{11}	120	0.056	4.7
0.388	6×10^{-17}	1×10^{-12}	3×10^{11}	120	5.6	4.7
0.444	1.5×10^{-15}	1.5×10^{-14}	3×10^{11}	120	1.3	4.7
0.444	1.5×10^{-15}	1.5×10^{-13}	3×10^{11}	120	12.8	4.7
0.444	1.5×10^{-15}	5×10^{-14}	3×10^{11}	120	4.3	4.7
0.444	1.5×10^{-15}	5×10^{-14}	3×10^{11}	200	7.2	7.4
0.444	1.5×10^{-15}	5×10^{-14}	1.5×10^{11}	200	3.6	2.1

Table 10.4.1.: Calculation of the contribution of the current ΔI induced by the $H(220K)$ defect to the leakage current and comparison to the current from I-V measurements at 200 V in the corresponding sensor.

In conclusion, the calculated current values using an activation energy of about $\Delta E_a = 0.44$ eV and the capture cross sections in the range of $\sigma_n \approx 1.5 \times 10^{-15}$ cm^2 and $\sigma_p \approx 5 \times 10^{-14}$ cm^2 are compatible with the measured values for the diodes FZ120Y-06 Diode1 and FZ200Y-02 Diode1. During the diffusion at high temperatures, lattice stress may be created, therefore it can be speculated that the defect is a stacking fault. Such a stacking fault may have a temperature and/or voltage dependent capture cross section. Further investigations are planned.

10.5. Influence of the shallow donor *E(61K)* defect on the doping profile of the sensors

As mentioned in Sec. 10.2.3, the doping profiles of the diodes reveal the possible presence of a shallow donor that contributes positively to the space charge. Defects with impact on the space charge are often very shallow, since they need to be ionised at room temperature. As the DLTS setup sensitivity is limited to 28 K we may not be able to see defects that could contribute to the space charge and have activation energies of about $\Delta E_a < 0.04$ eV. Nevertheless, there are some defects visible in the DLTS spectra that can be studied. This section will show a correlation of the $E(61K)$ defect to the N_{eff}.
The donor-like $E(61K)$ defect peak position exhibits a dependence on the applied

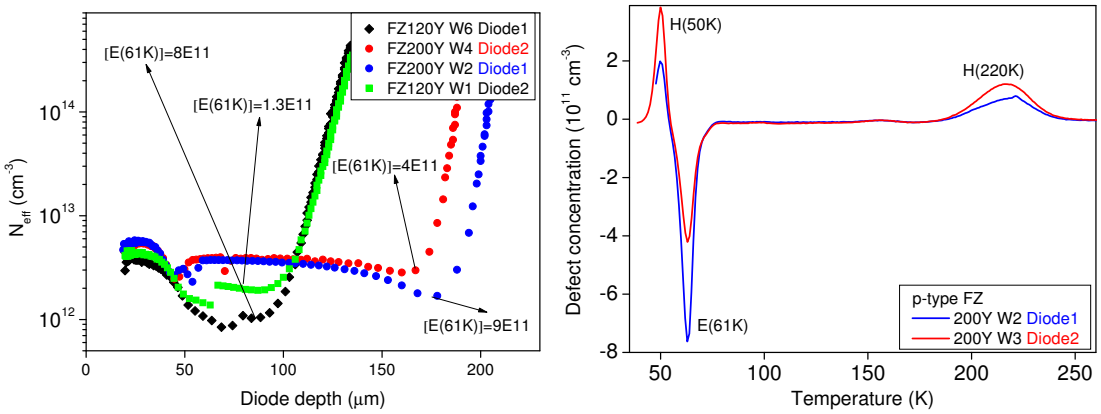

Figure 10.5.1.: Depth profile of the effective doping concentration N_{eff} from C-V measurements for four diodes with 120 µm and 200 µm thickness. The corresponding defect concentrations of the $E(61K)$ defect from DLTS measurements over the entire diode thickness is given in the figure (a). The DLTS spectra of the two 200 µm thick sensors (b) reflect the correlation between the dip in the N_{eff} from (a) and the concentration of the $E(61K)$ defect.

voltage, also called *Poole-Frenkel* effect. Therefore we know that the defect contributes to the positive space charge and is a good candidate for the sought-after donor. For p-type diodes, a positive space charge compensates parts of the B-doping of the silicon material. This too would match with the observation in N_{eff}. Since the inhomogeneity of the N_{eff} is stronger for thinner materials, this is expected also for the concentration of the responsible defect.
A study was performed on four p-spray diodes, two with 200 µm thickness and two with 120 µm thickness. Firstly depth profiles of N_{eff} were taken from C-V measurements, they are represented in Fig. 10.3.5 (a). Then DLTS measurements were performed in order to extract the defect concentration of $E(61K)$. The concentrations are displayed in the same figure. It is well visible that the depth of the dip in the N_{eff} correlates with the qualitative[3] defect concentration.
Fig. 10.5.1 (b) presents corresponding DLTS spectra for the two 200 µm diodes, red matches the FZ200Y-03 Diode2, blue shows the results for FZ200Y-02 Diode1. The concentration of the $E(61K)$ defect is reflected in the depth of the dip.
Since we believe that the $E(61K)$ defect is responsible for the change of the N_{eff}, the defect concentration has to be added to the P-doping for n-type diodes to explain the depth profile. Fig. 10.5.2 shows the depth profile of a FZ120N sensor (red squares)

[3]Note that the guard ring was not connected and furthermore if possible the measurements were performed on the entire thickness of the sensor. A comparison of the defect concentration between 200 µm and 120 µm thick diodes is not useful, since the defect concentration is very inhomogeneous, as seen in Fig. 10.3.3 (b).

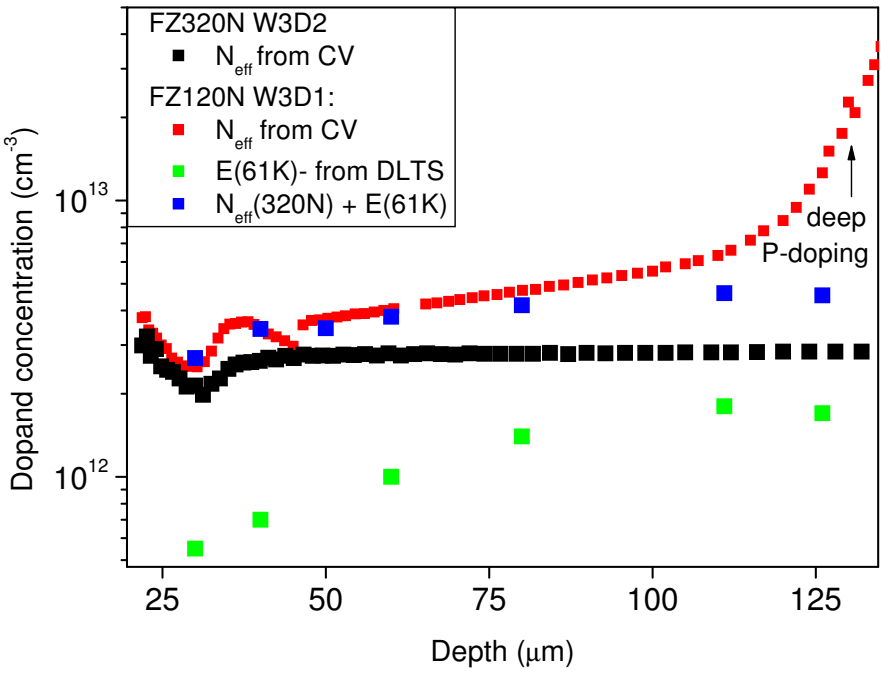

Figure 10.5.2.: Dopant concentration as function of depth in FZ120N (red squares) and FZ320N (black squares). The difference can be explained by the $E(61K)$ defect concentration (green squares), extracted by a DLTS depth profile. The sum (blue squares) of the concentration of $E(61K)$ and the *uneffected* N_{eff} profile from FZ320N reproduces the first 100 µm of the FZ120N very well (compare red and blue squares).

compared to FZ320N sensor (black squares). Because the *deep-diffusion* process did not influence the main part of the 320 µm n-type diodes, the original doping of the starting material (before processing and *deep-diffusion*) seems to match best with the very homogeneous FZ320N diode. A depth profile of the $E(61K)$ defect measured by DLTS is shown in this figure as green squares, as well. This depth-dependent concentration added to the original doping profile of the FZ320N diode should reproduce the N_{eff} vs. depth profile of the diode, if $E(61K)$ is responsible for the change of the doping profile. This was done for the FZ120N diode, and is presented with blue squares in the same figure. The comparison between the N_{eff} profile measured by C-V of the FZ120N sensor and the sum of the original doping concentration from FZ320N with the defect profile of $E(61K)$ reveals that the first 100 µm can be reproduced very well with the help of the $E(61K)$ defect concentration.
This shows that the $E(61K)$ defect fulfills all requirements to change the doping profile of the thin n-type sensor. At the rear side towards the *deep-diffusion* layer, the P-doping leads to the observed steep increase of the N_{eff}. This matches the expectations from Fig. 10.3.4.
In conclusion, the measurements reveal that the $E(61K)$ defect is responsible for the

change of the effective doping concentration in the *n*-type and *p*-spray diodes.

10.5.1. Résumé

The investigations concerning the future HL LHC CMS test-structures revealed the presence of defects in the non-irradiated FZ material. A deep acceptor labelled $H(220K)$ was found to be a possible current generator. Two defects with impact on the effective doping concentration were correlated to the depth profile of the N_{eff}. A shallow acceptor, labelled $H(50K)$, with the main concentration in the first 50 µm was found to be the origin of the change of the N_{eff} in the front part of the diodes. Furthermore, a shallow donor, labelled $E(61K)$, with increasing concentration towards the rear side was correlated to the change of the N_{eff} at the rear side of the material.
The concentration of the material defects is correlated to the thickness of the sensors. The thinner the diodes the higher the defect concentrations. Moreover, an variation of the thicknesses of the active volume and the capacitance is found to be related to the position on the wafer. The oxygen concentration ([O]$= 1 - 10 \times 10^{17}$ cm^{-3}) of the FZ test-structures, communicated by the company, is much higher than expected for pure FZ material. From the dependence of the active diode thickness on the position on the wafer as well as the dependence of the introduction of material defects on the thickness of the diffusion-region it can be concluded that the defects were introduced into the material during the newly applied *deep-diffusion* process. The size of the 6 inch wafer is quite large which may e.g. lead to an inhomogeneous heat treatment throughout the *deep-diffusion* process. It seems likely, that the heat applied during the *deep-diffusion* process in combination with the very high oxygen concentration led to the creation of material defects with impact on the detector properties. Due to the high oxygen content in the silicon material, it can be assumed, that *thermal donors (TDD)* were created. This would also explain the position dependent inhomogeneity of diode thicknesses within one wafer. Furthermore it is very likely, that lattice stress was created during the *deep-diffusion* process, due to the migration of impurities and heating/cooling treatment of the material.
In conclusion, the characterisation of test-structures after irradiation will be influenced by the material defects that are already present inside the non-irradiated silicon. From the test-structures analysed in this work, only the 320 µm thick *n*- and *p*-type sensors behave as expected for highly pure silicon, aside from the $H(50K)$ defect at the front side of the diode that can be found in all test-structures. It is not clear yet, if the material defects will influence the results of the following radiation campaign. The concentrations of material defects found in the 200 µm thick sensors are small compared to the concentration of irradiation induced defects after a fluence of $\Phi_{eq} = 1 \times 10^{14}$ cm^{-2}. Nevertheless, a combination of the material defects with newly created irradiation induced defects has to be expected. The highest impact of material-defects on the results after irradiation is expected for the 120 µm thick sensors. Future irradiation studies will give further insight into the interplay of irradiation induced defects and defects introduced during production.

Due to the high levels of defects introduced during the processing of the silicon wafers in the 120 µm thin material, it will be very difficult to reliably study radiation damage for that material.

11. Summary and conclusion

The main damage expected in future HL LHC silicon sensors is generated by hadronic irradiation, which creates a mixture of point and cluster defects. It is shown in this work that the main sensor deterioration after hadron irradiation can be related to the generation of cluster defects, while point defects are of minor importance. Cluster related defects introduce several levels in the band gap with impact on the electrical properties of silicon sensors. The main result of this work is summarised in the following.

Leakage current
An investigation of the leakage current in combination with analyses of the defects by DLTS and TSC was performed for different materials (Float Zone, Magnetic Czochralski, epitaxial silicon). Isochronal and isothermal annealing procedures were done in order to be able to separate defect levels in the cluster region ($E4$, $E5$, $E205a$, V_2) by different techniques, e.g. by using difference spectra.
In this work a major break-through concerning the identification of the origin of leakage current was achieved. Two defects with impact on the generation of leakage current were observed, one of them, the $E5$ level at E_C-0.460 eV, is responsible for the main part (about 60 %) of the generation of leakage current after hadron irradiation. Here, E_C denotes the energy with respect to the edge of the conduction band. The $E205a$ level at E_C-0.395 eV is responsible for less than 30 % of the total leakage current. This defect anneals out between 100-200 °C.
The $E5$ level exhibits a bistability, which results in two configurations of the defect. The $E4/E5$ defect levels vanish during annealing at low temperatures (room temperature to 200 °C) and a shallow defect $E75$ appears. By applying a high forward current density ($J_{forw} > 2$ A cm^{-2} for 10 min), it is possible to recover the full concentration of the $E4/E5$ defect levels and $E75$ vanishes. With help of this bistability it could be shown that $E5$ can be assigned to the singly charged state of the tri-vacancy ($E5$= $V_3^{-/0}$ and $E4$= $V_3^{=/-}$). Detailed studies revealed a direct and reproducible correlation between the leakage current and the $E5$ level.
Isochronal annealing studies have shown that V_3 transforms to the L defect in oxygen rich material in a similar way as V_2 to V_2O. Following the same argumentation, the assignment for the L defect was proposed to be V_3O. The out-annealing of the V_3 was analysed and the reaction kinetics for the transformation of $V_3 \rightarrow V_3O$ was studied. The activation energy for migration was observed to be $E_a = 1.77 \pm 0.08$ eV with a pre-exponential factor of $k_0 = 5 \times 10^{13}$ s^{-1}. The V_3 defect anneals out starting at 250 °C, depending on the oxygen concentration of the material.

An influence of the disordered region on the leakage current was observed and investigated. The annealing of the damaged region leads to a decrease of the leakage current independent of the material. Further investigation of the recovery of one of the bistable V_3 configurations ($E4/E5$), leads to the conclusion that potential barriers surrounding the damaged region influence the filling of defects inside the damaged region. This influence is also seen for several defects (e.g. VO_i), also changing defect properties like capture probabilities for electrons and holes.
The V_3 defect transforms at room temperature from the $E4/E5$ levels to a non-current generation level ($E75$). This is usually referred to as out-annealing (although it is not real annihilation) which is used for HL-LHC scenarios (sometimes referred to as sLHC scenarios) where the current is reduced by annealing during maintenance periods. Due to the fact that the recovery of the current generating $E5$ configuration was found to start at a minimum forward current density of 0.08 A cm^{-2}, it cannot be recovered by accidental high reverse current during operation times for highly irradiated samples. Independent of the material, the total recovery was found for forward currents densities higher than 2 A cm^{-2}.

Effective doping concentration

Oxygen enriched and standard epitaxial silicon samples were irradiated with $\Phi_{eq} = 2 \times 10^{14}$ cm^{-2} and $\Phi_{eq} = 1 \times 10^{15}$ cm^{-2} reactor neutrons. *Capacitance-voltage* C-V (at 10 and 100 kHz) and *current-voltage* I-V characteristics were carried out at room temperature during isothermal annealing studies. In parallel TSC measurements were performed in order to extract the concentration of defects with impact on the effective doping concentration.
A strong correlation between the annealing behaviour of the defect concentrations and the effective doping concentration as extracted from C-V was found for the $\Phi_{eq} = 2 \times 10^{14}$ cm^{-2} fluence for the whole annealing time. For highly irradiated samples ($\Phi_{eq} = 1 \times 10^{15}$ cm^{-2}) only the reverse annealing of N_{eff} can be reproduced by the defects detected in the sensors.
The deep acceptor levels $H(116K)$, $H(140K)$ and $H(151K)$ in combination with two donor levels $E(30K)$ and a bistable donor BD were proven to be responsible for the long term annealing of epitaxial sensors with high and low oxygen concentrations at high neutron fluences ($\Phi_{eq} = 1 \times 10^{15}$ cm^{-2}). However, at that high fluences, some inconsistencies concerning the temperature dependence of the E-center (VP) and the short-term annealing hint to the existence of another defect with influence on the N_{eff}, which has not yet been identified.
A comparison of neutron and proton irradiated samples reveals, that the sensors independent of the material undergo type inversion from n to p after irradiation with neutrons, while there is no type inversion seen after proton irradiation. This behaviour can be explained by the interplay of the deep acceptors ($H(116K)$, $H(140K)$, $H(151K)$), the shallow donors ($E(30K)$, BD) and the generation of the VP defect.
Some problems inherent to the TSC measurement technique came out during the preparation of this work. On the one hand the importance of the filling time and

filling current for highly irradiated sensors should be mentioned. This factor must be controlled during the whole measurement process. The complete filling of the defects is essential for the evaluation of absolute concentrations.

New materials characterisation

In the frame of the CMS tracker upgrade, an ongoing comprehensive measurement campaign on test-structures made of all common silicon materials is performed by several institutes including Hamburg University. The aim of this investigation is the characterisation of the radiation tolerance of the available materials.
In this work, Float Zone (FZ) *n*-type and *p*-type diodes were analysed. These sensors were produced in 120 µm, 200 µm and 320 µm active layer thickness and a physical thickness of 320 µm. The thinning of the sensors was achieved by in-diffusion of a high concentration of dopants from the rear side, creating a low ohmic substrate layer. The diffusion of boron and phosphorus through a large distance (200 µm resp. 120 µm) is a new process, called the *deep diffusion process*.
The silicon diodes investigated in this study revealed an unexpected capacitance-voltage and current-voltage characteristics behaviour of the unirradiated sensors. The capacitance curve of the 120 µm and 200 µm diodes shown a transition region between active layer thickness and low ohmic rear side layer that is less sharp than expected. From the capacitance curve, the effective doping concentration as function of diode depth can be calculated. The doping profiles reveal inhomogeneous doping concentrations in both, *n*- and *p*-type sensors. Furthermore, it can be shown that the thinner diodes generate higher currents than the thicker diodes.
The reason for this behaviour was assumed to be a result of bulk defects that were introduced in the material during the processing. Investigations with the *Deep Level Transient Spectroscopy* were performed in order to revealed the presence of several defects in the non-irradiated FZ material. A deep hole trap labelled $H(220K)$ was found to be a possible current generator. Two defects with impact on the effective doping concentration were correlated to the depth profile of the N_{eff}. A shallow acceptor, labelled $H(50K)$, with the main concentration in a layer of 50 µm below the surface was found to be the origin of the change of the N_{eff} in the front part of the diodes. Furthermore, a shallow donor, labelled $E(61K)$, with increasing concentration towards the rear side was correlated to the change of the N_{eff} in that region.
The concentration of the material defects is correlated to the thickness of the sensors. The thinner the diodes the higher the defect concentrations. Moreover, an inhomogeneity of the thicknesses of the active volume and the capacitance is found to be related to the position on the wafer. The oxygen concentration ([O]$= 1 - 10 \times 10^{17}$ cm^{-3}) of the FZ test-structures, communicated by the company, is much higher than expected for pure FZ material. From the thickness dependence of the defect concentration, the resulting diode properties and the inhomogeneity of the material across the 6 inch wafer it can be concluded that the defects were introduced into the material during the newly applied *deep-diffusion process*. It seems likely, that the heat applied during

the *deep-diffusion process* in combination with the very high oxygen concentration led to the creation of material defects with impact on the detector properties. Due to the high oxygen content in the silicon material, it can be assumed that *thermal donors (TDD)* were created. Furthermore it is very likely that dislocations were created during the diffusion process.
In conclusion, the characterisation of test-structures after irradiation will be influenced by the material defects that are already present inside the non-irradiated silicon. From the test-structures analysed in this work, only the 320 µm thick *n*- and *p*-type sensors behave as expected for highly pure silicon, aside from the $H(50K)$ defect at the front side of the diode that can be found in all test-structures. It is not clear yet if the material defects will influence the sensor performance after irradiation. The concentrations of material defects found in the 200 µm thick sensors are small compared to the concentration of irradiation induced defects after a fluence of $\Phi_{eq} = 1 \times 10^{14}$ cm^{-2}. Nevertheless, a combination of the material defects with newly created irradiation induced defects has to be expected. The highest impact of material defects on the results after irradiation is expected for the 120 µm thick sensors. Future irradiation studies will given further insight into the interplay of defects created by radiation and defects introduced during processing.
Due to the high level of defect concentrations introduced during the processing of the silicon wafers in the 120 µm thin material, it will be very difficult to get reliable results from defect studies.

Outlook

Find the origin of *trapping*!

Bibliography

[1] M. A. Green, Intrinsic concentration, effective densities of states, and effective mass in silicon., J. Appl. Phys. 67-6 (6) (1990) 2944–2954. doi:10.1063/1.345414.

[2] S. M. Sze, K. K. Ng, Physics of semiconductor devices, 3rd Edition, John Wiley & Sons, 2007.

[3] M.Moll, simplified, scaled from ATLAS TDR.

[4] E. Fretwurst, et al., Recent advancements in the development of radiation hard semiconductor detectors for S-LHC, Nuclear Instruments and Methods in Physics Research A 552 (2005) 7–19. doi:10.1016/j.nima.2005.05.039.

[5] The RD50 CERN collaboration, Radiation hard semiconductor devices for very high luminosity colliders, http://rd50.web.cern.ch/rd50/.

[6] F. Shimura (Ed.), Oxygen in silicon, Vol. 42 of Semiconductors and Semimetals, Academic Press, INC., 1994.

[7] H. Theuerer, U.S. patent 3,060,123 (1962).

[8] Siltronic AG, Hanns-Seidel-Platz 4, 81737 München, Deutschland (www.siltrocic.com (last checked: 12.04.2011)).

[9] SIMS laboratory, Physics Institute of the Polish Academy of Science, Warsaw, Poland.

[10] ITE, Institute of Electron Technology, Al. Lutnikow 32/46, 02-668 Warsaw, Poland.

[11] J. Czochralski, Metalle, Z. Phys. Chem., 92:219.

[12] Okmetic Oyj, P.O. Box 44, FI-01301 Vantaa, Piitie 2, FI-01510 Vantaa, Finland, www.okmetic.com (last checked:12.04.2011).

[13] RD50 Status Report 2007, Radiation hard semiconductor devices for very high luminosity colliders, CERN-LHCC-2008-001 and LHCC-RD-015.

[14] CiS, Institut für Mikrosensorik GmbH, Erfuhrt, Germany.

[15] J. Lange, Radiation Damage in Proton-Irradiated Epitaxial Silicon Detectors (Diploma Thesis, Universität Hamburg, DESY-THESIS-2009-022, July 2009).

[16] B. Langhanki, Electron Paramagnetic Resonance of Process-Induced Defects in Silicon, Ph.D. thesis, Universität Paderborn (2001).

[17] A. Gorišek, V. Cindro, I. Dolenc, H. Frais-Kölbl, E. Griesmayer, H. Kagan, S. Korpar, G. Kramberger, I. Mandiċ, M. Meyer, M. Mikuž, H. Pernegger, S. Smith, W. Trischuk, P. Weilhammer, M. Zavrtanik, Atlas diamond Beam Condition Monitor, Nuclear Instruments and Methods in Physics Research Section A 572 (1) (2007) 67 – 69, frontier Detectors for Frontier Physics - Proceedings of the 10th Pisa Meeting on Advanced Detectors.
doi:10.1016/j.nima.2006.10.348.

[18] S. I. Parker, C. J. Kenney, J. Segal, 3D - A proposed new architecture for solid-state radiation detectors, Nuclear Instruments and Methods in Physics Research Section A 395 (3) (1997) 328 – 343, Proceedings of the Third International Workshop on Semiconductor Pixel Detectors for Particles and X-rays.
doi:10.1016/S0168-9002(97)00694-3.

[19] U. Parzefall, G.-F. D. Betta, S. Eckert, L. Eklund, C. Fleta, K. Jakobs, S. Kühn, G. Pahn, C. Parkes, D. Pennicard, S. Ronchin, A. Zoboli, N. Zorzi, Silicon microstrip detectors in 3D technology for the sLHC, Nuclear Instruments and Methods in Physics Research Section A 607 (1) (2009) 17 – 20, Radiation Imaging Detectors 2008 - Proceedings of the 10th International Workshop on Radiation Imaging Detectors.
doi:10.1016/j.nima.2009.03.122.

[20] J. Lange, J. Becker, E. Fretwurst, R. Klanner, G. Lindström, Properties of a radiation-induced charge multiplication region in epitaxial silicon diodes, Nuclear Instruments and Methods in Physics Research A 622 (2010) 49–58.
doi:10.1016/j.nima.2010.07.036.

[21] G. Kramberger, et al., Investigation of Irradiated Silicon Detectors by Edge-TCT, Nuclear Science, IEEE Transactions on , vol.57, no.4, pp.2294-2302, doi: 10.1109/TNS.2010.2051957.

[22] W. Grant, Solid-State Electron. 16, 1189 (1189).

[23] G. Casse, A. Affolder, P. Allport, H. Brown, M. Wormald, Enhanced efficiency of segmented silicon detectors of different thicknesses after proton irradiations up to 1×10^{16} n_{eq} cm^2, Nuclear Instruments and Methods in Physics Research A 624 (2010) 401–404.
doi:10.1016/j.nima.2010.02.134.

[24] S. M. Sze, SEMICONDUCTOR DEVICES Physics and Technology, John Wiley & Sons, 1985.

[25] H. Ibach, H. Lüth, Festkörperphysik, 4th Edition, Springer, 1995.

[26] E. Fermi, Sulla quantizzazione del gas perfetto monoatomico (ital.), Rend. Lincei 3, translated as On the Quantization of the Monoatomic Ideal Gas. 1999-12-14. arXiv:cond-mat/9912229. Bibcode 1999cond.mat.12229Z (1926) 145–9.

[27] P. A. M. Dirac, On the Theory of Quantum Mechanics, Proceedings of the Royal Society, Series A 112 (762) (1926) 661–77.

doi:10.1098/rspa.1926.0133.Bibcode1926RSPSA.112..661D.

[28] O. Marti, A. Plettl, Vorlesungsskript Physikalische Elektronik und Messtechnik (Universität Ulm, 2007).

[29] WIKIPEDIA, http://de.wikipedia.org/wiki/datei:tetrahedral-3d-balls.png (Version: 12. December 2006, 6:21 PM) [cited 12. December 2006, 6:21 PM].
URL http://de.wikipedia.org/wiki/Datei:Tetrahedral-3D-balls.png

[30] W. Shockley, Electrons and holes in semiconductors, with applications to transistor electronics, 7th Edition, The Bell Telephone Laboratories series, Van Nostrand, 1959.

[31] H. Feick, Radiation Tolerance of Silicon Particle Detectors for High-Energy Physics Experiments, Ph.D. thesis, Universität Hamburg, Internal Report: DESY F35D-97-08 (August 1997).

[32] M. Moll, Radiation Damage in Silicon Particle Detectors - microscopic defects and macroscopic properties -, Ph.D. thesis, Universität Hamburg, DESY-THESIS-1999-040 (December 1999).

[33] M. McPherson, B. Jones, T. Sloan, Effects of radiation damage in silicon p-i-n photodiodes, Semicond. Sci. Technol. 12 (1997) 1187–1194.

[34] V. V. Lint, T. Flanagan, R. Leadon, J. Naber, V. Rogers, Mechanisms of Radiation Effects in Electronic Materials, John Wiley & Sons, 1980.

[35] J. F. Ziegler, Particle interactions with matter: http://www.srim.org/, last checked (January 2011) [cited 21.01.2011].
URL http://www.srim.org/

[36] M. Huhtinen, Simulation of non-ionising energy loss and defect formation in silicon, Nuclear Instruments and Methods in Physics Research A 491 (2002) 194–215.
doi:10.1016/S0168-9002(02)01227-5.

[37] M. Lazo, D. Woodall, P. McDaniel, Silicon and silicon dioxide neutron damage functions, In Proc. Fast Burst React. Workshop 1986 Sandia National Laboratories [Tech. Rep.] Sand, SAND87-0098 Vol. 1 (1987) 85–103.

[38] A. E722-85, Standard Practice for Characterizing Neutron Fluences Spectra in Terms of an Equivalent Monoenergetic Neutron Fluence for Radiation-Hardness Testing of Electronics., ASTM-09e1 (revision).

[39] P. Griffin, et al., Neutron cross sections taken from ENDF/B-VI, ORNL, unpublished but available from G. Lindström, Hamburg (gunnar.lindstroem@desy.de).

[40] A. Y. Konobeyev, et al., Neutron displacement cross-sections for structural materials below 800 MeV., J. Nucl. Mater. 186 (1992) 117.

[41] M. Huhtinen, P. Aarino, Pion induced displacement damage in silicon devices, Nucl. Instr. & Meth. in Physics Research A 335 (1993) 580.
doi:10.1016/0168-9002(93)91246-J.

[42] G. Summers, et al., Damage correlations in semiconductors exposed to gamma, electron and proton radiations, IEEE Transaction on Nuclear Science, NS-40 (1993) 1372.

[43] M. Huhtinen, P. Aarino, Estimation of pion induced displacement damage in silicon, HU-SEFT R 1993-02.

[44] G. Lindström, et al, Radiation hard silicon detectors-developments by the RD48 (ROSE) collaboration, Nuclear Instruments and Methods in Physics Research A 466 (2) (2001) 308–326.
doi:10.1016/S0168-9002(01)00560-5.

[45] D. Zontar, Study of radiation damage in silicon detectors for high luminosity experiments at LHC, Ph.D. thesis, Ljubljana (1998).

[46] B. Gossick, Disordered Regions in Semiconductors Bombarded by Fast Neutrons, Journal of Applied Physics 30(8) (8) (1959) 1214–1218.
doi:10.1063/1.1735295.

[47] A. Sieck, Structure and physical properties of silicon cluster and of vacancy clusters in bulk silicon, Ph.D. thesis, Universität Paderborn (July 2000).

[48] E. Holmström, K. Nordlund, M. Hakala, Amorphous defect clusters of pure Si and type inversion in Si detectors, Phys. Rev. B 82 (10) (2010) 104111.
doi:10.1103/PhysRevB.82.104111.

[49] A. Junkes, Radiation induced Point and Cluster defects, Diploma thesis, Universität Hamburg (November 2007).

[50] A. Junkes, D. Eckstein, I. Pintilie, L. F. Makarenko, E. Fretwurst, Annealing study of a bistable cluster defect, Nuclear Instruments and Methods in Physics Research A 612 (2010) 525–529.
doi:10.1016/j.nima.2009.08.021.

[51] B. G. Svensson, B. Mohadjeri, A. Hallén, J. H. Svensson, J. W. Corbett, Divacancy acceptor levels in ion-irradiated silicon, Rhysical Review B 43 (3) (1991) 2292–2298.
doi:10.1103/PhysRevB.43.2292.

[52] S. J. Watts, J. Matheson, I. H. Hopkins-Bond, A. Holmes-Siedle, A. Mohammadzadeh, R. Pace, A new model for generation-recombination in silicon depletion regions after neutron irradiation, IEEE Transaction on Nuclear Science, 43(6) (1996) 2587–2596.

[53] K. Gill, G. Hall, B. MacEvoy, Bulk damage effects in irradiated silicon detectors due to clustered divacancies, Journal of Applied Physics 82 (1) (1997) 126–136.
doi:10.1063/1.365790.

[54] W. M. Chen, B. Monemar, E. Janzén, J. L. Lindström, Direct observation of intercenter charge transfer in dominant nonradiative recombination channels in silicon, Phys. Rev. Lett. 67 (14) (1991) 1914–1917.
doi:10.1103/PhysRevLett.67.1914.

[55] I. Pintilie, E. Fretwurst, G. Lindström, Cluster related hole traps with enhanced-field-emission-the source for long term annealing in hadron irradiated Si diodes, Applied Physics Letters 92 (2008) 024101.
doi:10.1063/1.2832646.

[56] W. S. Lau, Infrared Characterization for Microelectronics, World Scientific Publishing Co. Pte. Ltd., 1999.

[57] T. R. Waite, Theoretical Treatment of the Kinetics of Diffusion-Limetied Reactions, Phys. Rev. 107 (2) (1952) 463–470.
doi:10.1103/PhysRev.107.463.

[58] B. Svensson, J. Lindtröm, Kinetic study of the 830- and 889 cm^{-1} infrared bands during annealing of irradiated silicon, Physical Review B 34 (12) (1986) 8709–8717.
doi:10.1103/PhysRevB.34.8709.

[59] R. Wunstorf, Systematische Untersuchungen zur Strahlenresistenz von Silizium-Detektoren für die Verwendung in Hochenergiephysik-Experimenten, Ph.D. thesis, Universität Hamburg (October 1992).

[60] TRIGA Mark II, Training, Research, Isotopes, General Atomic), Operator: Jozef Stefan Institute Ljubljana, Slovenia, http://www.ujv.gov.si/en/nuclear_and_radiation_facilities/research_reactor_triga_mark_ii_with_hot_cell/ last checked: 12.02.2011.

[61] Jožef Stefans Institute Ljubljana and Department of Physics, University of Ljubljana, SI-1000 Ljubljana, Slovenia.

[62] D. Žontar, V. Cindro, G. Kramberger, M. Mikuž, Time development and flux dependence of neutron-irradiation induced defects in silicon pad detectors, Nuclear Instruments and Methods in Physics Research A 426 (1) (1999) 51–55.
doi:10.1016/S0168-9002(98)01468-5.

[63] G. Kramberger, Signal Development in Irradiated Silicon Detectors, Ph.D. thesis, University of Ljubljana (2001).

[64] M. Glaser, L. Durieu, F. Lemeilleur, M. Tavlet, C. Leroy, P. Roy, New irradiation zones at the CERN-PS, Nuclear Instruments and Methods in Physics Research A 426 (1999) 72—77.
doi:10.1016/S0168-9002(98)01472-7.

[65] GafChromic, XR Type R, HD and MD radiochromic dosimetry film, background information and characteristic performance data available

at: http://online1.ispcorp.com/_layouts/Gafchromic/index.html. Manufacturer: International Speciality Products (ISP) (available online at http://www.ispcorp.com) (last checked: 22.02.2011).

[66] M. Glaser, F. Ravotti, M. Moll, Dosimetry Assessments in the Irradiation Facilities at the CERN-PS Accelerator, IEEE Transaction on Nuclear Science 53 No. 4 (2006) 2016–2022.

[67] https://irradiation.web.cern.ch/irradiation/BPM/ [online] (date: 12.02.2011) [cited https://irradiation.web.cern.ch/irradiation/BPM/].
[link].

[68] E. Léon-Florián, C. Leroy, C. Furetta, Particle fluence measurements by activation technique for radiation damage studies, cERN Divisional Report CERN-ECP-95-15 (1995).

[69] ATT SYSTEMS, Fraunhoferstr. 11, 82152 Martinsried, Germany, www.att-systems.com (last checked:20.04.2011).

[70] D. V. Lang, Deep-level transient spectroscopy: A new method to characterize traps in semiconductors, J. Appl. Phys. 45 (7) (1974) 3023–3032.
doi:10.1063/1.1663719.

[71] S. Weiss, Halbleiteruntersuchungen mit dem DLTFS- (Deep Level Transient Fourier Spectroscopy) Verfahren, Ph.D. thesis, Universität Kassel (January 1991).

[72] J. Stahl, Defect Characterization in High-Purity Silicon after γ- and Hadron Irradiation, Ph.D. thesis, University of Hamburg, DESY-THESIS-2004-028 (July 20004).

[73] P. Blood, J. Orton, The Electrical Characterization of Semiconductors: Majority Carriers and Electron States, Vol. 14 of Techniques of Physics, Academic Press, Harcourt Brace Jovanovich, 1992.

[74] PhysTech GmbH, Am Mühlbachbogen 55d, D-85368 Moosburg, www.phystech.de (last checked: 29.04.2011).

[75] S. Weiss, DLTS-program, version 3.2 (10.03.2011), PhysTech GmbH.

[76] S. Weiss, HERA-DLTS. Software, Hardware and Theory Manuals.

[77] I. Pintilie, L. Pintilie, M. Moll, E. Fretwurst, G. Lindström, Thermally stimulated current method applied on diodes with high concentration of deep trapping levels, Appl. Phys. Lett. 78 4 (2001) 550–552.
doi:10.1063/1.1335852.

[78] I. R. Weisenberg, H. Schade, A technique for trap determinations in low-resistivity semiconductors, J. Appl. Phys. 39 (11) (1968) 5149–5151.
doi:10.1063/1.1655936.

[79] L. Forbes, C. T. Sah, On the determination of deep level center energy and concentration by thermally stimulated conductivity measured using reverse-biased p-n junctions, Solid-State Electron. 14 (1971) 182–183.

[80] M. Kuhnke, Microscopic Investigations on Various Silicon Materials Irradiated with Different Particles with the DLTS Method, Ph.D. thesis, Universität Hamburg, DESY-THESIS-2001-009 (February 2001).

[81] Boonton, Instruction Manual Model 72B Capacitance Meter 7/88.

[82] F. Hönniger, Radiation Damage in Silicon - Defect Analysis and Detector Properities -, Ph.D. thesis, Universität Hamburg, DESY-THESIS-2008-002 (January 2008).

[83] J. Pankove, N. Johnson (Eds.), Hydrogen in semiconductors, Vol. 34 of Semiconductors and Semimetals, Academic Press, INC., 1991.

[84] S. D. Brotherton, P. Bradley, Defect roduction and lifetime control in electron and γ-irradiated silicon, Journal of Applied Physics 53 (8) (1982) 5720–5732. doi:10.1063/1.331460.

[85] Y.-H. Lee, J. W. Corbett, EPR studies of defects in electron-irradiated silicon: A triplet state of vacancy-oxygen complexes, Phys. Rev. B 13 (6) (1976) 2653–2666.
doi:10.1103/PhysRevB.13.2653.

[86] I. Pintilie, E. Fretwurst, G. Lindström, J. Stahl, Close to midgap trapping level in ^{60}Co gamma irradiated silicon detectors, Applied Physics Letters 81 (1) (2002) 165–167.
doi:10.1063/1.1490397.

[87] I. Pintilie, E. Fretwurst, G. Lindström, J. Stahl, Second-order generation of point defects in gamma-irradiated float-zone silicon, an explanation for "type inversion", Applied Physics Letters 82 (13) (2003) 2169–2171.
doi:10.1063/1.1564869.

[88] E. V. Monakhov, B. S. Avset, A. Hallèn, B. G. Svensson, Formation of a double acceptor center during divacancy annealing in low-doped high-purity oxygenated Si, Phys. Rev. B 65 233207.
doi:10.1103/PhysRevB.65.233207.

[89] E. V. Monakhov, G. Alfieri, B. S. Avset, A. Hallèn, B. G. Svensson, Laplace transform transient spectroscopy study of a divacancy-related double acceptor centre in Si, J. Phys.: Condens. Matter 15 S2771–S2777.

[90] V. P. Markevich, A. R. Peaker, S. B. Lastovskii, L. I. Murin, J. L. Lindström, Defect reactions associated with divacancy elimination in silicon, J. Phys.: Condens. Matter 15 S2779–S2789.

[91] M. Mikelsen, E. V. Monakhov, G. Alfieri, B. S. Avset, B. G. Svensson, Kinetics of divacancy annealing and divacancy-oxygen formation in oxygen-enriched high-purity silicon, Phys. Rev. B 72 195207.
doi:10.1103/PhysRevB.72.195207.

[92] M. Petasecca, F. Moscatelli, D. Passeri, G. U. Pignatel, Numerical Simulation of Radiation Damage Effects in p-Type and n-Type FZ Silicon Detectors, IEEE Transactions on Nuclear Science 53 (5) (2006) 2971–2976.

[93] B. Svensson, C. Jagadish, J. Williams, Generation rate of point defects in silicon irradiated by MeV ions, Nucl. Instr. & Meth. in Physics Research B 80-81 (Part 1) (1993) 583–586.
doi:10.1016/0168-583X(93)96186-G.

[94] I. Pintilie, E. Fretwurst, G. Lindström, J. Stahl, Results on defects induced by ^{60}Co gamma irradiation in standard and oxygen-enriched silicon, Nuclear Instruments and Methods in Physics Research A 514 (2003) 18–24.
doi:10.1016/j.nima.2003.08.079.

[95] I. Pintilie, E. Fretwurst, G. Kramberger, G. Lindström, Z. Li, J. Stahl, Second-order generation of point defects in highly irradiated float zone silicon—annealing studies, Physica B 340–342 (2003) 578–582.

[96] G. Alfieri, E. V. Monakhov, B. S. Avset, B. G. Svensson, Evidence for identification of the divacancy-oxygen center in Si, Phys. Rev. B 68 (23) (2003) 233202.
doi:10.1103/PhysRevB.68.233202.

[97] I. Pintilie, G. Lindstroem, A. Junkes, E. Fretwurst, Radiation-induced point- and cluster-related defects with strong impact on damage properties of silicon detectors, Nuclear Instruments and Methods in Physics Research A 611 (2009) 52–68.
doi:10.1016/j.nima.2009.09.065.

[98] The ROSE Collaboration, R & D On Silicon for future Experiments, CERN-RD48 Collaboration.

[99] J. H. Bleka, L. Murin, E. V. Monakhov, B. S. Avset, B. G. Svensson, On the identity of a crucial defect contributing to leakage current in silicon particle detectors, Applied Physics Letters 93 (2008) 132102 1–3.
doi:10.1063/1.2896313.

[100] G. Davies, Modeling damage in silocon, Presentation helt at the 5th WODEAN meeting, NIMP Bucharest 2010.

[101] R. M. Fleming, C. H. Seager, D. V. Lang, E. Bielejec, J. M. Campbell, Defect-driven gain bistability in neutron damaged, silicon bipolar transistors, Appl. Phys. Lett. 90 172105.
doi:10.1063/1.2731516.

[102] R. M. Fleming, C. H. Seager, D. V. Lang, P. J. Cooper, E. Bielejec, J. M. Campbell, Effects of clustering on the properties of defects in neutron irradiated silicon, Journal of Applied Physics 102 043711.
doi:10.1063/1.2769783.

[103] WODEAN, Workshop on Defect Analysis in silicon detectors.

[104] V. P. Markevich, A. R. Peaker, S. B. Lastovskii, L. I. Murin, J. Coutinho, V. J. B. Torres, P. R. Briddon, L. Dobaczewski, E. V. Monakhov, B. G. Svensson, Trivacancy and trivacancy-oxygen complexes in silicon: Experiments and ab initio modeling, Physical Review B 80 235207.
doi:10.1103/PhysRevB.80.235207.

[105] M. Mikelsen, E. V. Monakhov, G. Alfieri, B. S. Avset, J. Härkönen, B. G. Svensson, Annealing of defects in irradiated silicon detector materials with high oxygen content, J. Phys.: Condens. Matter 17 S2247–S2253.
doi:10.1088/0953-8984/17/22/012.

[106] L. I. Murin, T. Hallberg, V. P. Markevich, J. L. Lindström, Experimental Evidence of the Oxygen Dimer in Silicon, Phys. Rev. Lett. 80 (1) (1998) 93–96.
doi:10.1103/PhysRevLett.80.93.

[107] J. Lindström, T. Hallberg, J. Hermansson, L. Murin, B. Komarov, V. Markevich, M. Kleverman, B. Svensson, Interaction between self-interstitials and the oxygen dimer in silicon, Physica B 308–310 (2001) 284–289.

[108] M. Mikelsen, J. H. Bleka, J. S. Christensen, E. V. Monakhov, B. G. Svensson, J. Härkönen, B. S. Avset, Annealing of the divacancy-oxygen and vacancy-oxygen complexes in silicon, Phys. Rev. B 75 155202.
doi:10.1103/PhysRevB.75.155202.

[109] M. Stavola, J. R. Patel, L. C. Kimerling, P. E. Freeland, Diffusivity of oxygen in silicon at the donor formation temperature, Appl. Phys. Lett. 42 (1) (1983) 73–75.
doi:10.1063/1.93731.

[110] P. Pellegrino, P. Lévêque, J. Lalita, A. Hallén, C. Jagadish, B. G. Svensson, Annealing kinetics of vacancy-related defects in low-dose MeV self-ion-implanted n-type silicon, Phys. Rev. B 64 (19) (2001) 195211.
doi:10.1103/PhysRevB.64.195211.

[111] M. Mikelsen, E. V. Monakhov, B. S. Avset, B. G. Svensson, On the formation of the L-centre in silicon during heat treatment in the temperature range 205–285 °C, Phys. Scr. T126:81–84.
doi:10.1088/0031-8949/2006/T126/019.

[112] L. Murin, B. G. Svensson, J, V. P. Markevich, C. A. Londos, Trivacancy-oxygen comples in silicon: Local Vibrational Mode characterization, 2010.

[113] J. W. Corbett, Electron Radiation Damage in Semiconductors and Metals, Academic Press, New York and London, 1966.

[114] C. Kittel, Introduction to Solid State Physics, 7th Edition, Wiley, New York, 1996.

[115] C. Neubüser, Annealing of the bistability of the $E4/E5$-defect, Bachelor-Arbeit, Universität Hamburg (November 2010).

[116] K. Koch, Strahlenhärte von epitaktischen, Floatzone- und Magnetic Czochralski-Siliziumdioden nach Neutronenbestrahlung, Master's thesis, Universität Hamburg (2007).

[117] G. Kramberger, V. Cindro, I. Dolenc, I. Mandic, M. Mikuz, M. Zavrtanik, Performance of silicon pad detectors after mixed irradiations with neutrons and fast charged hadrons, Nuclear Instruments and Methods in Physics Research Section A 609.
doi:10.1016/j.nima.2009.08.030.

[118] K.-H. Hoffmann, Campaign to Identify the Baseline Sensor Technology for the Phase ll Tracker Upgrade, Paper presented at the 8^{th} International Conference on Radiation Effects on Semiconductor Materials Detectors and Devices, held in Florence-Italy (12-15 Octobre 2010).

[119] K. A. Jackson, W. Schröter (Eds.), Handbook of semiconductor technology: Electronic Structure and Properties of Semiconductors, Vol. 1, Wiley-VCH, Weinheim, 2000.

[120] Y. P. Varshni, Temperature Dependence of the Energy Gap in Semiconductors, Physica 34 (1967) 149–154.

[121] V. Alex, S. Finkbeiner, J. Weber, Temperature dependence of the indirect energy gap in crystalline silicon, J. Appl. Phys. 79 (9) (1996) 6943–6946.
doi:10.1063/1.362447.

A. Appendix

A.1. Effective masses as extracted by Green [1]

The effective masses of electrons in the conduction band and holes in the valence band are two main parameters for calculations related to defect properties. The effective hole mass is inverse proportional to the slope of the valence band and can be obtained by fitting them [2], as seen in Fig. 3.2.2. For silicon we obtain two degenerated hole bands from the *spin-orbit coupling*, and therefore two masses for holes from the *heavy-* (m^*_{hh}) and *light-hole* band (m^*_{lh}) plus a *split-off* hole band (m^*_{so}). Then the effective mass is given by

$$m_{dV} = \left(m_{lh}^{*3/2} + m_{hh}^{*3/2} + [m^*_{so} \exp\left(-\Delta / k_B T\right)]^{3/2} \right) \tag{A.1.1}$$

with Δ is the difference between the energy maximum of the *split-off* hole band and the two *heavy-* and *light-hole* bands.
The conduction band however, consists of a number of sub-bands which results as a consequence in the indirect band gap for silicon. The effective masses can now be approximated from surfaces of constant energies in the *Brillouine zone* (see fig. A.1.1). For silicon there are six cigar-shaped ellipsoids in the [100], [010] and [001] direction. Fitting the ellipsoids gives two effective electron masses, m^*_l longitudinally or along the symmetry axes and m^*_t transverse to the symmetry axes. The resulting effective electron mass is given by

$$m_{dC} = M_C^{2/3} (m^*_l m^{*2}_t)^{1/3} \tag{A.1.2}$$

where M_C is the number of equivalent minima in the conduction band (here $M_C = 6$).

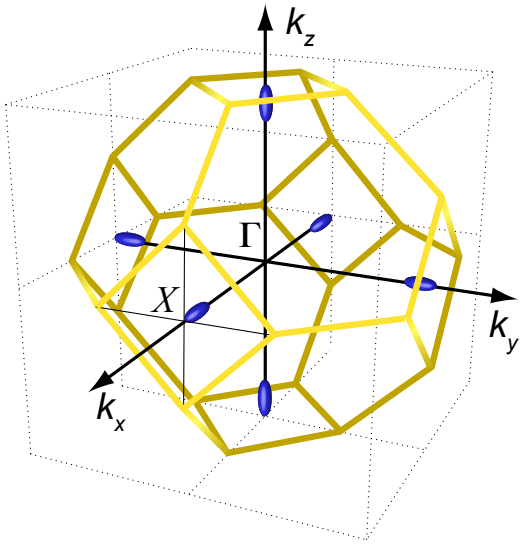

Figure A.1.1.: Ellipsoid surfaces of constant energies (valence bands) located in the *Brilluin zone*.

The measurements for obtaining lattice defect concentrations performed in this work were usually done during a temperature scan between 5 K to 300 K. This wide temperature difference requires taking into account the temperature dependence of effective masses, the band gap and the density of states. The parameterisations shown in the following were used for this work's calculations concerning concentrations and electrical properties of defects.
The **band gap** temperature dependence can be calculated by the *Varshni equation* [120]:

$$E_g(T) = E_g(0) - \frac{\alpha_g \cdot T^2}{T + \beta_g}. \tag{A.1.3}$$

Values for the parameterisation were taken from [121]: $E_g(0) = 1.1602\,\mathrm{eV}$, $\alpha_g = (4.9 \pm 0.2) \times 10^{-4}\,\mathrm{eV\,K^{-1}}$ and $\beta_g = (655 \pm 49)\,\mathrm{K}$. Fig. A.1.2 (a) shows the evolution of the band gap for temperatures in the range, necessary for this work.

The **density of states effective masses** can be calculated using the method of Green [1]. The temperature dependence can be described by the following parameterisation for electrons m_{dC} and holes m_{dV}:

$$m_{dC} = M_C^{2/3}(m_t^{*2} m_l^*)^{1/3} \tag{A.1.4}$$

$$\text{with} \quad m_t^*/m_0 = 0.1905 \times \frac{E_g(0)}{E_g(T)},\ M_c = 6 \quad \text{and} \quad m_l^*/m_0 = 0.9163 \tag{A.1.5}$$

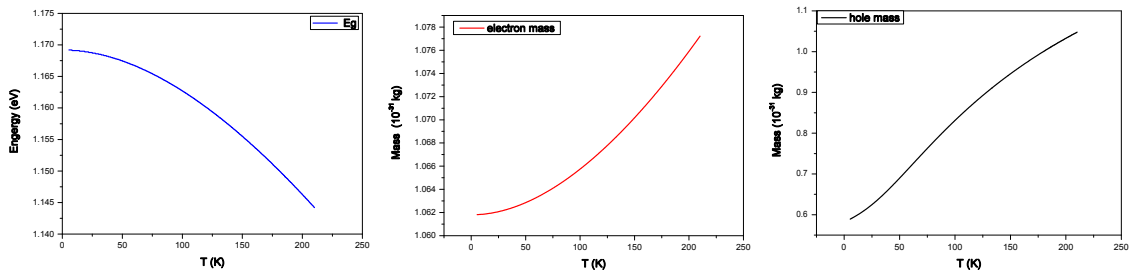

Figure A.1.2.: Temperature dependence of the band gap using Eq. A.1.3 (a) the temperature dependence of electron calculated by Eq. A.1.4 (b) and hole masses from Eq. A.1.6 (c).

and

$$\frac{m_{dV}}{m_0} = \left(\frac{a + bT + cT^2 + dT^3 + eT^4}{1 + fT + gT^2 + hT^3 + iT^4}\right)^{2/3} \tag{A.1.6}$$

with the parameters

a=0.443 587 0	b=0.360 952 8 $\times 10^{-2}$	c=0.117 351 5 $\times 10^{-3}$
d=0.126 321 8 $\times 10^{-5}$	e=0.302 558 1 $\times 10^{-8}$	f= 0.468 338 2 $\times 10^{-2}$
g=0.228 689 5 $\times 10^{-3}$	h= 0.746 927 1 $\times 10^{-6}$	i= 0.172 748 1 $\times 10^{-8}$

A.2. Fitting parameters for leakage current annealing

T_α (°C)	α_I (10^{-17} A cm^{-1})	τ_I (min)	α_0 (10^{-17} A cm^{-1})	β (10^{-18} A cm^{-1})	t_0 (min)
21	1.23	1.4×10^4	7.07	3.29	1
49	1.28	260	5.36	3.11	1
60	1.26	94	4.87	3.16	1
80	1.13	9	4.23	2.83	1
106	-	-	3.38	2.97	1

Table A.2.1.: Fit parameters for current annealing at different temperatures T_α according to Eq. 5.2.2. The results are shown in Fig. 5.2.2 as solid lines. Data taken from [32].

A.2.1. Instruments

Instrument	Type	Purpose
Agilent E4980A	LCR Meter	C-V

Continue next page ...

Instrument	Type	Purpose
ATT Mbla	Chuck system	T meas.
CTI-Cryogenics Model 22C	Close cycle refrigerator	cooling
Hameg HMP2020	Power Supply	Voltage source
HP4263	LCR Meter	C-V
Keithley 6517A/B	Electrometer/	Voltage source
	High Resistance meter	I-V
Keithley 195 A	Digital Multimeter	T measl
Keithley 485	Picoamperemeter	I-V
Keithley 6487	Electrometer/	Voltage source
	High Resistance meter	I-V
Keithley 6485	Picoamperemeter	I-V
Keithley 2700	Digital Multimeter	T-meas.
LakeShore 340	Digital Multimeter	T-meas.
Pfeiffer	Vacuum Pump	DLTS/TSC
PhysTech	FT 1030 Deep-Level	DLTS
	Transient Spectroscopy system	
Sumito heavy industries Ltd.	CKW-21	Close cycle refrigerator
Sumito heavy industries Ltd.	model RDK-205D	cold head

Table A.2.2.: Instruments used for C-V, I-V, DLTS and TSC measurements.

List of Tables

List of Figures

List of Publications

First author

2010	*Annealing study of a bistable cluster defect*, NIM A 612 (2010), pp. 525-529
2008	*Influences of cluster related defects on silicon detector properties* Proceedings to the 2008^{th} Radecs conference
2007	*Radiation induced point and cluster defects*, Diplomathesis, Universität Hamburg (November 2007)

Contributing author

2009	I. Pintilie, G. Lindström, A. Junkes and E. Fretwurst, *Radiation-induced point- and cluster-related defects with strong impact on damage properties of silicon detectors*, NIM A 611 (2009) pp. 52-68.

Last words

I wish to thank Eckhart Fretwurst without whom this work would not have been possible. Thank you Eckhart and Robert Klanner for supervising this thesis, for your patience, advice and support. Thanks also to Peter Schleper who made it possible for me to be part of the detector laboratory and to work in this amazing environment between particle physics and solid state physics.
Many thanks also to Doris Eckstein and Georg Steinbrück, they encouraged me during the whole time and pushed me to complete this work. Furthermore I want to thank Gunnar Lindström and Ioana Pintilie for their helpful comments and discussions and for the fun we had during the WODEAN conference in Bucharest.
I am grateful to the referees of my thesis and the defence: Lutz Feld, Erika Garutti and Robert Klanner.
I had a lot of fun with my Bachelor student Coralie Neubüser, thank you for doing all the measurements! To all the group members of the detector laboratory, I am very thankful for the friendly working atmosphere. You made my work in this group much easier, due to BBQing and lunch talks. Thanks Julian Becker, Joachim Erfle, Heiko Fischer, Vladymyr Khomenkov, Henning Kröhnke, Jörn Lange, Thomas Pöhlsen, Cristian Scharf, Roxana Radu, Sergej Schuwalow, Jörn Schwandt, Ajay Srivastava and Jiaguo Zhang. I wish to thank Friederike Januschek, Hanno Perrey and Thorben Theed for the interesting talks apart from physics during prolonged lunch breaks... During our discussions three hours were sometimes gone in a few minutes, at least it felt this way.
Thank you RD50 members, it was a great time and I am happy to be part of this community! Thank you Nicola Pacificio, for being a friend.
Furthermore many thanks to Dipl. Ing. Uwe Pein, who hopefully enjoys his retirement. Thank you Peter Buhmann, for the coffee supply and for the nice chat apart from physical topics (compare [49]). And of course thank you Michael Matysek, what would I have done without your support.
I learned a lot during the time at DESY-PR, and thanks to the PR-Studies Marc, Markus, Sebastian and Sergei and of course Veronika Werschner I also had a lot of fun. Many thanks!
Ausserdem möchte ich meiner Familie danken. Allen voran Robert, Du hast meine *Vielarbeiterei* genauso wie die Höhen und Tiefen miterlebt und getragen. Vielen Dank! Dank gilt natürlich auch meinen Eltern Jürgen und Hannelore, meinem kleinen nunmehr recht grossen Bruder Niclas Titus, meiner Schwester Isabell, ihrem Freund Niko und meinen Grosseltern Ruth und Günter Vagt. Ihr habt mich alle in dieser doch recht turbulenten Zeit unterstützt und bei vielen kleinen Dingen geholfen.